

Halûk Sucuođlu
Sinan Akkar

Basic Earthquake Engineering

From Seismology to Analysis
and Design



Springer

Basic Earthquake Engineering

Halûk Sucuođlu · Sinan Akkar

Basic Earthquake Engineering

From Seismology to Analysis
and Design



Springer

Halûk Sucuođlu
Department of Civil Engineering
Middle East Technical University
Ankara
Turkey

Sinan Akkar
Earthquake Engineering Department
Kandilli Observatory and Earthquake
Research Institute
Bođaziçi University
İstanbul
Turkey

ISBN 978-3-319-01025-0 ISBN 978-3-319-01026-7 (eBook)
DOI 10.1007/978-3-319-01026-7
Springer Cham Heidelberg New York Dordrecht London

Library of Congress Control Number: 2014934113

© Springer International Publishing Switzerland 2014

This work is subject to copyright. All rights are reserved by the Publisher, whether the whole or part of the material is concerned, specifically the rights of translation, reprinting, reuse of illustrations, recitation, broadcasting, reproduction on microfilms or in any other physical way, and transmission or information storage and retrieval, electronic adaptation, computer software, or by similar or dissimilar methodology now known or hereafter developed. Exempted from this legal reservation are brief excerpts in connection with reviews or scholarly analysis or material supplied specifically for the purpose of being entered and executed on a computer system, for exclusive use by the purchaser of the work. Duplication of this publication or parts thereof is permitted only under the provisions of the Copyright Law of the Publisher's location, in its current version, and permission for use must always be obtained from Springer. Permissions for use may be obtained through RightsLink at the Copyright Clearance Center. Violations are liable to prosecution under the respective Copyright Law. The use of general descriptive names, registered names, trademarks, service marks, etc. in this publication does not imply, even in the absence of a specific statement, that such names are exempt from the relevant protective laws and regulations and therefore free for general use.

While the advice and information in this book are believed to be true and accurate at the date of publication, neither the authors nor the editors nor the publisher can accept any legal responsibility for any errors or omissions that may be made. The publisher makes no warranty, express or implied, with respect to the material contained herein.

Cover image created by iyiofis, Istanbul

Printed on acid-free paper

Springer is part of Springer Science+Business Media (www.springer.com)

Preface

Objectives

Earthquake engineering is generally considered as an advanced research area in engineering education. Most of the textbooks published in this field cover topics related to graduate education and research. There is a growing need, however, for the use of basic earthquake engineering knowledge, especially, in the earthquake resistant design of structural systems. Civil engineering graduates who are concerned with structural design face the fundamental problems of earthquake engineering more frequently in their professional careers. Hence, an introductory level textbook covering the basic concepts of earthquake engineering and earthquake resistant design is considered as an essential educational instrument to serve for this purpose.

This book aims at introducing earthquake engineering to senior undergraduate students in civil engineering and to master's students in structural engineering who do not have a particular background in this area. It is compiled from the lecture notes of a senior level undergraduate course and an introductory level graduate course thought over the past 12 years at the Middle East Technical University, Ankara, Turkey. Those students who take the course learn the basic concepts of earthquake engineering and earthquake resistant design such as origin of earthquakes, seismicity, seismic hazard, dynamic response, response spectrum, inelastic response, seismic design principles, seismic codes and capacity design. A prior knowledge of rigid body dynamics, mechanics of vibrations, differential equations, probability and statistics, numerical methods and structural analysis, which are thought in the second and third year curriculum of undergraduate civil engineering education, is sufficient to grasp the focus points in this book. Experience from the past 12 years proved that students benefitted enormously from this course, both in their early professional careers and in their graduate education, regardless of their fields of expertise in the future.

The main objective of the book is to provide basic teaching material for an introductory course on structural earthquake engineering. Advanced topics are intentionally excluded, and left out for more advanced graduate courses. The

authors believe that maintaining simplicity in an introductory textbook is a major challenge while extending the coverage to advanced topics is trivial. Hence, the majority of the information provided in the book is deliberately limited to senior undergraduate and introductory graduate levels while a limited number of more advanced topics are included as they are frequently encountered in many engineering applications. Each chapter contains several examples that are easy to follow, and can mostly be solved by a hand calculator or a simple computational tool.

Organization of Chapters

Chapter 1 discusses the basic physical and dynamic factors triggering earthquakes; global tectonics, fault rupture, formation of ground shaking and its effect on the built environment. Measurement of earthquake size and intensity is also defined in this chapter.

Chapter 2 introduces basic elements of probabilistic and deterministic seismic hazard assessment. Uniform hazard spectrum concept is the last topic covered in **Chap. 2**.

Chapter 3 presents dynamic response of simple (single degree of freedom) systems to earthquake ground motions. Analytical and numerical solutions of the equation of motion are developed. Response spectrum, inelastic response and force reduction concepts in seismic design are discussed herein.

Chapter 4 introduces linear elastic earthquake design spectra and the inelastic (reduced) design spectra. This chapter also presents the fundamentals of seismic hazard map concept employed in seismic design codes, particularly in Eurocode 8 and NEHRP provisions, together with ASCE 7 standards.

Chapter 5 develops the dynamic response analysis of building structures under ground shaking. Modal superposition, equivalent lateral load analysis, response spectrum analysis and pushover analysis are presented progressively. Analysis of base isolated structures is also included.

Chapter 6 extends the analysis methods in **Chap. 5** to three-dimensional, torsionally coupled buildings. Basic design principles and performance requirements for buildings in seismic design codes are presented.

Chapter 7 is particularly devoted to the capacity design of reinforced concrete structures in conformance with the modern design codes including Eurocode 8 and ASCE 7. Ductility in concrete and capacity design principles are discussed in detail. This chapter is concluded with a comprehensive example on the design and detailing of a reinforced concrete frame.

Suggestions for Instructors

The material in this book may serve for developing and teaching several courses in the senior undergraduate and graduate levels of civil engineering education during a 13- or 14-week semester of about three lecture hours per week.

Earthquake Engineering at Senior Undergraduate Level

A selected coverage of topics is suggested from the book for an introductory course on earthquake engineering at the undergraduate level. [Chapter 1](#) can be summarized in a week in a slide presentation form. [Chapter 2](#) may also be summarized in a week through describing the fundamentals of seismic hazard analysis methodology. Sections 3.6.3–3.6.7 can be excluded from [Chap. 3](#) in teaching an undergraduate course. [Chapter 4](#) is advised to be given in a practical manner, with more emphasis on defining the design spectra directly according to Eurocode 8 and ASCE 7. Sections 5.8 and 5.9 can also be excluded from [Chap. 5](#). Full coverage of [Chaps. 6](#) and [7](#) is necessary for introducing the basics of earthquake resistant building design.

Earthquake Engineering at Graduate Level

The entire book can be covered in a first course on earthquake engineering at the graduate level. [Chapter 2](#) can be shortened by introducing the classical probabilistic and deterministic hazard assessment methods with emphasis on their elementary components, while step-by-step descriptions of probabilistic and deterministic hazard assessment methods can be ignored. Assuming that the students have already taken structural dynamics, Sects. 3.1, 3.2, 3.4.1 and 3.4.2 can be skipped in [Chap. 3](#). Similarly Sects. 5.1, 5.2 and 5.5 can be excluded from [Chap. 5](#).

Engineering Seismology and Hazard Assessment at Graduate Level

The first four chapters of the book can be good teaching sources for a graduate level engineering seismology course for civil engineering students. The content of the [Chap. 1](#) can be extended by the cited reference text books and can be given to the student in the first 3 weeks of the course. Seismic hazard assessment covered in [Chap. 2](#) can be taught in 4–5 weeks. The instructor can start refreshing the basics of probability before the main subjects in seismic hazard assessment. The elastic

response spectrum concept that is discussed in [Chap. 3](#) can follow the seismic hazard assessment and simple applications on the computation of uniform hazard spectrum can be given to the students from the materials taught in [Chaps. 2](#) and [3](#). The last 2 or 3 weeks of the course can be devoted on the code approaches for the definition of elastic seismic forces that are discussed in [Chap. 4](#).

Acknowledgments

The authors gratefully acknowledge the support of Kaan Kaatsız, Soner Alıcı, Tuba Erođlu and Sadun Tanıřer who contributed to the illustrations and examples in the text.

The authors also thank Dr. Erdem Canbay for providing several figures in [Chap. 7](#), and Dr. Michael Fardis for reviewing [Chaps. 6](#) and [7](#).

January 2014, Ankara

Halûk Sucuođlu
Sinan Akkar

Contents

1	Nature of Earthquakes	1
1.1	Dynamic Earth Structure	1
1.1.1	Continental Drift	4
1.1.2	Theory of Global Plate Tectonics	6
1.2	Earthquake Process and Faults	14
1.3	Seismic Waves	17
1.4	Magnitude of an Earthquake	21
1.5	Intensity of an Earthquake	24
1.5.1	Instrumental Intensity	24
1.5.2	Observational Intensity	28
1.6	Effects of Earthquakes on Built Environment	34
1.6.1	Strong Ground Shaking	34
1.6.2	Fault Rupture	34
1.6.3	Geotechnical Deformations	36
2	Seismic Hazard Assessment	41
2.1	Introduction	41
2.2	Seismicity and Earthquake Recurrence Models	42
2.3	Ground-Motion Prediction Equations (Attenuation Relationships)	50
2.4	Probabilistic Seismic Hazard Analysis	53
2.5	Deterministic Seismic Hazard Analysis	61
2.6	Uniform Hazard Spectrum	63
2.7	Basic Probability Concepts	63
3	Response of Simple Structures to Earthquake Ground Motions	75
3.1	Single Degree of Freedom Systems	75
3.1.1	Ideal SDOF Systems: Lumped Mass and Stiffness	75
3.1.2	Idealized SDOF Systems: Distributed Mass and Stiffness	76
3.2	Equation of Motion: Direct Equilibrium	77
3.3	Equation of Motion for Base Excitation	78
3.4	Solution of the SDOF Equation of Motion	79
3.4.1	Free Vibration Response	79

- 3.4.2 Forced Vibration Response: Harmonic Base Excitation. 85
- 3.4.3 Forced Vibration Response: Earthquake Excitation 87
- 3.4.4 Numerical Evaluation of Dynamic Response 87
- 3.4.5 Integration Algorithm 91
- 3.5 Earthquake Response Spectra 93
 - 3.5.1 Pseudo Velocity and Pseudo Acceleration Response Spectrum 95
 - 3.5.2 Practical Implementation of Earthquake Response Spectra 97
- 3.6 Nonlinear SDOF Systems 98
 - 3.6.1 Nonlinear Force-Deformation Relations 98
 - 3.6.2 Relationship Between Strength and Ductility in Nonlinear SDOF Systems 100
 - 3.6.3 Equation of Motion of a Nonlinear SDOF System 102
 - 3.6.4 Numerical Evaluation of Nonlinear Dynamic Response 102
 - 3.6.5 Ductility and Strength Spectra for Nonlinear SDOF Systems 106
 - 3.6.6 Ductility Reduction Factor (R_μ) 108
 - 3.6.7 Equal Displacement Rule 110
- 4 Earthquake Design Spectra 117**
 - 4.1 Introduction 117
 - 4.2 Linear Elastic Design Spectrum 118
 - 4.2.1 Elastic Design Spectrum Based on Eurocode 8 119
 - 4.2.2 Elastic Design Spectrum Based on NEHRP Provisions and ASCE 7 Standards 124
 - 4.2.3 Effect of Damping on Linear Elastic Design Spectrum 135
 - 4.2.4 Structure Importance Factor (I) 136
 - 4.3 Reduction of Elastic Forces: Inelastic Design Spectrum 137
 - 4.3.1 Minimum Base Shear Force 141
- 5 Response of Building Frames to Earthquake Ground Motions 145**
 - 5.1 Introduction 145
 - 5.2 Equations of Motion Under External Forces 146
 - 5.3 Equations of Motion Under Earthquake Base Excitation 147
 - 5.4 Static Condensation 149
 - 5.5 Undamped Free Vibration: Eigenvalue Analysis 151
 - 5.5.1 Vibration Modes and Frequencies 153
 - 5.5.2 Normalization of Modal Vectors 157
 - 5.5.3 Orthogonality of Modal Vectors 158
 - 5.5.4 Modal Expansion of Displacements 159

- 5.6 Solution of Equation of Motion Under Earthquake Excitation. 160
 - 5.6.1 Summary: Modal Superposition Procedure. 161
 - 5.6.2 Response Spectrum Analysis 162
 - 5.6.3 Modal Combination Rules 162
 - 5.6.4 Equivalent Static (Effective) Modal Forces 164
- 5.7 Limitations of Plane Frame (2D) Idealizations
for 3D Frame Systems 183
- 5.8 Nonlinear Static (Pushover) Analysis 184
 - 5.8.1 Capacity Curve for Linear Elastic Response. 186
 - 5.8.2 Capacity Curve for Inelastic Response. 186
 - 5.8.3 Target Displacement Under Design Earthquake 187
- 5.9 Seismic Response Analysis of Base Isolated Buildings 190
 - 5.9.1 General Principles of Base Isolation 190
 - 5.9.2 Equivalent Linear Analysis of Base Isolation Systems
with Inelastic Response 194
 - 5.9.3 Critical Issues in Base Isolation 196
- 6 Analysis Procedures and Seismic Design Principles
for Building Structures 203**
 - 6.1 Introduction 203
 - 6.2 Rigid Floor Diaphragms and Dynamic Degrees of Freedom
in Buildings 204
 - 6.3 Equations of Motion for Buildings Under Earthquake
Base Excitation 205
 - 6.3.1 Mass Matrix 205
 - 6.3.2 Stiffness Matrix 206
 - 6.4 Free Vibration (Eigenvalue) Analysis. 210
 - 6.4.1 The Effect of Building Symmetry on Mode Shapes. 212
 - 6.5 Analysis Procedures for Buildings in Seismic Codes 215
 - 6.6 Modal Response Spectrum Analysis 216
 - 6.6.1 Summary of Modal Response Spectrum Analysis
Procedure. 217
 - 6.6.2 The Minimum Number of Modes 218
 - 6.6.3 Accidental Eccentricity 218
 - 6.7 Equivalent Static Lateral Load Procedure. 223
 - 6.7.1 Base Shear Force in Seismic Codes 225
 - 6.7.2 Estimation of the First Mode Period T_1 226
 - 6.7.3 Lateral Force Distribution in Seismic Codes. 227
 - 6.8 Basic Design Principles and Performance Requirements
for Buildings. 228
 - 6.9 Structural Irregularities. 230
 - 6.9.1 Irregularities in Plan 230
 - 6.9.2 Irregularities in Elevation. 231
 - 6.9.3 Selection of the Analysis Procedure 232

6.10	Deformation Control in Seismic Codes	233
6.10.1	Interstory Drift Limitation	233
6.10.2	Second Order Effects.	235
6.10.3	Building Separations	237
7	Seismic Design of Reinforced Concrete Structures.	241
7.1	Introduction	241
7.2	Capacity Design Principles	242
7.3	Ductility in Reinforced Concrete	243
7.3.1	Ductility in Reinforced Concrete Materials	243
7.3.2	Ductility in Reinforced Concrete Members	244
7.4	Seismic Design of Ductile Reinforced Concrete Beams	246
7.4.1	Minimum Section Dimensions	246
7.4.2	Limitations on Tension Reinforcement	246
7.4.3	Minimum Compression Reinforcement	247
7.4.4	Minimum Lateral Reinforcement for Confinement	247
7.4.5	Shear Design of Beams	248
7.5	Seismic Design of Ductile Reinforced Concrete Columns.	250
7.5.1	Limitation on Axial Stresses.	250
7.5.2	Limitation on Longitudinal Reinforcement.	251
7.5.3	Minimum Lateral Reinforcement for Confinement	251
7.5.4	Strong Column-Weak Beam Principle	253
7.5.5	Shear Design of Columns	254
7.5.6	Short Column Effect	259
7.6	Seismic Design of Beam-Column Joints in Ductile Frames.	260
7.6.1	Design Shear Force	260
7.6.2	Design Shear Strength	263
7.7	Comparison of the Detailing Requirements of Modern and Old Seismic Codes	263
7.8	Seismic Design of Ductile Concrete Shear Walls	264
7.8.1	Seismic Design of Slender Shear Walls	265
7.8.2	Seismic Design of Squat Shear Walls	270
7.9	Capacity Design Procedure: Summary	272
	References	283
	Index	285

Chapter 1

Nature of Earthquakes

Abstract This chapter introduces some of the basic concepts in Engineering Seismology that should be familiar to earthquake engineers who analyze and design structures against earthquake induced seismic waves. The majority of these concepts are also used as tools to assess seismic hazard for quantifying earthquake demands on structures. The chapter begins with a summary of the main components of Earth's interior structure and their interaction with each other in order to describe the physical mechanism triggering the earthquakes. These introductory discussions lead to the definitions of earthquake types, their relation with global plate movements and resulting faulting styles. The magnitude scales for determining the earthquake size as well as primary features of seismic waveforms that are used to quantify earthquake intensity follow through. The characteristics of accelerograms that are mainly used to compute the ground-motion intensity parameters for engineering studies as well as the macroseismic intensity scales that qualitatively inform about the earthquake influence over the earthquake affected area are discussed towards the end of the chapter. The chapter concludes by a brief overview on the effects of earthquake shake on the built and geotechnical environment to emphasize the extent of earthquake related problems and broad technical areas that should be focused by earthquake engineers.

1.1 Dynamic Earth Structure

The internal structure of the Earth is one of the key parameters to understand the major seismic activity around the world. The Earth may be considered to have three concentric layers (Fig. 1.1). The innermost part of the Earth is the core and it is mainly composed of iron. The core has two separate parts: the inner core and outer core. The inner core is solid and the outer core is liquid. The mantle is between the crust (outermost layer of the earth) and the core. The abrupt changes in the propagation velocity of seismic waves (Fig. 1.2) differentiate the mantle, the outer core and the inner core. The sudden variation in the seismic wave velocity close to the

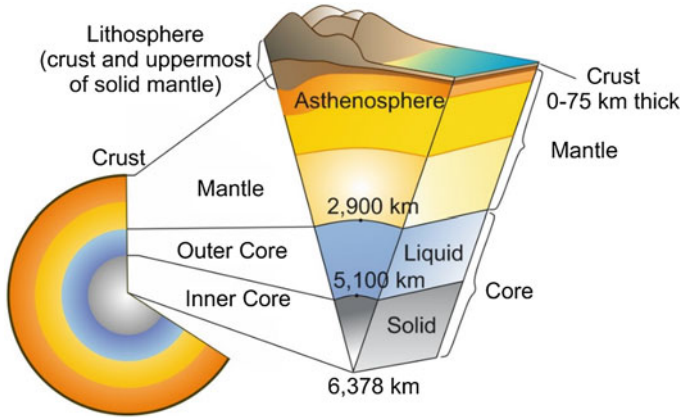
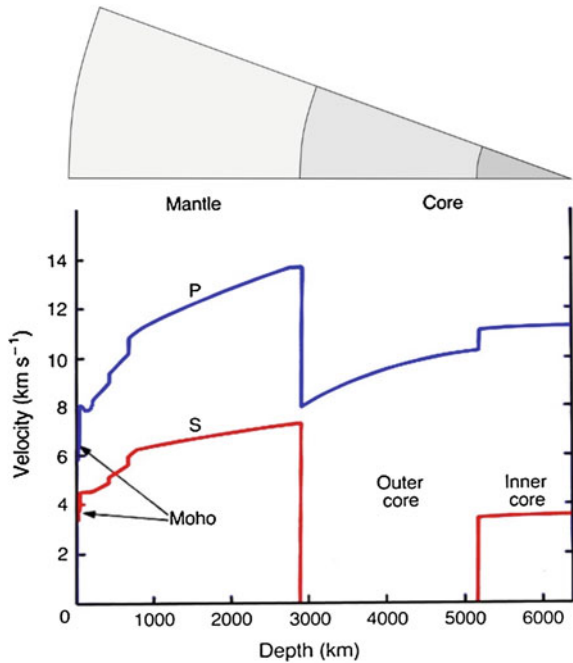


Fig. 1.1 Earth's interior structure: major layers

Fig. 1.2 Variation of P- and S-wave velocities along different layers of Earth (modified from Shearer 1999)



crustal surface is due to Moho discontinuity (recognized by the Croatian seismologist Mohorovičić in 1909) and it is accepted as the boundary between the mantle and the crust (Fig. 1.2). The crust thickness is approximately 7 km under the oceans. Its average thickness is 30 km under the continents and attains even thicker

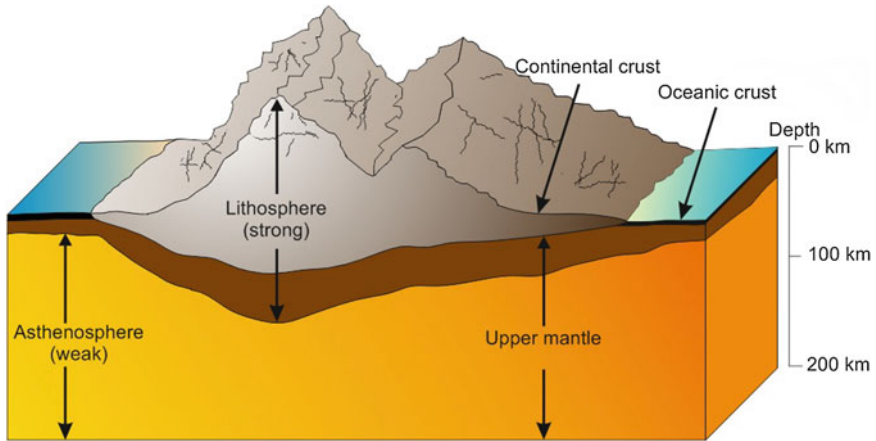
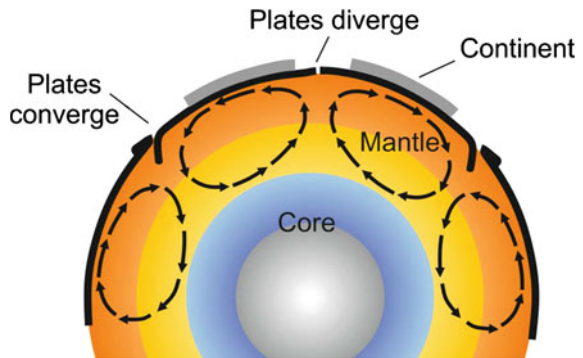


Fig. 1.3 Illustration of the lithosphere and asthenosphere (modified from Press and Siever 1986)

Fig. 1.4 Heat convection mechanism and the relative motion of lithospheric plates due to heat convection currents (modified from Press and Siever 1986)



values under the mountain ranges. The crust has basaltic structure under the oceans whereas it is mainly comprised of basalt and granite under the continents.

The lithosphere and asthenosphere are the two outermost boundaries of the Earth that are defined in terms of material strength and stiffness (Fig. 1.3). The lithosphere is rigid and relatively strong. It is mainly formed of the crust and the outermost part of the mantle. The thickness of lithosphere is approximately 125 km. The asthenosphere lies below the lithosphere and it forms mainly the weak part of the mantle (a softer layer) that can deform through creep. The lithosphere can be considered to float over the asthenosphere.

The interior of the Earth is in constant motion that is driven by heat. The source of heat is the radioactivity within the core. The temperature gradient across

the Earth sets up a heat flow towards the surface from the outer core and the mechanism of heat transfer is convection. Convection currents within the asthenosphere moves the lithospheric plates (tectonic plates) like a conveyor belt (Fig. 1.4). The movement of these plates results in two slabs diverging from each other, or converging to each other. When two slabs converge to each other, they collide and one slab descends beneath the other one.

1.1.1 Continental Drift

The physical process described in the previous section also explains the continuous motion of the continents. In fact, 225 million years ago all of the continents had formed a single landmass, called Pangaea. This continent broke up, initially forming two continents, Laurasia and Gondwanaland, about 200 million years ago. By 135 million years ago, Laurasia had split into the continents of North America and Eurasia, and Gondwanaland had divided into the continents of India, South America, Africa, Antarctica and Australia. These continents have continued to move and have come to their current configuration, including the collision of India with Eurasia about 50 million years ago. The entire process is illustrated in Fig. 1.5.

The pioneering explanations about the motion of continents were done by a few geologists in the second half of the 20th century. One of these earth scientists was Richard Field who studied the geology of the ocean floor. The discovery of mountain chains (ridges) along the major oceans as shown in Fig. 1.6 and observations on the dense seismic activity along the oceanic ridges indicated that these zones are under continuous deformation. In 1960, Harry Hess proposed the theory of sea-floor spreading and suggested that the ocean floor is formed continuously by the magma that rises up from within the mantle into the central gorges of the oceanic ridges (Fig. 1.7). The magma spreading out from the gorges pushes the two sides of the ridge apart. This mechanism separates the two tectonic plates from each other as in the case of African and South American continents. Today the continuous formation of ocean floor still moves these two continents apart from each other. The separation of African and South American continents was first documented by the German meteorologist Alfred Wegener in 1915 by comparing the geological structures, mineral deposits and fossils of both flora and fauna from the two sides of the Atlantic Ocean. Wegener's hypothesis on continental drift was not appreciated by the scientific community at those days as he failed to provide the physical explanation behind the separation process.

The new oceanic crust that is formed continuously at the mid-oceanic ridges should expand the Earth unless another mechanism consumes the older material that is in excess due to the newly formed material. There are regions in the oceanic floor where the lithosphere is descending into the mantle, being consumed at the same rate that new crust is being generated at the oceanic ridges (Fig. 1.8). This process is known as subduction and it occurs where two plates collide and one is

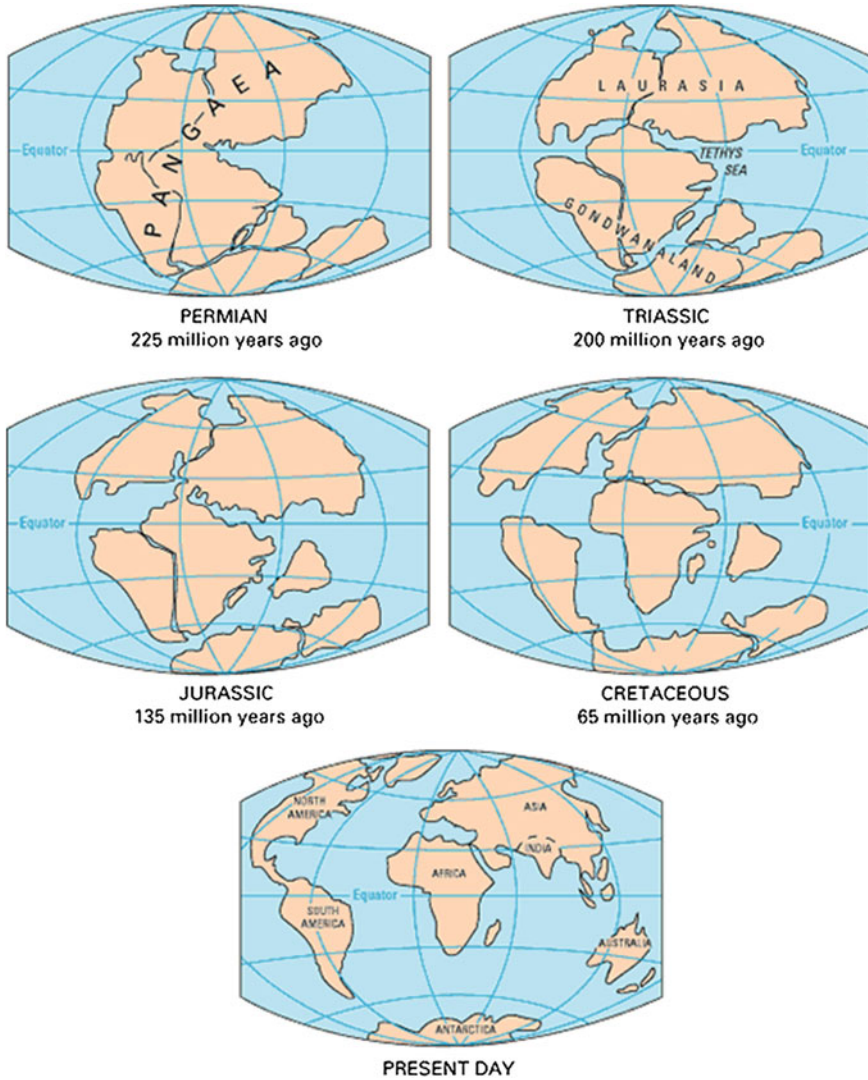


Fig. 1.5 Motion of the continents during the past 225 million years (<http://pubs.usgs.gov/gip/dynamic/historical.html>)

pushed down below the other. The seismic activity is intense in subduction regions as in the case of mid-oceanic ridges due to high deformation rates between the colliding slabs. Volcanic activity is the other specific feature observed in the subduction regions. These are discussed further in the theory of global plate tectonics.



Fig. 1.6 Mid-oceanic ridges on the sea floor of Atlantic Ocean

1.1.2 Theory of Global Plate Tectonics

The evidence provided by the mechanisms of mid-oceanic ridges and subduction regions as well as high seismic activity at these zones was used to formulate the theory of global plate tectonics (e.g., Isacks et al. 1968; McKenzie 1968). The Earth's surface is divided into a number of lithospheric slabs called tectonic plates and they move relative to each other as a result of the underlying convection currents in the mantle. The vectors in Fig. 1.9 show the directions of relative motions of tectonic plates. Tectonic plates interact at their boundaries in one of the three ways as shown in Fig. 1.10. At the ocean ridges, plates move apart from each other and they are called as divergent plate boundaries. At convergent boundaries (where two plates collide), one plate will usually be driven below the other in the process of subduction. Oceanic plate is subducted below continental plate along the Pacific coast of South and Central America; oceanic crust is subducted below oceanic crust in the Caribbean arc. In the subduction process, the younger

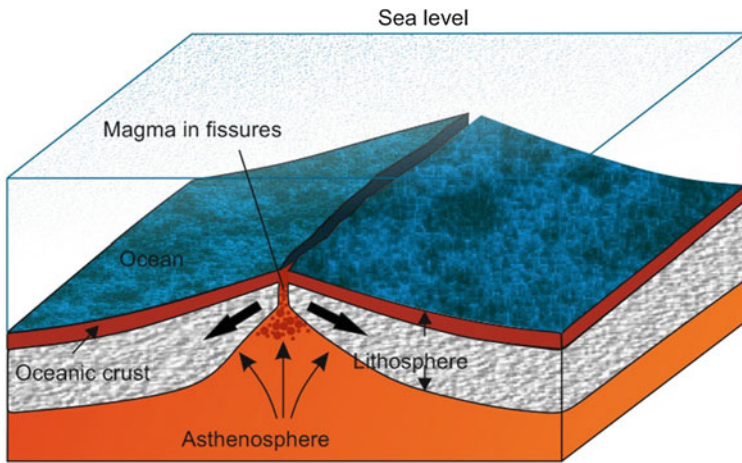


Fig. 1.7 Basic mechanism of sea-floor spreading: the magma rising up from the mantle pushes the two sides of the ridge apart, cools off in time and forms the new oceanic slab

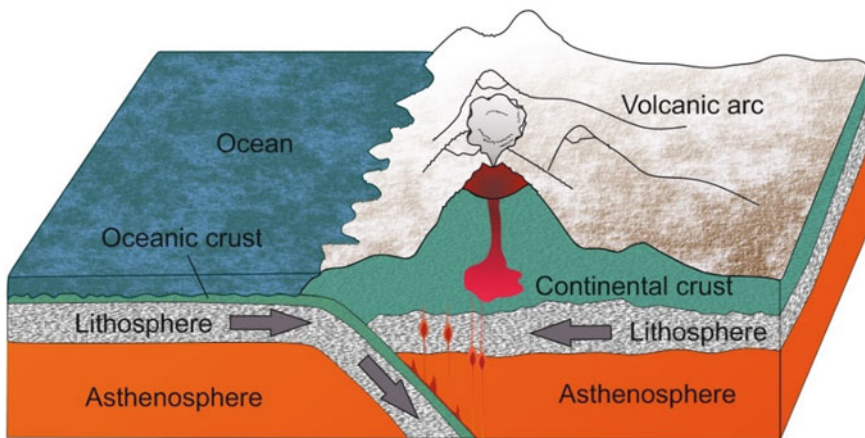


Fig. 1.8 Subduction mechanism. The relatively younger and denser oceanic crust subducts beneath the continental crust. Volcanic activity is frequently observed along the active margins of subduction zones

lithospheric slab descends below the older one as it is the denser of the colliding slabs. As oceanic crust is continuously formed due to sea-floor spreading, it is younger and denser than the continental crust. Thus, it is the oceanic slab subducting beneath the continental slab when the oceanic and continental slabs collide. If two continental plates collide, there is enormous deformation and thickening of the lithosphere along the boundary (e.g., the Himalayas). Two plates can also move horizontally, pass one another at transform (or transcurrent) boundaries. Such

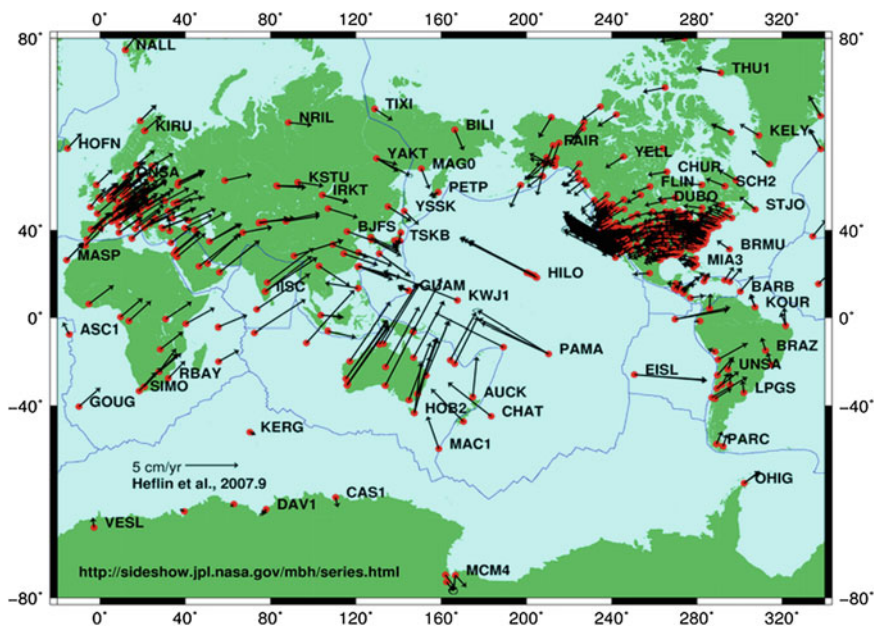


Fig. 1.9 Vectors (*arrows*) showing the major directions of relative motions of the global tectonic plates (<http://sideshow.jpl.nasa.gov/mbh>)

boundaries can be seen along long and well-defined faults such as the San Andreas Fault in California, which is the boundary between the North American and Pacific plates. The North Anatolian Fault in Turkey constitutes another example of transform boundary between the Eurasian and Anatolian plates. Figure 1.11 shows the distribution of three major plate boundaries around the globe.

The majority of seismic activity can be explained by the relative motion of tectonic plates as emphasized in the above paragraphs. Figure 1.12 shows that almost all earthquakes around the world are located along the boundaries of tectonic plates and they are called as interplate earthquakes. The circumference of Pacific Ocean where generally subduction process occurs between the oceanic and continental slabs is the most active boundary region in this sense. The Mediterranean Sea and surroundings including the Azores islands in the Atlantic Ocean as well as a significant portion of Asia constitute the other plate boundary regions generating interplate earthquakes. The interplate earthquakes in these regions result from all types of tectonic plate interactions: convergent, divergent and transform.

The earthquakes that occur away from plate boundaries (e.g., earthquakes occurring in the northeast America, Australia, central India and northeast Brazil) are called as intraplate earthquakes. The driving mechanisms of interplate and intraplate earthquakes are different. High deformations along plate boundaries trigger the interplate events. No such clear boundaries exist in regions generating

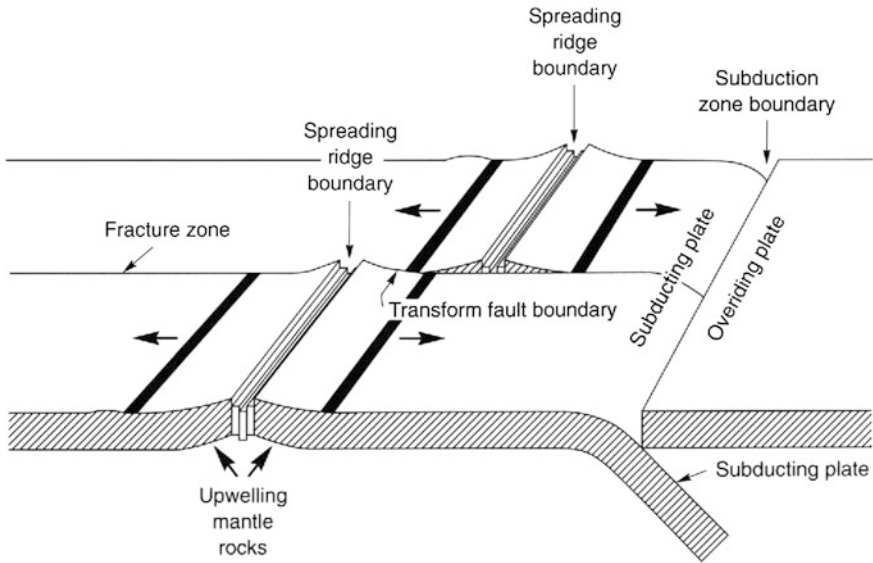


Fig. 1.10 Divergent (along oceanic ridges), convergent (along subduction regions) and transform plate boundaries and their interaction with each other (Shearer 1999). New crust is formed at divergent boundaries and existing material is consumed at convergent boundaries. Transform boundaries neither consumes nor generates new material

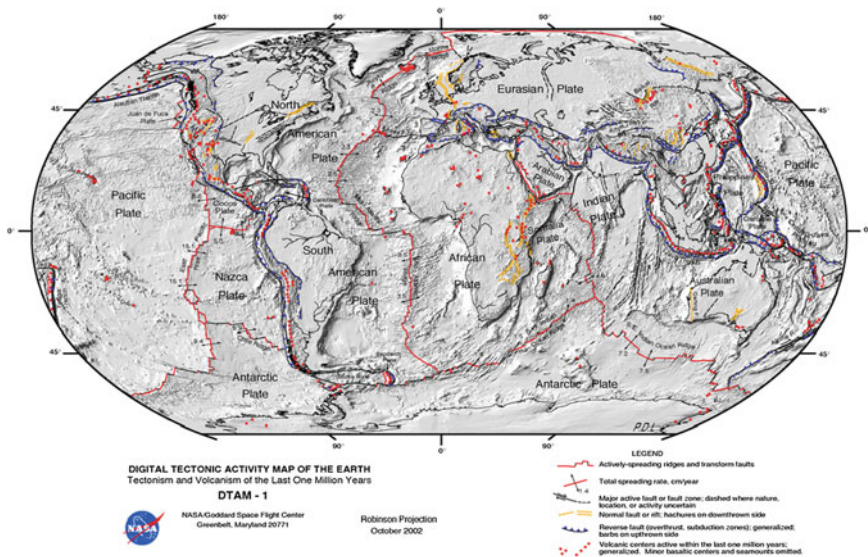


Fig. 1.11 Global tectonic plates and the nature of their boundaries

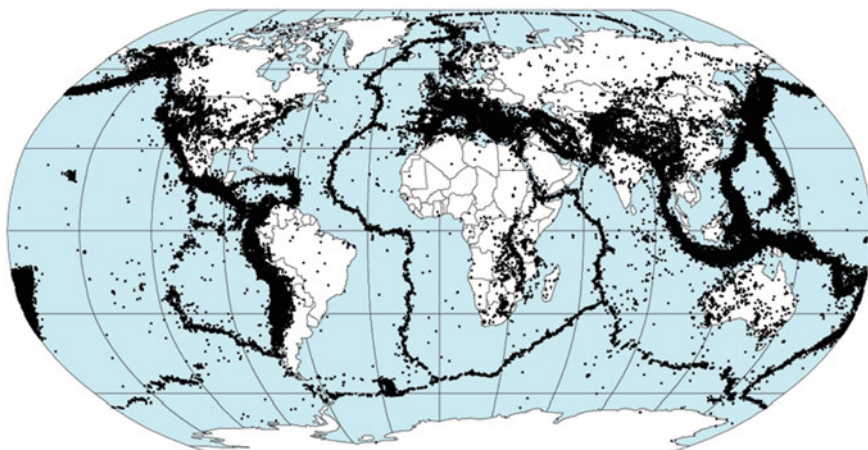


Fig. 1.12 Earthquake activity around the world in the period from 1977 to 1994 (<http://denali.gsfc.nasa.gov/dtam/seismic/>)

intraplate earthquakes and their explanation is not straightforward as in the case of interplate earthquakes. The regions where intraplate events observed are called stable continental regions. Their seismic activity is low when compared to the seismic activity of plate boundaries. Although large earthquakes in stable continental regions are not frequent, their sizes can be significant whenever they occur. For example, three intraplate earthquakes having magnitudes between 7.5 and 7.7 occurred in the New Madrid Zone in the central United States between December 1811 and February 1812. The New Madrid Zone is one of the well-known stable continental regions in the world and the three aforementioned earthquakes are among the top largest events in North America during the past 200 years. Their locations as well as the distribution of seismic activity in the New Madrid Zone are presented in Fig. 1.13. The map in Fig. 1.13 also shows the Wabash Valley and its seismicity that is identified as another stable continental region in the North America.

Figure 1.14 details the subduction mechanism for an oceanic slab undergoing beneath a continental slab. The earthquake activity in the subducted oceanic slab takes place at significantly large depths that can reach as much as 750 km. There are also shallower earthquakes in the subduction regions that occur along the interface between the oceanic and continental plates. Seismologists distinguish the latter type of earthquakes as interface earthquakes whereas the deep subduction earthquakes are generally called as inslab earthquakes. The large contact surfaces between the oceanic and crustal slabs along the interface result in large-size interface earthquakes. Volcanic activity is also frequently observed in subduction regions as illustrated in Fig. 1.14. The gradual temperature increase towards the interior of Earth heats the oceanic crust. When the lower density material forming the oceanic crust comes to the melting point, it rises towards the surface and erupts

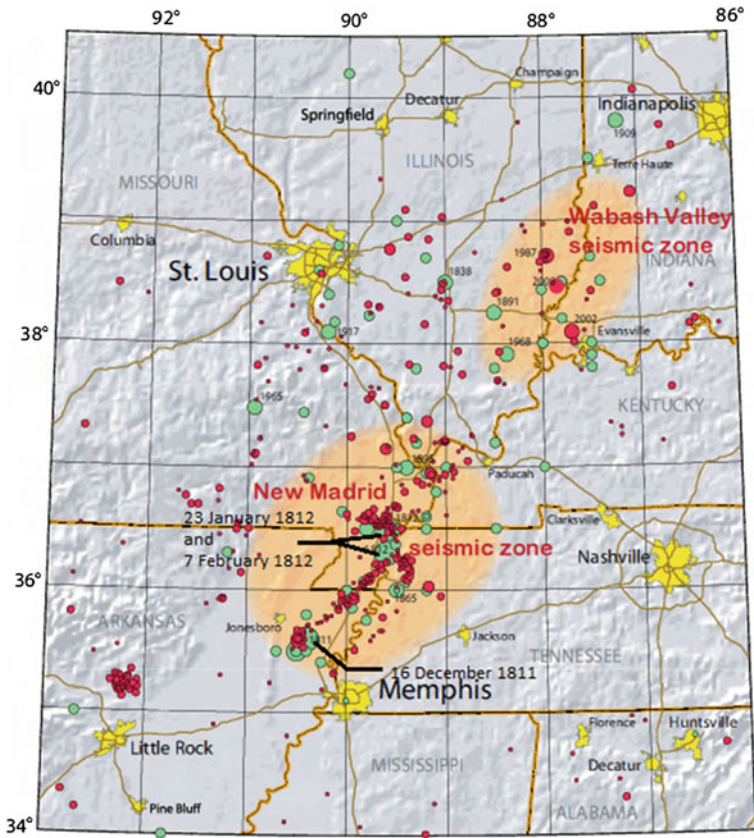


Fig. 1.13 Seismic activity in the New Madrid and Wabash Valley zones (orange patches) in the central US. The map also shows the earthquakes (circles) in these regions between 1974 and 2002 (red circles) and before 1974 (green circles). Larger earthquakes are represented by larger circles. The locations of the three large earthquakes that occurred between 1811 and 1812 are shown by solid black lines on the map (<http://earthquake.usgs.gov/earthquakes/states/events/1811-1812.php>)

at the weakest point on the crust. This mechanism forms the volcanos and triggers the volcanic activity.

Table 1.1 lists the worldwide occurrences of earthquakes in each year for different magnitude¹ intervals. This table gives an overall idea about the annual seismic activity around the globe. As one can infer from Table 1.1, moderate-to-large magnitude earthquakes (magnitudes 5 and above) constitute a relatively small fraction of overall annual seismicity. The number of small magnitude

¹ Magnitude is a measure of earthquake size and discussed in the subsequent sections of this chapter.

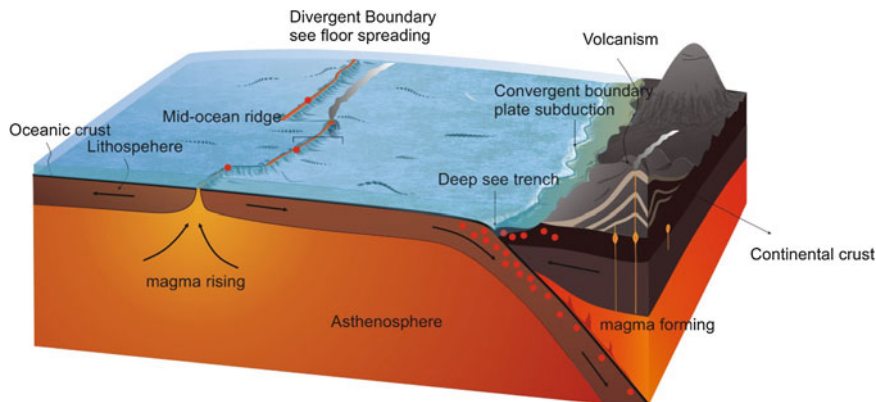


Fig. 1.14 Illustration of subduction mechanism. The *red circles* on the descending oceanic crust are the earthquakes. The interface earthquakes are those occurring along the contact surface between the oceanic and continental crust. The in slab earthquakes occur at large depths due to rupturing of subducting oceanic crust (modified from Press and Siever 1986). Volcanic activity is part of subduction mechanism as illustrated in the sketch

Table 1.1 Annual occurrence of earthquakes in the world (earthquake.usgs.gov/earthquakes/eqarchives/year/eqstats.php)

Magnitude	Annual average
8 and higher	1 ^a
7–7.9	15 ^a
6–6.9	134 ^b
5–5.9	1,319 ^b
4–4.9	13,000 (estimated)
3–3.9	130,000 (estimated)
2–2.9	1,300,000 (estimated)

The list is extracted by the United States Geological Survey from the Centennial Catalog (Engdahl and Villaseñor 2002) and PDE (Preliminary Determination of Earthquakes) Bulletin (earthquake.usgs.gov/research/data/pde.php)

^a Based on observations since 1900

^b Based on observations since 1990

earthquakes is significant and their accuracy in terms of size and quantity is directly correlated with the density of global and local seismic networks deployed all around the world. The increase in the number of seismic recording stations will improve the detection and location of small magnitude events that would eventually yield more reliable statistics about their occurrence rates. Table 1.2 lists the largest and deadliest earthquakes in the World between 1990 and 2012 that is compiled by the United States Geological Survey (USGS). Some of these events, although not as large as many others listed in the table, caused significant casualties due to poorly engineered or non-engineered structures in regions where they occurred (e.g., 12 January 2010, Haiti earthquake).

Table 1.2 The most remarkable earthquakes in the world between 1990 and 2012 (<http://earthquake.usgs.gov/earthquakes/eqarchives/year/byyear.php>)

Date	Magnitude	Fatalities	Region
11 April 2012	8.6		Off the west coast of northern Sumatra
06 February 2012	6.7	113	Negros–Cebu region, Philippines
11 March 2011	9.0	20,896	Near the east coast of Honshu, Japan
27 February 2010	8.8	507	Offshore Maule, Chile
12 January 2010	7.0	316,000	Haiti
30 September 2009	7.5	1,117	Southern Sumatra, Indonesia
29 September 2009	8.1	192	Samoa Islands region
12 May 2008	7.9	87,587	Eastern Sichuan, China
12 September 2007	8.5	25	Southern Sumatera, Indonesia
15 August 2007	8.0	514	Near the coast of central Peru
15 November 2006	8.3	0	Kuril Islands
26 May 2006	6.3	5,749	Java, Indonesia
08 October 2005	7.6	80,361	Pakistan
28 March 2005	8.6	1,313	Northern Sumatra, Indonesia
26 December 2004	9.1	227,898	Off west coast of northern Sumatra
26 December 2003	6.6	31,000	Southeastern Iran
25 September 2003	8.3	0	Hokkaido, Japan Region
03 November 2002	7.9	0	Central Alaska
25 March 2002	6.1	1,000	Hindu Kush region, Afghanistan
23 June 2001	8.4	138	Near coast of Peru
26 January 2001	7.7	20,023	India
16 November 2000	8.0	2	New Ireland region, P.N.G.
04 June 2000	7.9	103	Southern Sumatera, Indonesia
20 September 1999	7.7	2,297	Taiwan
17 August 1999	7.6	17,118	Marmara, Western Turkey
30 May 1998	6.6	4,000	Afghanistan–Tajikistan border region
25 March 1998	8.1	0	Balleney Islands region
14 October 1997	7.8	0	South of Fiji Islands
10 May 1997	7.3	1,572	Northern Iran
05 May 1997	7.8	0	Near east coast of Kamchatka
17 February 1996	8.2	166	Irian Jaya region Indonesia
03 February 1996	6.6	322	Yunnan, China
30 July 1995	8.0	3	Near coast of northern Chile
09 October 1995	8.0	49	Near coast of Jalisco Mexico
16 January 1995	6.9	5,530	Kobe, Japan
04 October 1994	8.3	11	Kuril Islands
06 June 1994	6.8	795	Colombia
29 September 1993	6.2	9,748	India
08 August 1993	7.8	0	South of Mariana Islands
12 December 1992	7.8	2,519	Flores Region, Indonesia
19 October 1991	6.8	2,000	Northern India

(continued)

Table 1.2 (continued)

Date	Magnitude	Fatalities	Region
22 April 1991	7.6	75	Costa Rica
22 December 1991	7.6	0	Kuril Islands
16 July 1990	7.7	1,621	Luzon, Philippine Islands
20 June 1990	7.4	50,000	Iran

1.2 Earthquake Process and Faults

The dynamic process of Earth's interior that is discussed in the previous section explains the driving force behind the relative motion of the tectonic plates. This continuous activity results in the occurrence of earthquakes along the major plate boundaries. The actual mechanism of earthquakes can be explained by the elastic rebound theory that is introduced after the 1906 San Francisco earthquake by Reid (1911). The elastic rebound theory is put forward before the theory of plate tectonics and it is the first physically justifiable scheme that relates earthquake process with the geological faults.

Earth scientists studied the 1906 San Francisco earthquake in great detail (Lawson 1908). The rupture that was traced for a distance of more than 400 km along the San Andreas Fault showed a predominant right-lateral horizontal slip that was measured from the offsets of fences or roads. Figure 1.15 is a snapshot of the right-lateral motion on one of the ruptured segments of the San Andreas Fault after the 1906 San Francisco earthquake. The field measurements indicated that, on average, the slip between the two sides of the fault varied between 2 to 4 m.

The measured displacements along the ruptured fault segments of the San Andreas Fault after the 1906 San Francisco earthquake as well as the re-examination of past geodetic measurements of the survey points along the San Andreas Fault revealed that the opposite sides of the fault had been in continuous motion before the earthquake. The slip directions of past geodetic measurements were consistent with the slip direction observed after the San Francisco earthquake. On the basis of these observations, Harry Fielding Reid proposed the theory of elastic rebound to explain the mechanism for earthquake occurrence. The elastic rebound theory is now accepted universally. Figure 1.16 illustrates the complete cycle for the occurrence of an earthquake according to this theory. As plates on opposite sides of a fault are subjected to stress, they accumulate energy and deform gradually until their internal strength capacity is exceeded (top row sketches in Fig. 1.16). At that time, a sudden movement occurs along the fault, releasing the accumulated energy, and the rocks snap back to their original undeformed shape (bottom row sketches in Fig. 1.16).

The elastic rebound theory is the first theory that describes fault rupture as the source of strong ground shaking. Before this principle the fault rupture was believed to be the result of earth shaking. With the exception of volcanic earthquakes that are the results of sudden and massive movements of magma, all

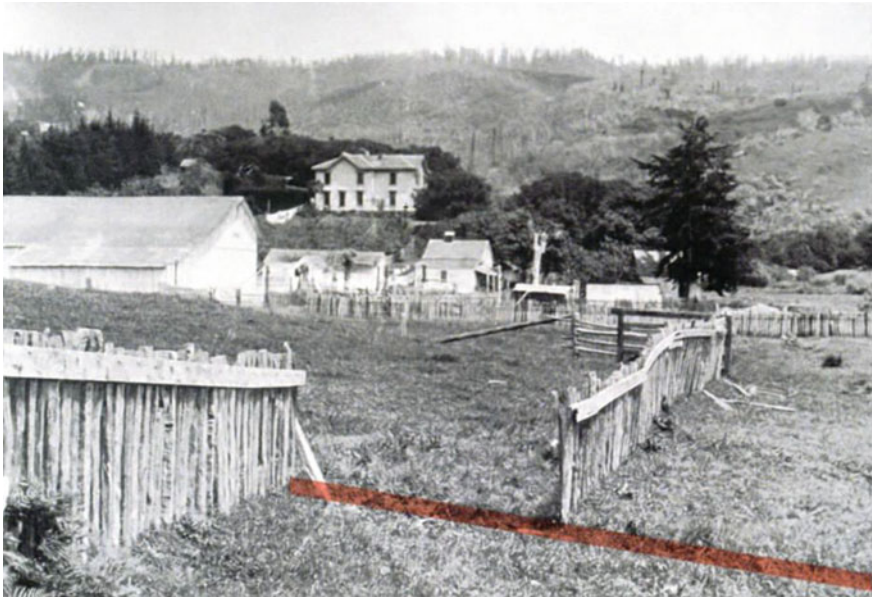
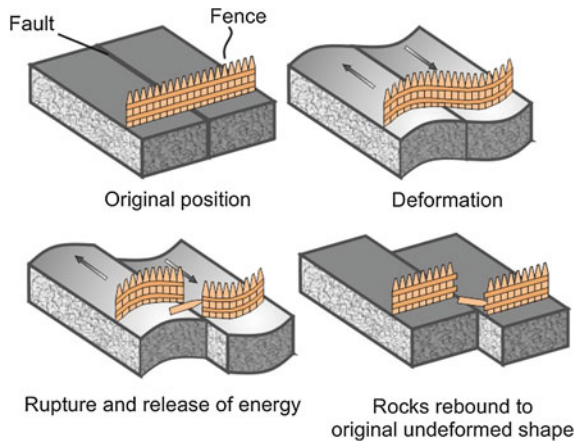


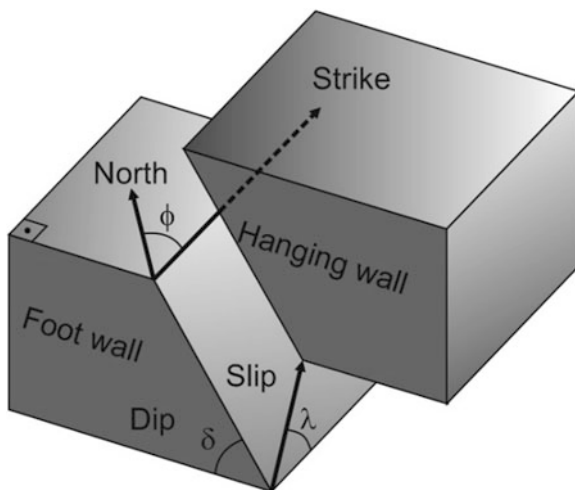
Fig. 1.15 An illustration showing the lateral offset of a fence located on one of the ruptured segments of San Andreas Fault after the 1906 San Francisco earthquake. The *red strip* is used to mark the right lateral offset (<http://smithsonianscience.org/2011/09/qa-with-smithsonian-volcanologist-richard-wunderman-regarding-the-recent-east-coast-earthquake/>)

Fig. 1.16 Schematic illustration of the elastic rebound theory



earthquakes are caused by rupture on geological faults. The rupture begins at one particular point and then propagates along the fault plane very rapidly: average velocities of fault rupture are between 2 and 3 km/s.

Fig. 1.17 Geometrical properties of define faults (modified from Shearer 1999)



Fault ruptures are often very complex but they can be idealized as rectangular blocks to describe their overall behavior. This is illustrated in Fig. 1.17. The crustal blocks above and below the fault plane are defined as the hanging wall and footwall, respectively. The hanging wall moves with respect to footwall. The angle between the fault plane and horizontal ground surface is the dip angle δ . It is measured downwards from the horizontal surface and it takes values between 0 and 90° . The strike ϕ is the clockwise angle relative to North and it varies between 0 and 360° . It shows the direction of fault strike that is defined as the line of intersection of the fault plane and the ground surface. The strike of a fault is defined such that the hanging wall is always on the right and footwall block is on the left. Rake angle λ shows the direction of relative motion of hanging wall with respect to footwall. It is measured relative to fault strike and it varies between $\pm 180^\circ$.

Figure 1.18 shows the faulting styles that are classified according to the geometrical properties defined in the previous paragraph. The rupture in strike-slip faults takes place along the fault strike. Based on the definitions of fault strike and rake angle, the strike-slip fault is left-lateral (sinistral), if the hanging wall (right side of the fault) moves away from an observer standing on the fault and looking in the strike direction. The rake angle for left-lateral strike-slip faults is $\lambda = 0^\circ$. The strike-slip fault is right-lateral (dextral), if the hanging wall moves towards the observer ($\lambda = \pm 180^\circ$). If the hanging wall moves up or down, the fault motion is classified as dip-slip. When the movement of hanging wall is in upwards direction (i.e., $\lambda > 0^\circ$), the faulting is defined as either reverse or thrust depending on the value of rake (smaller rake angles, $0^\circ < \lambda < 30^\circ$, refer to thrust faulting). The faulting style is normal, if hanging wall moves in the downwards direction (i.e., $\lambda < 0^\circ$). Reverse faults occur when two tectonic plates converge (zones of compression) whereas normal faults are the result of tectonic extension (when two

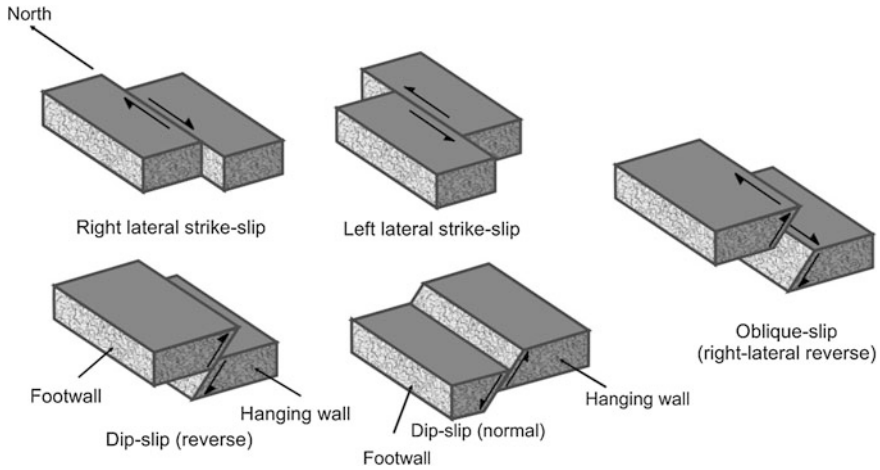


Fig. 1.18 Types of faulting mechanisms and basic slip directions for each faulting mechanism (modified from Reiter 1990)

plates diverge). Strike-slip faults typically exist in transform boundaries. In general, the slip direction of the faults has both horizontal and vertical components. Such faults are known as oblique faults and are described by considering the dominant slip direction (e.g., normal-oblique if dominant slip component is in downwards direction). Figure 1.19 shows illustrative pictures from each major style-of-faulting that are taken from nature.

1.3 Seismic Waves

Rupture of a fault (Fig. 1.20) results in a sudden release of strain energy that radiates from the ruptured fault surface in the form of seismic waves. Seismic wave propagation from the ruptured fault is modulated either in compression or in shear, which corresponds to P- and S-waves, respectively. P-waves are faster than the S-waves. Consequently, the arrival times of P-waves are shorter than the arrival of S-waves and P-waves are the first waveforms observed in seismic recordings (seismograms). Different phases of S-waves are observed after P-waves on the seismograms. Equations (1.1) and (1.2) express the propagation velocities of P-waves (V_p) and S-waves (V_s) that depend on the elastic properties of the medium where they travel.

$$V_p = \sqrt{\frac{E(1-\nu)}{\rho(1+\nu)(1-2\nu)}} \quad (1.1)$$

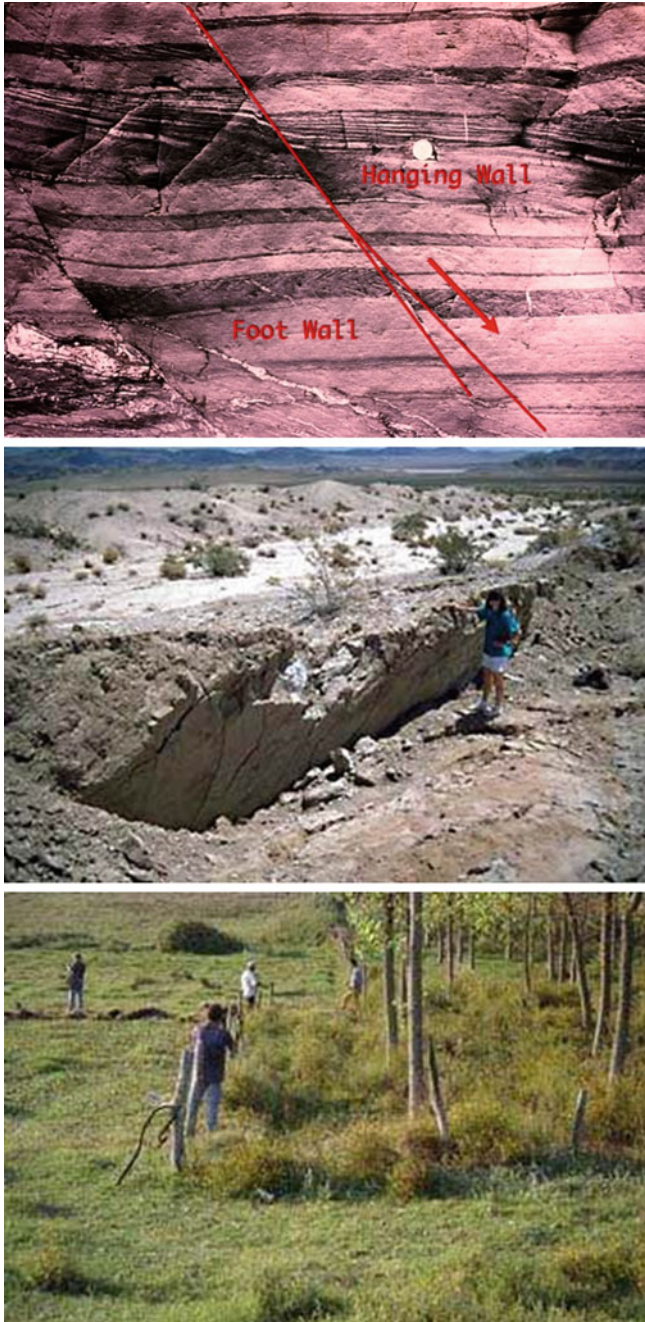


Fig. 1.19 Images of normal (*top*), reverse (*middle*) and strike-slip (*bottom*) faults

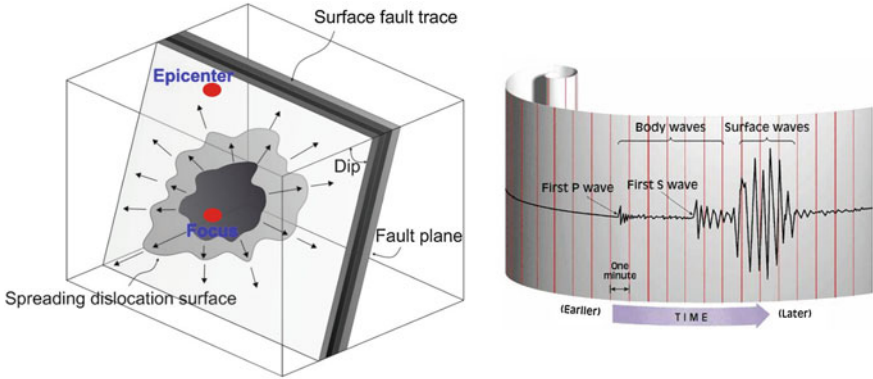


Fig. 1.20 Drawing on the *left* shows the simplified rupture mechanism and wave propagation from the source. Focus is the starting (nucleation) point of the rupture. Epicenter is the vertical projection of focus on the Earth’s surface. Illustration on the *right* represents different arrival times of P- and S-waves observed on a seismogram

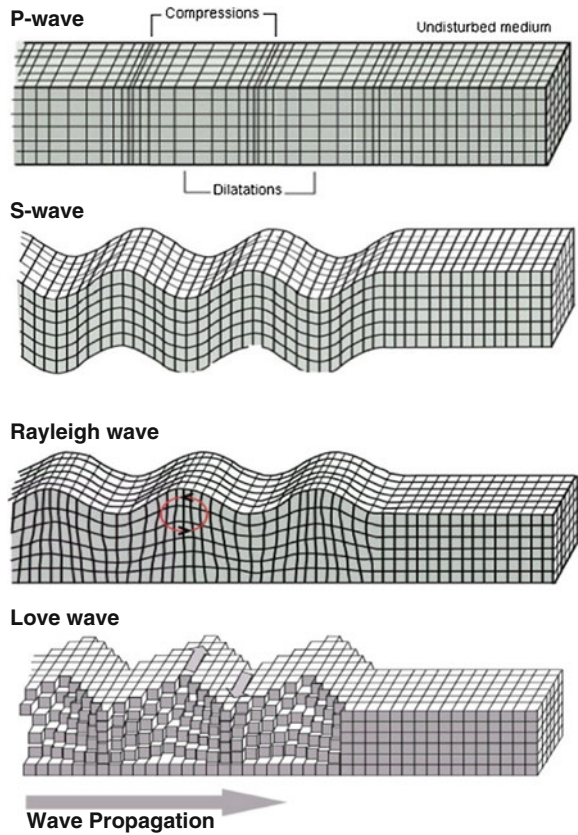
$$V_S = \sqrt{\frac{E}{2\rho(1 + \nu)}} = \sqrt{\frac{G}{\rho}} \tag{1.2}$$

The parameters E and ρ are the modulus of elasticity and mass density of the elastic medium, respectively. ν is Poisson’s ratio (~ 0.25) and G is the shear modulus in Eqs. (1.1) and (1.2). P- and S-wave velocities increase with depth as E and G attain larger values towards the interior part of the crust. Typical values of P- and S-wave velocities within the crust are $V_p = 6$ km/s and $V_s = 4$ km/s. In general, P-waves are expected to travel about $\sqrt{3}$ times faster than S-waves.

The particle motion of P-waves is in the direction of wave propagation whereas particles move in the direction perpendicular to the S-wave propagation. Thus, P-waves are classified as longitudinal waves and S-waves are called as shear waves according to the polarization of particle motion. The generic illustrations of P- and S-wave particle motions are given in the first two panels of Fig. 1.21. S-waves cannot travel along a liquid medium (e.g., outer core). Their particle motion is in the transversal direction to the wave propagation and liquids cannot transmit shear motion. S-waves are further decomposed into SH and SV waves according to the particle motions in the horizontal and vertical planes, respectively. The particle motion of SH waves takes place in the horizontal plane and they generate lateral shaking that may result in large dynamic deformation demands on structures. As P- and S-waves are generated immediately after the fault rupture and propagate in the solid body of the Earth’s crust, the common name given to these wave forms is body waves.

Trapped body waves that propagate across Earth’s surface are called surface waves. The amplitudes of surface waves decrease with increasing depth and they do not travel towards the inner part of the crust. They are divided into two types

Fig. 1.21 Particle motions of body waves (*P*- and *S*-waves) and surface waves (*Love* and *Rayleigh* waves) based on their propagation in elastic medium



and are called as Love (LQ) and Rayleigh (LR) waves. Love waves are trapped SH waves that propagate along a horizontal layer between the free surface and the underlying elastic half space. Trapped SH waves travel across by reflecting from the top and bottom of the horizontal layer. The velocity of the Love waves lies between the shear-wave velocities of the horizontal layer and the underlying half space. The particle motion of propagating Rayleigh waves is polarized in the vertical plane due to trapped P and SV waves. The velocity of Rayleigh waves is approximately 90 % of the shear-wave velocity of the elastic medium if the Poisson's ratio ν is assumed as 0.25. The last 2 panels of Fig. 1.21 show the particle motions of Love and Rayleigh waves. Since surface waves are trapped within a boundary, they can travel long distances along the Earth's surface. Their wave lengths and periods are longer. Their propagation velocities depend on the elastic properties of the medium and their periods.

1.4 Magnitude of an Earthquake

Magnitude scales measure the size and energy release of earthquakes. The first magnitude scale is proposed by Richter (1935) for quantifying the sizes of earthquakes in southern California from the maximum amplitudes (A in mm) of seismograms recorded by the Wood-Anderson seismographs. Equation (1.3) gives the local magnitude (M_L) expression proposed by Richter.

$$M_L = \log(A) - \log(A_0). \quad (1.3)$$

Note that Eq. (1.3) calibrates M_L with base amplitude A_0 . This parameter corresponds to the amplitude of a base earthquake that would yield a maximum trace amplitude of 0.001 mm on a Wood-Anderson seismograph located at an epicentral distance of 100 km. Richter (1935) provides the calibration factor $-\log(A_0)$ for epicentral distances up to 1000 km for the average conditions in southern California. The computation of M_L can also be done from the nomogram given in Fig. 1.22 that requires P- and S-wave arrival times and the maximum amplitude readings on a Wood-Anderson seismograph. The calibration by base amplitude A_0 is embedded into the nomogram. If the difference between P- and S-wave arrival times is 25 s and the maximum amplitude of the Wood-Anderson seismogram is 20 mm, M_L is graphically estimated as 5 from the nomogram. Needless to say, the computed M_L represents the general crustal features in southern California.

Definition of local magnitude is based on seismic waveform amplitudes recorded by the Wood-Anderson seismograph and the amplitude calibrations that reflect the regional attenuation characteristics of southern California. Thus, the seismic networks reporting M_L should properly account for the instrumental differences if maximum waveform amplitudes are measured by another type of seismograph. The differences in regional attenuation should also be considered thoroughly by the seismic networks as the original calibrations proposed by Richter are only valid for southern California. The local magnitude proposed by Richter has limitations in application and may not provide globally consistent estimation of earthquake size if the above stated factors are overlooked by seismic agencies.

Teleseismic magnitude scales are alternatives to M_L . They describe the size of the earthquake from the maximum amplitudes of seismic waveforms normalized by the natural period T of the seismograph. The use of normalized amplitudes makes the magnitude computations independent of the seismograph type. The body-wave (m_b) and surface-wave (M_s) magnitudes are the two types of teleseismic magnitude scales. They are estimated from the seismic waveforms recorded by short-period (m_b) and long-period seismograms (M_s). As the earthquakes become larger in size, they generate very long-period waves that reflect the seismic energy released by the ruptured fault. The amplitudes of these waveforms cannot be detected properly by seismographs used for the computation of m_b and M_s . Thus, neither of these magnitude scales will be able to quantify the actual size of the earthquakes when they become larger. In other words, the increase in

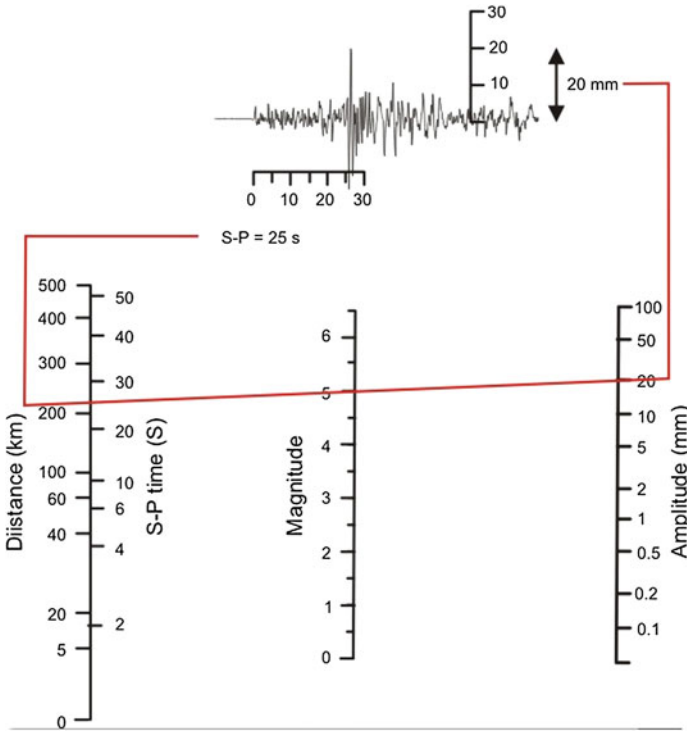
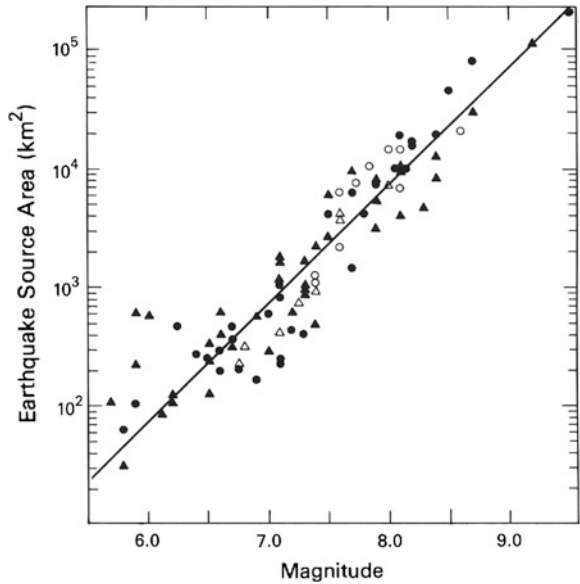


Fig. 1.22 Nomogram for estimating M_L for a fictitious event occurred in southern California. The difference in S-P arrival time is 25 s and the maximum amplitude of Wood-Anderson seismograph is 20 mm (see the Wood-Anderson seismogram in the figure). The estimated local magnitude of the earthquake is M_L 5 as shown on the nomogram

earthquake size will not yield a consistent increase in m_b and M_s as the corresponding seismographs will misrepresent the increase in the maximum amplitudes of very long-period waveforms. This phenomenon is called as magnitude saturation (failing to distinguish the size of earthquakes after a certain level). The magnitude saturation effect is also a concern in M_L computations. The natural period of Wood-Anderson seismograph is approximately 1.25 s and it is not sufficient for the accurate detection of very long seismic waveforms radiated from larger earthquakes.

Seismic moment (M_0) that is directly proportional to the ruptured fault area as well as the average slip between the moving blocks does not suffer from the saturation affects. It defines the force required to generate the recorded waves after an earthquake. It is also related to the total seismic energy released by the fault rupture. This quantity is used to define the moment magnitude (M_w) that is proposed by Hanks and Kanamori (1979). Equation (1.4) gives the relationship between M_w and M_0 . To increase one unit of M_w , fault rupture area should be 32 times larger as there is a logarithmic relationship between M_w and M_0 , and M_0 is directly proportional to the rupture area.

Fig. 1.23 An empirical model relating the fault rupture area and magnitude (Reiter 1990)

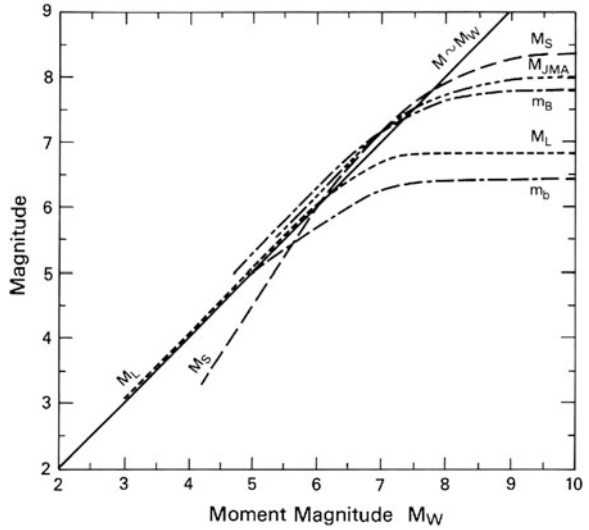


$$M_w = \frac{2}{3} \log_{10}(M_0) - 6. \tag{1.4}$$

Figure 1.23 shows the relationship between rupture area and magnitude. Larger rupture areas indicate large-magnitude earthquakes. The rupture area of small magnitude events (i.e., magnitudes less than 6) can be represented by a circle and such seismic sources are referred to as point-source in seismology. The rupture area tends to become rectangular (i.e., extended source) for larger magnitudes. For such cases the rupture geometry is characterized by the width (W) and length (L) of the rupture area. There are many empirical models in the literature that relate the magnitude of earthquakes with the rupture dimensions (e.g., Wells and Coppersmith 1994). These relationships are used in the hazard assessment studies as will be discussed in the [Chap. 2](#).

Figure 1.24 compares different magnitude scales. The magnitude saturation phenomenon is clearly illustrated for local, body-wave and surface-wave magnitudes (two types of body-wave magnitudes are illustrated: m_b and m_B that are computed from seismographs of different natural periods – m_B is computed from a slightly longer period seismograph–). These magnitude scales fail to distinguish the size of the earthquakes after a certain magnitude level. The adverse effects of magnitude saturation shows up at relatively larger magnitudes for M_s as waveforms recorded by longer period seismographs are used for its computation. The moment magnitude, M_w , is the only magnitude scale that does not suffer from magnitude saturation for reasons described in the above paragraph. This figure also compares the specific magnitude scale used in Japan, M_{JMA} that has a trend similar to M_s .

Fig. 1.24 Comparison of moment magnitude scale with other magnitude scales (Reiter 1990)



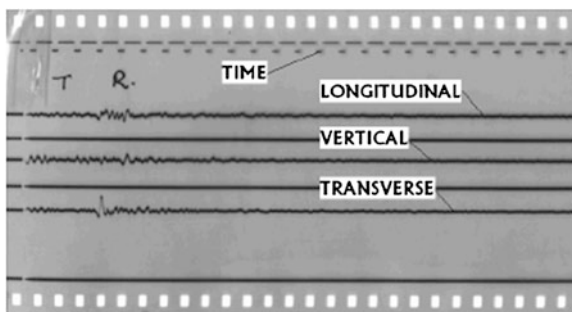
1.5 Intensity of an Earthquake

Recordings of seismic instruments and subjective personal observations on the earthquake area are the quantitative and qualitative measurements of ground-motion intensity, respectively. The latter description of earthquake intensity is made through predefined indices that are established under the macroseismic intensity concept. As these indices are generally developed under the common consensus of engineers and earth scientists, the level of bias in the estimation of earthquake intensity is accepted as minimum. Instrumental recordings from earthquakes on the other hand are the most reliable measurements of earthquake intensity. The instrumental and observational intensities are discussed briefly in the following subsections.

1.5.1 Instrumental Intensity

For essential earthquake engineering related studies, ground shaking recorded by an accelerograph contains the most useful data to describe the ground-motion intensity. As the name implies, accelerographs record the time-dependent variation of particle acceleration under ground shaking. The recordings of accelerographs are either called as accelerograms or accelerometric data. The accelerographs are generally deployed in the vicinity of active seismic sources in free-field conditions to capture the strong ground shaking of engineering concern. They usually record three mutually perpendicular components of motion in the vertical and two orthogonal horizontal directions.

Fig. 1.25 A typical analog recording on a film paper. The film includes time marks as well as two horizontal and vertical acceleration components. The traces on the film are digitized by expert operators



Accelerographs are either analog or digital. The analog accelerographs are the first generation instruments and they record on film papers (Fig. 1.25). They operate on trigger mode that requires a threshold acceleration level for the instrument to start recording the incident waveforms. The trigger mode operation conditions would fail to capture the first arrivals of seismic waves if the waveform amplitudes are below the threshold acceleration. The missing first arrivals of seismic waves may cause ambiguity in the computation of ground velocity and displacement from analog accelerograms. As analog accelerographs record on film papers, the recorded waveform quality is limited. They are digitized for their use in engineering and seismological analyses that further reduces the recording quality as digitization introduces additional noise to the original waveform.

Digital accelerographs started to operate almost 50 years after the first analog accelerographs. Thus, they are technologically more advanced. They operate continuously and use a pre-event memory. They record the waveforms in higher resolution and the noise level is significantly less with respect to their analog counterparts as they have wider dynamic ranges. The acceleration traces recorded by these accelerographs are already in digital format so there is no need of an intermediate step for analog-to-digital waveform conversion. Figure 1.26 shows a typical digital accelerogram. Note that the pre-event buffer (memory) of this accelerogram is approximately 15 s. In other words, all three components show the state of recording approximately 15 s before the actual waveforms start arriving in the recording station. This feature helps the instrument to capture the first wave arrivals that is particularly useful for the computation of more reliable particle velocity and displacement from the ground acceleration.

Accelerograms contain significant information about the nature of ground shaking and also about the highly varied characteristics that differ from one earthquake to the other or within an earthquake at different locations (Fig. 1.27). Ground-motion parameters (e.g., peak ground acceleration, velocity or spectral ordinates) that are obtained from the accelerograms quantitatively describe the intensity of ground shaking. The state of structural damage as well as loss after an earthquake can also be estimated from the ground-motion parameters computed from accelerograms.

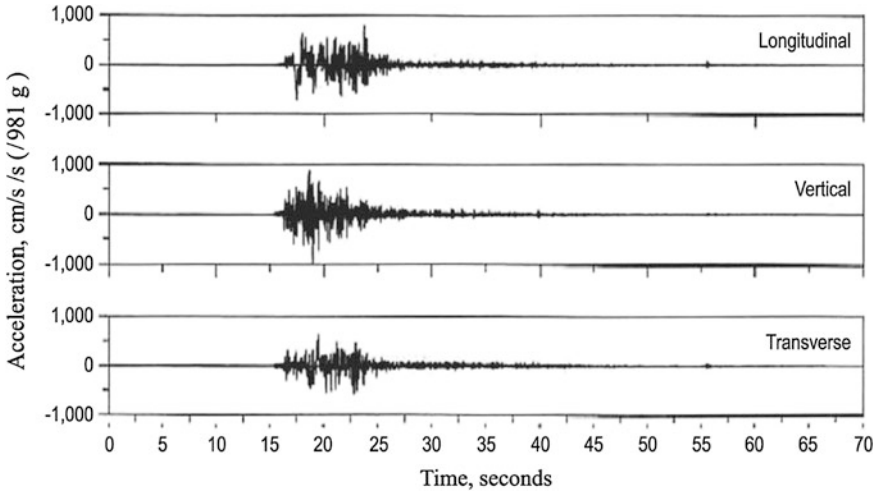


Fig. 1.26 A digital accelerogram with acceleration time series in two horizontal (*transverse* and *longitudinal*) and vertical directions

Accelerogram traces, such as those given in Fig. 1.27, also reflect the basic characteristics of the fault rupture and the travel path of seismic waves. The durations of accelerograms, as given in this figure, increase with increasing magnitude. The increase in magnitude is the result of larger rupture areas that eventually implies to longer rupture duration. This is naturally reflected into the duration of accelerogram.

If the fault rupture and seismic waves propagate towards the recording station (forward directivity), the accelerogram usually contains a pulse due to the coherent wave forms. If the fault rupture propagates away from the station (backward directivity), no such pulses dominate the accelerogram and the amplitudes of waveforms are lower. The forward directivity effects are observed in accelerograms recorded in the vicinity of ruptured faults. Accelerograms featuring backward directivity effects generally have longer durations with respect to those carrying the signature of forward directivity.

The softer sites mostly amplify the seismic waveforms with respect to rock sites that is described by *site amplification* in earthquake engineering. Moreover, the increase in distance from the ruptured fault generally decreases the amplitudes of ground acceleration which is called *ground motion attenuation*. This phenomenon is further discussed in the following chapter.

Integration of accelerograms (through some special data processing) yields the time-dependent variation of particle velocity and displacement. The velocity and displacement time histories can reveal other important characteristics of earthquakes. An illustrative example that shows the ground velocity and displacement computed from an accelerogram is given in Fig. 1.28.

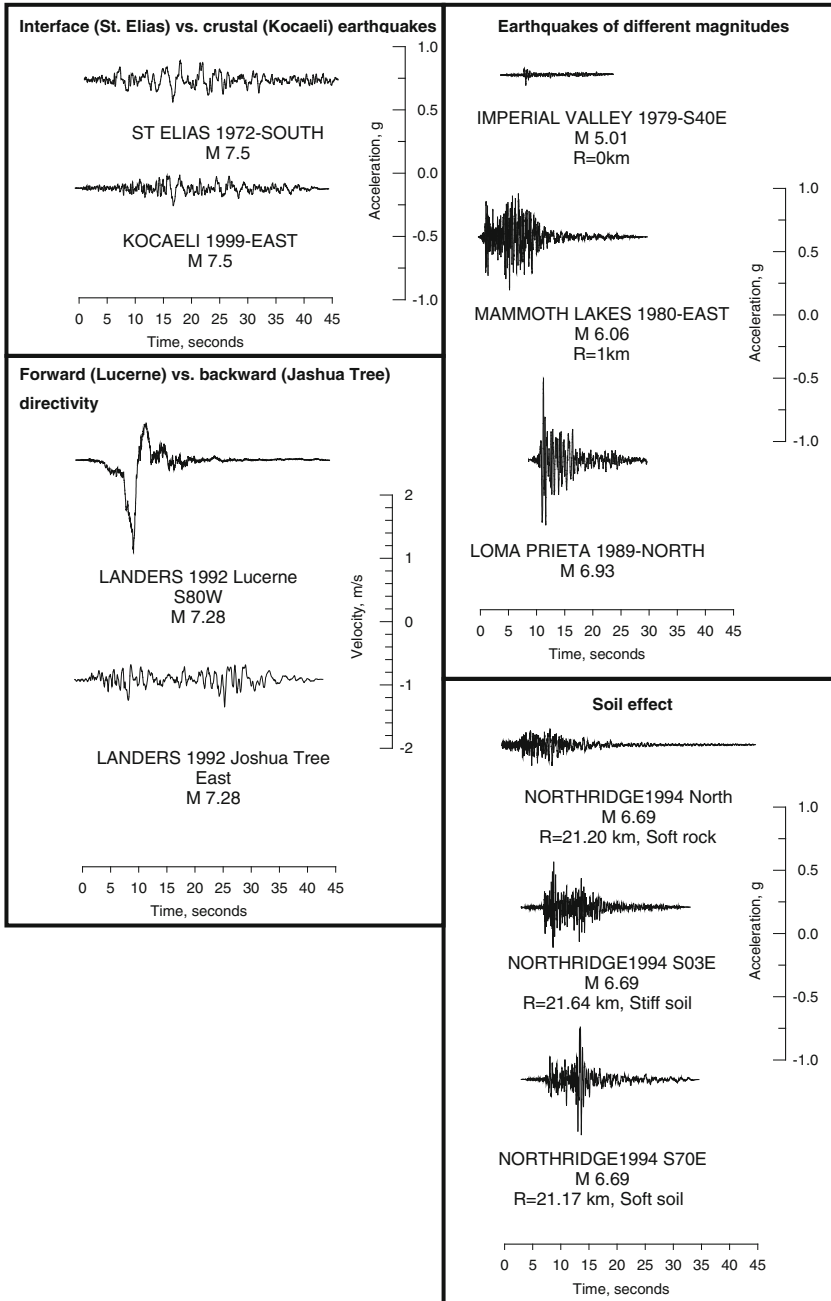


Fig. 1.27 Accelerograms from various types of earthquakes (*interface vs. crustal*), directivity (*forward vs. backward directivity*) and soil conditions (soft rock to soft soil) to illustrate the variability in the nature of strong ground-motion

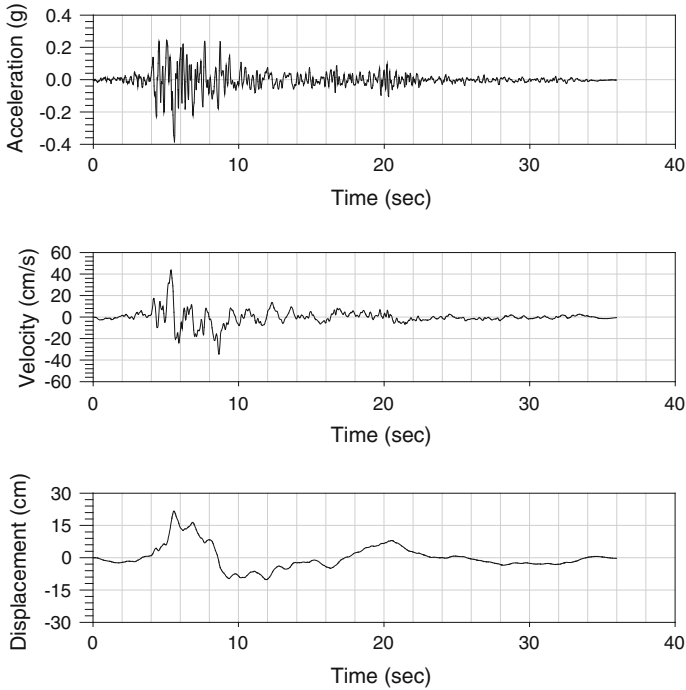


Fig. 1.28 Processed acceleration time series (EW component) of the Rio Dell Overpass recording station triggered during the 1992 Cape Mendocino, California earthquake and corresponding velocity and displacement time series. The closest distance between the station and the ruptured fault is ~ 14 km (<http://peer.berkeley.edu/nga/data?doi=NGA0829>)

1.5.2 Observational Intensity

The qualitative measurement of the influence of ground shaking on structural systems as well as over the entire earthquake affected area is done through macroseismic intensity; an index that reflects the strength of ground shaking at a particular location during an earthquake. This definition clearly indicates that the macroseismic intensity is a classification of the severity of ground shaking on the basis of observed effects over a particular area. Although microseismic studies seem to be less significant after the advanced developments in instrumental seismicity, they are essential for the revision of historical seismicity that is used in source characterization in seismic hazard assessment (see [Chap. 2](#) for details of seismic hazard assessment). Microseismic studies are also important for structural vulnerability (susceptibility of damage under earthquakes) and seismic risk (risk of damage to build environment) assessment.

Although the first intensity scale to be used internationally was the 10° Rossi-Farel scale (1883), simplified quantifications of damage had been started earlier by Schiantorelli (1783) and Sarconi (1784). The 12° scale by Sieberg (1912, 1923)

Table 1.3 EMS intensity scales and their description (Grunthal 1998)

EMS intensity	Definition
I. Not felt	(a) Not felt, even under the most favorable circumstances (b) No effect (c) No damage
II. Scarcely felt	(a) The tremor is felt only at isolated instances (<1 %) of individuals at rest and in a specially receptive position indoors (b) No effect (c) No damage
III. Weak	(a) The earthquake is felt indoors by a few. People at rest feel a swaying or light trembling (b) Hanging objects swing slightly (c) No damage
IV. Largely observed	(a) The earthquake is felt indoors by many and felt outdoors only by very few. A few people are awakened. The level of vibration is not frightening. The vibration is moderate. Observers feel a slight trembling or swaying of the building, room or bed, chair etc. (b) China, glasses, windows and doors rattle. Hanging objects swing. Light furniture shakes visibly in a few cases. Woodwork creaks in a few cases (c) No damage
V. Strong	(a) The earthquake is felt indoors by most, outdoors by few. A few people are frightened and run outdoors. Many sleeping people awake. Observers feel a strong shaking or rocking of the whole building, room or furniture (b) Hanging objects swing considerably. China and glasses clatter together. Small, top-heavy and/or precariously supported objects may be shifted or fall down. Doors and windows swing open or shut. In a few cases window panes break. Liquids oscillate and may spill from well-filled containers. Animals indoors may become uneasy (c) Damage of grade 1 to a few buildings of vulnerability class A and B
VI. Slightly damaging	(a) Felt by most indoors and by many outdoors. A few persons lose their balance. Many people are frightened and run outdoors (b) Small objects of ordinary stability may fall and furniture may be shifted. In few instances dishes and glassware may break. Farm animals (even outdoors) may be frightened (c) Damage of grade 1 is sustained by many buildings of vulnerability class A and B; a few of class A and B suffer damage of grade 2; a few of class C suffer damage of grade 1
VII. Damaging	(a) Most people are frightened and try to run outdoors. Many find it difficult to stand, especially on upper floors (b) Furniture is shifted and top-heavy furniture may be overturned. Objects fall from shelves in large numbers. Water splashes from containers, tanks and pools (c) Many buildings of vulnerability class A suffer damage of grade 3; a few of grade 4. Many buildings of vulnerability class B suffer damage of grade 2; a few of grade 3. A few buildings of vulnerability class C sustain damage of grade 2. A few buildings of vulnerability class D sustain damage of grade 1

(continued)

Table 1.3 (continued)

EMS intensity	Definition
VIII. Heavily damaging	(a) Many people find it difficult to stand, even outdoors (b) Furniture may be overturned. Objects like TV sets, typewriters etc. fall to the ground. Tombstones may occasionally be displaced, twisted or overturned. Waves may be seen on very soft ground (c) Many buildings of vulnerability class A suffer damage of grade 4; a few of grade 5. Many buildings of vulnerability class B suffer damage of grade 3; a few of grade 4. Many buildings of vulnerability class C suffer damage of grade 2; a few of grade 3. A few buildings of vulnerability class D sustain damage of grade 2
IX. Destructive	(a) General panic. People may be forcibly thrown to the ground (b) Many monuments and columns fall or are twisted. Waves are seen on soft ground. (c) Many buildings of vulnerability class A sustain damage of grade 5. Many buildings of vulnerability class B suffer damage of grade 4; a few of grade 5. Many buildings of vulnerability class C suffer damage of grade 3; a few of grade 4. Many buildings of vulnerability class D suffer damage of grade 2; a few of grade 3. A few buildings of vulnerability class E sustain damage of grade 2
X. Very destructive	(a) Most buildings of vulnerability class A sustain damage of grade 5. Many buildings of vulnerability class B sustain damage of grade 5. Many buildings of vulnerability class C suffer damage of grade 4; a few of grade 5. Many buildings of vulnerability class D suffer damage of grade 3; a few of grade 4. Many buildings of vulnerability class E suffer damage of grade 2; a few of grade 3. A few buildings of vulnerability class F sustain damage of grade 2
XI. Devastating	(a) Most buildings of vulnerability class B sustain damage of grade 5. Most buildings of vulnerability class C suffer damage of grade 4; many of grade 5. Many buildings of vulnerability class D suffer damage of grade 4; a few of grade 5. Many buildings of vulnerability class E suffer damage of grade 3; a few of grade 4. Many buildings of vulnerability class F suffer damage of grade 2; a few of grade 3
XII. Completely devastating	(a) All buildings of vulnerability class A, B and practically all of vulnerability class C are destroyed. Most buildings of vulnerability class D, E and F are destroyed. The earthquake effects have reached the maximum conceivable effects

constitutes the basis of modern intensity scales and its later version is known as the MCS (Mercalli-Cancani-Sieberg) scale (1932). The 1923 version of Sieberg's work was translated into English by Wood and Neumann in 1931 (named as Modified Mercalli—MM—scale) and it was entirely revisited by Richter in 1956. This version is called as Modified Mercalli Scale of 1956 (MM56). In 1964 Medvedev, Sponheuer and Karnik published the MSK scale that was based on MCS, MM56 as well as the previous work of Medvedev in Russia. This scale was widely used in Europe until the publication of European Macroseismic Scale (EMS) (Grunthal 1998).

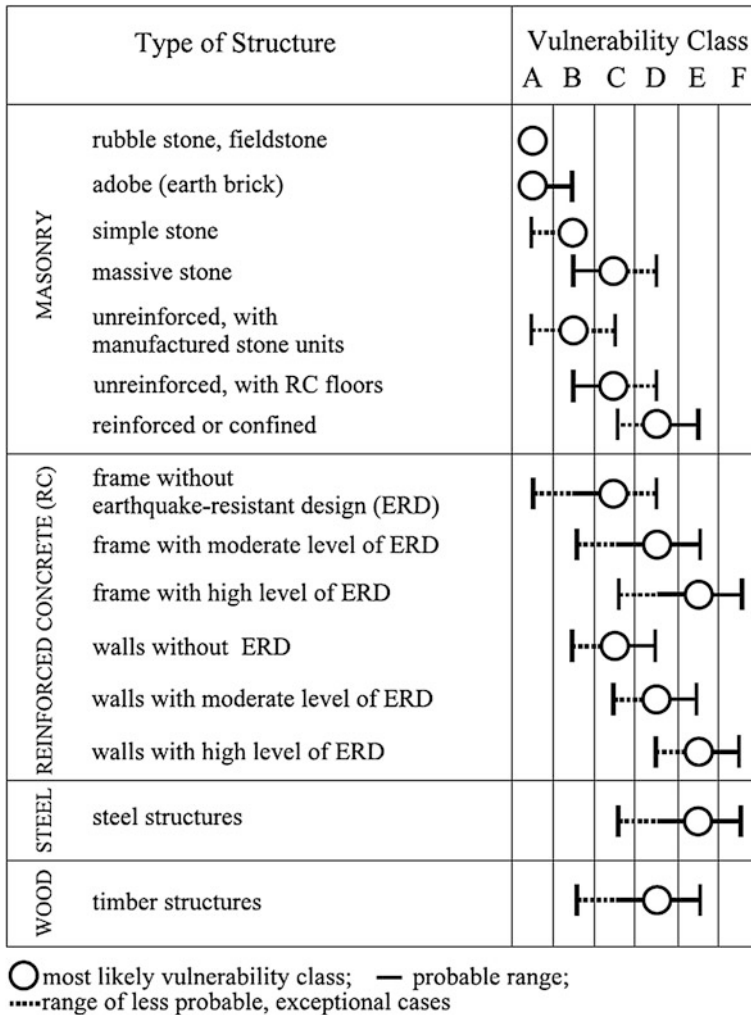


Fig. 1.29 Definitions of vulnerability classes in EMS (Grunthahl 1998). The vulnerability class letters (A–F) indicate the level of increasing vulnerability for different structural systems (Grunthahl 1998)

The EMS intensity scales are reproduced in Table 1.3. The descriptions of intensities are given by considering the effects on (a) humans, (b) objects and nature, and (c) buildings (in terms of damage). The descriptions also involve six vulnerability classes that consider the construction type, workmanship and structural condition. These vulnerability classes are given in Fig. 1.29 and are used to assess the intensity from damage. The damage is described as structural and nonstructural with five damage grades: negligible-to-slight; moderate; substantial-to-heavy; very

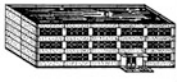
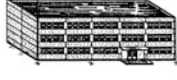
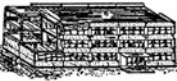
Classification of damage to masonry buildings		Classification of damage to buildings of reinforced concrete	
	Grade 1: Negligible to slight damage (no structural damage, slight non-structural damage) Hair-line cracks in very few walls. Fall of small pieces of plaster only. Fall of loose stones from upper parts of buildings in very few cases.		Grade 1: Negligible to slight damage (no structural damage, slight non-structural damage) Fine cracks in plaster over frame members or in walls at the base. Fine cracks in partitions and infills.
	Grade 2: Moderate damage (slight structural damage, moderate non-structural damage) Cracks in many walls. Fall of fairly large pieces of plaster. Partial collapse of chimneys.		Grade 2: Moderate damage (slight structural damage, moderate non-structural damage) Cracks in columns and beams of frames and in structural walls. Cracks in partition and infill walls; fall of brittle cladding and plaster. Falling mortar from the joints of wall panels.
	Grade 3: Substantial to heavy damage (moderate structural damage, heavy non-structural damage) Large and extensive cracks in most walls. Roof tiles detach. Chimneys fracture at the roof line; failure of individual non-structural elements (partitions, gable walls).		Grade 3: Substantial to heavy damage (moderate structural damage, heavy non-structural damage) Cracks in columns and beam column joints of frames at the base and at joints of coupled walls. Spalling of concrete cover, buckling of reinforced rods. Large cracks in partition and infill walls, failure of individual infill panels.
	Grade 4: Very heavy damage (heavy structural damage, very heavy non-structural damage) Serious failure of walls; partial structural failure of roofs and floors.		Grade 4: Very heavy damage (heavy structural damage, very heavy non-structural damage) Large cracks in structural elements with compression failure of concrete and fracture of rebars; bond failure of beam reinforced bars; tilting of columns. Collapse of a few columns or of a single upper floor.
	Grade 5: Destruction (very heavy structural damage) Total or near total collapse.		Grade 5: Destruction (very heavy structural damage) Collapse of ground floor or parts (e. g. wings) of buildings.

Fig. 1.30 Description of damage grades in masonry (*left panel*) and reinforced concrete (*right panel*) buildings from EMS (Grunthal 1998)

heavy and destruction. These grades are described verbally and visually in EMS and are presented for masonry and reinforced concrete buildings in Fig. 1.30.

The EMS reduces the significance of ground failures (e.g., landslides, rock falls, cracks in ground) in intensity scales as they are strongly influenced by other factors (e.g., existing hydrological conditions in the earthquake area) that sometimes can mask the direct effects of earthquake shaking. The EMS does not consider the effects of ground failures in intensity descriptions but associate them separately with different ranges of intensities. Note that the lower intensities are mainly described by human reactions. The intensities of engineering concern are generally VII and above. Intensity level XII represents a very rare strong ground shaking and intensities X and XI can be defined as the upper bound.

Under a certain ground shaking, the buildings of equivalent strength may sustain different forms of damage. There is a modal (most frequent) level of observed damage with some buildings suffering less and others more. The EMS is designed such that the modal level of damage will define the earthquake intensity for the area of interest. It should be noted that EMS is not the measure of building damage. It qualitatively defines the level of ground motion intensity from building behavior that is mapped onto the intensities via vulnerability classes and damage grades as given in Figs. 1.29 and 1.30. The intensities are not continuous and their

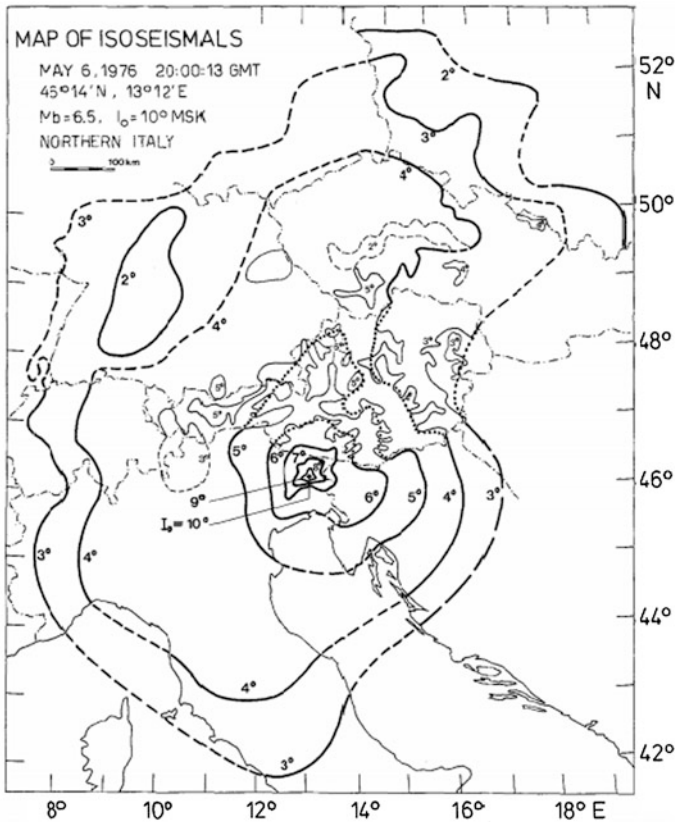


Fig. 1.31 Sample isoseismal map after the 1976 Friuli sequence (Karnik et al. 1978)

scaling is not linear. Therefore, an increase from intensity IV to V and from intensity VII to VIII would not indicate similar changes in the level of ground shaking.

The intensity data is represented in the form of a map to observe the influence of earthquake in the area hit by the earthquake. The intensity points are used and a contour map of equal intensity is drawn. This map is called as isoseismal map. Figure 1.31 shows the example of an isoseismal map obtained after the main shock of the 1976 Friuli earthquake in Italy. An isoseismal contour immediately shows where the ground shaking was strong enough to cause damage and the area over which the ground shaking was felt. The isoseismals will tend to be more or less concentric about the fault rupture that caused the earthquake and the epicenter would be expected to lie within or very close to the highest isoseismals. The distribution of the isoseismals, and in particular the distances between them reflect primarily the magnitude and the focal depth of the earthquake; the isoseismals of

shallow earthquakes tend to be more closely spaced, whereas deeper earthquakes, in subduction zones, will generally produce lower values of intensity but with isoseismals enclosing much larger areas.

1.6 Effects of Earthquakes on Built Environment

The effects of earthquakes on the built environment can be studied under two categories: direct effects and indirect effects. Strong ground shaking underneath the foundation of a structure is the primary effect of an earthquake, which directly affects the structures in the area hit by the earthquake. A fault rupture crossing a long structure or an infrastructure network (lifeline) such as a viaduct, a pipeline system or a road network is also considered as a direct effect of an earthquake. Indirect effects are basically geotechnical failures as a result of strong ground shaking, which in turn affects the structures located in that geotechnical environment. Liquefaction, lateral spread and earthquake induced landslides are examples of geotechnical failures. Tsunami and fire resulting from earthquakes are also considered as the indirect effects of earthquakes. Indirect effects are by no means less important. In fact, the death toll and economic losses due to tsunamis during the 2004 Indonesia (Sumatra) and 2011 Japan (Tohoku) earthquakes were far more severe than the losses due to the direct effects of these earthquakes.

1.6.1 Strong Ground Shaking

Strong ground shaking during an earthquake develops inertial forces acting on the mass of a structure according to Newton's law of motion. The effect of strong ground motions on structures is the main scope of the following chapters. When the inertial forces in the lateral direction exceed the lateral resistance of structures, they deform beyond their linear elastic deformation ranges and sustain damage. If a structure does not have sufficient inelastic deformation capacity, it collapses. A group of buildings are shown in Fig. 1.32 (left panel) which collapsed during the 1999 Marmara Earthquake. Note that some of the buildings at the same location collapsed while the others did not. Although they are subjected to the same ground shaking, differences in their lateral strengths lead to the observed dramatic differences in the seismic performances of these buildings. Total collapse of a building usually causes life losses (Fig. 1.32, right panel).

1.6.2 Fault Rupture

When the surface fault rupture crosses a structure, it places large horizontal or vertical differential displacement demands equivalent to the fault displacement



Fig. 1.32 *Left* Uneven distribution of damage in buildings located in the same area, subjected to the same ground motion. *Right* Totally collapsed buildings, which killed their occupants



Fig. 1.33 Fault rupture crossing a railway track (*left*) and a viaduct (*right*)

across the fault line. There is a larger chance that a fault crosses a long structure, such as a highway, railway, a viaduct or a pipeline system. A fault crossing a railway bends the rails (Fig. 1.33, left panel). This type of damage is easily repairable since a railway track is a flexible structure and the deformed part can be replaced without much difficulty. However, when a fault crosses a stiffer structure such as a concrete viaduct, then it causes permanent damage. Fault rupture during the 1999 Marmara earthquake crossed the Bolu Viaduct on the Ankara-Istanbul motorway (Fig. 1.33, right panel) with an oblique angle of incidence (Fig. 1.34, left panel) and caused separation of two adjacent piers by about 1.5 m. The deck structure above could not accommodate this horizontal displacement difference, and the deck girders almost fell off the pier caps (Fig. 1.34, right panel). The entire deck was dismantled after the earthquake and reconstructed, which kept the motorway closed for two years. The main reason for this damage was the mis-located fault and the wrong estimation of expected fault displacement during design.



Fig. 1.34 Fault trace running across the Bolu Viaduct piers (*left*) and the damage caused at the deck structure due to static differential movement of the piers along the ruptured fault



Fig. 1.35 Ground failure in a highway (*left panel*) and extensive settlement in a railroad bridge abutment (*right panel*) during the 2010 Maule, Chile earthquake (EERI Earthquake Photo Gallery)

1.6.3 Geotechnical Deformations

Strong ground shaking causes settlements in soil deposits which are not compacted sufficiently. Highways and railways constructed over deposited soil layers are typical examples of such ground deformations induced by severe ground shaking. Ground failure in two lane highway during the 2010 Maule, Chile earthquake is shown in the left panel of Fig. 1.35. During the same earthquake, a railroad bridge abutment settled extensively and slipped under the railroad tracks, hence the tracks suspended in the air (Fig. 1.35, right panel).

Saturated soil deposits lose their strength under cyclic stresses driven by strong ground shaking and they flow as a plastic material. This is termed as *liquefaction*. Bearing capacity of the liquefied soil reduces below the static gravity stresses imposed by the structures above, which in turn result in large vertical deformations. Such structures usually sink into the soil and tilt with a rigid body motion during the earthquake (Fig. 1.36). Ground accelerations in liquefied soils are usually quite low and do not lead to significant structural damage. Hence, liquefaction usually does not cause life losses or injuries, but it causes significant economic losses due to tilted or displaced structures. In some cases, extensive ground displacements may lead to partial collapse, loss of stability and significant damage.



Fig. 1.36 Tilted buildings on liquefied soils in Adapazarı during the 1999 Marmara earthquake



Fig. 1.37 Lateral spreading in the Olas development landscaping during the 2010 Maule, Chile earthquake (*left panel* EERI Earthquake Photo Gallery) and buildings dragged into the sea due to lateral spreading in Gölcük during the 1999 Marmara earthquake (*right panel*)

Practical evaluation of liquefaction potential could be assessed from field tests such as Standard Penetration Test (SPT) and Cone Penetration Test (CPT). The general idea behind these evaluation schemes is to compare and quantify the cyclic resistance ratio, (CRR) with cyclic stress ratio (CSR) within a deterministic or probabilistic framework.

When soil slopes are subjected to strong ground shaking, they may deform laterally in an incremental form as shown in the left panel of Fig. 1.37. This phenomenon is called *lateral spreading*. Liquefied soils spreading laterally can drag the structures resting above them, sometimes into the sea at a shoreline (Fig. 1.37, right panel). Its deformation mechanism can be explained as cumulative residual displacement observed along the down-hill direction during seismic excitation. Extent of lateral spreading may be estimated by making use of predictive methods, simplified analytical models, or numerical (finite elements, finite difference, etc.) methods. Clearly, precision and accuracy are expected to increase



Fig. 1.38 Landslide at a highway embankment during the 1999 Düzce earthquake (*left panel*) and landslide directly above structure during the 2010 Maule, Chile earthquake (*right panel*, EERI Earthquake Photo Gallery)

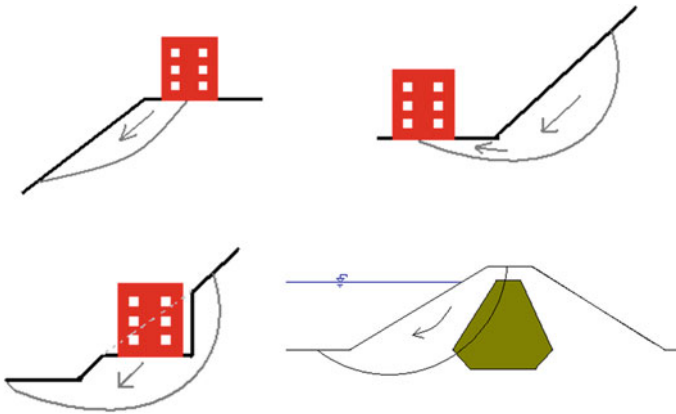


Fig. 1.39 Cases where seismic slope stability analysis is required

from predictive methods to finite element methods while time and effort-consumption also increase.

Soil slopes that are stable under static conditions may lose their stability during earthquakes due to additional dynamic stresses. This causes an *earthquake induced landslide* as shown in Fig. 1.38. Current evaluation of seismic slope performance is through irreversible (or residual) slope displacements. Similar to the evaluation of lateral spreading, irreversible slope displacements could be estimated by means of predictive frameworks, simplified analytical models or numerical methods. The cases where seismic slope stability analysis is required for buildings and dams are illustrated in Fig. 1.39.

Geotechnical deformations and consequent ground failures due to ground shaking during earthquakes are studied under a separate branch of earthquake engineering, called *Geotechnical Earthquake Engineering*. Seismically induced geotechnical deformations are introduced in this section briefly. The analysis of geotechnical deformations under seismic effects are beyond the scope of this book.

Exercises

1. Explain the magnitude and intensity of earthquakes.
2. What is measured by the magnitude of an earthquake?
3. Explain the formation of earthquakes.
4. What are the basic differences between a seismograph and a strong motion accelerograph?
5. What causes tectonic plate motion (continental drift) in the earth crust?
6. (a) Explain elastic rebound theory. (b) What causes ground shaking during an earthquake?
7. Explain the basic types of seismic waves? Can we separate them in a seismogram or in a strong motion accelerogram signal?
8. Which waves travel faster? What are their propagation velocities?
9. Which type of seismic waves is more destructive? Why?
10. Explain magnitude saturation. Why and when does it occur?
11. What is measured by the intensity of an earthquake?
12. What are the basic characteristics of accelerograms, as related to the fault rupture and the travel path of seismic waves?
13. (a) What is observational (subjective) intensity? How is it measured and expressed?
(b) What is instrumental (objective) intensity? How is it measured?
14. What are the basic shapes of isoseismal lines in different types of fault ruptures?
15. What is the use of isoseismal (intensity) maps in earthquake engineering?
16. Explain the basic factors affecting the intensity of strong ground shaking.
17. What are the basic variables accounted for in assigning an intensity level in the European Macroseismic Scale (EMS)?
18. Describe the effects of earthquakes on structures. How do we consider these effects in building design?
19. Can we build on a land where significant residual geotechnical deformations are expected during an earthquake? Explain the basic engineering measures or decisions against geotechnical deformations.

Chapter 2

Seismic Hazard Assessment

Abstract This chapter describes the fundamentals of seismic hazard assessment that constitutes the basis in the definition of seismic design forces. The classical probabilistic and deterministic hazard assessment methods are introduced with emphasis on their elementary components. The discussions on common and different elements of probabilistic and deterministic hazard assessment are followed by step-by-step descriptions of each method. The chapter ends with the introduction of uniform hazard spectrum that is one of the main outputs of probabilistic seismic hazard assessment. This concept is implemented in many modern seismic design codes while deriving the elastic seismic forces. As the basis of probabilistic seismic hazard assessment relies on the probability theory, the last part of the chapter is devoted to fundamental topics in probability.

2.1 Introduction

Seismic hazard assessment (SHA) estimates the level of a ground-motion intensity parameter (e.g., peak ground acceleration, PGA, peak ground velocity, PGV, and spectral acceleration, S_a ,¹ at different vibration periods, etc.) that would be produced by future earthquakes. When design or seismic performance of structures is of concern, one of the major objectives of SHA is to describe ground-motion intensities of design level earthquakes. When seismic hazard (ground-motion intensity) is

¹ Spectral acceleration is a response spectrum quantity that is discussed in [Chap. 3](#). Response spectrum shows the absolute maxima of various response parameters of damped (or undamped) elastic oscillators (single degree of freedom systems) for a set of vibration periods under an earthquake ground motion. The response spectrum ordinates (e.g., spectral acceleration) are defined as ground-motion intensity parameters (just like PGA and PGV) because they give information about the ground-motion intensity by considering the time and frequency domain characteristics of accelerograms. Ground-motion intensity parameters are used by SHA to define the hazard level quantitatively.

combined with human exposure and seismic vulnerability (damage susceptibility of the built environment to earthquake effects), seismic risk is obtained.

SHA primarily considers the fundamental features of the seismic sources (e.g., faults) that would produce earthquakes in the vicinity of project site. The information gathered from seismic sources is elaborated to estimate the ground-motion intensity parameters, which are likely to be produced by the future earthquakes. SHA can be treated either deterministically or probabilistically. This chapter first describes the main components in the deterministic and probabilistic SHA (abbreviated as DSHA and PSHA, respectively) and it is followed by explaining the major steps in PSHA and DSHA. The latter methodology can be considered as the special case of the former. The discussions on PSHA are used to introduce the uniform hazard spectrum (UHS) that is implemented by current seismic design codes for defining design spectrum. The chapter ends by introducing the fundamentals of probability theory to grasp the essentials in some of the intermediate steps in PSHA.

2.2 Seismicity and Earthquake Recurrence Models

The first step in SHA is to study the seismic sources and evaluate past seismic events affecting the project site. Seismic sources (faults, area sources etc.) are mainly characterized by geological and seismotectonic studies. Seismic activity (frequency of earthquakes occurring in the region of interest) is investigated from earthquake catalogs. Earthquake catalogs list the location and size of earthquakes around the project site that are of engineering interest (i.e., events larger than a minimum magnitude threshold). These earthquakes are then associated with the seismic sources through geological and seismotectonic studies. Figure 2.1 presents a map that shows the locations of active seismic sources (S_1 and S_2 as faults, and S_3 as an area source) and distribution of earthquakes around a fictitious project site that is located in the center of study area. The boundaries of study area should cover all relevant seismic activity that would affect the project site.

The frequency of earthquakes generated by seismic sources defines the earthquake recurrence model that is used in PSHA. For a certain magnitude (m^*), the earthquake recurrence model gives the mean yearly number of earthquakes exceeding m^* . The pioneering study by Gutenberg and Richter (1944) proposed the simplest, nevertheless very useful, earthquake recurrence relationship as given in Eq. (2.1). The earthquake recurrence model of Gutenberg and Richter (1944) was derived by compiling the earthquake catalog in Southern California and sorting them by the total number of earthquakes exceeding different magnitudes (M). The total number of earthquakes exceeding each magnitude is normalized by the total time span covered by the earthquake catalog to describe the mean annual rate of exceedance v_m , of an earthquake of magnitude m^* .

$$\log_{10}(v_m) = a - bm. \quad (2.1)$$

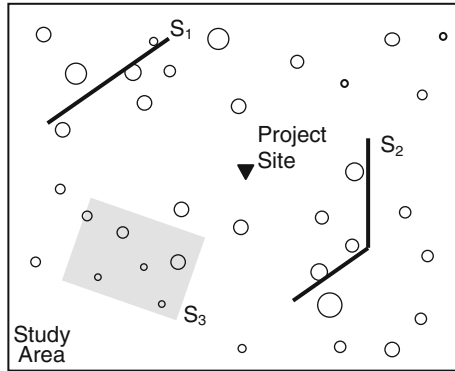


Fig. 2.1 A sample illustration that shows the faults (*black solid lines*), the area source (*gray rectangular box*) and spatial distribution of seismic events (*circles with different sizes*) in the vicinity of a fictitious project site. Different sizes of earthquakes designate earthquakes with different magnitudes. The information extracted from geological and seismotectonic studies serve for characterizing the seismic sources that affect the study area

Being a logarithmic relationship, Eq. (2.1) implies exponential probability distribution to compute the probability of mean annual exceedance rates of earthquakes in the study area. The parameter 10^a in Eq. (2.1) represents the mean annual number of events above m_{min} , which describes the minimum seismic activity rate in the study area². Thus, large a implies higher seismic activity. The slope term b defines the ratio of small to large magnitude events. A steep slope means the dominancy of smaller magnitude events with respect to larger magnitudes. In contrast, smaller b values indicate a higher contribution of large magnitude events to the seismic activity of the considered seismic source.

Calculating the earthquake recurrence model as suggested by Gutenberg and Richter is a straightforward procedure as given in Fig. 2.2. After compiling earthquake catalog for the seismic source of interest and removing the foreshocks and aftershocks (to warrant independency between seismic events) the earthquake data are sorted in ascending magnitude order (left panel in Fig. 2.2). The cumulative numbers of earthquakes of magnitude m^* or greater are found and they are normalized by the time span covered by the catalog to compute the mean annual exceedance rate of earthquakes (v_m). The total catalog duration is 102 years in this example. The black circles on the semi-log plot (right panel in Fig. 2.2) are the mean annual exceedance rates as a function of M . A straight line fit to these points yields the Gutenberg-Richter earthquake recurrence model. This straight line is

² The strict definition of Gutenberg-Richter earthquake recurrence relationship describes 10^a as the number of earthquakes with magnitudes greater than or equal to zero. The “zero-magnitude” concept may be difficult to understand for some readers who are not familiar with this notation. Thus, this book uses the “minimum magnitude, m_{min} ” terminology and neglects the earthquakes below the minimum magnitude level in the Gutenberg-Richter earthquake recurrence model.

M	# of events of magnitude M or greater (N)	N normalized by catalogue duration (ν)
4.05	95	0.93
4.15	87	0.85
4.25	77	0.75
4.35	74	0.73
4.45	63	0.62
4.55	57	0.56
4.65	50	0.49
4.75	44	0.43
4.85	33	0.32
4.95	22	0.22
5.05	20	0.20
5.15	17	0.17
5.25	14	0.14
5.35	10	0.10
5.45	8	0.08
5.65	5	0.05
5.95	2	0.02
6.15	1	0.01

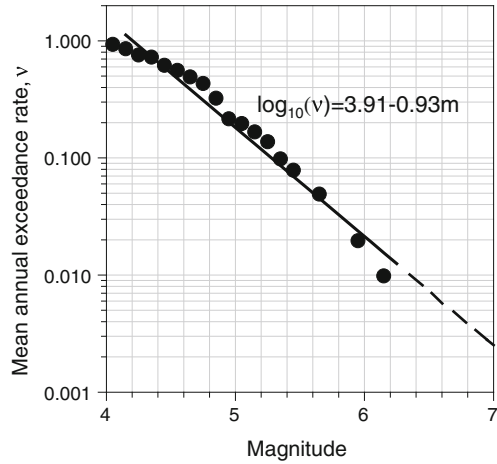
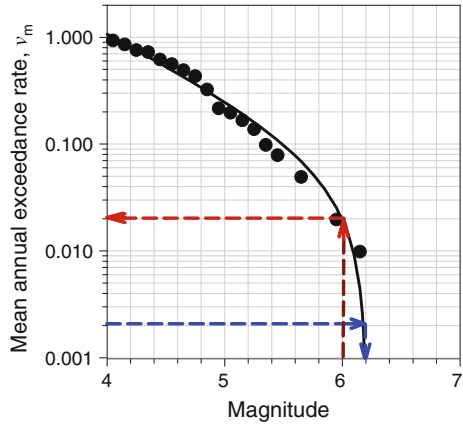


Fig. 2.2 Application of Gutenberg-Richter earthquake recurrence model on a real data set. (Dashed straight line indicates $\nu_m(M > m^*)$ estimates for magnitudes greater than the observed earthquake magnitudes in the catalog)

also shown on the right panel of Fig. 2.2 suggesting that the mean annual exceedance rate of earthquakes is, for example, ~ 0.02 for $M \geq 6$ and it is approximately 0.2 for earthquakes of $M \geq 5$. This is the expected behavior from earthquake recurrence models: the mean annual rate of exceedance of small magnitudes is greater than that of large magnitudes. In passing, an important remark that should be emphasized is the importance of using a uniform magnitude scale in earthquake catalogs for developing consistent magnitude recurrence models.

A careful consideration of Fig. 2.2 suggests that the straight line fit deviates from the actual variation of data (black circles) at the large-magnitude end: the data tend to truncate towards larger magnitudes. This observation can be explained by considering the physical limitations of seismic sources in generating earthquakes above a certain magnitude. As shown in Fig. 2.2, the maximum event produced by the considered seismic source has a magnitude of ~ 6.2 . The straight line model, due to its inherent nature, cannot cap the observed maximum magnitude (m_{max}) and would estimate unrealistic (or physically unjustifiable) mean annual exceedance rates for magnitudes that are not likely to occur on the considered seismic source. This fact is illustrated by the dashed line segment on Fig. 2.2, which estimates mean annual exceedance rates for magnitudes greater than the maximum magnitude that are almost impossible to occur on this source. Such inconsistencies can be prevented by using more rigorous magnitude versus annual frequency relationships to fine tune the earthquake recurrence models.

Fig. 2.3 Truncated Gutenberg-Richter earthquake recurrence model (solid line) using the data presented in Fig. 2.2 (The dashed arrows are discussed later in this section)



The observed saturation towards larger magnitudes can be addressed by using the truncated Gutenberg-Richter earthquake recurrence model (McGuire and Arabasz 1990). This model caps the annual frequency of earthquakes for a given m_{max} . Although there are more complicated earthquake recurrence models in the literature (e.g., characteristic earthquake recurrence model; Youngs and Coppersmith 1985), their description and differences with respect to those mentioned in the text is out of scope of this chapter.

Figure 2.3 shows the truncated Gutenberg-Richter earthquake recurrence model for the data given in Fig. 2.2. As indicated in the previous paragraph, truncated Gutenberg-Richter requires m_{max} information to describe the maximum earthquake size that can be generated by the considered seismic source. m_{max} is determined either from the compiled catalog information (e.g., Mueller 2010) or from the empirical expressions that estimate m_{max} by using fault rupture dimensions (e.g., Wells and Coppersmith 1994; Leonard 2010). The former approach is of relevance for area sources but it can also be used for faults. If catalog information is used for m_{max} , the seismic hazard expert can consider the largest observed magnitude in the earthquake catalog with an additional increment (e.g., 0.5 units) to account for the uncertainty in the largest possible future earthquake. Note that the empirical relationships involve regression on limited datasets and produce the expected magnitude value associated with a standard deviation. Thus, upon the use of empirical equations in determining m_{max} , their standard deviations should be considered to draw an upper bound for m_{max} as a proxy for the uncertainty in the maximum possible future earthquake size. For the example given in Fig. 2.3, however, none of the above approaches are followed and m_{max} is assumed as 6.2, which is determined directly from the compiled catalog (see the table in Fig. 2.2). Table 2.1 lists some empirical relationships from Wells and Coppersmith (1994) for estimating m_{max} in terms of fault rupture dimensions (surface rupture length and total rupture area). These relationships also consider the faulting mechanisms while estimating the maximum magnitudes in terms of fault rupture areas and rupture lengths.

Table 2.1 Empirical relationships to predict maximum moment magnitude (M_w) in terms of surface rupture length (l_{rup}) and rupture area (A_{rup}) that are proposed by Wells and Coppersmith (1996)

Fault mechanism	Relationship	σ_{M_w}
Strike-slip	$M_w = 5.16 + 1.12\log_{10}l_{rup}$	0.28
Reverse	$M_w = 5.00 + 1.22\log_{10}l_{rup}$	0.28
Normal	$M_w = 4.86 + 1.32\log_{10}l_{rup}$	0.34
Strike-slip	$M_w = 3.98 + 1.02\log_{10}A_{rup}$	0.23
Reverse	$M_w = 4.33 + 0.90\log_{10}A_{rup}$	0.23
Normal	$M_w = 3.93 + 1.02\log_{10}A_{rup}$	0.25

The last column gives the standard deviations of each empirical relationship

The reciprocal of mean annual exceedance rate in earthquake recurrence models describes the recurrence interval of events. The recurrence interval is also referred to as *return period* of earthquakes. For example, the recurrence interval of $M \geq 6.0$ event is 50 years ($=1/0.02$) in the example given in Fig. 2.3 (red dashed arrows). In other words, the average time between the occurrences of two consecutive events of $M \geq 6.0$ is 50 years for the given case. The distribution of earthquakes within a time period, as emphasized in this simple example, is more meaningful to assess the level of hazard at a site or a region. In general, the temporal distribution of earthquake recurrence in PSHA is characterized by the Poisson process.

If a random process generates events at some mean rate, ν , and occurrence of an event is independent of time, then it is a Poisson process. The framework of Poisson process implies equal chances of occurrence between the consecutive events and their independency from each other. In probabilistic seismic hazard assessment, the random process is the earthquake mechanism and the mean exceedance rate of events, $\nu_m(M > m^*)$, is computed from the earthquake recurrence models as described in the previous paragraphs. Following the example discussed in Figs. 2.2 and 2.3, the mean exceedance rate of earthquakes with magnitudes greater than 5 [i.e., $\nu_m(M > 5)$] is ~ 0.225 . This statistic would indicate that every 4–5 years one would expect an earthquake of $M > 5$ in the considered study area.

As far as the physics of earthquakes are of concern (elastic rebound theory), given a region, the occurrence of earthquakes are not independent of each other. Thus, the seismic activity should depend on past earthquakes. The stresses released in one fault segment due to the occurrence of an earthquake should decrease the occurrence probability of the next earthquake having approximately the same size as of the previous one on the same fault segment. To this end, being stationary in time and having no memory on the occurrence of earthquakes, the Poisson process does not fully represent the actual earthquake mechanism. However, earthquakes can be assumed as randomly occurring, independent events in time when the foreshocks and aftershocks are removed from earthquake catalogs. (This is, in fact, the major reason behind the removal of foreshocks and aftershocks from earthquake

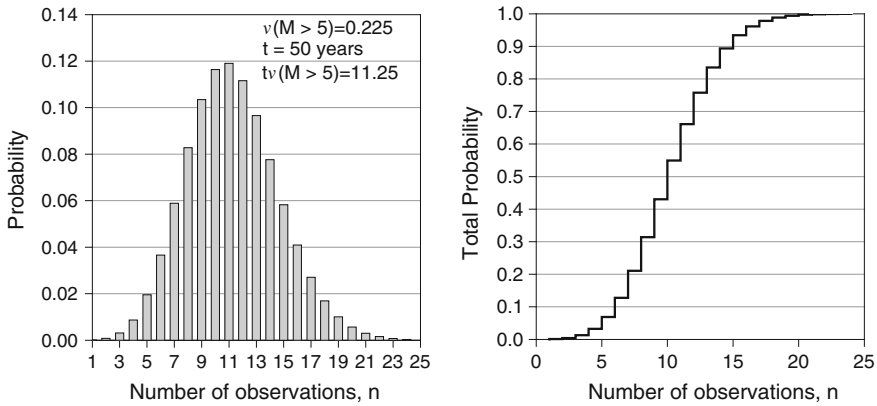


Fig. 2.4 Illustration of Poisson probability distribution assuming that the earthquake occurrence is a Poisson process

catalogs as indicated previously). The time interval, t , in the Poisson process is referred to as exposure time and it is generally considered as the nominal economic life time of structures such as 50 years. For a Poisson earthquake process with a mean exceedance rate of events larger than m^* , $v_m(M > m^*)$, the probability of observing n events having magnitudes above m^* in time interval t is

$$P(M > m^*) = \frac{\exp(-t \cdot v_m(M > m^*)) (t \cdot v_m(M > m^*))^n}{n!}. \tag{2.2}$$

Implication of Eq. (2.2) can be understood better from the earthquake recurrence case study discussed in Figs. 2.2 and 2.3. If the mean exceedance rate of events with magnitudes greater than 5 [i.e., $v_m(M > 5)$] is considered once again, the probability of observing n earthquakes for an exposure time of $t = 50$ years is illustrated in Fig. 2.4. The probabilities displayed on the left panel of Fig. 2.4 are computed by varying n from 1 to 24 for $v_m(M > 5) = 0.225$ and $t = 50$ years. For the given range of observations, the probability becomes maximum at $n = 11$ because it is the closest observation number to the expected number of events with $M > 5$ (i.e., $v_m(M > 5) \cdot t = 0.225 \cdot 50 = 11.25$) in 50-year time interval. Note that the conclusive remark in the previous paragraph for $v_m(M > 5)$ is the expectation of observing one such event for every 4–5 years that is entirely consistent with the discussions in this paragraph. The expected number of observations is ~ 11 for an interval of 50 years where the occurrence probability becomes maximum. The Poisson distribution expresses the occurrence probability of discrete number of random events in a fixed time interval but the increase in number of observations makes its behavior similar to bell-shaped normal probability distribution as depicted in Fig. 2.4 (left panel). Note that the sum of probabilities of all observations given on the right panel in Fig. 2.4 is unity.

The probabilistic seismic hazard assessment is not interested in the successive occurrence of n earthquakes with $M > m^*$ but, rather, focuses on the likelihood

of at least one event of $M > m^*$ within a time interval t . This probability is known as the *probability of exceedance*. It is computed by subtracting the probability of observing no earthquake [$n = 0$ in Eq. (2.2)] within the time interval t from unity. Equation (2.3) gives the probability of exceedance relationship. Note that the probability of one describes the occurrence of infinite number of earthquakes for the magnitude interval of concern.

$$P(M > m^*) = 1 - \exp(-t \cdot v_m(M > m^*)) \quad (2.3)$$

Equation (2.4) is the modified version of Eq. (2.3). It gives the relationship between the probability of exceedance of an earthquake above a certain magnitude, m^* [i.e., $P(M > m^*)$] and corresponding mean annual exceedance rate ($v_m(M > m^*)$) for a predetermined exposure time t .

$$v_m(M > m^*) = -\frac{\ln(1 - P(M > m^*))}{t}. \quad (2.4)$$

For an exposure time of $t = 50$ years and for 10 % probability of exceedance of events with magnitudes greater than m^* (i.e., $P(M > m^*) = 0.1$), the mean annual exceedance rate is approximately 2.1×10^{-3} [computed from Eq. (2.4)]. If the computed mean annual exceedance rate is used as input in the earthquake recurrence model presented in Fig. 2.3, the corresponding magnitude is approximately $m^* = 6.2$ (see blue dashed arrows in Fig. 2.3). This simple calculation indicates that within a 50-year time period from today, the probability of having an event with $M \geq 6.2$ is 10 % for the area of interest. The validity of this conclusion is fairly definitive unless the applicability of Poisson process is questioned for the study area.

Example 2.1 The Gutenberg-Richter earthquake recurrence model yields the following relationship for a hypothetical area source:

$$\log_{10} v_m = 4 - m. \quad (\text{E2.1.1})$$

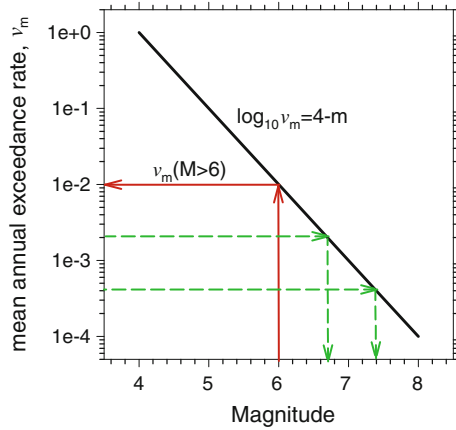
Assuming that the earthquakes follow Poisson process, calculate:

- The probability that at least one earthquake of $M > 6$ will occur in 50-year and 100-year recurrence intervals.
- The probability that exactly one earthquake of $M > 6$ will occur in 50-year and 100-year recurrence intervals.
- The magnitude that would have a 10 % probability of exceedance in 50-year recurrence interval.
- The magnitude that would have a 2 % probability of exceedance in 50-year recurrence interval.

Solution

Figure 2.5 shows the earthquake recurrence model given in the example problem. The mean annual exceedance rate for $M > 6$ is calculated as $v_m(M > 6) = 0.01$ and it is given on the same plot (red arrows). The solutions to the questions are as follows:

Fig. 2.5 Earthquake recurrence model for the hypothetical area source



- (a) By using Eq. (2.3), the probability that at least one earthquake of $M > 6$ will occur in 50-year is

$$P(M > 6) = 1 - \exp(-50 \cdot 1e - 2) = 0.393 \quad (\text{or } P(M > 6) \text{ is } 39.3 \% \text{ in } 50 \text{ years}).$$

In a similar way, the probability that at least one earthquake of $M > 6$ will occur in 100-year is

$$P(M > 6) = 1 - \exp(-100 \cdot 1e - 2) = 0.632 \quad (\text{or } P(M > 6) \text{ is } 63.2 \% \text{ in } 50 \text{ years}).$$

- (b) The probability of having exactly one earthquake with $M > 6$ is calculated from Eq. (2.2). For 50 and 100-year return periods, these probabilities are, $P(M > 6) = \exp(-50 \cdot 1e - 2)(50 \cdot 1e - 2) = 0.303$ (for 50-year return period)

$$P(M > 6) = \exp(-100 \cdot 1e - 2)(100 \cdot 1e - 2) = 0.368 \quad (\text{for } 100\text{-year return period})$$

- (c) Equation (2.4) is used to compute the mean annual exceedance rate for a magnitude of having 10 % probability of exceedance in 50-year period. This calculation is given below:

$$v_M(M > m^*) = -\frac{\ln(1 - p(M > m^*))}{t} = -\frac{\ln(1 - 0.10)}{50} \approx 0.002107.$$

The computed mean annual exceedance rate is then inserted into Eq. (E2.1.1) to compute the magnitude, m^* , corresponding to the given probability of exceedance in 50-year period:

$$\log_{10}(0.002107) = 4 - m^* \Rightarrow m^* = 6.67.$$

Figure 2.5 shows the computed magnitude as well as the corresponding mean annual exceedance rate with green dashed arrows.

- (d) Following the same procedure as above, the magnitude is computed as $m^* = 7.39$. The corresponding mean annual exceedance rate is 0.000404. These values are also shown with green dashed arrows in Fig. 2.5.

2.3 Ground-Motion Prediction Equations (Attenuation Relationships)

Ground-motion prediction equations (GMPEs) estimate the ground-motion intensity parameters (e.g., PGA, PGV, spectral ordinates such as S_a at different vibration periods etc.) at a specific location by considering the source, path and site effects. These effects are mainly described by independent variables such as magnitude (M), source-to-site distance (R), site class (SC) and style-of-faulting (SoF).³ Consideration of magnitude and style-of-faulting describes the source effects, the source-to-site distance accounts for the variation of seismic-wave amplitudes due to path effects and site class maps the influence of soil behavior on to ground-motion amplitudes. Ground-motion predictive models are developed using regression analysis and they are based on empirical ground-motion datasets. The randomness in ground-motion intensity parameters that is described by large ground-motion datasets is the fundamental reason behind the use of regression analysis while producing GMPEs. The exponential functional form of GMPEs is given in Eq. (2.5) and it is originated from earthquake source theory (Joyner and Boore 1981).

$$Y = \exp(f(M) \cdot f(R) \cdot f(SC) \cdot f(SoF)). \quad (2.5)$$

As one can infer from Eq. (2.5), the ground-motion intensity parameter Y is computed as a result of multiplicative process. The independent estimator parameters M , R , SC and SoF are used in various functions and Y is treated as a log-normally distributed random variable. Equation (2.6) is the most general format used by GMPE model developers.

$$\ln(Y) = \theta(M, R, SC, SoF) + \varepsilon \cdot \sigma_{\ln y}. \quad (2.6)$$

$\theta(M, R, SC, SoF)$ is a general functional term that represents the combined effects of $f(M)$, $f(R)$, $f(SC)$ and $f(SoF)$. It is the predicted logarithmic mean μ , of $\ln(Y)$. In a similar way, $\sigma_{\ln y}$ is the standard deviation (sigma) of $\ln(Y)$ and ε is a standard normal variable that describes the number of standard deviations above (positive ε values) or below (negative ε values) the predicted logarithmic mean (median), μ . Thus, ε is a representative of observed variability in $\ln(Y)$. In essence, from PSHA view point, GMPEs model the probability distributions of ground-motion intensity parameters conditioned on the independent variables used in their derivation. As the logarithm of a log-normal variate is normal, the exceedance probabilities of Y for different thresholds, y , are computed from the normal probability density function as given in Eq. (2.7).

³ The independent variables indicated here can be accepted as the fundamental ones. There are more complicated independent estimator parameters that are used by many GMPE developers. Descriptions of these independent parameters or their consideration are not the scope of this chapter. The book will refer to M , R , SC and SoF as the fundamental seismological estimators while discussing the behavior of ground-motion intensity parameters.

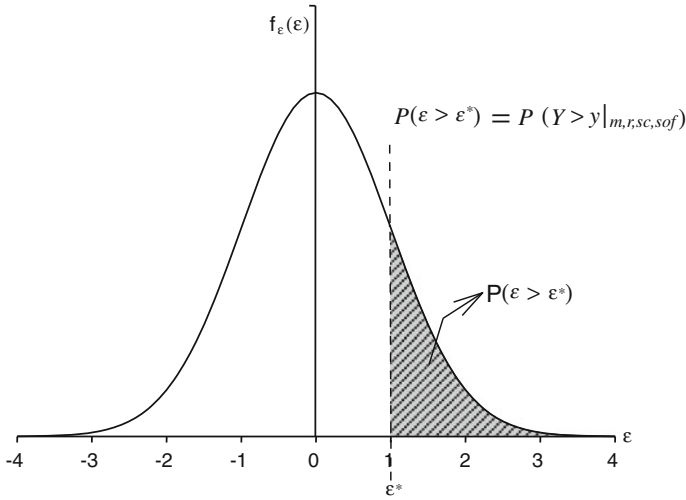


Fig. 2.6 Standard normal probability distribution of ε to describe the exceedance probability calculations in GMPEs

$$P\left(Y > y|_{m,r,sc,sof}\right) = \int_y^{\infty} \frac{1}{\sigma_{\ln Y} \sqrt{2\pi}} \exp\left[-\frac{1}{2} \left(\frac{\ln y - \mu}{\sigma_{\ln Y}}\right)^2\right] dy \quad y \geq 0. \quad (2.7)$$

The integrand in Eq. (2.7) is the normal probability density function, $f_Y(y|_{m,r,sc,sof})$. This equation can also be represented by the standard normal probability distribution of ε , $f_\varepsilon(\varepsilon)$ with zero mean and unit variance.

$$P\left(Y > y|_{m,r,sc,sof}\right) = \int_{\varepsilon^*}^{\infty} f_\varepsilon(\varepsilon) d\varepsilon. \quad (2.8)$$

The theoretical framework given in Eq. (2.8) is illustrated in Fig. 2.6. When ε takes a value of zero the estimated ground-motion intensity parameter has 50 % probability of exceedance (i.e., $P(Y > y|_{m,r,sc,sof}) = 0.5$). That is why the fitted curve in the form of Eq. (2.6) with $\varepsilon = 0$ is called as the “median curve”. When $\varepsilon = 1$ (i.e., median + σ estimation), $P(Y > y|_{m,r,sc,sof})$ is approximately 16 %. The normality of epsilon implies that consideration of, for example, $\pm 3\varepsilon$ range accounts for ~ 99 % of the uncertainty in the estimated ground-motion intensity parameter, Y .

Figure 2.7 illustrates the discussed concepts by using the variation of a GMPE derived for estimating PGA (peak ground acceleration). The predictive model is fitted on the PGA values of stiff soil conditions that are obtained from several strong-motion accelerograms of magnitudes ranging from 6.0 to 7.0. The solid curve describes the median variation of the estimated PGA as a function of distance. The dashed curves show the PGA estimations for median $\pm \sigma$.

Fig. 2.7 Median and median \pm sigma curves of stiff site PGA. The scatter points are the observed stiff site PGA values of $6.0 \leq M \leq 7.0$

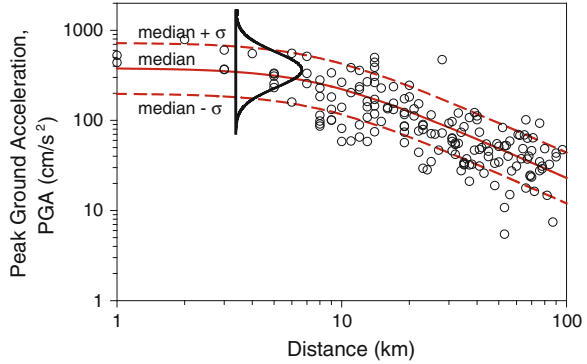


Table 2.2 Probabilities of $S_{a0.2s}$ exceeding 0.75 g at different distances

$R(\text{km})$	$\ln(S_{a0.2s}), \mu$	$\sigma_{\ln y}$	$P(S_{a0.2s} > 0.75 \text{ g})$ in percent
5	-0.2706	0.695	50.98
20	-1.05401	0.695	13.51
30	-1.40576	0.695	5.38
50	-1.87779	0.695	1.11
75	-2.26289	0.695	0.22

The exceedance probability of the estimated PGAs is $\sim 16\%$ for the median $+\sigma$ curve, whereas this probability is $\sim 84\%$ for the median $-\sigma$ curve. The probability plot associated with the PGA curves illustrates these interpretations better.

Example 2.2 The ground-motion prediction equation of Akkar and Bommer (2010) has the following form for estimating S_a at $T = 0.2$ s ($S_{a0.2s}$) for a rock site when earthquake is generated by a strike-slip fault.

$$\ln(S_{a0.2s}) = -4.769 + 2.229M - 0.182M^2 + (-2.493 + 0.218M) \ln \sqrt{R^2 + 8.219^2}. \quad (\text{E2.2.1})$$

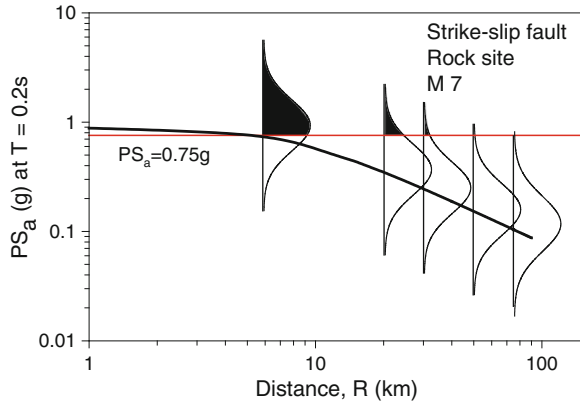
The associated standard deviation (sigma) is $\sigma_{\ln y} = 0.695$. Determine the probabilities of $S_{a0.2s} > 0.75$ g at distances of 5, 20, 30, 50 and 75 km for $M = 7$.

Note The original Akkar and Bommer (2010) GMPE is rescaled for estimating the spectral accelerations in terms of gravitational acceleration, g . It is also originally in \log_{10} that is modified for natural logarithm for consistency with the notations used in the text.

Solution

The logarithmic means of Eq. (E2.2.1) for the designated distances and $M = 7$ are given in Table 2.2. These values and the associated logarithmic standard deviation ($\sigma_{\ln y} = 0.695$) are used in Eq. (2.7) to compute $P(S_{a0.2s} > 0.75 \text{ g})$. The computed probabilities are given in the last column of Table 2.2. Figure 2.8 shows the probability distribution functions for each case. The shaded areas in the probability distribution functions correspond to the exceedance probabilities of 0.75 g.

Fig. 2.8 Probability distributions of Eq. (E2.2.1) at discrete distances ($R = 5, 20, 30, 50, 75$ km). *Shaded areas* in each probability density function show the exceedance probabilities of 0.75 g. The level of 0.75 g is shown by *solid red line*. The *thick black line* shows the variation of Eq. (E2.2.1) as a function of distance (Colour figure only for online)



2.4 Probabilistic Seismic Hazard Analysis

The probabilistic seismic hazard analysis (PSHA) accounts for all possible earthquake scenarios and ground-motion levels that can occur on the seismic sources affecting the project site. The proponent of this method is Cornell (1968). The ground-motion levels are determined as a range of sigma values above or below the median ground-motion estimate. In a sense, PSHA pools a large number of earthquake scenarios (i.e., all possible magnitude, distance and sigma combinations) that can be generated by the seismic sources. It computes the mean annual rate of the ground-motion intensity parameter of interest (e.g., PGA) exceeding a specific threshold level. The computed mean annual exceedance rate can be expressed as a probability for a given exposure time by assuming that the ground-motion intensity parameters also follow Poisson distribution.⁴

Given a seismic source, the computation of mean annual rate (γ) for ground-motion intensity parameter Y exceeding a threshold level y can be described by the integral given in Eq. (2.9).

$$\gamma(Y > y) = v_m(M > m_{min}) \int_{m_{min}}^{m_{max}} \int_0^{r_{max}} f_M(m) f_R(r) P(Y > y |_{m,r}) dm dr. \quad (2.9)$$

In this expression, $v_m(M > m_{min})$ is the mean annual exceedance rate of earthquakes with magnitudes greater than m_{min} for the considered seismic source. The probability density functions of earthquake recurrence and source-to-site distance are described by $f_M(m)$ and $f_R(r)$, respectively. The theoretical concept under earthquake recurrence models for seismic sources is discussed in Sect. 2.2. $f_R(r)$ accounts for the location uncertainty of events occurring on the seismic

⁴ There are more complicated models than the Poisson process to describe the probabilities of mean occurrence rates of earthquakes. These models are out of scope of this chapter.

source. In general, earthquakes are assumed to be uniformly distributed within a seismic source. The probability density function, $f_R(r)$, transforms this assumption into the uncertainty in source-to-site distance depending on the seismic source geometry. (Problems illustrating the derivations of $f_M(m)$ and $f_R(r)$ for some specific cases are given in Sect. 2.7). $P(Y > y|_{m,r})$ expresses the variability in the ground-motion intensity parameter of interest. Note that the soil conditions of the project site and faulting mechanism of the seismic source are assumed to be known and held fixed in the computations. $P(Y > y|_{m,r})$ is determined from the chosen ground-motion predictive model (see discussions in Sect. 2.3). The chosen GMPE should address the overall seismotectonic features of the seismic source (style-of-faulting, shallow vs. deep earthquake regions, etc.) and it should properly reflect the soil conditions in the site. The soil conditions can be classified in terms of generic site classes such as rock, stiff or soft soil that are compatible with seismic code provisions. The soil conditions can also be determined in terms of average shear-wave velocity in the upper 30 m soil profile (V_{S30}) computed through in situ geophysical analysis in the project site. Many seismic design codes classify soil conditions by using different V_{S30} intervals.

Equation (2.9) incorporates the knowledge about rates of annual exceedance of earthquakes, the possible magnitude ranges and source-to-site distances of those earthquakes and the distribution of Y into the computation of mean annual rate of Y exceeding a certain threshold level, y . The consideration of all uncertainties in the hazard integral components makes the analytical solution of Eq. (2.9) almost impossible and impractical. Thus, the computations are generally based on discretizing the magnitude and distance ranges into n_m and n_r segments, respectively. This approach transforms the integral operations into summation as given in Eq. (2.10). This equation also accounts for the existence of multiple (n_s) seismic sources that have the potential of affecting the project site.

$$\gamma(Y > y) = \sum_{i=1}^{n_s} v_{m_i} (M_i > m_{min}) \sum_{j=1}^{n_m} \sum_{k=1}^{n_r} P(Y > y|_{m_j, r_k}) P(M = m_j) P(R = r_k). \quad (2.10)$$

As Eq. (2.10) discretizes the magnitudes and source-to-site distances, the probability terms $f_M(m)$ and $f_R(r)$ in Eq. (2.9) are described by $P(M = m_j)$ and $P(R = r_k)$, respectively in this expression. Implementation of the above theory is explained in the following steps by the help of representative illustrations given in Fig. 2.9.

1. Develop a set of earthquake scenarios by considering the seismic activity of the source(s) in the considered area. This step requires the determination of minimum and maximum magnitude events that is discussed in Sect. 2.2. The hazard expert considers a range of discrete scenario magnitudes between m_{min} and m_{max} that represent scenario earthquakes that are likely to occur on the source(s). The minimum magnitude is generally determined from the size of minimum earthquake of engineering significance for the specific project.

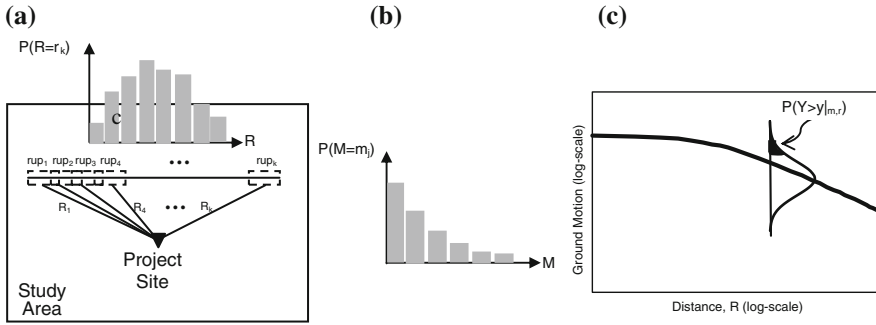


Fig. 2.9 Main components of PSHA assuming that the project site is affected by a single source

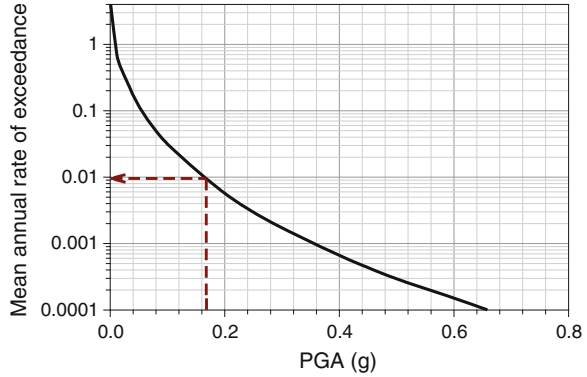
The probabilities of discrete scenario magnitudes, $P(M = m_j)$ are calculated from the probability density function(s), $f_M(m)$, of the magnitude recurrence model(s) derived for the seismic source(s) (Fig. 2.9b).

2. For each scenario magnitude, estimate the rupture length (l_{rup}) from the empirical M versus l_{rup} relationships that have formats similar to those given in Table 2.1 (e.g., $\log_{10} l_{rup} = a + b \times M_w$). Depending on the size of rupture, the considered scenario earthquake can occur at any location within the source. As illustrated in Fig. 2.9a, $n_r (r = 1 \dots k)$ different discrete rupture locations can be set for a given scenario magnitude. Assuming that the rupture location is uniformly distributed within the seismic source (i.e., $P(\text{location}|_{\text{scenario}}) = 1/n_r$), the probabilities of source-to-site distances, $P(R = r_k)$, are calculated as shown on the top of Fig. 2.9a. Note that the reliable computation of source-to-site distance probabilities depends on the proper consideration of source-to-site distance metric that is used by the ground-motion predictive model. The computation of some source-to-site distance metrics requires source geometry. Such information is not always available from geological studies. The hazard expert should make some proper and physically justifiable assumptions in the absence of such information. The existing methodologies for such kind of computations are out of scope of this chapter.
3. Contributions from each possible combination of source-to-site distance and scenario magnitude on the seismic source(s) are used to compute the mean annual exceedance rate $\gamma(Y > y)$. For a given source i , this step involves the summation of following discrete rates.

$$\gamma_i(Y > y) = v_{m_i}(M_i > m_{min}) \sum_{j=1}^{n_m} \sum_{k=1}^{n_r} P(Y > y|_{m_j, r_k}) P(M = m_j) P(R = r_k). \tag{2.11}$$

The above rate calculations are repeated upon the existence of multiple sources in the study area. The total mean annual rate for exceeding the threshold y is:

Fig. 2.10 A sample hazard curve computed for PGA



$$\gamma(Y > y) = \sum_{i=1}^{n_s} \gamma_i(Y > y). \quad (2.12)$$

4. If the entire process is repeated for different threshold values, the so-called “seismic hazard curve” for the ground-motion intensity parameter of interest is obtained. The hazard curves are of particular use for engineering design as they can describe the levels of ground motions (e.g., PGA, S_a at different vibration periods) for different annual exceedance rates. This information is used by the engineer to design or verify the performance of structural systems under earthquake induced seismic demand. An example of seismic hazard curve is given in Fig. 2.10 for PGA assuming that it is the ground-motion intensity parameter of interest.

As discussed throughout this section, PSHA is a probabilistic process that produces hazard curves to inform design engineer about the mean annual exceedance rates of ground motions for a certain threshold. The overall computations are based on a set of possible earthquake scenarios on the seismic source(s). The hazard curve presented in Fig. 2.10 depicts that the mean annual rate of PGA exceeding 0.16 g is 0.01. In other words, the average time between the occurrences of this PGA level is 100 years ($1/0.01$) for the project site at which the specific hazard curve (Fig. 2.10) is calculated. The average time (reciprocal of mean annual rates given in the hazard curve) between the occurrences of a certain ground-motion intensity level is called *return period* in PSHA. If the occurrence of ground-motion intensities is also assumed to be Poisson as in the case of earthquake occurrence, the return periods of ground-motion intensities can be expressed in terms of different probabilities for an exposure time of t years. Using Eq. (2.4) and assuming $t = 50$ years, the exceedance probability for a ground-motion intensity of $\gamma = 0.0004$ is calculated as $\sim 2\%$. That is, the ground-motion intensities with a mean annual rate of $\gamma = 0.004$ have 2% exceedance probability for a building service life of 50 years. The same exceedance probability is $\sim 10\%$ for ground-motion intensities corresponding to $\gamma = 0.002$ when t is taken as 50-year.

Table 2.3 Magnitude probabilities of the fictitious strike-slip fault with Gutenberg-Richter earthquake recurrence model

m_j	$F_M(m_j)$	$P(M = m_j)$
5.00	0.000	0.438
5.25	0.438	0.246
5.50	0.684	0.138
5.75	0.822	0.078
6.00	0.900	0.044

Example 2.3 An energy power plant will be built at a rock site that is 25 km away from a strike-slip fault. The project site is located in a region prone to shallow active crustal earthquakes and the fault can produce earthquakes with a maximum moment magnitude of M_w 6. The minimum considered magnitude for engineering design is M_w 5 and seismic source characterization studies indicated that the mean annual exceedance rate of $M_w \geq 5$ is 0.15 (i.e., $v_m(M_w > 5) = 0.15$). The earthquakes occurring on the fault are assumed to follow Gutenberg-Richter earthquake recurrence model with a b value of 1. This information yields the discrete probabilities of magnitudes between $5 \leq M_w \leq 6$ as listed in Table 2.3. The engineering company needs S_a at $T = 0.5$ s ($S_{a0.5s}$) for a return period of 475-year to design the main building of the power plant. The chosen vibration period ($T = 0.5$ s) corresponds to the fundamental period of the building. Determine the corresponding S_a at $T = 0.5$ s. Assume that earthquakes and ground-motion intensity parameters follow Poisson process for the solution.

Solution

This problem is a simple case to show the PSHA calculation steps described in Sect. 2.4. The magnitude range that is expected to occur on the given fault is discretized by using a small number of intervals to follow the calculations easily (Table 2.3). In real PSHA, the magnitude range is divided into larger number of intervals to obtain more precise results. The strike-slip fault is assumed to be a point source. This assumption disregards the actual fault geometry. Thus, the solution waives the uncertainty in spatial distribution of earthquakes (i.e., $P(R = 25) = 1$); which is another simplification in the solution. The selected ground-motion prediction equation is the Akkar and Bommer (2010) model and it is given in the following lines for the case considered in this example:

$$\ln(S_{a0.5s}) = -6.376 + 4.22M_w - 0.304M_w^2 + (-2.13 + 0.169M_w) \ln \sqrt{R^2 + 7.174^2}. \quad (\text{E2.3.1})$$

This GMPE predicts S_a in cm/s^2 and its standard deviation is $\sigma_{\ln y} = 0.7576$ at $T = 0.5$ s. The original functional form is in \log_{10} units and it is modified for natural logarithms, which is the logarithmic unit used throughout the text. Table 2.4 lists the exceedance probabilities for a set of threshold acceleration values for each possible magnitude-distance combination considered in the solution [i.e., $P(S_{a0.5s} > y|_{m_j, r=25})$]. Note that the source-to-site distance is constant for

Table 2.4 Probabilities of exceedance for $S_{a0.5s}$ at different threshold acceleration values

M_w	μ	σ_{lny}	Preselected threshold acceleration values, y , in cm/s^2										
			1	5	10	20	50	100	200	300	500	750	1000
			$P(P_{S_{a0.5s}} > y m_{j,r} = 2.5)$										
5.00	2.9336	0.7576	0.9999	0.9598	0.7976	0.4673	0.0982	0.0137	0.0009	0.0001	7.42E-06	5.68E-07	7.77E-08
5.25	3.3470	0.7576	1.0000	0.9891	0.9160	0.6786	0.2279	0.0484	0.0050	0.0009	0.0001	7.78E-06	1.30E-06
5.50	3.7225	0.7576	1.0000	0.9974	0.9696	0.8313	0.4012	0.1220	0.0188	0.0045	0.0005	0.0001	1.31E-05
5.75	4.0600	0.7576	1.0000	0.9994	0.9898	0.9200	0.5775	0.2359	0.0511	0.0150	0.0022	0.0004	0.0001
6.00	4.3595	0.7576	1.0000	0.9999	0.9967	0.9641	0.7226	0.3729	0.1076	0.0380	0.0072	0.0014	0.0004

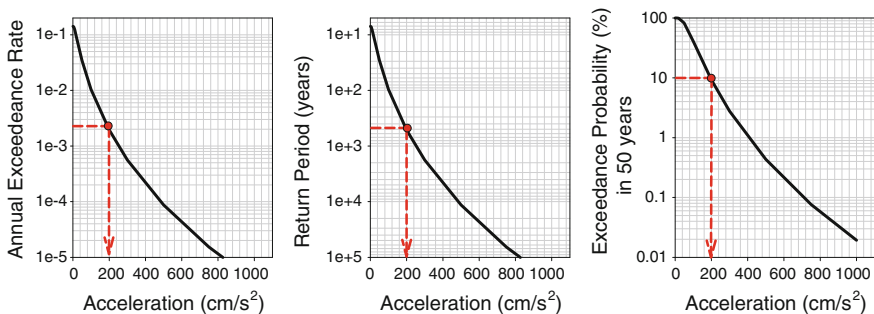


Fig. 2.11 Hazard curves for S_a at $T = 0.5$ s in terms of annual exceedance rate (*left panel*), return period (*middle panel*) and exceedance probability assuming the service life of the building is 50 years

all scenarios and it is $R = 10$ km. The variable μ in Table 2.4 is the logarithmic mean acceleration for each magnitude-distance combination that is computed from the Akkar and Bommer (2010) expression as given above. The probability calculations are done using Eq. (2.7). The annual rate of $S_{a0.5s}$ exceeding a given threshold acceleration value [i.e., $\gamma(S_{a0.5s} > y)$] is the sum of the products of $P(S_{a0.5s} > y | m_j, r=25)$, $P(M = m_j)$, $P(R = 25)$ and $v_m(M_w > 5)$ corresponding to the M - R combinations contributing to $\gamma(S_{a0.5s} > y)$. The contributions of M - R combinations to the final annual rate of each threshold acceleration value are given in Table 2.5. The final annual rates are indicated in bold. Figure 2.11 describes the hazard curves for $S_{a0.5s}$ in terms of annual rates (left panel), return periods (middle panel) and exceedance probabilities (right panel). The return periods are the reciprocals of annual exceedance rates whereas probabilities are computed using Eq. (2.4) assuming that the service life (exposure time) of the subject building is $t = 50$ years. For convenience, the modified form of Eq. (2.4) for computing probabilities, $P(S_{a0.5s} > y)$, from annual exceedance rates is given in Eq. (E2.3.2).

$$P(S_{a0.5s} > y) = 1 - \exp(-t \cdot \gamma(S_{a0.5s} > y)). \tag{E2.3.2}$$

The plots in Fig. 2.11 also show the design spectral acceleration value at $T = 0.5$ s (red dashed arrows). The 475-year return period that corresponds to an annual exceedance rate of 0.0021 ($=1/475$), or 10 % probability of exceedance in 50 years, yields a spectral acceleration of ~ 200 cm/s^2 for the design of power plant building.

Table 2.5 Annual rates for $S_{d,0.5s}$ exceeding different threshold acceleration values

		Preselected threshold acceleration values, y , in cm/s^2													
M_w	$v_M (M_w > 5)$	$P(M = M_w)$	$P(R = 25)$	γ_1	5	10	20	50	100	200	300	500	750	1000	
					γ_5	γ_{10}	γ_{20}	γ_{50}	γ_{100}	γ_{200}	γ_{300}	γ_{500}	γ_{750}	γ_{1000}	
5.00	0.150	0.4380	1.0000	0.0657	0.0631	0.0524	0.0307	0.0065	0.0009	0.0001	0.0000	4.87E-07	3.73E-08	5.10E-09	
5.25	0.150	0.2460	1.0000	0.0369	0.0365	0.0338	0.0250	0.0084	0.0018	0.0002	0.0000	2.83E-06	2.87E-07	4.79E-08	
5.50	0.150	0.1380	1.0000	0.0207	0.0206	0.0201	0.0172	0.0083	0.0025	0.0004	0.0001	1.04E-05	1.35E-06	2.71E-07	
5.75	0.150	0.0780	1.0000	0.0117	0.0117	0.0116	0.0108	0.0068	0.0028	0.0006	0.0002	0.0000	4.25E-06	9.97E-07	
6.00	0.150	0.0440	1.0000	0.0066	0.0066	0.0066	0.0064	0.0048	0.0025	0.0007	0.0003	0.0000	9.39E-06	2.54E-06	
				0.1416	0.1385	0.1244	0.0901	0.0347	0.0104	0.0019	0.0006	0.0001	1.53E-05	3.86E-06	

The table lists the contributions from all possible M - R combinations to the annual rates that are considered in the case study

2.5 Deterministic Seismic Hazard Analysis

DSHA can be considered as the special case of PSHA in which a particular earthquake scenario (i.e., a magnitude and source-to-site distance pair) is specified for the controlling earthquake. To this end, DSHA focuses on the maximum ground motion that can be generated by the seismic sources in the study area. The earthquake producing the maximum ground motion is the controlling earthquake and it describes the seismic hazard in the project site. The ground-motion intensity parameter of interest (i.e., PGA, S_a at a given vibration period etc.) computed from the controlling earthquake scenario is used either for design or seismic performance assessment of structures. DSHA specifies the level of controlling-earthquake ground motion either as median ($\varepsilon = 0$) or median $+\sigma$ ($\varepsilon = 1$). Specification of ground motions either as median or median $+\sigma$ resembles the consideration of inherent uncertainty in ground-motion amplitudes. Since the entire DSHA methodology is based on the controlling earthquake scenario, there is no return period concept at the end of the calculations. In other words, no information is provided on the occurrence probability of the controlling earthquake at the end of DSHA. To this end, DSHA always focuses on the worst-case scenario without quantifying its likelihood during the service life of the structure. However, the decision on the worst-case scenario is still subjective as the choices made for the controlling earthquake or the corresponding ground motion are strongly dependent on the hazard expert. Essentially, the deterministic earthquake or the ground motion identified at the end of DSHA may not be the “true” worst-case as the possibility of having larger earthquakes or ground motions always exists in this approach. Figure 2.12 shows a schematic illustration to explain the major steps in DSHA. The following steps summarize DSHA:

1. Define the seismic source(s), if possible with style-of-faulting information, in the study area (e.g., S_1 and S_2 are the active faults that are likely to affect the hazard in the project site as given on Fig. 2.12).
2. Estimate the magnitudes of maximum probable events that can occur on the identified seismic sources ($(M_{max})_1$ and $(M_{max})_2$). This information can be obtained from the compiled earthquake catalog (Sect. 2.2). The alternative can be the use of empirical magnitude (M) versus fault rupture length (l_{rup}) relationships similar to those given in Table 2.1 (e.g., $\log_{10} M_w = a + b \times l_{rup}$). The latter option assumes the rupture of entire fault length (or a significant portion of it) during the controlling earthquake. As discussed in Sect. 2.2, the hazard expert can consider an additional 0.5 magnitude units or can include the standard deviation of the empirical M versus l_{rup} relationship in estimating the maximum magnitude to account for the uncertainty in the largest possible future earthquake.

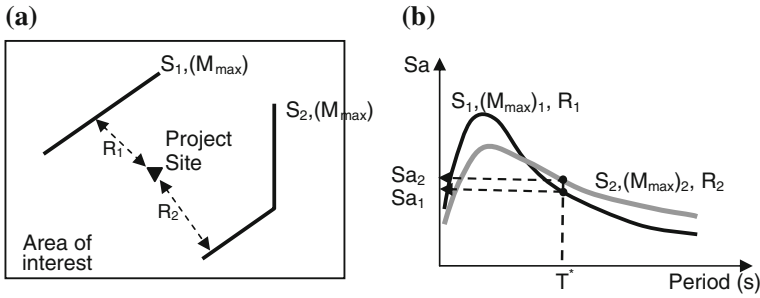


Fig. 2.12 An illustrative figure that shows the basic steps followed in DSHA

3. Determine the shortest source-to-site distance between the identified sources and the site. These are represented as R_1 and R_2 for S_1 and S_2 , respectively in Fig. 2.12a. (Refer to the discussion on the source-to-site distance computation in the previous section).
4. Determine the soil conditions at the site through in situ geotechnical studies (refer to the previous section about identification of soil conditions).
5. Use a proper ground-motion prediction equation to estimate the ground-motion parameter of interest using the magnitude, source-to-site distance, site class and style-of-faulting information obtained in the previous steps. As it is the case in Fig. 2.12b, the ground-motion parameter of interest can be the spectral acceleration (S_a) ordinate at the fundamental period (T^*) of the structure to be designed or to be assessed for its seismic performance against the controlling event. In general, the ground-motion parameter of interest is computed either as the median (i.e., $\varepsilon = 0$) or median $+\sigma$ (i.e., $\varepsilon = 1$) level using the chosen GMPE. Some analysts prefer using the median values of ground motions whereas others chose the latter level. This choice can be specific to the project conditions.
6. Compare the ground-motion parameter of interest (given as $S_a(T^*)$ in Fig. 2.12b) computed from each source and chose the largest one to be used in the design (or seismic performance assessment). The corresponding scenario is the controlling earthquake specific to the considered design or performance assessment project. Note that if the median ground motion is chosen, the ground motion has 50 % chance of exceedance whereas upon the choice of the median $+\sigma$ ground motion, it has 16 % chance of being exceeded provided that the controlling event hits the project site from the location where the shortest source-to-site distance is calculated.

Example 2.4 Determine the design spectral acceleration for the power plant building in Example 2.3 using DSHA.

Solution

The maximum moment magnitude (M_w 6.0) and the shortest source-to-site distance ($R = 25$ km) are inserted into Eq. (E2.3.1) to obtain the median S_a at $T = 0.5$ s corresponding to the controlling earthquake for the given seismic source

and site configuration. The computed spectral acceleration is $\sim 78 \text{ cm/s}^2$. If the median $+\sigma$ level is used in Eq. (E2.3.1) to account for the uncertainty in ground motions, the computed design S_a at $T = 0.5 \text{ s}$ is $\sim 167 \text{ cm/s}^2$. These calculations are shown below:

$$78.2 = e^{(-6.376+4.22 \times 6 - 0.304 \times 6^2 + (-2.13+0.169 \times 6) \ln \sqrt{25^2+7.174^2})}$$

$$166.8 = e^{(-6.376+4.22 \times 6 - 0.304 \times 6^2 + (-2.13+0.169 \times 6) \log_{10} \sqrt{25^2+7.174^2+0.7576})}$$

Note that the difference between the above two calculations is the consideration of logarithmic standard deviation ($\sigma_{\ln y} = 0.7576$) in the power term of second expression. The decision between these two spectral ordinates for the design of fictitious building is subjective as it entirely depends on the view point of the expert who is in charge of design. When these results are compared with the one obtained from PSHA (Example 2.3), one may infer that the spectral ordinates identified by DSHA may fail to represent the critical seismic demands for the design of power plant building as PSHA suggests using a larger S_a in the design process.

2.6 Uniform Hazard Spectrum

This section introduces the uniform hazard spectrum (UHS) concept that is used to define various levels of ground motions for seismic design or performance assessment in the current seismic provisions. Hazard curves derived for a set of acceleration spectral ordinates are used in the construction of UHS. The spectral ordinates corresponding to a predefined mean annual exceedance rate (e.g., $\gamma = 0.000404$ corresponding to 2475-year return period) are identified from the seismic hazard curves computed for a set of spectral periods. These spectral values constitute the ordinates of the uniform hazard spectrum (Fig. 2.13) and they pose the same exceedance probability for a given exposure time, t .

2.7 Basic Probability Concepts

The discussions in this chapter involve some fundamentals of probability theory. This section briefs these fundamentals to help the reader in understanding some of the intermediate calculation steps throughout the text that are not detailed for brevity.

One of the major objectives of probability theory is to define the nature of random variables that may conceptually take a set of different values. Random variables can be either discrete or continuous. Discrete random variables can take a countable number of values whereas continuous random variables take any value (i.e., infinite number of values) within a sample space, S .

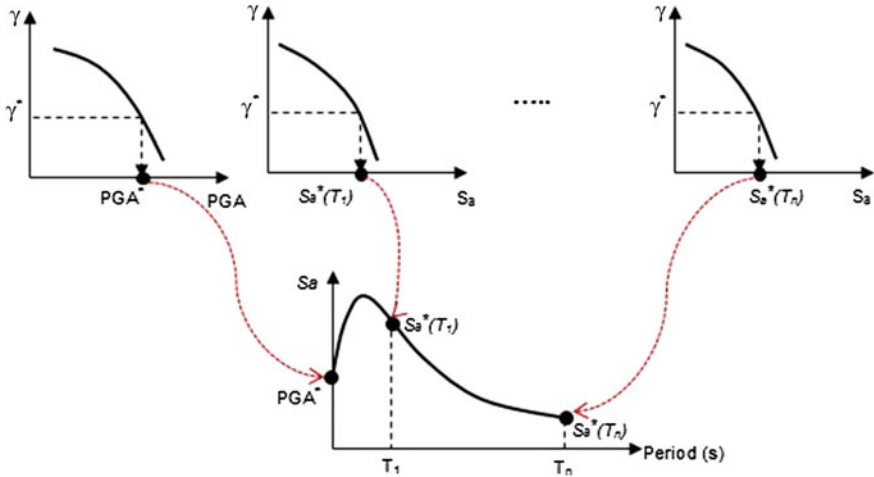


Fig. 2.13 Uniform hazard spectrum concept: the spectral ordinates of UHS given in the bottom row describe the same level of mean annual exceedance rate

Before going into the details of topics treating random variables, there is a need to introduce the terminology *event* (E) that is defined as the subset of a sample space, S . An event contains some of the outcomes in a sample space. The probability of an event can range between 0 and 1 (i.e., $0 \leq P(E) \leq 1$). The union of events ($E_1 \cup E_2$) and intersection of events ($E_1 \cap E_2$ or E_1E_2) are of common interest in probability computations and $P(E_1 \cup E_2) = P(E_1) + P(E_2) - P(E_1 \cap E_2)$. A *certain event* contains all possible outcomes in a sample space. Thus, the probability of a certain event is unity. Since sample space S contains all possible outcomes, $P(S) = 1$. A *null event* (ϕ) contains no outcomes of a sample space and its probability is zero ($P(\phi) = 0$). Events are called as *mutually exclusive* if they have no common outcomes (e.g., $E_1E_2 = \phi$). If events E_1 and E_2 are mutually exclusive, $P(E_1 \cup E_2) = P(E_1) + P(E_2)$. When the union of events contains all possible outcomes in a sample space (e.g., $E_1 \cup E_2 = S$), they are called as *collectively exhaustive* events. Events E_1 and E_2 are mutually exclusive and collectively exhaustive when $E_1E_2 = \phi$ and $E_1 \cup E_2 = S$. These definitions and their corresponding probabilities constitute the *axioms of probability*.

In general, the occurrence probability of an event depends on the occurrence probability of another event. In such cases one needs to define the conditional probability, $P(E_1|E_2)$ that is given in Eq. (2.13).

$$P(E_1|E_2) = \frac{P(E_1E_2)}{P(E_2)}; \quad P(E_1E_2) = P(E_1|E_2)P(E_2). \quad (2.13)$$

If events E_1 and E_2 are independent, then Eq. (2.13) reduces to Eq. (2.14).

$$P(E_1|E_2) = P(E_1). \quad (2.14)$$

Equation (2.14) indicates that the occurrence probability of E_1 is not affected from the occurrence probability of E_2 . If Eqs. (2.13) and (2.14) are considered together, one can obtain the following relationship for two independent events E_1 and E_2 :

$$P(E_1E_2) = P(E_1)P(E_2). \quad (2.15)$$

The *total probability theorem* conveys the computation of the probability of an event A from the known probabilities of a set of mutually exclusive and collectively exhaustive events E_1, E_2, \dots, E_n and the probabilities of A conditioned on each one of these E_i 's. The above statement of the total probability theorem is formulated in Eq. (2.16). It is generally used to compute the probability of event A when its direct computation is difficult but it can be obtained from the known probabilities of events whose occurrences and occurrence of A depend on each other.

$$P(A) = \sum_{i=1}^n P(A|E_i)P(E_i). \quad (2.16)$$

Example 2.5 A big city is under the influence of several hypothetical seismic sources. The probabilities of earthquake occurrences generated by short-, intermediate- and far-distance seismic sources are given as

$$P(\text{short-distance}) = 0.2$$

$$P(\text{intermediate-distance}) = 0.4$$

$$P(\text{far-distance}) = 0.4$$

A statistical study on past earthquakes indicated the following probabilities of large-to-small magnitude events conditioned on above source-to-site distance ranges

$$P(\text{large-magnitude}|\text{short-distance}) = 0.3$$

$$P(\text{moderate-magnitude}|\text{short-distance}) = 0.5$$

$$P(\text{small-magnitude}|\text{short-distance}) = 0.2$$

$$P(\text{large-magnitude}|\text{intermediate-distance}) = 0.2$$

$$P(\text{moderate-magnitude}|\text{intermediate-distance}) = 0.4$$

$$P(\text{small-magnitude}|\text{intermediate-distance}) = 0.4$$

$$P(\text{large-magnitude}|\text{far-distance}) = 0.1$$

$$P(\text{moderate-magnitude}|\text{far-distance}) = 0.3$$

$$P(\text{small-magnitude}|\text{far-distance}) = 0.6$$

An engineering company in the city is interested in the probability of severe damage caused by earthquakes of different sizes. Their statistical studies suggest that probabilities of damage conditioned on large, moderate and small magnitude

events are 0.6, 0.3 and 0.1 regardless of source-to-site distance from the causative seismic source. Compute the probability of severe damage in the city for a future earthquake considering the surrounding seismicity.

Solution

One can determine the probabilities of large-, moderate- and small-magnitude earthquakes by using the total probability theorem. From the given information, the probability of large magnitude earthquakes is

$$\begin{aligned}
 P(\text{large-magnitude}) &= P(\text{large-magnitude}|\text{short-distance}) \cdot P(\text{short-distance}) \\
 &\quad + P(\text{large-magnitude}|\text{intermediate-distance}) \cdot P(\text{intermediate-distance}) \\
 &\quad + P(\text{large-magnitude}|\text{far-distance}) \cdot P(\text{far-distance}) \\
 &= 0.3 \cdot 0.2 + 0.2 \cdot 0.4 + 0.1 \cdot 0.4 \\
 &= 0.18
 \end{aligned}$$

$$\begin{aligned}
 P(\text{moderate-magnitude}) &= P(\text{moderate-magnitude}|\text{short-distance}) \cdot P(\text{short-distance}) \\
 &\quad + P(\text{moderate-magnitude}|\text{intermediate-distance}) \cdot P(\text{intermediate-distance}) \\
 &\quad + P(\text{moderate-magnitude}|\text{far-distance}) \cdot P(\text{far-distance}) \\
 &= 0.5 \cdot 0.2 + 0.4 \cdot 0.4 + 0.3 \cdot 0.4 \\
 &= 0.38
 \end{aligned}$$

$$\begin{aligned}
 P(\text{small-magnitude}) &= P(\text{small-magnitude}|\text{short-distance}) \cdot P(\text{short-distance}) \\
 &\quad + P(\text{small-magnitude}|\text{intermediate-distance}) \cdot P(\text{intermediate-distance}) \\
 &\quad + P(\text{small-magnitude}|\text{far-distance}) \cdot P(\text{far-distance}) \\
 &= 0.2 \cdot 0.2 + 0.4 \cdot 0.4 + 0.6 \cdot 0.4 \\
 &= 0.44
 \end{aligned}$$

The probability of severe damage after a future earthquake can now be computed by making use of the total probability theorem for the second time:

$$\begin{aligned}
 P(\text{damage}) &= P(\text{damagelarge-magnitude}) \cdot P(\text{large-magnitude}) \\
 &\quad + P(\text{damagemoderate-magnitude}) \cdot P(\text{moderate-magnitude}) \\
 &\quad + P(\text{damagelarge-magnitude}) \cdot P(\text{small-magnitude}) \\
 &= 0.6 \cdot 0.18 + 0.3 \cdot 0.38 + 0.1 \cdot 0.44 \\
 &= 0.266
 \end{aligned}$$

The probability of a continuous random variable is defined either by the probability density function (*PDF*; $f_X(x)$) or cumulative distribution function (*CDF*; $F_X(x)$). The relationship between CDF and PDF is given in Eq. (2.17). The area under PDF between $-\infty$ and x is the probability of random variable X having

values less than or equal to x (i.e., $F_X(x)$). The derivative of CDF yields PDF. Thus, one of them can be obtained from the other by integration or differentiation. If the random variable is discrete, the probability mass function (PMF; $p_X(x)$) describes its probability distribution. Equation (2.18) shows the relation between CDF and PMF for discrete random variables. Figure 2.14 illustrates the relationships given in Eqs. (2.17) and (2.18).

$$F_X(x) = P(X \leq x) = \int_{-\infty}^x f_X(x) dx; \quad f_X(x) = \frac{d}{dx} F_X(x) \quad (2.17)$$

$$F_X(a) = \sum_{\text{all } x_i \leq a} p_X(x_i) \quad (2.18)$$

Example 2.6 Derive CDF and PDF for Gutenberg-Richter earthquake recurrence model for a range of magnitudes larger than m_{min} .

Solution

The definition of CDF for the given problem statement is

$$F_M(m) = P(M \leq m | M > m_{min})$$

This conditional probability can be described by the following expression

$$F_M(m) = \frac{\text{Rate of earthquakes with } m_{min} < M \leq m}{\text{Rate of earthquakes with } M > m_{min}} = \frac{v_{m_{min}} - v_m}{v_{m_{min}}}$$

The numerator in the above expression is the rate of earthquakes between m_{min} and m ($m > m_{min}$). The denominator is rate of earthquakes having magnitudes greater than m_{min} . Upon the use of Eq. (2.1), the final form of CDF becomes

$$F_M(m) = \frac{10^{a-bm_{min}} - 10^{a-bm}}{10^{a-bm_{min}}} = 1 - 10^{-b(m-m_{min})}; \quad m > m_{min}$$

The corresponding PDF is

$$f_M(m) = \frac{d}{dm} F_M(m) = \frac{d}{dm} [1 - 10^{-b(m-m_{min})}] = b \ln(10) 10^{-b(m-m_{min})}; \quad m > m_{min}$$

Note that the truncated Gutenberg-Richter is the physically meaningful magnitude recurrence model as discussed in Sect. 2.2 because it can impose an upper bound for the maximum magnitude. Following the procedure described above the CDF and PDF for truncated Gutenberg-Richter earthquake recurrence model is

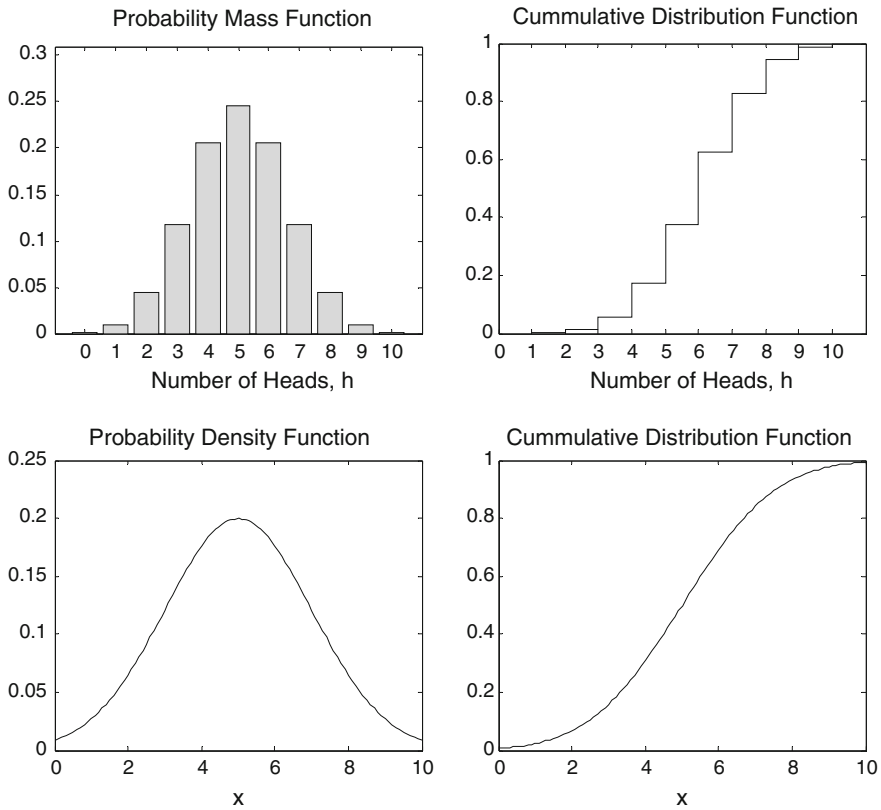


Fig. 2.14 Discrete (*upper row*) and continuous (*lower row*) probability distributions. The discrete probabilities represent the probability of number of heads tossed in 11 coin tosses. The *left panel* in the first row shows the PMF for number of heads for successive trials ($p_H(h_i)$). For example, probability of 5 heads in 11 tosses is approximately 0.25 (i.e., $p_H(h = 5) \approx 0.25$). The *right panel* in the first row shows the CDF of this process. For example, probability of 5 or less heads tossed in 11 coin tosses is approximately 0.4 (i.e., $F_H(5) \approx 0.40$). The *lower left panel* is the normal PDF with mean equals 5 and standard deviation equals 2. The *lower right panel* is the corresponding CDF

$$F_M(m) = \frac{1 - 10^{-b(m-m_{\min})}}{1 - 10^{-b(m_{\max}-m_{\min})}}; \quad f_M(m) = \frac{b \ln(10) 10^{-b(m-m_{\min})}}{1 - 10^{-b(m_{\max}-m_{\min})}}$$

As PSHA uses discrete sets of magnitude, the above continuous distributions of magnitude should be converted into discrete magnitude values. Let the magnitude band is divided into a set of discrete intervals. Then the probability of M taking the value m_j is

$$P(M = m_j) = F_M(m_{j+1}) - F_M(m_j), \quad m_j < m_{j+1}$$

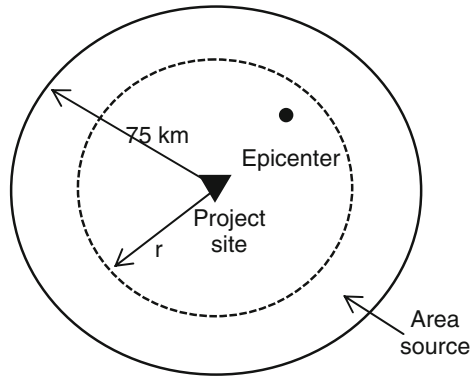
Example 2.7 A site is located in an area source that is capable of producing earthquakes with equal probability anywhere within a radius of 75 km from the site. Define the probability density and cumulative distribution functions of the source-to-site distance to describe the locations of earthquakes with respect to the site.

Solution

Figure 2.15 shows the area source and the location of the project site. As the earthquakes occur with equal probability within the circular area source, the probability of an earthquake epicenter being located within a distance of r is

$$P(R \leq r) = F_R(r) = \frac{\pi r^2}{\pi(75)^2} = \frac{r^2}{5625}$$

Fig. 2.15 Area source in Example 2.7



The above CDF is valid for $0 \text{ km} \leq r \leq 75 \text{ km}$. The corresponding PDF and its range of applicability is given below. Outside the designated range, the probabilities computed from the given PDF will be zero.

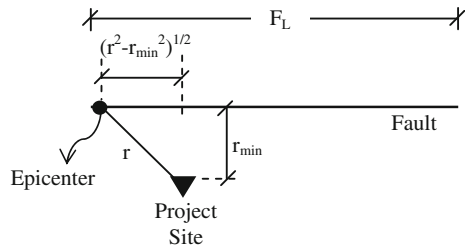
$$f_R(r) = \frac{d}{dr} F_R(r) = \frac{r}{2812.5}; \quad 0 \text{ km} \leq r \leq 75 \text{ km}$$

Example 2.8 For the fault shown in Fig. 2.16, it is assumed that earthquakes are uniformly distributed over the fault length. Derive CDF and PDF of source-to-site distance for the configuration given in Fig. 2.16.

Solution

As in the case of Example 2.7, the probability of epicenter located within a distance r is

Fig. 2.16 Fault source in Example 2.8



$$P(R \leq r) = F_R(r) = \frac{2(r^2 - r_{min}^2)^{1/2}}{F_L}$$

The above expression indicates that the probability of observing a distance less than r is the ratio of fault segment within a radius of r to total fault length F_L . This expression is also the cumulative distribution function (CDF) for epicentral distances. PDF is the derivative of CDF as given below.

$$f_R(r) = \frac{d}{dr} F_R(r) = \frac{2r}{F_L(r^2 - r_{min}^2)^{1/2}}$$

Exercises

1. The seismic activity of two seismic sources is represented with the Gutenberg-Richter earthquake recurrence model. The table below presents the seismic characteristics of these sources. Determine the exceedance probabilities of earthquakes generated by these seismic sources for magnitudes of 5.5, 6.5 and 7.5. Assume that earthquakes in these seismic sources follow Poisson process and the exposure time considered is 100 years specific to the engineering project. Based on these computations, which one of the seismic sources are more likely to produce earthquakes with the associated magnitudes.

Seismic source characteristics of the seismic sources in Problem 1

Source	a	B	M_{max}
I	6	0.8	7.0
II	2	1.0	7.5

2. The hazard curves for a set of threshold acceleration values (between 0.01 and 3 g) for the spectral periods $T \leq 3.0$ s are given in the following table. Determine the uniform hazard spectrum for 10 % exceedance probability in 75 years. Repeat the same computation for an exceedance probability of 2 % in 75 years. If necessary, use linear interpolation between the given mean annual exceedance rates and spectral ordinates.

Hazard curves for a set of threshold acceleration values corresponding to spectral periods less or equal to 3.0 s

Period	Preslected threshold acceleration values, y , in g														
	γ 0.01 g	γ 0.02 g	γ 0.05 g	γ 0.07 g	γ 0.1 g	γ 0.2 g	γ 0.3 g	γ 0.4 g	γ 0.5 g	γ 0.7 g	γ 1 g	γ 2 g	γ 3 g		
PGA	5.34E-03	4.74E-03	2.59E-03	1.56E-03	7.16E-04	6.72E-05	9.41E-06	1.77E-06	4.12E-07	3.49E-08	1.77E-09	1.83E-12	1.68E-14		
0.05	5.38E-03	4.87E-03	2.99E-03	1.99E-03	1.05E-03	1.44E-04	2.70E-05	6.44E-06	1.83E-06	2.14E-07	1.59E-08	3.81E-11	6.06E-13		
0.10	5.47E-03	5.12E-03	3.73E-03	2.82E-03	1.78E-03	3.92E-04	1.02E-04	3.15E-05	1.11E-05	1.83E-06	1.99E-07	1.08E-09	2.88E-11		
0.15	5.53E-03	5.27E-03	4.18E-03	3.38E-03	2.34E-03	6.27E-04	1.84E-04	6.14E-05	2.28E-05	4.06E-06	4.75E-07	2.83E-09	7.78E-11		
0.20	5.57E-03	5.39E-03	4.42E-03	3.65E-03	2.60E-03	7.47E-04	2.30E-04	7.91E-05	3.02E-05	5.57E-06	6.78E-07	4.36E-09	1.25E-10		
0.25	5.57E-03	5.41E-03	4.41E-03	3.60E-03	2.52E-03	6.86E-04	2.02E-04	6.71E-05	2.48E-05	4.37E-06	5.03E-07	2.85E-09	7.57E-11		
0.30	5.58E-03	5.41E-03	4.33E-03	3.48E-03	2.39E-03	6.32E-04	1.86E-04	6.26E-05	2.35E-05	4.29E-06	5.20E-07	3.44E-09	1.03E-10		
0.40	5.58E-03	5.41E-03	4.20E-03	3.28E-03	2.15E-03	5.02E-04	1.35E-04	4.21E-05	1.49E-05	2.47E-06	2.69E-07	1.41E-09	3.66E-11		
0.50	5.57E-03	5.33E-03	3.84E-03	2.83E-03	1.72E-03	3.41E-04	8.34E-05	2.45E-05	8.31E-06	1.30E-06	1.34E-07	6.62E-10	1.69E-11		
0.75	5.52E-03	5.07E-03	3.00E-03	1.97E-03	1.05E-03	1.62E-04	3.50E-05	9.61E-06	3.12E-06	4.66E-07	4.72E-08	2.43E-10	6.69E-12		
1.00	5.46E-03	4.78E-03	2.35E-03	1.39E-03	6.53E-04	7.68E-05	1.41E-05	3.42E-06	1.01E-06	1.31E-07	1.14E-08	4.39E-11	1.02E-12		
1.50	5.20E-03	4.00E-03	1.42E-03	7.33E-04	2.97E-04	2.71E-05	4.40E-06	1.00E-06	2.84E-07	3.51E-08	2.99E-09	1.18E-11	2.94E-13		
2.00	4.76E-03	3.13E-03	8.09E-04	3.66E-04	1.29E-04	9.25E-06	1.33E-06	2.79E-07	7.48E-08	8.60E-09	6.87E-10	2.50E-12	6.07E-14		
3.00	3.72E-03	1.80E-03	2.65E-04	9.46E-05	2.58E-05	1.08E-06	1.13E-07	1.87E-08	4.17E-09	3.61E-10	2.13E-11	4.22E-14	7.12E-16		

3. The fictitious rock site is under the influence of several seismic sources as given in the figure below. The seismic characteristics of faults A and B are listed in the table next to the figure. The earthquake catalog for a radius of 100 km surrounding the project site yields the background seismic activity information given in the tabulated form. The earthquake catalog information covers a period of 95 years. The magnitude recurrence models of all seismic sources can be described by truncated Gutenberg Richter. An earth-fill dam will be constructed in the site and the critical parameter is PGA to design the embankment. The ground-motion predictive model proposed by Cornell et al. (1979) is used to describe the variation of PGA as given in the below expression. The logarithmic standard deviation of the given GMPE is $\sigma_{\ln y} = 0.57$.

$$\ln(PGA) = -0.152 + 0.859M - 1.803 \ln(R + 25).$$

Determine the PGA level for a 475-year return period using PSHA as this value is required by the codes for the design of embankment. Compare PGA_{475} with the hazard result obtained from DSHA. Compare the hazard controlling seismic sources in DSHA and PSHA.

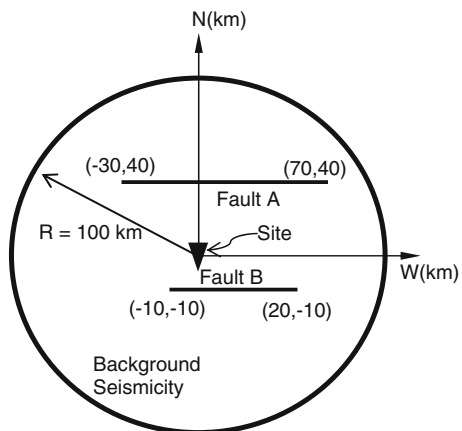
Hint: Divide the source-to-site distances and magnitudes into 10 equal segments while implementing PSHA.

Seismic characteristics of faults in Problem 3

	b	$v_m(M > 5)$	M_{max}
Fault A	0.85		7.7
Fault B	0.95		6.5

Seismic activity in the background

Magnitude interval	Number of earthquakes
5.0–5.1	18
5.1–5.2	16
5.2–5.3	13
5.3–5.4	9
5.4–5.5	7
5.5–5.6	6
5.7–5.8	4
5.8–5.9	3
5.9–6.0	1



Seismic sources and the project site in Problem 3

Chapter 3

Response of Simple Structures to Earthquake Ground Motions

Abstract Our approach starts with developing response analysis procedures for a single degree of freedom system. We present the derivation of the equations of motion governing its free vibration response (simple harmonic motion) and forced vibration response. Then we solve the equations of motion of undamped and damped systems first under harmonic force excitation by developing classical, closed form analytical solution procedures, and then solve them under earthquake ground excitations by developing numerical solution procedures. This solution under earthquake ground excitations also leads to earthquake response spectra. Finally these procedures are extended to systems with nonlinear force-deformation relations where hysteresis rules are defined and the concepts of ductility, strength, ductility reduction factor, strength spectra and ductility spectra are introduced.

3.1 Single Degree of Freedom Systems

When the deformed shape of a structural system at any instant of motion t can be represented in terms of a single dynamic displacement coordinate $u(t)$, then it is called a *single degree of freedom system*, and that coordinate is called the degree of freedom. All internal dynamic forces in a Single Degree of Freedom (SDOF) system that are resisting the external dynamic force are functions of dynamic displacement $u(t)$ or its time derivatives, i.e. velocity $\dot{u}(t)$ and acceleration $\ddot{u}(t)$. Single degree of freedom systems can be either “ideal SDOF systems”, or “idealized SDOF systems”.

3.1.1 Ideal SDOF Systems: Lumped Mass and Stiffness

The entire mass and stiffness of the system is lumped at a point where the dynamic coordinate $u(t)$ is defined. The rigid block in Fig. 3.1a has a mass m and connected to a fixed end with a spring with stiffness k . It is a typical ideal SDOF system

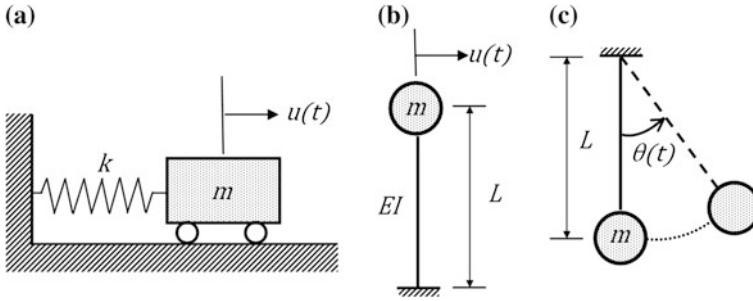


Fig. 3.1 Ideal SDOF systems: **a** a car on rollers, **b** an inverted pendulum structure, **c** a pendulum swinging in the gravity field

because it is free to move on rollers only in the lateral direction. An inverted pendulum type of structure where the lumped mass m is connected to the fixed base with a massless cantilever column is also an ideal SDOF system (Fig. 3.1b). In this case the spring stiffness is identical to the lateral stiffness of the cantilever column, i.e. $k = 3EI/L^3$. The motion of the mass and the elastic force which develops in the spring at any time t can be represented by the dynamic displacement $u(t)$, which is the single degree of freedom in both systems. On the other hand, a pendulum where the mass m connected with a chord of length l that swings about the fixed end of the chord in the gravity field g is another example of an ideal SDOF system (Fig. 3.1c). In this case the degree of freedom is the angle of rotation θ .

3.1.2 Idealized SDOF Systems: Distributed Mass and Stiffness

More complicated dynamic systems with distributed mass and stiffness can also be idealized as SDOF systems. Let's consider a cantilever column and a simple multistory frame in Fig. 3.2 where the lateral deformation distribution along the height exhibits variation with time during motion. Both systems can be defined as idealized SDOF systems if the lateral dynamic deformation distribution $u(x, t)$ along height x can be expressed as

$$u(x, t) = \varphi(x) \cdot \bar{u}(t) \quad (3.1)$$

where $\varphi(x)$ is the normalized deformation profile, i.e. $\varphi(L) = 1$. Lateral displacement $\bar{u}(t)$ at the top is the *single degree of freedom*. Note that $\varphi(x)$ is assumed to be constant and not changing with time. This is not exactly correct, but practically acceptable. This assumption is valid for simple structural systems. For example, $\phi(x) = (x/L)^2$

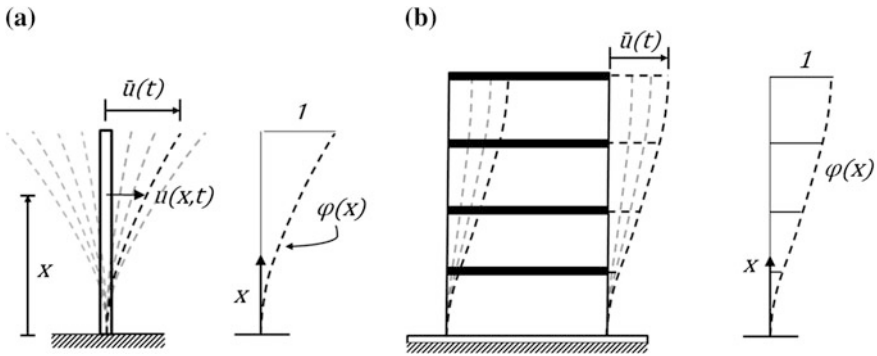


Fig. 3.2 Idealized SDOF systems: **a** cantilever column, **b** multistory frame

is an acceptable normalized deformation shape for both SDOF systems in Fig. 3.2 since it satisfies the boundary conditions $u(0) = 0$ and $u'(0) = 0$ at $x = 0$.

3.2 Equation of Motion: Direct Equilibrium

Let's consider two ideal SDOF systems in Fig. 3.3 with a mass, spring and damper. Damper is the only difference between Figs. 3.2 and 3.3, which represents internal friction mechanism in an actual mechanical system that is idealized as a SDOF system. Internal friction develops in deforming mechanical systems due to rubbing of the molecules with respect to each other during dynamic deformations. Internal friction leads to energy loss in a vibrating system.

When the mass moves by a positive displacement $u(t)$ and with a positive velocity $\dot{u}(t)$ under an external force $F(t)$, the spring develops a resisting force which is equal to $ku(t)$, and the damper develops a resisting force which is equal to $c\dot{u}(t)$, both in the opposite direction. Free body and kinetic diagrams of the masses in both SDOF systems are shown in Fig. 3.4.

Applying Newton's second law of motion $\sum F = ma$ for dynamic equilibrium of the mass in the lateral direction leads to

$$F(t) - ku - c\dot{u} = m\ddot{u} \tag{3.2a}$$

or

$$m\ddot{u} + c\dot{u} + ku = F(t). \tag{3.2b}$$

This is a 2nd order linear ordinary differential equation (ODE) with constant coefficients m , c and k .

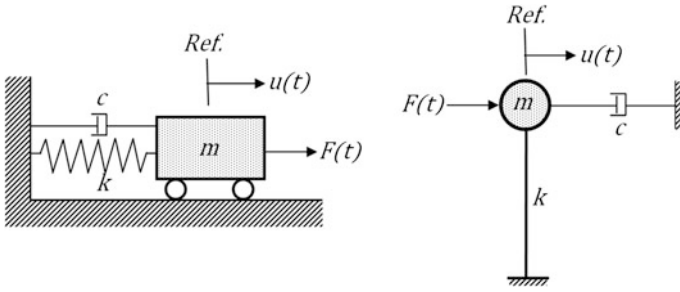
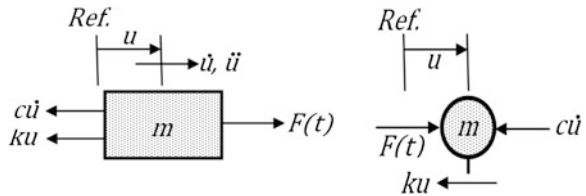


Fig. 3.3 Ideal SDOF systems with mass m , stiffness k and damping c

Fig. 3.4 Free body diagrams of the masses when they displace by $u(t)$ and moving with a velocity of $\dot{u}(t)$ and an acceleration of $\ddot{u}(t)$ at time t



3.3 Equation of Motion for Base Excitation

The base of the inverted pendulum moves with the ground during an earthquake ground shaking with a ground displacement of $u_g(t)$ as shown in Fig. 3.5a. There is no direct external force $F(t)$ acting on the mass when ground moves, but inertial force develops on the mass according to Newton’s 2nd law ($F = ma$) where a is the total acceleration of the mass ($a = \ddot{u}^{total}$). It is the sum of ground acceleration and the acceleration of the mass relative to the ground.

$$\ddot{u}^{total} = \ddot{u}_g + \ddot{u}. \tag{3.3}$$

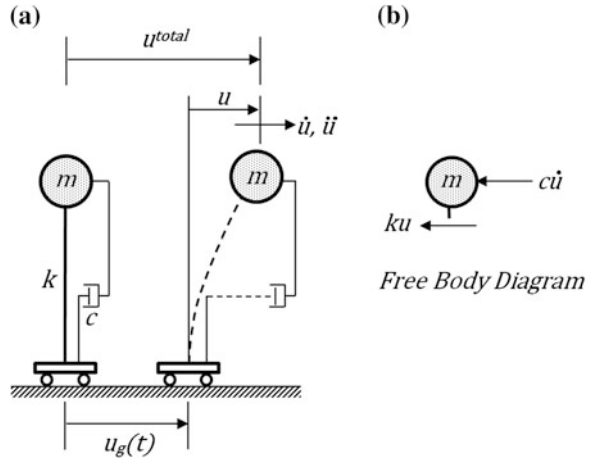
Free body diagram of the mass is shown in Fig. 3.5b. Then, according to Newton’s 2nd law, $\sum F = \ddot{u}^{total}$ yields

$$-c\dot{u} - ku = m\ddot{u}^{total} \tag{3.4}$$

or

$$m(\ddot{u}_g + \ddot{u}) + c\dot{u} + ku = 0. \tag{3.5}$$

Fig. 3.5 **a** An SDOF system under base excitation, **b** free body diagram of the mass when it displaces by $u(t)$, while moving with a velocity of $\dot{u}(t)$ and an acceleration of $\ddot{u}(t)$ at time t



Transforming Eq. (3.5) into the standard form of Eq. (3.2b) leads to,

$$m\ddot{u} + c\dot{u} + ku = -m\ddot{u}_g(t) \equiv F_{eff}(t) \tag{3.6}$$

where $-m\ddot{u}_g(t)$ is considered as an effective force.

3.4 Solution of the SDOF Equation of Motion

The solution of a 2nd order ODE is obtained in two parts:

$$u(t) = u_h(t) + u_p(t). \tag{3.7}$$

Here u_h is the homogeneous solution and u_p is the particular solution. In a vibration problem, u_h represents the free vibration response ($F = 0$) and u_p represents the forced vibration response ($F \neq 0$).

3.4.1 Free Vibration Response

The motion is imparted by the initial conditions at $t = 0$: $u(0) = u_0$ (initial displacement) and $\dot{u}(0) = v_0$ (initial velocity). The equation of free vibration is given by

$$m\ddot{u} + c\dot{u} + ku = 0. \tag{3.8}$$

Dividing all terms by the mass m gives

$$\ddot{u} + \frac{c}{m}\dot{u} + \frac{k}{m}u = 0. \tag{3.9}$$

Fig. 3.6 Undamped free vibrations of a SDOF system

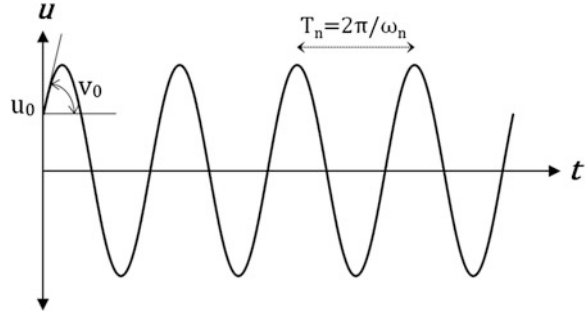
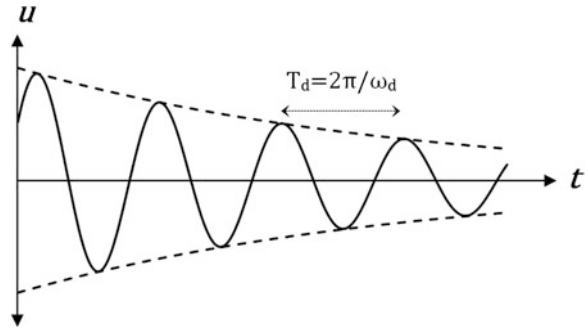


Fig. 3.7 Free vibration of a damped (under-damped) SDOF system



Let $\frac{c}{m} = 2\xi\omega_n$ and $\frac{k}{m} = \omega_n^2$. This is a simple replacement of the two normalized coefficients $\frac{c}{m}$ and $\frac{k}{m}$ in terms of two new coefficients ξ and ω_n , which have distinct physical meanings. The dimensionless parameter ξ is the critical damping ratio, and ω_n is the natural frequency of vibration (rad/s). Vibration occurs only if $\xi < 1$. Then Eq. (3.9) can be written as,

$$\ddot{u} + 2\xi\omega_n\dot{u} + \omega_n^2u = 0. \tag{3.10}$$

3.4.1.1 Undamped Free Vibration ($\xi = 0$)

When damping is zero, Eq. (3.10) reduces to

$$\ddot{u} + \omega_n^2u = 0. \tag{3.11}$$

Equation (3.11) represents simple harmonic motion. Only a harmonic function with a harmonic frequency of ω_n satisfies Eq. (3.11). Its most general form is a combination of sin and cos functions with arbitrary amplitudes.

$$u(t) = A \sin \omega_n t + B \cos \omega_n t. \tag{3.12}$$

Table 3.1 Typical damping ratios for basic structural systems

Structural type	Damping ratio (%)	
	<50 % yield	~ yield
Steel (welded connections)	2–3	3–5
Reinforced concrete	3–5	5–10
Prestressed concrete	2–3	3–5
Masonry	5–10	10–20

A and B are determined by introducing the initial conditions $u(0) = u_0$ and $\dot{u}(0) = v_0$, leading to

$$u(t) = u_0 \cos \omega_n t + \frac{v_0}{\omega_n} \sin \omega_n t. \quad (3.13)$$

Equation (3.13) is shown graphically in Fig. 3.6.

3.4.1.2 Damped Free Vibration ($0 < \zeta < 1$)

The presence of damping in free vibration imposes a decaying envelope on the undamped free vibration cycles in Fig. 3.6. Decay is exponential, and decay rate depends on $\omega_n t$, as given in Eq. (3.14).

$$u(t) = e^{-\zeta \omega_n t} \left[u_0 \cos \omega_d t + \frac{v_0 + u_0 \zeta \omega_n}{\omega_d} \sin \omega_d t \right]. \quad (3.14)$$

The amplitude of harmonic vibration reduces exponentially at each cycle, and approaches zero asymptotically as shown in Fig. 3.7.

Note that the term in brackets in Eq. (3.14) is similar to Eq. (3.13) where ω_n is replaced by ω_d , which is the “damped” natural frequency given by Eq. (3.15).

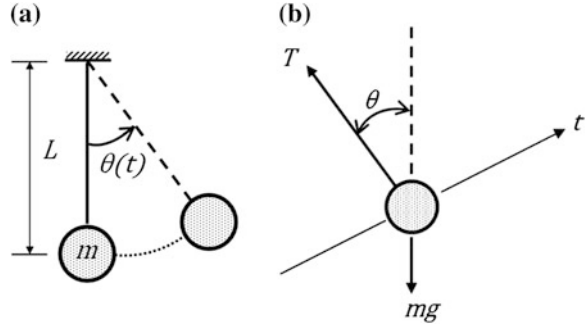
$$\omega_d = \omega_n \sqrt{1 - \zeta^2}. \quad (3.15)$$

In general $\zeta \leq 0.20$ for structural systems, hence $\omega_d \approx \omega_n$. Typical viscous damping ratios that can be assigned to basic structural systems are given in Table 3.1.

Example 3.1 Consider the pendulum in Fig. 3.8a with mass m connected to a chord of length L , oscillating in the gravity field.

- Determine its equation of motion.
- Solve the equation of motion for small oscillations θ when the motion starts with an initial displacement θ_0 .

Fig. 3.8 **a** Simple pendulum, **b** free body diagram



Solution

(a) At any $\theta(t)$, free body diagram of the mass is shown in Fig. 3.8b, where T is the tension in the chord. Equation of motion in the t (tangential) direction can be written as

$$\sum F = ma_t.$$

From Fig. 3.8b,

$$-mg \sin \theta = ma_t \equiv mL\ddot{\theta}.$$

Rearranging,

$$mL\ddot{\theta} + mg \sin \theta = 0. \quad (1)$$

(b) Equation (1) is a 2nd order nonlinear ODE. Nonlinearity is due to the $\sin \theta$ term. For small oscillations, $\sin \theta \approx \theta$. Hence, the equation of motion becomes linear.

$$mL\ddot{\theta} + mg \theta = 0,$$

or

$$\ddot{\theta} + \frac{g}{L}\theta = 0.$$

With similitude to Eq. (3.11),

$$\omega_n^2 = \frac{g}{L} \text{ or } T_n = 2\pi\sqrt{\frac{L}{g}}.$$

The solution from Eq. (3.12) is,

$$\theta(t) = A \sin \omega_n t + B \cos \omega_n t. \quad (2)$$

Substituting $\theta(0) = \theta_0$ and $\dot{\theta}(0) = 0$ into Eq. (2), we obtain

$$\theta(t) = \theta_0 \cos \sqrt{\frac{g}{L}} t.$$

Example 3.2 Determine the natural frequency of vibration for the system shown in Fig. 3.9a where the bar AB is rigid and it has no mass.

The system in Fig. 3.9a is a SDOF system where the vertical displacement of end B can be employed as the DOF. The displacement variation of the SDOF system is always linear from A to B with a fixed shape as shown in Fig. 3.9b.

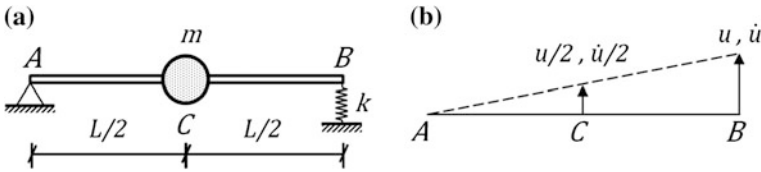


Fig. 3.9 a Rigid body assemblage, b kinematic diagram

Solution

Since all forces are not directly acting on the mass, a direct formulation of the equation of motion is not possible. Conservation of energy principle provides a simpler approach.

$$T + U = Constant \tag{1}$$

where T is the kinetic energy and U is the potential energy at any time t , given by

$$T = \frac{1}{2} m \dot{u}^2 \text{ and } U = \frac{1}{2} k u^2. \tag{2}$$

Here, we should consider from Fig. 3.9b that the velocity of the mass in terms of the DOF u is $\frac{\dot{u}}{2}$. Hence, $T = \frac{1}{2} m \left(\frac{\dot{u}}{2}\right)^2$. Substituting into Eq. (1), and taking time derivative of both sides,

$$m \frac{\dot{u}}{2} \ddot{u} + k u \dot{u} = 0$$

or

$$4 \frac{k}{m} + \ddot{u} = 0.$$

Accordingly,

$$\omega_n = \sqrt{\frac{k}{m}}$$

in similitude with Eq. (3.11).

Example 3.3 A single story, single bay portal frame is given below in Fig. 3.10a.

- (a) Determine the equation of free vibration and the natural period of free vibration,
 (b) Determine the equation of motion under base excitation $\ddot{u}_g(t)$.

Solution

- (a) The portal frame is a SDOF system with the fixed deflection shape shown in Fig. 3.10b. Lateral displacement u of the mass m at the roof is the degree of freedom. Free body diagram of the roof mass is given in Fig. 3.10c.

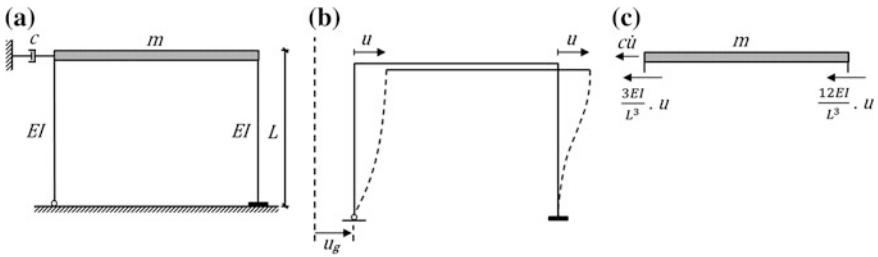


Fig. 3.10 a Portal frame, b deflected shape, c free body diagram

Applying Newton's second law of motion $\sum F = ma$ for dynamic equilibrium of the mass in the lateral direction leads to

$$-c\dot{u} - \frac{3EI}{L^3}u - \frac{12EI}{L^3}u = m\ddot{u}. \quad (1)$$

Rearranging,

$$m\ddot{u} + c\dot{u} + \frac{15EI}{L^3}u = 0.$$

$\frac{15EI}{L^3}$ is the effective stiffness of the portal frame, and m is the mass. Accordingly,

$$\omega_n^2 = \frac{15EI}{mL^3} \quad \text{and} \quad T_n = 2\pi\sqrt{\frac{mL^3}{15EI}}$$

- (b) Equation (1) can be written for base excitation as,

$$-c\dot{u} - \frac{15EI}{L^3}u = m\ddot{u}^{total} \equiv m(\ddot{u} + \ddot{u}_g)$$

or,

$$m\ddot{u} + c\dot{u} + \frac{15EI}{L^3}u = -m\ddot{u}_g.$$

3.4.2 Forced Vibration Response: Harmonic Base Excitation

Harmonic excitation can either be applied as an external harmonic force, or an effective harmonic force due to a harmonic base excitation ($\ddot{u}_g(t) = a_0 \sin \bar{\omega}t$). Equation of motion under harmonic excitation can then be written as

$$m\ddot{u} + c\dot{u} + ku = F_0 \sin \bar{\omega}t \equiv -ma_0 \sin \bar{\omega}t \quad (3.16)$$

The homogeneous solution is identical to the damped free vibration response in Eq. (3.14), where vibration occurs at the free vibration frequency ω_d .

$$u_h = e^{-\xi\omega_n t} (A_1 \sin \omega_d t + A_2 \cos \omega_d t) \quad (3.17)$$

A_1 and A_2 are the arbitrary amplitudes that have to be determined from the initial conditions at $t = 0$. However the initial conditions are imposed on the general (total) solution, not on the homogeneous solution alone.

The particular solution is assumed to be composed of sin and cos functions where vibration occurs at the forced vibration frequency $\bar{\omega}$.

$$u_p = G_1 \sin \bar{\omega}t + G_2 \cos \bar{\omega}t \quad (3.18)$$

The arbitrary harmonic amplitudes G_1 and G_2 are determined by using the method of undetermined coefficients in the solution of ordinary differential equations, leading to

$$G_1 = \frac{F_0}{k} \frac{1 - \beta^2}{(1 - \beta^2)^2 + (2\xi\beta)^2}; \quad G_2 = \frac{F_0}{k} \frac{-2\xi\beta}{(1 - \beta^2)^2 + (2\xi\beta)^2} \quad (3.19)$$

where $\beta = \frac{\bar{\omega}}{\omega_n}$ is the forcing frequency ratio, and $F_0 = -ma_0$ is the effective harmonic force amplitude.

3.4.2.1 General Solution

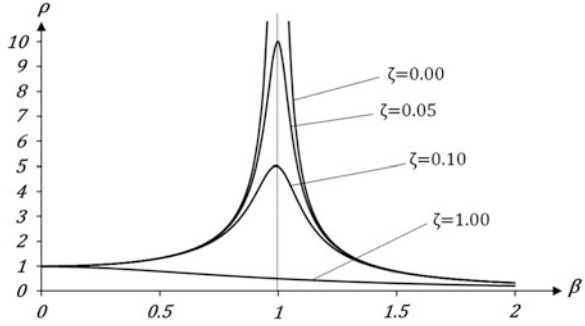
General solution is the combination of homogeneous and particular solutions from Eqs. (3.17) and (3.18), respectively. Substituting G_1 and G_2 from Eq. (3.19) into Eq. (3.18), simplifying and collecting into $u(t) = u_h(t) + u_p(t)$, we obtain

$$u(t) = e^{-\xi\omega_n t} (A_1 \sin \omega_d t + A_2 \cos \omega_d t) + \frac{F_0 (1 - \beta^2) \sin \bar{\omega}t - 2\xi\beta \cos \bar{\omega}t}{k (1 - \beta^2)^2 + (2\xi\beta)^2}. \quad (3.20)$$

A_1 and A_2 are determined from the initial conditions as indicated above.

In damped systems under harmonic excitation, u_h is called the transient and u_p is called the steady-state response since the transient part decays with time as

Fig. 3.11 Frequency response function for damped systems under harmonic excitation



shown in Fig. 3.7. If the transient part is ignored under harmonic excitation, then the remaining component u_p can also be expressed as

$$u = u_p = \rho \sin(\bar{\omega}t - \theta) \quad (3.21)$$

where

$$\rho = \frac{F_0/k}{\left[(1 - \beta^2)^2 + (2\xi\beta)^2\right]^{1/2}}, \quad \theta = \tan^{-1} \frac{2\xi\beta}{1 - \beta^2}. \quad (3.22)$$

Here, ρ is the amplitude, and θ is the phase delay between u_p and $F_0 \sin \bar{\omega}t$, and $F_0 = -ma_0$. It can be shown by expanding $\sin(\bar{\omega}t - \theta)$, that Eq. (3.21) with Eq. (3.22) is identical to the second (steady-state) term in Eq. (3.20). The variation of ρ with the frequency ratio β and the damping ratio ξ is plotted in Fig. 3.11, which is called the *frequency response function*. It can be observed that the response displacement amplitude amplifies as β approaches to unity whereas increase in damping ratio reduces the level of amplification.

3.4.2.2 Resonance

When $\beta = 1$, i.e. the forcing frequency $\bar{\omega}$ is equal to the natural frequency of vibration ω_n in Eqs. (3.18) and (3.19) reduces to

$$u(t) = \frac{F_0/k}{2\xi} (e^{-\xi\bar{\omega}t} - 1) \cos \bar{\omega}t. \quad (3.23)$$

Equation (3.23) is plotted in Fig. 3.12a. The amplitude of displacement cycles increase at every cycle and asymptotically approach $\frac{F_0/k}{2\xi}$. Meanwhile, if $\xi \rightarrow 0$, L'Hospital rule gives

$$u(t) = \frac{F_0/k}{2} (\sin \bar{\omega}t - \omega t \cos \bar{\omega}t). \quad (3.24)$$

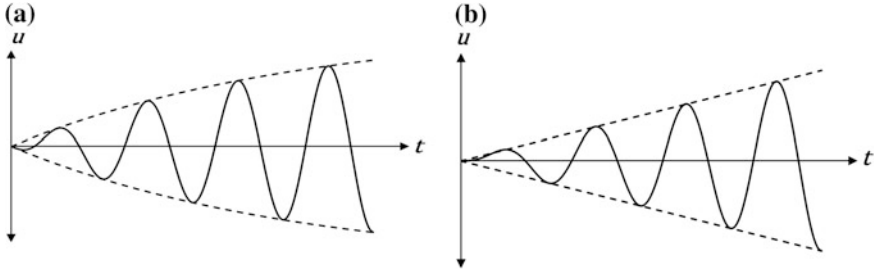


Fig. 3.12 Resonance in **a** damped, **b** undamped SDOF systems under harmonic excitation

The second term in the parenthesis indicates a linear increase of displacement amplitude with time, without any bound. Equation (3.24) is plotted in Fig. 3.12b.

Equations (3.23) and (3.24) define a vibration phenomenon called the *resonance*. In mechanical systems, resonance causes very high displacements which usually lead to collapse.

During resonance, as t increases and eventually approaches infinity, inertial resistance $m\ddot{u}$ and elastic resistance ku become totally out of phase, hence they cancel out each other. External force in this case is only resisted by the damping resistance $c\dot{u}$, which requires very high velocities to maintain dynamic equilibrium. This condition can be verified from Eq. (3.23) as t approaches infinity.

3.4.3 Forced Vibration Response: Earthquake Excitation

A SDOF system under earthquake ground acceleration is shown in Fig. 3.13. The excitation function $F(t)$ or $-m\ddot{u}_g(t)$ can rarely be expressed by an analytical function in the case of earthquake ground excitation. Ground acceleration $\ddot{u}_g(t)$ recorded by an accelerograph can be expressed numerically. Closed-form analytical solution similar to Eq. (3.20) is not possible, hence the solution is obtained by using numerical integration techniques. The most practical and also the most popular method is the *step-by-step direct integration* of the equation of motion (Newmark 1956).

3.4.4 Numerical Evaluation of Dynamic Response

Let's consider the equation of motion of a SDOF system at time $t = t_i$ and $t = t_{i+1} \equiv t_i + \Delta t$ where Δt is small.

$$m\ddot{u}_i + c\dot{u}_i + ku_i = F_i \equiv -m\ddot{u}_g(t_i) \quad (3.25a)$$

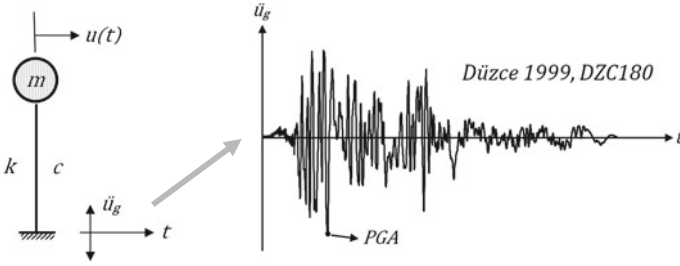


Fig. 3.13 A SDOF system under earthquake excitation

$$m\ddot{u}_{i+1} + c\dot{u}_{i+1} + ku_{i+1} = F_{i+1} \equiv -m\ddot{u}_g(t_{i+1}). \quad (3.25b)$$

Subtracting (3.25a) from (3.25b) gives,

$$m(\ddot{u}_{i+1} - \ddot{u}_i) + c(\dot{u}_{i+1} - \dot{u}_i) + k(u_{i+1} - u_i) = F_{i+1} - F_i \quad (3.26)$$

or

$$m\Delta\ddot{u}_i + c\Delta\dot{u}_i + k\Delta u_i = \Delta F_i \quad (3.27)$$

where

$$\Delta(\cdot)_i = (\cdot)_{i+1} - (\cdot)_i. \quad (3.28)$$

Equation (3.27) contains three unknowns (Δu_i , $\Delta \dot{u}_i$, $\Delta \ddot{u}_i$). Therefore it is indeterminate. However, we may impose two kinematical relations between these three response parameters, such as ($d\dot{u} = \ddot{u}dt$) and ($du = \dot{u}dt$). This can be achieved by assuming a variation of acceleration $\ddot{u}(t)$ over Δt , then integrating twice to calculate $\dot{u}(t)$ and $u(t)$ within Δt . We assume that \ddot{u}_i , \dot{u}_i and u_i at the beginning of a time step are known from the previous step.

Two common assumption can be made on the variation of $\ddot{u}(t)$ over Δt : constant average acceleration and linear acceleration variation. Numerical evaluation is developed by using the simpler constant average acceleration assumption below.

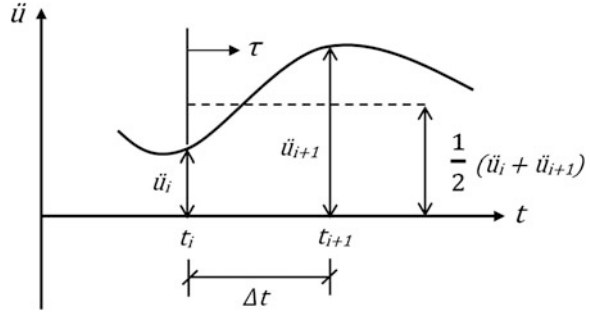
3.4.4.1 Constant Average Acceleration

The variation of acceleration $\ddot{u}(t)$ over a time step Δt is shown in Fig. 3.14. This actual variation can be estimated by an approximate, constant average acceleration variation given in Eq. (3.29).

$$\ddot{u}(\tau) = \frac{1}{2}(\ddot{u}_i + \ddot{u}_{i+1}); \quad 0 < \tau < \Delta t. \quad (3.29)$$

It should be noted here that the actual variation of acceleration within Δt on the left hand side of Eq. (3.29) is not yet known, and hence \ddot{u}_{i+1} on the right hand side is

Fig. 3.14 Actual and estimated acceleration variations over a time step Δt



also an unknown. This is merely a transfer of unknown from a function to a discrete value by the assumption of constant average acceleration variation over Δt .

We can integrate the constant acceleration variation given in Eq. (3.29) twice, in order to obtain the variations of velocity and displacement over the time step Δt , respectively. This process is schematized in Fig. 3.15.

The first integration is from acceleration to velocity, i.e. the integration of $du = \ddot{u}d\tau$.

$$\int_{\dot{u}_i}^{\dot{u}} d\dot{u} = \int_{t_i}^t \ddot{u}d\tau. \tag{3.30}$$

Substituting \ddot{u} from Eq. (3.29) into Eq. (3.30) and integrating, we obtain

$$\dot{u}(\tau) = \dot{u}_i + \frac{\tau}{2}(\ddot{u}_i + \ddot{u}_{i+1}). \tag{3.31}$$

Equation (3.31) can also be written for $\tau = \Delta t$ at the end of the time step, which gives

$$\dot{u}_{i+1} = \dot{u}_i + \frac{\Delta t}{2}(\ddot{u}_i + \ddot{u}_{i+1}). \tag{3.32}$$

Then, substituting \dot{u} from Eq. (3.31) into $du = \dot{u}d\tau$ and integrating over Δt ,

$$\int_{u_i}^{u_{i+1}} du = \int_{t_i}^{t_i+\Delta t} \dot{u}d\tau \tag{3.33}$$

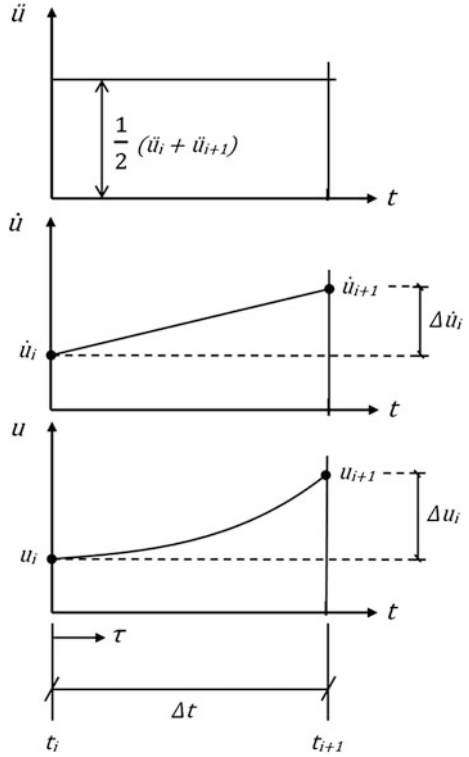
we obtain

$$u_{i+1} = u_i + \dot{u}_i\Delta t + \frac{\Delta t^2}{4}(\ddot{u}_i + \ddot{u}_{i+1}). \tag{3.34}$$

The terms u_{i+1} , \dot{u}_{i+1} and \ddot{u}_{i+1} at t_{i+1} in Eqs. (3.32) and (3.34) are the unknowns.

Let $(\ddot{u}_i + \ddot{u}_{i+1}) \equiv \ddot{u}_{i+1} - \ddot{u}_i + 2\ddot{u}_i \equiv \Delta\ddot{u}_i + 2\ddot{u}_i$. When this identity is substituted into Eqs. (3.32) and (3.34) and rearranged, two new equations are obtained:

Fig. 3.15 Integration of constant average acceleration variation over the time step Δt



$$\Delta \dot{u}_i = \frac{\Delta t}{2} (\Delta \ddot{u}_i + 2\ddot{u}_i) \tag{3.35}$$

$$\Delta u_i = \dot{u}_i \Delta t + \frac{\Delta t^2}{4} (\Delta \ddot{u}_i + 2\ddot{u}_i). \tag{3.36}$$

Δu_i , $\Delta \dot{u}_i$ and $\Delta \ddot{u}_i$ are the new three unknowns in Eqs. (3.35) and (3.36). Combining these equations with Eq. (3.27) forms a system of three coupled linear equations with three unknowns, and can be solved through elimination.

Let's rearrange (3.35) and (3.36) to express $\Delta \ddot{u}_i$ and $\Delta \dot{u}_i$ in terms of Δu_i . From Eq. (3.36),

$$\Delta \ddot{u}_i = \frac{4}{\Delta t^2} \Delta u_i - \frac{4}{\Delta t} \dot{u}_i - 2\ddot{u}_i. \tag{3.37}$$

Substituting Δu_i above into Eq. (3.35),

$$\Delta \dot{u}_i = \frac{2}{\Delta t} \Delta u_i - 2\dot{u}_i. \tag{3.38}$$

Finally, substituting $\Delta \ddot{u}_i$ and $\Delta \dot{u}_i$ from Eqs. (3.37) and (3.38) into Eq. (3.27) and rearranging, we obtain

$$k_i^* \Delta u_i = \Delta F_i^* \quad (3.39)$$

where

$$k_i^* = k + \frac{2c}{\Delta t} + \frac{4m}{\Delta t^2} \quad (3.40)$$

is the instantaneous dynamic stiffness, and

$$\Delta F_i^* = \Delta F_i + \left(\frac{4m}{\Delta t} + 2c \right) \dot{u}_i + 2m\ddot{u}_i \quad (3.41)$$

is the effective dynamic incremental force. Note that $k_i^* = k^*$ in Eq. (3.40), i.e. dynamic stiffness does not change at each time step i .

The recursive solution starts at $i = 0$ with $u(0) = 0$ and $\dot{u}(0) = 0$ as the initial conditions. This procedure is unconditionally stable: Errors do not grow up with the recursion steps. However $\frac{\Delta t}{T_n} \leq 10$ is required for accuracy.

3.4.5 Integration Algorithm

The step-by-step direct integration procedure described above is formulated as an algorithm below, which can be easily coded with conventional software (FORTRAN, MatLab, Excel, etc.).

1. Define $m, c, k, u(0) = 0, \dot{u}(0) = 0, F_i = F(t_i)$ and Δt
2. $\ddot{u}_0 = \frac{1}{m}(F_0 - c\dot{u}_0 - ku_0)$
3. Calculate k^* from Eq. (3.40)
4. $i = i + 1$
5. Calculate ΔF_i^* from Eq. (3.41)
6. $\Delta u_i = \Delta F_i^* / k^*$
7. Calculate $\Delta \dot{u}_i$ and $\Delta \ddot{u}_i$ from Eqs. (3.37) and (3.38)
8. $(\cdot)_{i+1} = (\cdot)_i + \Delta(\cdot)_i$ for $(\cdot) = u, \dot{u}, \ddot{u}$
9. Go to 4

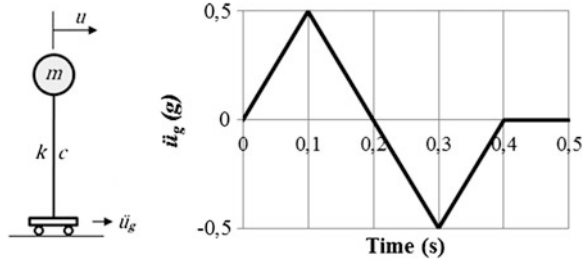
Example 3.4 A linear elastic SDOF system is given in Fig. 3.16 with $T_n = 1$ s, $m = 1$ kg (unit), $\xi = 5\%$, $u(0) = 0, \dot{u}(0) = 0$ (initially at rest). Determine the displacement response $u(t)$ under the base excitation $\ddot{u}_g(t)$ defined below. Use $\Delta t = 0.1$ s in calculations.

Solution

All units are in Newton, meter and seconds.

$$\omega_n = \frac{2\pi}{T_n} = 6.28 \text{ rad/s}^2, \quad k = \omega_n^2 m = 39.478 \text{ N/m}, \quad c = 2\xi m \omega_n = 0.628 \text{ N s/m}$$

Fig. 3.16 A linear elastic SDOF system subjected to a ground pulse



$$\ddot{u}_0 = \frac{1}{m} [-m\ddot{u}_{g(0)} - c\dot{u}_0 - ku_0] = 0, \quad k^* = k + \frac{2c}{\Delta t} + \frac{4m}{\Delta t^2} = 452.045 \text{ N/m}$$

<i>m</i>	<i>T_n</i> (s)	ω_n (rad/s)	ζ	Δt (s)	<i>c</i>	<i>k</i>	<i>u</i> ₀	\dot{u} (0)	\ddot{u} (0)	<i>k</i> [*]
1	1	6.28	0.05	0.1	0.628	39.478	0	0	0	452.045

$$\Delta F_i^* = \Delta F_i + \left(\frac{4m}{\Delta t} + 2c\right)\dot{u}_i + 2m\ddot{u}_i \quad \text{where } \Delta F_i = -m(\ddot{u}_{g(i+1)} - \ddot{u}_{g(i)}).$$

i = 0

$$\begin{aligned} \Delta F_0^* &= -1 * (0.5 - 0) * 9.81 + \left[\left(\frac{4 * 1}{0.1}\right) + 2 * 0.628\right] * (0) + 2 * 1 * (0) \\ &= -4.905 \text{ N} \end{aligned}$$

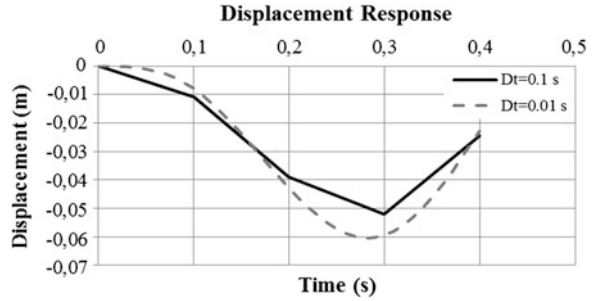
$$\begin{aligned} \Delta u_0 &= -\frac{4.905}{452.045} = -0.0109; \quad \Delta \dot{u}_0 = \frac{2}{\Delta t}(-0.0109) = -0.217; \quad \Delta \ddot{u}_0 = \frac{4}{\Delta t^2}(-0.0109) = -4.34 \\ u_1 &= 0 - 0.0109 = -0.0109; \quad \dot{u}_1 = 0 - 0.217 = -0.217; \quad \ddot{u}_1 = 0 - 4.34 = -4.34. \end{aligned}$$

The procedure continues with *i* = 1, as summarized in the tabular form below.

<i>i</i>	<i>t</i>	<i>u_i</i>	\dot{u}_i	\ddot{u}_i	ΔF_i^*	Δu_i	$\Delta \dot{u}_i$	$\Delta \ddot{u}_i$	<i>u_{i+1}</i>	\dot{u}_{i+1}	\ddot{u}_{i+1}
0	0	0	0	0	-4.905	-0.0109	-0.2170	-4.3403	-0.0109	-0.2170	-4.3403
1	0.1	-0.0109	-0.2170	-4.3403	-12.729	-0.0282	-0.1291	6.0978	-0.0390	-0.3462	1.7575
2	0.2	-0.0390	-0.3462	1.7575	-5.861	-0.0130	0.4330	5.1448	-0.0520	0.0868	6.9023
3	0.3	-0.0520	0.0868	6.9023	12.482	0.0276	0.3786	-6.2330	-0.0244	0.4654	0.6693
4	0.4	-0.0244	0.4654	0.6693							

The solution is repeated with $\Delta t = 0.01$ s also, and the calculated displacement response is plotted below in Fig. 3.17 for both time intervals during the forced vibration phase. The exact displacements are $u(0.1) = 0.008$ and $u(0.2) = 0.044$. Therefore the solution with $\Delta t = 0.01$ s can be considered almost as exact for this problem.

Fig. 3.17 Displacement response of the SDOF system calculated for two different Δt



3.5 Earthquake Response Spectra

Let’s consider various SDOF systems with different T , but the same ζ , subjected to a ground excitation as shown in Fig. 3.18. Note that $T_1 < T_2 < T_3 < \dots$ in Fig. 3.18.

We can calculate the displacement response of each SDOF system $u(t)$ by direct integration. Time variations $u(t)$ and $\ddot{u}(t)$ of 5 % damped SDOF systems with $T_1 = 0.5$ s, $T_2 = 1.0$ s and $T_3 = 2.0$ s under the NS component of 1999 Düzce ground motion are plotted in Fig. 3.19.

We can select the peak displacement response from each $u(t)$ function, and define this value as the spectral displacement S_d , where,

$$S_d = \max|u(t)|. \tag{3.42}$$

Since each $u(t)$ is a function of T and ζ , S_d also varies with T and ζ . Hence,

$$S_d = S_d(T, \zeta). \tag{3.43}$$

Similarly, spectral acceleration can be defined as the peak value of total acceleration

$$S_a = \max|\ddot{u}(t) + \ddot{u}_g(t)|. \tag{3.44}$$

where

$$S_a = S_a(T, \zeta). \tag{3.45}$$

S_a and S_d values are marked on Fig. 3.19 for the response of each SDOF system.

Accordingly, S_d , and S_a in Eqs. (3.43) and (3.45) can be plotted as functions of T and ζ . When this process is repeated for a set of damping ratios, a family of S_a and S_d curves are obtained. The family of these curves is called the *acceleration response spectra* and *displacement response spectra* of an earthquake ground motion, respectively. Acceleration and displacement response spectra of the NS component of 1999 Düzce ground motion are plotted in Fig. 3.20. The peak values indicated in Fig. 3.19 are also marked on Fig. 3.20.

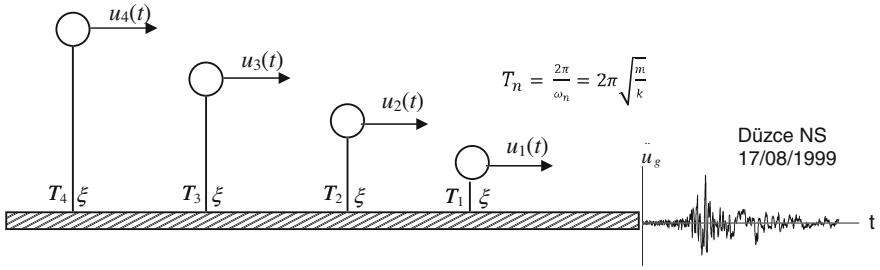


Fig. 3.18 Different SDOF systems under earthquake ground excitation

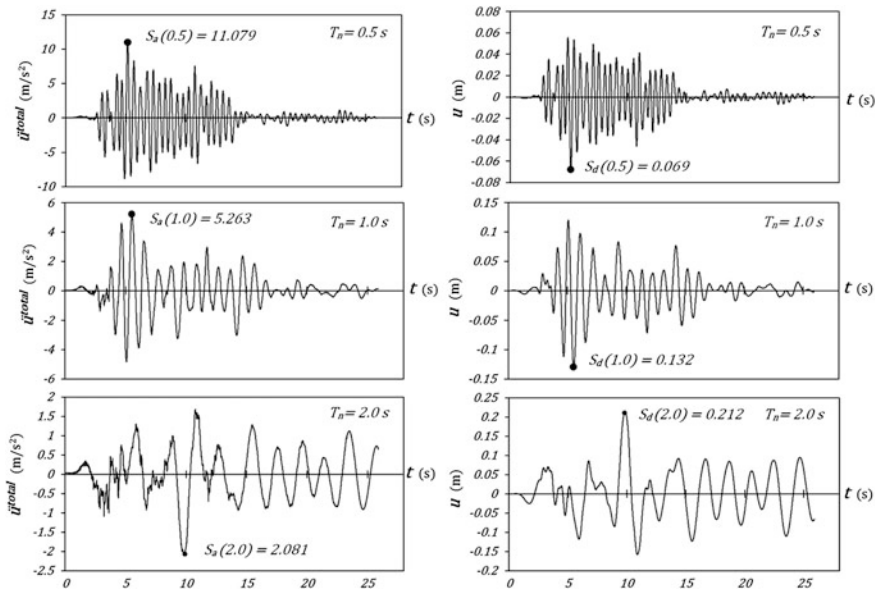


Fig. 3.19 Time variations of displacement and acceleration responses of several SDOF systems under the NS component of 1999 Düzce ground motion

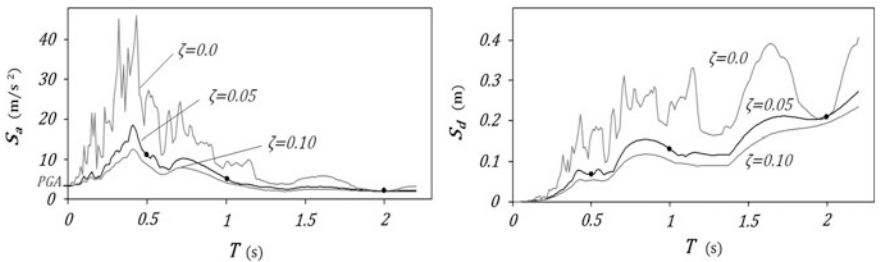


Fig. 3.20 Acceleration and displacement response spectra of the NS component of 1999 Düzce ground motion

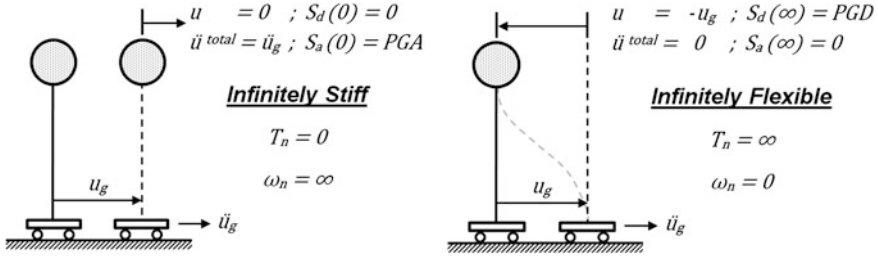


Fig. 3.21 Response of infinitely stiff and infinitely flexible SDOF systems to ground excitation

The effect of ground motion duration is almost lost in the spectral information since an earthquake response spectrum only considers the time when peak response occurs. This is practical for design, however a long duration ground motion may cause low cycle fatigue and consequent degradation. We cannot obtain such detailed information from a response spectrum.

It can be observed from Fig. 3.20 that when $T = 0$, $S_a = \ddot{u}_{g,max}$ (*PGA*) and $S_d = 0$. On the other hand, when T approaches infinity, S_a approaches zero and S_d approaches $u_{g,max}$ (*PGD*). These limiting situations can be explained with the aid of Fig. 3.21.

$T = 0$ is equivalent to $\omega_n = \infty$, i.e. the system is infinitely stiff. Thus the spring does not deform ($u = 0$, hence $S_d = 0$) and the motion of the mass becomes identical to the motion of ground. Accordingly, maximum acceleration of the mass becomes identical to the acceleration of the ground which makes their maximum values equal.

T approaches infinity when ω_n approaches zero as the system becomes infinitely flexible. An infinitely flexible system has no stiffness and it cannot transmit any internal lateral force from the ground to the mass above. Ground moves while the mass stays stationary during the earthquake. The total displacement of the mass is zero ($u^{total} = u + u_g = 0$). Accordingly $|u|_{max} = |u_g|_{max}$ or $S_d = PGD$. Similarly, the total acceleration of the mass is zero ($\ddot{u}^{total} = \ddot{u} + \ddot{u}_g = 0$) which makes $S_a = 0$ from Eq. (3.44).

3.5.1 Pseudo Velocity and Pseudo Acceleration Response Spectrum

Pseudo spectral velocity PS_v and pseudo spectral acceleration PS_a are alternative expressions for the velocity and acceleration response spectra, which provide simple and practical relations between spectral displacement, velocity and acceleration. PS_v and PS_a can be directly obtained from S_d . Their definitions are given in Eqs. (3.46) and (3.48) below. PS_v and PS_a are very close to S_v and S_a for $\xi < 0.20$.

3.5.1.1 Pseudo Velocity

$$PS_v(T, \xi) = \omega_n \cdot S_d = \frac{2\pi}{T_n} S_d(T, \xi). \quad (3.46)$$

$PS_v \approx S_v$ for $\xi < 0.20$. It is related to the maximum strain energy E_s stored in the SDOF system during the earthquake.

$$E_{s,max} = \frac{1}{2} k u_{max}^2 = \frac{1}{2} k S_d^2 = \frac{1}{2} k \left(\frac{PS_v}{\omega_n} \right)^2 = \frac{1}{2} m (PS_v)^2. \quad (3.47)$$

3.5.1.2 Pseudo Acceleration

$$PS_a(T, \xi) = \omega_n^2 S_d = \left(\frac{2\pi}{T_n} \right)^2 S_d(T, \xi) \quad (3.48)$$

$PS_a \approx S_a$ for $\xi < 0.20$. It is related to the maximum base shear force at the support of the SDOF system during the earthquake.

Let's consider an "undamped" SDOF system under a ground excitation \ddot{u}_g . Its equation of motion is,

$$m(\ddot{u} + \ddot{u}_g) + ku = 0. \quad (3.49)$$

Therefore,

$$m|(\ddot{u} + \ddot{u}_g)|_{max} = k|u|_{max}. \quad (3.50)$$

Then,

$$mS_a = kS_d \quad \text{or} \quad S_a = \omega_n^2 S_d \quad (3.51)$$

for $\xi = 0$. Comparison of Eqs. (3.48) and (3.51) indicates that $PS_a = S_a$ when $\xi = 0$.

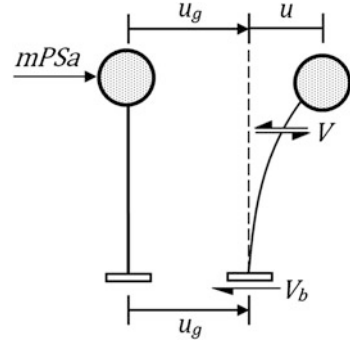
The shear (restoring) force and base shear force which develop in a SDOF system during an earthquake ground excitation are shown in Fig. 3.22. Base shear force becomes maximum when the relative displacement is maximum, i.e.

$$V_{b,max} = k u_{max} = k S_d = k \left(\frac{S_a}{\omega_n^2} \right) = m S_a. \quad (3.52)$$

Now, let's consider a "damped" SDOF system. Equation (3.52) is replaced by

$$V_{b,max} = k u_{max} = k S_d = k \left(\frac{PS_a}{\omega_n^2} \right) = m PS_a. \quad (3.53)$$

Fig. 3.22 Internal shear force and base shear force developing in an SDOF system under earthquake ground excitation



Hence, the maximum base shear force in a damped SDOF system can directly be obtained from PS_a through Newton’s second law.

3.5.2 Practical Implementation of Earthquake Response Spectra

If S_d , PS_v and PS_a are all available for an earthquake ground excitation, then we can easily obtain the maximum values of response displacement, strain energy, internal elastic force and base shear force of an SDOF system from these spectral graphics. The only data we need for a SDOF system is its natural vibration period T_n and viscous damping ratio ξ .

The maximum base shear force in Eq. (3.53) can be formulated as follows:

$$V_{b,max} = mPS_a = mg \frac{PS_a}{g} = W \cdot \frac{PS_a}{g} \tag{3.54}$$

where W is the weight in the gravity field. Then,

$$\frac{V_{b,max}}{W} = \frac{PS_a}{g} \tag{3.55}$$

The ratio of maximum base shear force to weight is called the *base shear coefficient*, which is a practical yet very important parameter in earthquake engineering analysis and design. It is denoted with C , and it can be obtained directly from PS_a .

$$C = \frac{V_{b,max}}{W} = \frac{PS_a}{g} \tag{3.56}$$

Example 3.5 Consider the portal frame in Example 3.3. The properties assigned are, column size: 0.40×0.50 m, $E = 250,000$ kN/m², $L = 3$ m and $m = 25$ tons. Determine the maximum displacement of the roof if the frame is subjected to the 1999 Düzce NS ground motion. Viscous damping ratio is 5 %.

Solution

The natural vibration period was defined in Example 3.3. When the numerical values given above are substituted, $T_n = 1.3$ s is calculated. Then the spectral acceleration can be determined from Fig. 3.20 at $T = 1.3$ s as $S_a = 4$ m/s².

The effective force acting at the roof mass is,

$$F_{eff} = m S_a = 25 \text{ tons} \times 4 \text{ m/s}^2 = 100 \text{ kN}.$$

The effective stiffness expression was also derived in Example 3.3. When the numerical values given above are substituted, $k_{eff} = 578.7$ kN/m is calculated. Finally,

$$u = \frac{F_{eff}}{k_{eff}} = 0.173 \text{ m}.$$

3.6 Nonlinear SDOF Systems

Lateral forces which act on linear elastic structural systems under strong earthquake ground motions are usually very large. Spectral acceleration shapes for a suit of 10 ground motions are shown in Fig. 3.23. It can be observed that the effective lateral forces ($m P S_a$) are at the order of the weight (mg) in the period range of 0.4–1.0 s. Fundamental vibration periods of most of the building structures fall into this period range. Designing structures for such high levels of lateral forces is not economical and feasible for a very seldom event such as a strong earthquake which may occur only with a small probability during its service life.

The preferred approach in seismic design is to provide a lateral strength F_y that is less than the elastic strength demand F_e , however implement a plastic deformation capacity to the system such that it can deform beyond the linear elastic range during a strong ground motion.

When the yield displacement capacity of the lateral load resisting system is exceeded, the slope of the restoring force-deformation curve, or stiffness softens. A typical force-deformation path of a SDOF system subjected to a single cycle of large ground acceleration is shown in Fig. 3.24. This type of nonlinear behavior is called *material nonlinearity* in mechanical systems because softening occurs due to the deterioration of material properties at large displacements, similar to the stress-strain behavior of steel and concrete materials. F_s is the restoring force (internal resistance), F_y is the yield force capacity and u_y is the yielding displacement in Fig. 3.24.

3.6.1 Nonlinear Force-Deformation Relations

Hysteresis relations are composed of a set of rules by which the variation of F_s is defined in terms of the variation history of u during the previous loading steps.

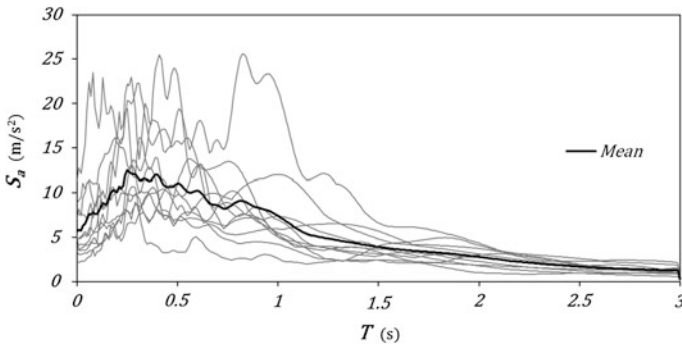


Fig. 3.23 Linear elastic acceleration response spectra of 10 ground motions

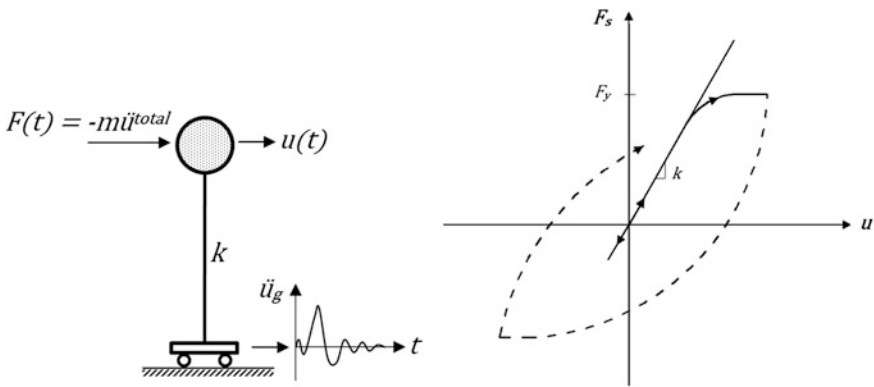


Fig. 3.24 Variation of internal force F_s with displacement u along a nonlinear force-deformation path

This is called a *hysteresis model*. Two basic hysteresis models are employed in earthquake engineering: Elasto-plastic and stiffness degrading models. The elasto-plastic model is usually employed for representing the hysteretic flexural behavior of steel structures whereas the stiffness degrading model represents the hysteretic flexural behavior of concrete structures respectively, under loading reversals induced by an earthquake ground motion.

The set of rules which define elasto-plastic and stiffness degrading hysteretic behavior with strain hardening are shown in Fig. 3.25 separately. F_y and u_y are the yield strength and yield displacement respectively, k is the initial elastic stiffness and αk is the strain hardening stiffness after yielding where α is usually less than 10 %. When $\alpha = 0$, the system has no strain hardening. Elasto-plastic systems with no strain hardening are called elastic-perfectly plastic.

3.6.1.1 Elasto-Plastic Model

There are two stiffness states in the elasto-plastic model (Fig. 3.25a): k or αk . Initial loading (0-1 or 0-1') starts with the stiffness k , and when the internal resistance reaches the plastic state, the system yields and deforms along the yield plateau with post-yield stiffness αk (1-2). Unloading and reloading (2-3; 4-5; 6-7) take place along the elastic paths with the initial stiffness k . When the direction of loading changes from loading to unloading or vice versa along these paths, the stiffness does not change. On the other hand, when the internal resistance reaches the plastic state along these paths at points (3, 5 or 7), plastic deformations occur along the yield plateau with post-yield stiffness αk (3-4 or 5-6).

3.6.1.2 Stiffness Degrading Model

In the stiffness degrading model (Fig. 3.25b), unloading and reloading stiffnesses are different. Unloading from the yield plateau takes place with the initial elastic stiffness k (2-3 or 5-6). Reloading then follows with a degraded stiffness defined from the point of complete unloading (3 or 6) to the maximum deformation point in the same direction which occurred during the previous cycles (points 4 or 2). Unloading from a reloading branch before reaching the yield plateau also takes place with the stiffness k (7-8).

3.6.2 Relationship Between Strength and Ductility in Nonlinear SDOF Systems

Under an earthquake excitation, nonlinear systems can only develop a resistance bounded by their lateral yield strength F_y , but they respond at larger displacements. Let's consider three elasto-plastic SDOF systems with the same initial stiffness k and period T , subjected to the same earthquake ground motion \ddot{u}_g (Fig. 3.26). Their properties, from the weakest to strongest are:

- System 1: Elasto-plastic with yield strength F_{y1} and yield displacement u_{y1}
- System 2: Elasto-plastic with yield strength F_{y2} and yield displacement u_{y2} ($F_{y2} > F_{y1}$)
- System 3: Ideal linear elastic, i.e. $F_y = \infty$

We can expect that the weakest system (System 1) deforms most, to an absolute maximum displacement of u_{max1} , while system 2 deforms to a lesser maximum displacement of u_{max2} . Meanwhile, the linear elastic system deforms to a maximum displacement of u_e under the same earthquake ground motion. These maximum absolute displacements u_{max1} , u_{max2} and u_e are called the *displacement demands* of the earthquake from systems 1, 2 and 3, respectively. We can also

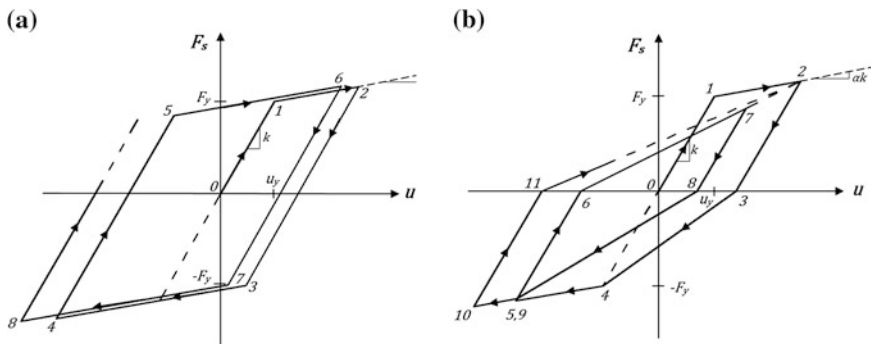


Fig. 3.25 Elasto-plastic and stiffness degrading hysteresis models. **a** Elasto-plastic model (Steel members). **b** Stiffness degrading model (RC members)

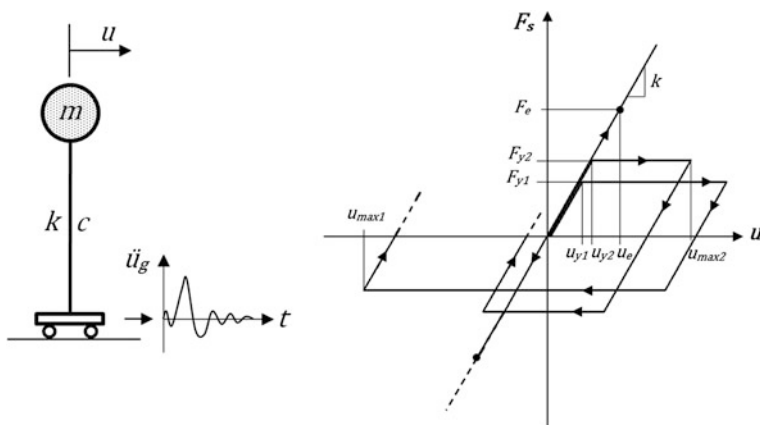


Fig. 3.26 Three SDOF systems with the same initial stiffness k , but different yield strengths F_{yi} , subjected to a strong ground excitation cycle

define these demands in terms of a dimensionless deformation ratio μ , called the *ductility ratio*.

$$\mu_i = \frac{u_{max,i}}{u_y} \tag{3.57}$$

Therefore, an earthquake ground motion demands more ductility from systems with less strength.

$$F_{y1} < F_{y2} < F_e \quad \Rightarrow \quad \mu_1 > \mu_2 > \mu_e \tag{3.58}$$

F_e is the elastic force demand, and $\mu_e = 1$ theoretically for linear elastic systems.

The force terms on the left in Eq. (3.58) are the strengths (capacities) whereas the terms on the right are the ductility ratios (demands).

3.6.3 Equation of Motion of a Nonlinear SDOF System

Equation of motion of a nonlinear SDOF system is also a 2nd order ordinary differential equation, but with a nonlinear mathematical term.

$$m\ddot{u} + c\dot{u} + F_s(u) = F(t) \equiv -m\ddot{u}_g. \quad (3.59)$$

The restoring force term F_s creates the nonlinearity in the equation of motion since $F_s(u)$ is a nonlinear (hysteretic) function. In a linear system, F_s is equal to $k \cdot u$ which is a linear relationship between F_s and u whereas $F_s = F_s(u)$ in a nonlinear system implies that the tangent stiffness k is not constant as in a linear system, but changes with the displacement u . The variation of F_s with u along a general nonlinear force-deformation path was schematized in Fig. 3.24.

Let's consider a smooth nonlinear system during a time step Δt , shown in Fig. 3.27. The equation of motion can be written in incremental form with the aid of Fig. 3.27.

$$m\Delta\ddot{u}_i + c\Delta\dot{u}_i + \Delta F_s(u)_i = \Delta F_i = -m\Delta\ddot{u}_{gi}. \quad (3.60)$$

The incremental variation of restoring force F_s with u can be estimated with

$$\Delta F_{s,i} \approx k_i(u_i)\Delta u_i \quad (3.61)$$

where

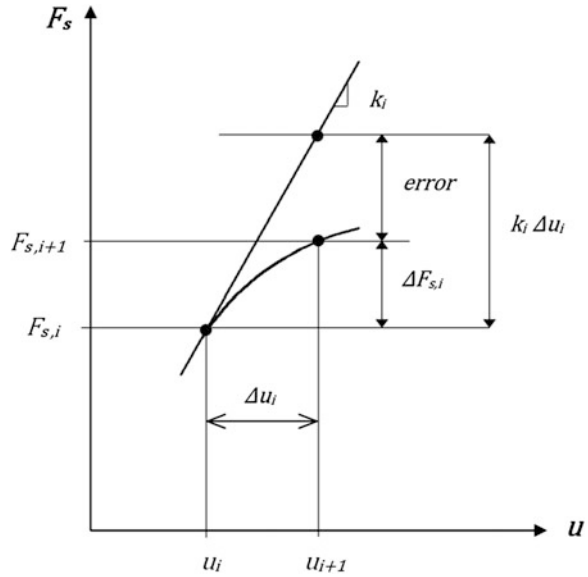
$$F_{s,i+1} = F_{s,i} + \Delta F_{s,i}; \quad u_{i+1} = u_i + \Delta u_i \quad (3.62)$$

and k_i is the tangent stiffness at u_i . Hence, the nonlinear equation of motion, i.e. Eq. (3.60) can be treated as an equivalent linear equation within each displacement increment Δu_i during the time step Δt by employing Eqs. (3.61) and (3.62).

3.6.4 Numerical Evaluation of Nonlinear Dynamic Response

Step-by-step direct integration algorithm developed for linear elastic systems in Sect. 3.4.5 can be applied to nonlinear systems if the hysteresis relationship $F_s = F_s(u)$ is known. Hence tangent stiffness $k_i(u_i)$ can be updated at each solution increment i and $\Delta F_{s,i}$ can be determined at the end of the time increment i , at the displacement u_{i+1} . However two types of errors are introduced if a slope change or a direction reversal occurs during the time increment. Let's discuss these errors on a piece-wise linear hysteresis model, either elasto-plastic or stiffness degrading, which are shown schematically in Fig. 3.28. The solid lines indicate the

Fig. 3.27 Incremental variation of the restoring force F_s and displacement u in a nonlinear system



actual (true) force-displacement paths, and the dashed lines indicate the approximate paths predicted by employing Eqs. (3.61) and (3.62).

3.6.4.1 Slope Change

If slope change is detected at the end of a time step, i.e. k_i is different from k_{i+1} , then the time step Δt can be sub-incremented into smaller time increments $\Delta t/n$ where n can be selected as a large integer. However 10 will be sufficient in practice. Such a reduction in time step will reduce the under-shooting errors significantly, and the displacement corresponding to slope change will be calculated accurately. Once the slope change is detected during a sub-increment, then the following steps shall proceed with k_{i+1} and with the original time increment Δt to speed up the solution.

A more precise solution to slope change can be obtained with the Newton-Raphson iteration, however sub-incrementation is more practical, and provides acceptable accuracy.

3.6.4.2 Direction Reversal

If sign of the velocity changes at the end of the time step, this is an indication of an under-shooting error as shown in Fig. 3.28b. Similar to slope change, the time increment can be sub-incremented into smaller time increments and the solution proceeds with these sub-increments until the time of direction reversal is captured accurately. Then the following steps proceed with the unloading stiffness and the original time increment Δt to accelerate the solution.

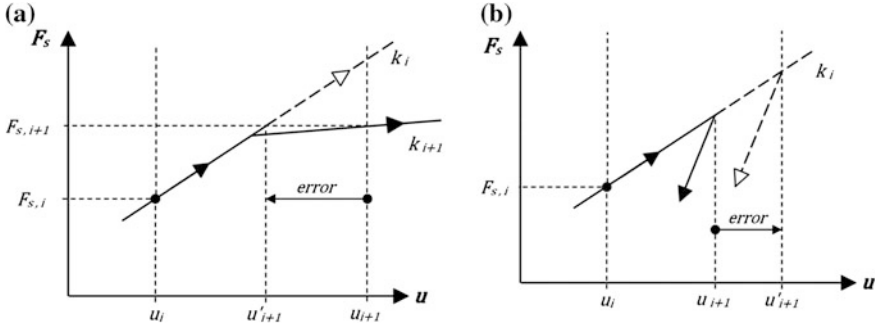


Fig. 3.28 a Slope change, b direction reversal within a displacement increment in a nonlinear system

3.6.4.3 Dynamic Equilibrium

In an iterative numerical solution, the exact solution can never be achieved although the errors can be acceptably small. These errors will inevitably disturb the instantaneous dynamic equilibrium at time t_{i+1} at the end of the time step. Dynamic equilibrium can be maintained by imposing total equilibrium at t_{i+1} . This is achieved by calculating \ddot{u}_{i+1} from total equilibrium given in Eq. (3.63) rather than calculating from the incremental solution $\ddot{u}_{i+1} = \ddot{u}_i + \Delta\ddot{u}_i$.

$$\ddot{u}_{i+1} = \frac{1}{m} [-m\ddot{u}_{g,i+1} - c\dot{u}_{i+1} - F_{s,i+1}]. \quad (3.63)$$

Accordingly, numerical errors are transferred to the kinematical relation between $\Delta\ddot{u}_i$ and Δu_i in Eq. (3.37).

3.6.4.4 Integration Algorithm

1. Define $m, c, k, u(0) = 0, \dot{u}(0) = 0, F_i = F(t_i)$ and Δt
2. $\ddot{u}_0 = \frac{1}{m} (-m\ddot{u}_{g,0} - c\dot{u}_0 - F_{s,0})$
3. $k_i^* = k + \frac{2c}{\Delta t} + \frac{4m}{\Delta t^2}$ (Eq. 3.40)
4. $i = i + 1$
5. $\Delta F_i^* = \Delta F_i + (\frac{4m}{\Delta t} + 2c)\dot{u}_i + 2m\ddot{u}_i$ from Eq. (3.41), where $\Delta F_i = -m(\ddot{u}_{g,i+1} - \ddot{u}_{g,i})$
6. $\Delta u_i = \Delta F_i^* / k_i^*$
7. Calculate $\Delta\dot{u}_i$ from Eq. (3.38)
8. $(\cdot)_{i+1} = (\cdot)_i + \Delta(\cdot)_i$ for $(\cdot) = u, \dot{u}$
9. Calculate \ddot{u}_{i+1} from Eq. (3.63)
10. Go to 4

Example 3.6 The SDOF system given in Example 3.4 is defined as an elasto-plastic system in Fig. 3.29 below, with $F_y = 0.1 \text{ mg}$ and $\alpha = 0$. Determine the displacement response, $u(t)$, under the same $\ddot{u}_g(t)$.

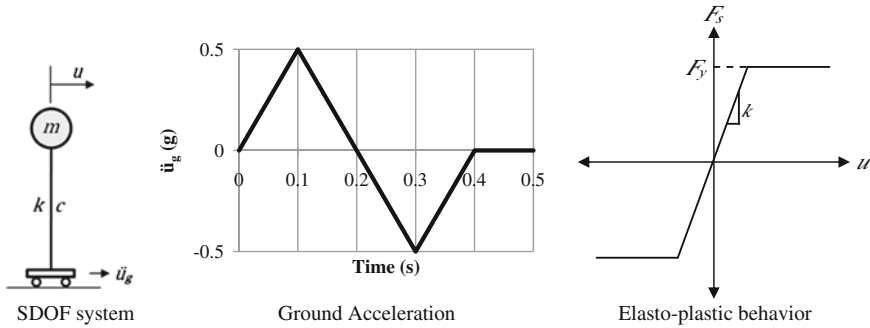


Fig. 3.29 An elasto-plastic SDOF system subjected to a ground excitation pulse

Solution

m	T_n (s)	ω_n (rad/s)	ζ	Δt (s)	c	$k_{elastic}$	α	f_y	u_0	\dot{u}_0	\ddot{u}_0	$F_{s(0)}$
1	1	6.28	0.05	0.1	0.628	39.478	0	0.981	0	0	0	0

$k_i^* = k_i + \frac{2c}{\Delta t} + \frac{4m}{\Delta t^2}$ where k_i is the tangent k at u_i .

$$\Delta F_{s(i)} = -m(\ddot{u}_{g,i+1} - \ddot{u}_{g,i}) - m\Delta\ddot{u}_i - c\Delta\dot{u}_i \quad \text{and}$$

$$\ddot{u}_{i+1} = \frac{1}{m}(-m\ddot{u}_{g,i+1} - c\dot{u}_{i+1} - F_{s,i+1}).$$

The solution steps are summarized in the table.

i	t	u_i	\dot{u}_i	\ddot{u}_i	k_i	k_i^*	ΔF_i^*	Δu_i	$\Delta\dot{u}_i$	$\Delta\ddot{u}_i$
0	0	0	0	0	39.478	452.045	-4.905	-0.0109	-0.2170	-43.403
1	0.1	-0.0109	-0.2170	-43.403	39.478	452.045	-12.729	-0.0282	-0.1291	60.978
2	0.2	-0.0390	-0.3462	11.985	0.000	412.566	-6.979	-0.0169	0.3540	46.826
3	0.3	-0.0559	0.0078	58.811	0.000	412.566	7.180	0.0174	0.3324	-51.139
4	0.4	-0.0385	0.3402	0.7672						

i	t	$F_{s,i}$	$\Delta F_{s,i}$	Calc. $F_{s,i+1}$	Actual $F_{s,i+1}$	u_{i+1}	\dot{u}_{i+1}	\ddot{u}_{i+1}
0	0	0	-0.428	-0.428	-0.428	-0.0109	-0.2170	-43.403
1	0.1	-0.428	-1.112	-1.540	-0.981	-0.0390	-0.3462	11.985
2	0.2	-0.981	0.000	-0.981	-0.981	-0.0559	0.0078	58.811
3	0.3	-0.981	0.000	-0.981	-0.981	-0.0385	0.3402	0.7672
4	0.4							

The solution obtained with $\Delta t = 0.1$ and $\Delta t = 0.01$ s are displayed graphically in Fig. 3.30. It can be observed that the difference in peak displacement is more than 20 %.

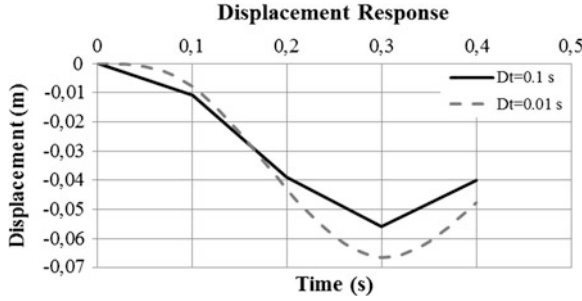


Fig. 3.30 Displacement response of the elasto-plastic SDOF system to the ground excitation pulse, calculated for two different integration time intervals

3.6.5 Ductility and Strength Spectra for Nonlinear SDOF Systems

We can solve the nonlinear equation of motion

$$m\ddot{u} + c\dot{u} + F_{s(u)} = -m\ddot{u}_g(t) \quad (3.64)$$

for different elasto-plastic systems with the same F_y and ξ , but different k_i (or T_i) under the same earthquake ground motion \ddot{u}_g . Accordingly, we can obtain the maximum displacement $u_{max,i}$ corresponding to each system with k_i or T_i . This is schematized in Fig. 3.31 under a strong ground excitation cycle.

Then, $\mu_i = \frac{u_{max,i}}{u_{y,i}}$ versus T_i can be plotted as a spectrum, called the ductility spectrum. If this process is repeated for different F_y values, we obtain *ductility spectra* for constant strength values F_y . Strength values are usually expressed as a ratio of mg in these charts. Ductility spectra obtained for the Düzce 1999 ground motion is shown in Fig. 3.32.

Next, we can convert the $\mu - T$ (ductility) spectra to an $F_y - T$ (strength) spectra by graphical interpolation. If we assume a constant ductility value on Fig. 3.32, it intersects each F_y curve at a different T value. Hence, a set of $F_y - T$ values are obtained for a constant ductility ratio of μ . We can plot the set of $F_y - T$ values for constant ductility as the strength spectrum. When this process is repeated for different constant ductility values, a family of constant ductility curves is obtained which is called the *strength spectra*. The strength spectra obtained for the Düzce 1999 ground

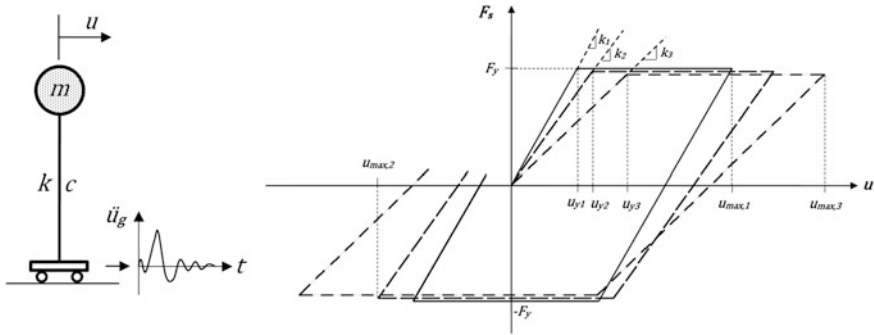


Fig. 3.31 Three SDOF systems with the same strength F_y , but different initial stiffnesses k_i , subjected to a strong ground excitation cycle

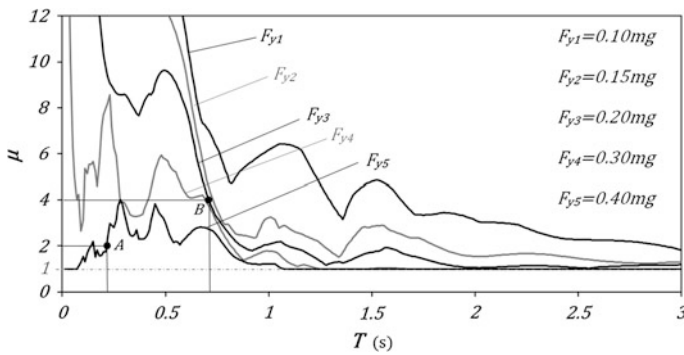


Fig. 3.32 Ductility spectra of the 1999 Düzce NS ground motion for different constant strength ratios

motion is shown in Fig. 3.33. This graphics is also called the *inelastic acceleration spectra* ($S_{a,i} - T$) for constant ductility μ .

The correspondence between the ductility spectra in Fig. 3.32 and the strength spectra in Fig. 3.33 can be explained with a simple example. Point A in Fig. 3.32 is on the $F_y = 0.40 \text{ mg}$ curve at $T = 0.21 \text{ s}$ with $\mu = 2$. Similarly, point B is on the $F_y = 0.20 \text{ mg}$ curve at $T = 0.71 \text{ s}$ with $\mu = 4$. These two points are also marked on Fig. 3.33, at the same period values on the corresponding constant ductility curves for $\mu = 2$ and 4. The associated F_y values are exactly the same.

If we know the period T and strength F_y of our SDOF system, then we can directly calculate the ductility demand of the earthquake ground motion from the inelastic acceleration spectra. On the other hand, if we have a given (estimated) ductility capacity μ for our system, then we can determine the required (minimum) strength for not exceeding this ductility capacity under the considered ground motion. This is very suitable for the force-based seismic design.

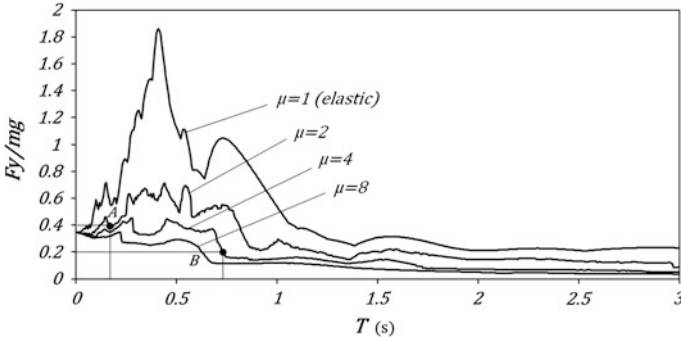
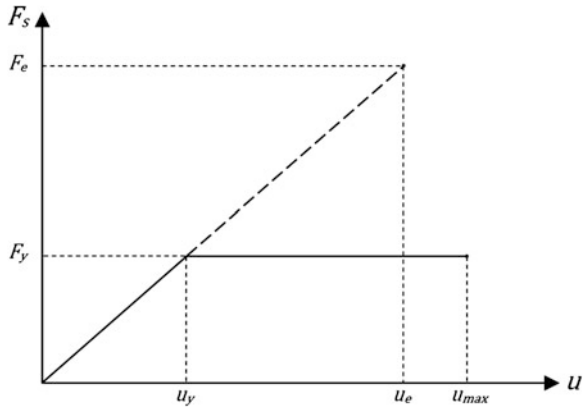


Fig. 3.33 Strength spectra or inelastic acceleration spectra of the 1999 Düzce NS ground motion for different constant ductility ratios

Fig. 3.34 Force-displacement responses of a linear elastic and a nonlinear SDOF system under an earthquake ground excitation \ddot{u}_g



3.6.6 Ductility Reduction Factor (R_μ)

R_μ is defined as the ratio of elastic force demand F_e to the yield capacity F_y of the nonlinear SDOF system with the same initial stiffness k , under the same earthquake ground excitation \ddot{u}_g (Eq. 3.65), which is depicted in Fig. 3.34.

$$R_\mu = F_e / F_y. \tag{3.65}$$

There is a corresponding ductility demand $\mu = u_{max} / u_y$ from the nonlinear system with the initial stiffness $k = F_y / u_y$ and the initial period $T = \frac{1}{2\pi} \sqrt{m/k}$. If this process is repeated for several nonlinear systems with different F_y and T values as in Fig. 3.32, a set of $R_\mu - \mu - T$ curves can be obtained, which can be plotted as a spectra. The $R_\mu - \mu - T$ spectra obtained for the Düzce 1999 and El Centro 1940 ground motions are shown in Fig. 3.35.

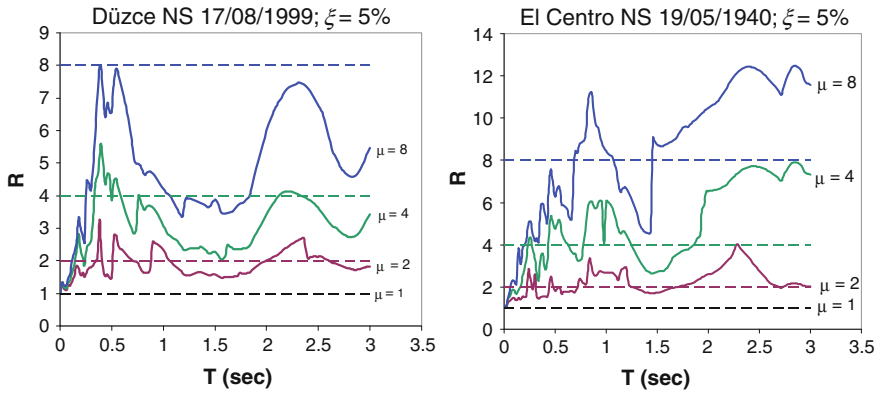


Fig. 3.35 $R_\mu - \mu - T$ spectra of the 1999 Düzce NS and 1940 El Centro NS ground motion components for different constant ductility ratios

Usually it is observed that R_μ oscillates around μ when $T > T_c$ where T_c is called the *corner period* of the ground motion. Then $R_\mu \rightarrow \mu$ when $T > T_c$. This assumption is valid for the mean $R_\mu - \mu - T$ spectrum of many ground motions, although it is a crude approximation for a single ground motion.

The mean $R_\mu - \mu - T$ spectrum can be idealized in a simple form shown in Fig. 3.36.

By using an exact $R_\mu - \mu - T$ spectrum, or the idealized one, we can obtain the inelastic acceleration spectrum S_{ai} and inelastic displacement spectrum S_{di} from the corresponding linear elastic acceleration and displacement spectra, S_{ae} and S_{de} , respectively. If we exploit the identities

$$R_\mu = \frac{F_e}{F_y} = \frac{F_e/m}{F_y/m} = \frac{S_{ae}}{S_{ai}} \quad \text{and} \quad R_\mu = \frac{F_e}{F_y} = \frac{ku_e}{ku_y} = \frac{S_{de}}{S_{di}/\mu}$$

we obtain

$$S_{ai} = \frac{S_{ae}}{R_\mu} \tag{3.66a}$$

and

$$S_{di} = \frac{\mu}{R_\mu} \cdot S_{de}. \tag{3.66b}$$

Equation (3.66a) can be employed for obtaining the inelastic acceleration response spectra S_{ai} directly from the linear elastic acceleration spectrum S_{ae} by selecting an R_μ ratio. This is very practical for seismic design since R_μ factors for different types of structural systems are defined in seismic design codes. Similarly, inelastic displacement response spectrum S_{di} can be obtained from the linear elastic displacement response spectrum S_{de} by using Eq. (3.66b). Inelastic acceleration (yield acceleration) spectra and inelastic displacement spectra calculated

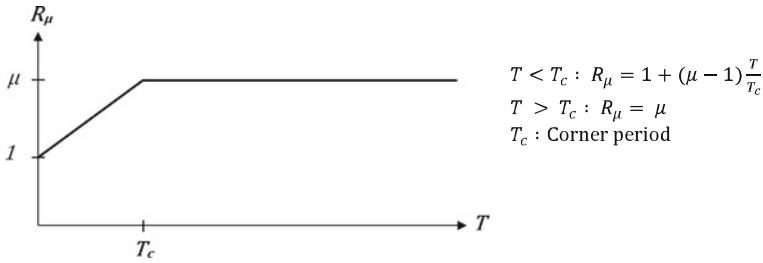


Fig. 3.36 Idealized form of the $R_\mu - \mu - T$ spectrum

for the Düzce 1999 ground motion by employing Eqs. (3.66a, 3.66b) are shown in Fig. 3.37a and b respectively for several R_μ factors.

It is noteworthy to compare the strength spectra in Fig. 3.33 with the yield acceleration spectra in Fig. 3.37a. In an elasto-plastic system, strength and yield acceleration are related through $F_y = m S_{ay}$. However inelastic spectral curves are slightly different at short periods. If R_μ was not constant for each curve in Fig. 3.30a, but it was a function of period as in Fig. 3.27a, then the two spectra would be the same.

Figure 3.37b implies that the response displacements of linear elastic and inelastic SDOF systems are very close. This property is discussed further in the following section.

3.6.7 Equal Displacement Rule

For medium and long period SDOF systems ($T > 0.5$ s), $R_\mu = \mu$ implies the *equal displacement rule*, which is derived in Eq. (3.67) below with the aid of Fig. 3.38, Eqs. (3.61) and (3.65).

$$k = \frac{F_e}{u_e} = \frac{F_y}{u_y} \Rightarrow \frac{F_e}{F_y} = \frac{u_e}{u_y} \equiv \frac{u_{max}}{u_y} \Rightarrow R_\mu = \mu. \quad (3.67)$$

Equal displacement rule can be simply tested by plotting the variation of inelastic displacement ratio u_{max}/u_e with T which is shown in Fig. 3.39 for the ground motions employed in Fig. 3.34. The rule is verified for $T > 0.1$ s since the mean u_{max}/u_e ratio roughly approaches unity at longer periods.

Equal displacement rule is employed as a practical tool in displacement-based seismic assessment and design. When it can be assumed that the equal displacement rule holds for ground motions in general, the maximum inelastic displacement of a yielding system can be obtained approximately from the linear elastic displacement response spectrum of its simpler counterpart.

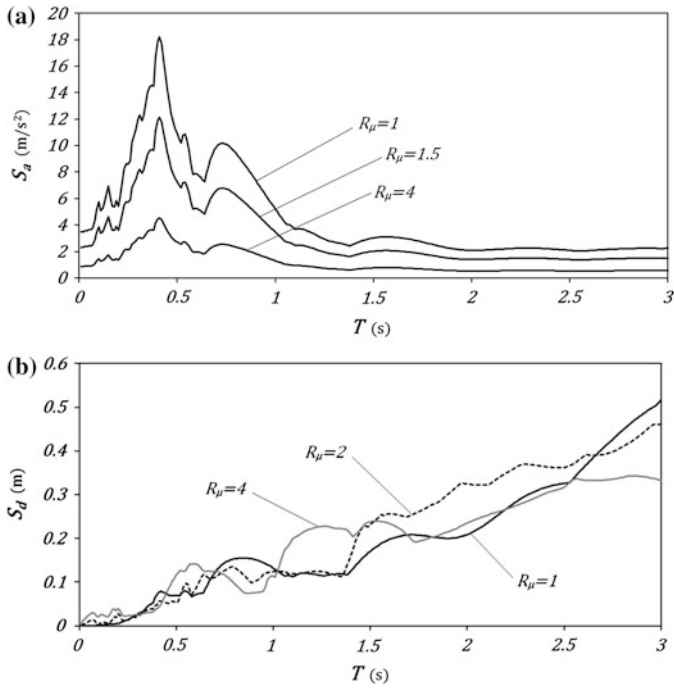


Fig. 3.37 Inelastic acceleration (yield acceleration) and displacement response spectra of the 1999 Düzce NS ground motion component for different R_μ factors

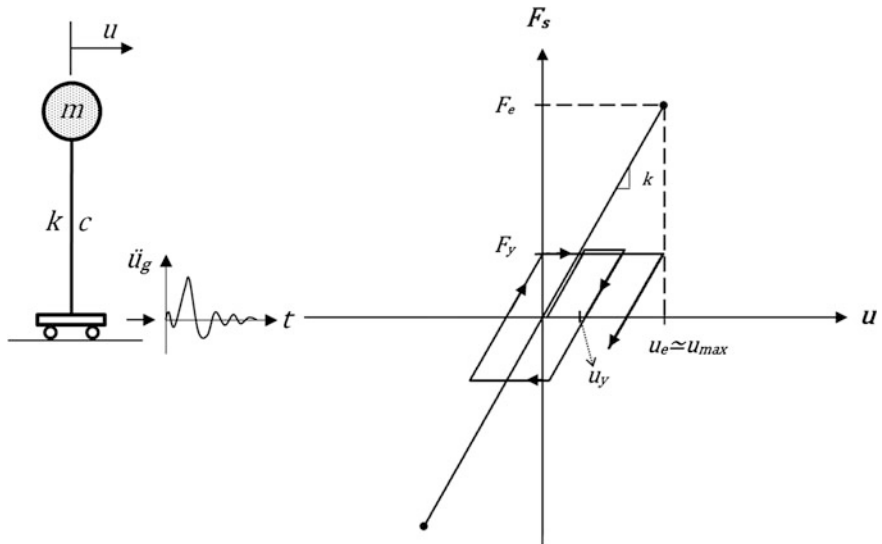
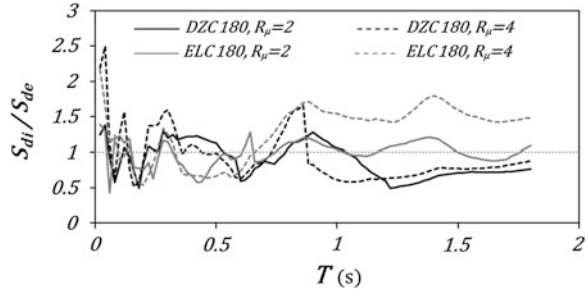


Fig. 3.38 Force-displacement relationships of linear elastic and nonlinear SDOF systems under a ground excitation. $u_e \approx u_{max}$ implies the equal displacement rule

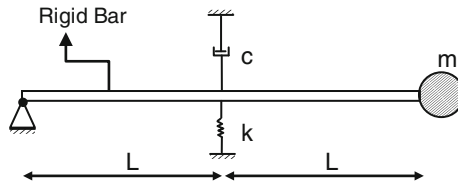
Fig. 3.39 Variation of inelastic-to-elastic maximum displacement ratio with period



Exercises

1. Two strong motion accelerographs are located at neighboring sites, one on stiff soil and the other on soft soil. What are the basic differences in the acceleration records recorded during an earthquake? Sketch them conceptually.
2. What are the basic differences between the acceleration spectra of the two records described in Question 1.
3. Consider the rigid bar assembly given below.
 - (a) Determine the equation of free vibration motion.
 - (b) Determine the undamped free vibration frequency ω_n and period T_n .
 - (c) Solve the equation of motion if the mass is initially displaced to u_0 , and released from rest. Assume $c = 0$.

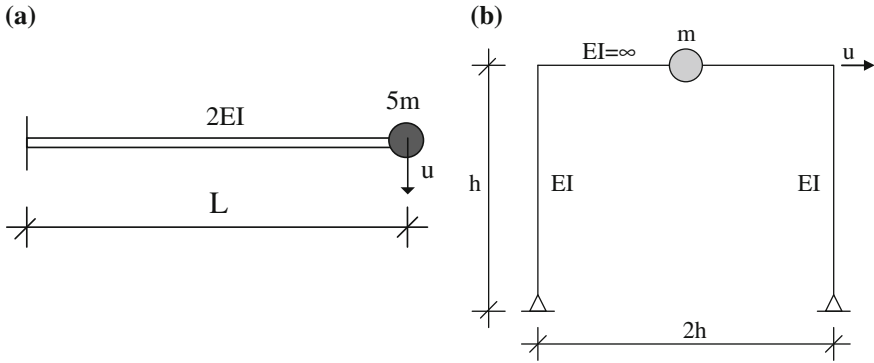
Note: m, c, k, L and u_0 are given.



Answers

- (a) $2m\ddot{u} + \frac{c}{2}\dot{u} + \frac{k}{2}u = 0$ ($2m, \frac{c}{2}$ and $\frac{k}{2}$ are the effective mass, damping and stiffness, respectively) (b) $\omega_n = \frac{1}{2}\sqrt{\frac{k}{m}}$ (c) $u(t) = u_0 \cos \omega_n t$

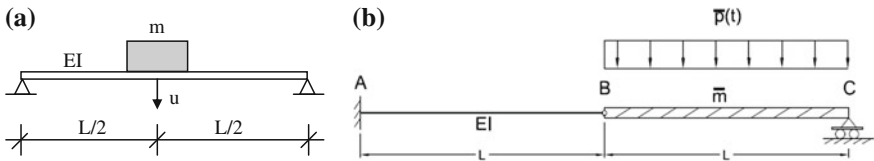
4. Determine the equations of motion for the following systems. Ignore damping and the masses of members.



Answers

(a) $5m\ddot{u} + \frac{6EI}{L^3}u = 0$ (b) $m\ddot{u} + \frac{6EI}{h^3}u = 0$

5. Determine the equations of motion for the following systems. Ignore damping and the masses of the members.



Answers

(a) $m\ddot{u} + \frac{48EI}{L^3}u = 0$ (b) $\frac{\bar{m}L^2}{3}\ddot{u} + \frac{3EI}{L^3}u = \frac{\bar{p}L^2}{2}$ where u is the vertical displacement of B.

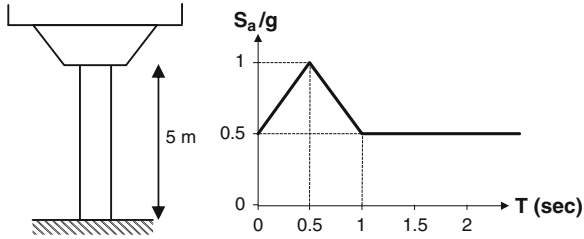
6. An undamped SDOF system with mass m and stiffness k is given. Determine the pseudo acceleration and displacement response spectra if it is subjected to free vibration induced by an initial velocity of $\dot{u}(0) = v_o$ while $u(0) = 0$, where u is the displacement response. Sketch PS_a and S_d versus T .

Answers

$$S_d = \frac{v_o}{2\pi} T \quad PS_a = 2\pi v_o \frac{1}{T}$$

7. A RC bridge pier carries a tributary mass of 100 tons. Mass of the pier is negligible compared to the tributary mass of the deck. It has a solid square section of 1 m x 1 m dimensions. Determine the maximum deflection of the deck, and maximum shear force and bending moment of the pier when it is

subjected to the ground motion with the acceleration spectrum shown. ($E_c = 20 \times 10^6 \text{ kN/m}^2$).



Answers

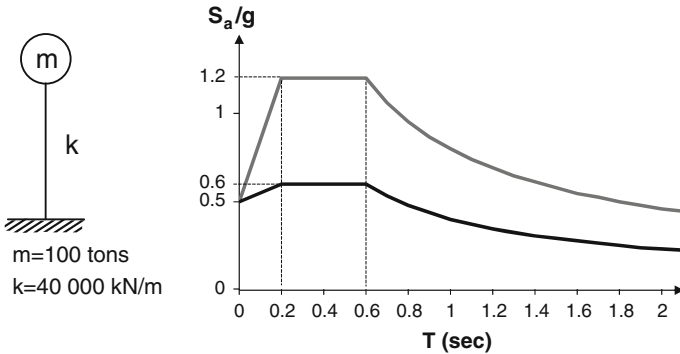
$u_{max} = 0.02 \text{ m}$

$V_{max} = 798.7 \text{ kN}$

$M_{max} = 3993.5 \text{ kN-m}$

8. An SDOF system, and the pair of linear elastic and inelastic acceleration spectra are given below.

- (a) Calculate the maximum elastic force and elastic displacement.
- (b) Calculate the maximum force capacity of the inelastic (elasto-plastic) system, its yield displacement and maximum inelastic displacement if $R_\mu = \mu$ at the period T_n of the SDOF system given.



Answers

$F_e = 1177.2 \text{ kN}$

$u_e = 0.0294 \text{ m}$

$F_y = 588.6 \text{ kN}$

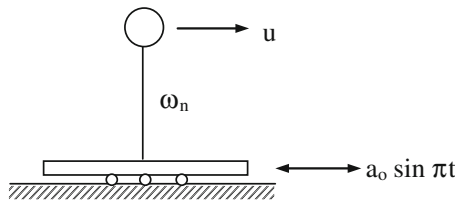
$u_y = 0.0147 \text{ m}$

$u_{max} = 0.0294 \text{ m}$

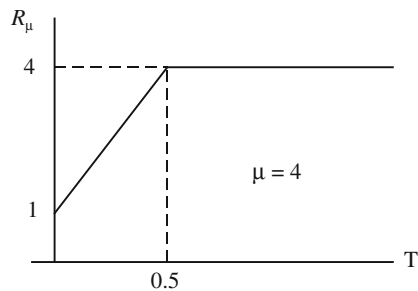
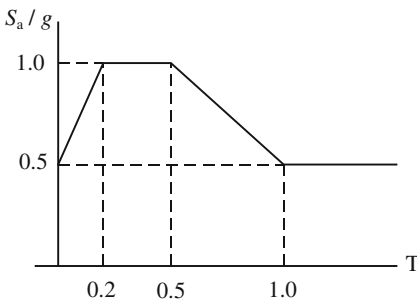
9. Calculate the total acceleration response spectrum for the linear elastic undamped SDOF system given below under the given harmonic base acceleration. Use forced vibration solution only. The vertical axis of the spectrum is the total acceleration (sum of relative acceleration \ddot{u} and the base acceleration) in terms of a_o , and the horizontal axis is the period of vibration T_n . Let $T_n \leq 2$ s and use increments of $\Delta T_n = 0.1$ s in your numerical calculations for plotting the response spectrum graphics.

Answer

$$S_a = \frac{a_0}{1 - (\frac{T}{2})^2}$$



10. An elastic undamped acceleration response spectrum, an elasto-plastic SDOF system and its $R_\mu - \mu - T$ spectrum are given below.
- Calculate the linear elastic displacement spectrum S_d .
 - Calculate the inelastic acceleration spectrum for $\mu = 4$.
 - Calculate the inelastic displacement spectrum for $\mu = 4$.



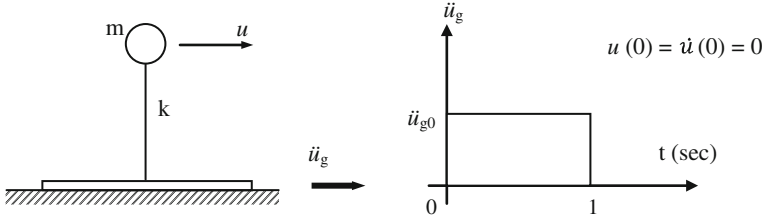
Answers

(a) $S_d = S_a \cdot T^2/39.48$

(b) $S_{ai} = (4.905 + 24.525T)/(1 + 6T)$, $T < 0.2$; $9.81/(1 + 6T)$, $0.2 < T < 0.5$; $3.68 - 2.45T$, $0.5 < T < 1$; 1.226 , $T > 1$.

(c) $S_{di} = S_{ai} \cdot T^2/9.87$

11. Determine the undamped acceleration response spectrum $S_a(T)$ under the ground acceleration pulse shown for $0 \leq T \leq 2$ s.

*Hint*

1. Try $u_p = G$ for particular solution, where G is an arbitrary constant.
2. When $T_n \leq 2$ s, maximum response occurs during the forced vibration phase.

Answer

$$S_a(0) = 2\ddot{u}_{g0}; \quad S_a(2) = 2\ddot{u}_{g0}; \quad S_a(4) = \ddot{u}_{g0}$$

Chapter 4

Earthquake Design Spectra

Abstract This chapter introduces the major concepts implemented in seismic design codes for determining the seismic design forces. Two main code streams are emphasized in the entire chapter. The Eurocode 8 (CEN 2004) and NEHRP provisions together with ASCE 7 standards are discussed to describe their approach for determining the minimum seismic design loads. The first part of the chapter discusses the computation of elastic design spectrum and the rest of the text presents the reduction of elastic design spectrum to inelastic design spectrum with the assumption of expected nonlinear behavior in code-conforming buildings. Example problems that are solved after each major topic reinforce the critical concepts discussed throughout the text.

4.1 Introduction

Major earthquakes with destructive power are less seldom than the other natural hazards such as wind and snow storms or floods that are typically considered in structural design. The challenge in earthquake hazard, however, is its pronounced impact on the built environment. This fact cannot be overlooked and it results in a more serious concern in design practice. Unlike the other natural hazards considered in design, it is generally impractical and uneconomical to proportion structural members to withstand a major earthquake elastically, as discussed in [Chap. 3](#). The structural members are proportioned such that they deform beyond their elastic limits in a controlled manner without endangering the human lives. Moreover, the lateral resisting system must have a robust configuration to provide a stable response against lateral deformation demands without the risk of collapse.

Seismic provisions recommend the structural design and the level of earthquake induced loads by considering the functionality of structural systems. While typical structures (residential buildings) are designed to have a minimal risk of collapse against major earthquakes, other structures, such as hospitals, fire stations and emergency operation centers have to be designed to continue responding to the

needs of the society immediately after the earthquake. Structures that shelter large number of people (schools, theaters, stadiums etc.) require a greater margin of safety in terms of earthquake induced seismic loads. Seismic regulations should also consider the design of non-structural elements (mechanical, electrical and plumbing systems, architectural components) to prevent the loss of system functionality after the earthquake. Modern building regulations provide the means to achieve the above targets so that a reasonable assurance of seismic performance for (a) human life protection (avoiding serious injury and life loss), (b) functional integrity of critical (important) facilities, and (c) cost effectiveness via preventing excessive damage in structural and non-structural components. Building codes for seismic design impose minimum design forces and detailing requirements so that buildings can comply with these performances.

This chapter introduces the fundamental concepts used by seismic provisions for describing the earthquake induced minimum design forces. The NEHRP (Natural Earthquake Hazard Reduction Program) provisions, ASCE 7 (American Society of Civil Engineers—Minimum Design Loads for Buildings and Other Structures) standards and Eurocode 8 (CEN 2004) are used as pillar codes while explaining the key aspects in the computation of seismic design forces. Discussions in [Chap. 3](#) have already indicated that the elastic response spectrum is the primary source of information to define earthquake loads. The amplitudes of design forces are directly related to the seismic activity in the region of interest and it is determined through seismic hazard assessment as discussed in [Chap. 2](#). Thus, this chapter starts with the description of elastic design spectrum by using the concepts covered in [Chaps. 2](#) and [3](#). This part is followed by inelastic design spectrum as structures are expected to sustain a controlled inelastic deformation under design earthquakes.

4.2 Linear Elastic Design Spectrum

The first edition of NEHRP recommended seismic provisions is published in 1985 and it is continuously being updated by incorporating the developments in earthquake engineering in the United States. The NEHRP provisions are now used for evaluating the design standards in the U.S. and convey new knowledge to ASCE 7 as well as the U.S. material design standards. The origins of Eurocode program started in 1975. The European Commission conducted the development of the Eurocodes Programme and the first generation of European codes was released by CEN (Committee for Standardization) in the late 1980s. The European standards provide common structural design rules for everyday use for the design of structures and their components of both traditional and innovative nature. To this end, Eurocode 8 (CEN 2004) sets the minimum standards for earthquake resistant design, and the definition of design ground motions constitutes an important part in this code.

The definition of elastic design spectrum bears on different approaches in Eurocode 8, NEHRP and ASCE codes. The reference (target) return periods as well as the anchoring spectral ordinates for the computation of design spectrum are

the major differences between these standards. The fundamental concepts implemented by these regulations while describing the elastic design spectrum are given in the following sub-sections.

4.2.1 Elastic Design Spectrum Based on Eurocode 8

Eurocode 8 expresses the design seismic action with a reference exceedance probability of 10 % in 50 years that can be modified by the importance factor I depending on the importance classes of structures. Reference peak ground acceleration (PGA) with an exceedance probability of 10 % in 50 years (i.e., mean annual exceedance rate of $\gamma \approx 0.0021$ or 475-year return period) is used to compute reference design seismic action. The importance factor I is described in terms of reference exceedance probability ($P_{LR} = 10\%$) or reference return period ($T_{LR} = 475$ years). Equation (4.1) presents the importance factor relations proposed in Eurocode 8. (This concept is discussed further in the subsequent sections). The variables P_L and T_L refer to target exceedance probability and return period for which the importance factor is calculated. The exponential term k depends on seismicity and its proposed value is 3 in Eurocode 8. These explanations indicate that the importance factor is unity for the reference design seismic action that corresponds to 475-year return period. The designed structure should not experience any local or total collapse under the design seismic action. This objective is called as *no-collapse requirement* in Eurocode 8.

$$I = \left(\frac{P_L}{P_{LR}} \right)^{-1/k} \quad \text{or} \quad I = \left(\frac{T_{LR}}{T_L} \right)^{-1/k}. \quad (4.1)$$

The 5 %-damped Eurocode 8 elastic design spectrum, $S_a(T)$ for horizontal ground motions is given in Eq. (4.2). Expressions in Eq. (4.2) are used for establishing design ground motions in the high-seismicity (Type 1) and low-seismicity (Type 2) regions of Europe. Eurocode 8 suggests using Type 1 spectrum whenever PSHA points the dominance of earthquakes with surface-wave magnitudes (M_s) greater than 5.5. If the contribution to seismic hazard is mostly from $M_s \leq 5.5$ earthquakes, Eurocode 8 implements Type 2 spectrum for the description of design seismic action.

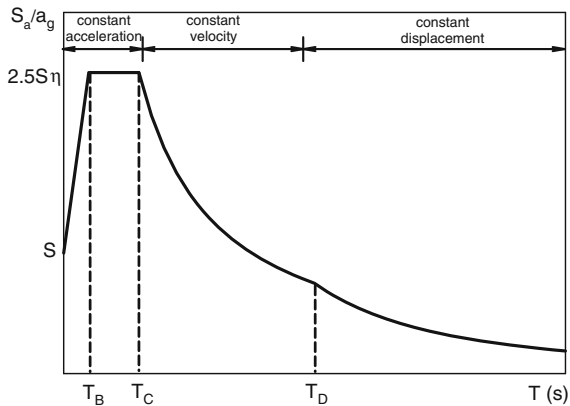
$$\begin{aligned} S_a(T) &= a_g \cdot S \cdot \left[1 + \frac{T}{T_B} (\eta \cdot 2.5 - 1) \right]; & 0 \leq T \leq T_B \\ S_a(T) &= a_g \cdot S \cdot \eta \cdot 2.5; & T_B \leq T \leq T_C \\ S_a(T) &= a_g \cdot S \cdot \eta \cdot 2.5 \cdot \left[\frac{T_C}{T} \right]; & T_C \leq T \leq T_D \\ S_a(T) &= a_g \cdot S \cdot \eta \cdot 2.5 \cdot \left[\frac{T_C \cdot T_D}{T^2} \right]; & T_D \leq T \leq 4.0 \text{ s} \end{aligned} \quad (4.2)$$

Table 4.1 Variation of site factors and corner periods in Eurocode 8 in terms of site class and seismic activity

Site	V_{S30} (m/s) ^a	S		T_B (s)		T_C (s)		T_D (s)	
		Type 1	Type 2	Type 1	Type 2	Type 1	Type 2	Type 1	Type 2
A	>800	1.00	1.00	0.15	0.05	0.40	0.25	2.0	1.2
B	360–800	1.20	1.35	0.15	0.05	0.50	0.25	2.0	1.2
C	180–360	1.15	1.50	0.20	0.10	0.60	0.25	2.0	1.2
D	<180	1.35	1.80	0.20	0.10	0.80	0.30	2.0	1.2
E ^b		1.40	1.60	0.15	0.05	0.50	0.25	2.0	1.2

^a V_{S30} is the average shear-wave velocity in the first 30 m of the soil profile. The V_{S30} intervals given in the table indicate the lower and upper limits for each site class

^b Soil profiles that consist of soft or very soft alluvium layer with a thickness varying between 5 and 20 m underlain by a rock material

Fig. 4.1 Eurocode 8 design spectrum envelope

In Eq. (4.2), a_g is the design PGA for site class A (rock site). a_g accounts for the importance factor, I , according to the classification of structures in Eurocode 8. The corner periods T_B , T_C and T_D delineate the constant-acceleration, constant-velocity and constant-displacement spectral regions. The site factor S modifies the elastic design spectrum for site conditions other than rock. In a similar fashion, η is the so-called damping scaling factor for modifying the 5%-damped spectral ordinates to other damping values. It is unity for 5% damping. The effect of damping on elastic design spectrum is discussed further in Sect. 4.2.3. The corner periods and site factors proposed by Eurocode 8 depend on the soil conditions and seismic activity (Type 1 vs. Type 2) in the region of interest. Table 4.1 lists the values attained by these parameters for the site conditions and seismic activity considered in Eurocode 8. Figure 4.1 shows the design spectrum envelope proposed by Eurocode 8.

The site factors presented in Table 4.1 indicate that Eurocode 8 amplifies the rock (site class A) spectral ordinates with decreasing V_{S30} (i.e., decreasing soil

Table 4.2 Vertical-to-horizontal PGA ratios proposed by Eurocode 8 for establishing the vertical design spectrum (modified from Table 3.4 of Eurocode 8)

Spectrum	a_{vg}/a_g	T_B (s)	T_C (s)	T_D (s)
Type 1	0.90	0.05	0.15	1.0
Type 2	0.45	0.05	0.15	1.0

stiffness). The amplifications are larger for weaker design ground motions (Type 2 vs. Type 1 spectrum). The site factors are constant along the entire spectral band and disregard the period-dependent relation between the nonlinear (hysteretic) soil behavior and ground-motion amplitude. Table 4.1 also suggests smaller corner periods for Type 2 spectrum regardless of site class. This observation indicates that Eurocode 8 accounts for the magnitude influence on the ground-motion frequency content: Long-period ground-motion components become richer with increasing magnitude that yields larger corner periods for Type 1 spectrum. However, the consideration of magnitude influence on the frequency content of ground motions is only limited to a single magnitude boundary that is selected as 5.5 in terms of surface-wave magnitude.

Eurocode 8 elastic design spectrum anchors the spectral ordinates to PGA (i.e., spectral ordinate at $T = 0$ s). The resulting elastic spectrum would fail to represent the uniform hazard spectrum described in Chap. 2 as the annual exceedance rates of spectral ordinates scaled by PGA will be different than that of PGA. This shortcoming would result in ambiguity in the description of seismic design forces because the target exceedance probability for design that is set by Eurocode 8 and the one obtained after establishing the design spectrum will be entirely different.

The vertical design spectrum expressions proposed in Eurocode 8 are given in Eq. (4.3). The format of these expressions is similar to those given in Eq. (4.2). The vertical design spectrum is scaled by vertical PGA (a_{vg}) that is in fact a fraction of the horizontal PGA, a_g . The vertical-to-horizontal PGA ratios are functions of seismicity (Type 1 vs. Type 2 spectrum) and they are given in Table 4.2. Note that the corner periods of vertical design spectrum are shorter with respect to horizontal design spectrum envelopes and they attain the same values for Type 1 and Type 2 spectra.

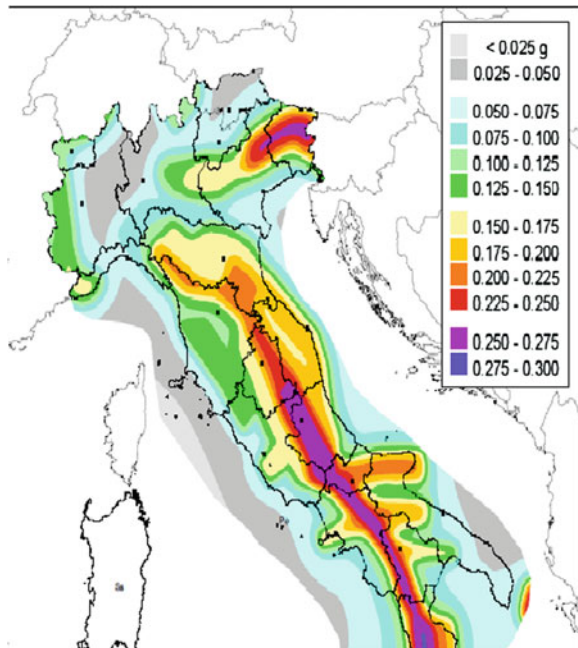
$$\begin{aligned}
 S_{va}(T) &= a_{vg} \cdot \left[1 + \frac{T}{T_B} (\eta \cdot 3.0 - 1) \right]; & 0 \leq T \leq T_B \\
 S_{va}(T) &= a_{vg} \cdot \eta \cdot 3.0; & T_B \leq T \leq T_C \\
 S_{va}(T) &= a_{vg} \cdot \eta \cdot 3.0 \cdot \left[\frac{T_C}{T} \right]; & T_C \leq T \leq T_D \\
 S_{va}(T) &= a_{vg} \cdot \eta \cdot 3.0 \cdot \left[\frac{T_C \cdot T_D}{T^2} \right]; & T_D \leq T \leq 4.0 \text{ s}
 \end{aligned} \tag{4.3}$$

Example 4.1 The structural engineer is supposed to design an office building in Italy. The rock PGA is 0.275 g for 475-year return period that falls into the most seismic prone region as given in Fig. 4.2. The in situ tests suggest a V_{S30} value of 300 m/s for the construction site. The importance factor of the building is defined as $I = 1$ by Eurocode 8. Compute the 5 %-damped horizontal and vertical design spectra to determine the elastic seismic design forces. If the building location is changed to a lesser seismically active seismic zone with $\text{PGA} = 0.1$ g, how would the design spectra change?

Solution

The engineer assumes Type 1 spectrum for the most seismic prone zone in Italy. The V_{S30} value given in the problem indicates that the soil conditions in the project area can be described as site class C according to Eurocode 8 (see Table 4.1). The corner periods of Type 1 spectrum are $T_A = 0.2$ s, $T_B = 0.6$ s and $T_D = 2$ s for site class C (see also Table 4.1). The site factor is $S = 1.15$ and $\eta = 1$ as the design spectrum is computed for 5 % damping.

Fig. 4.2 PGA map of Italy for $T_R = 475$ years (Istituto Nazionale di Geofisica e Vulcanologia)



The change of building location from a high-seismicity region to a low-seismicity region can be taken into account by using Type 2 spectrum in the Eurocode 8 design spectrum. PGA is given as 0.1 g in this case. The site factor S becomes 1.5 whereas corner periods are modified as $T_A = 0.1$ s, $T_B = 0.25$ s and $T_D = 1.2$ s for site class C. The damping scaling factor, η , is still unity for Type 2 spectrum as the calculations are done for 5 % damping.

Figure 4.3 shows the horizontal and vertical design spectra for this problem. The vertical-to-horizontal peak ground acceleration ratios are 0.9 and 0.45 for Type 1 and Type 2 spectra that are used in the computation of vertical design spectra (Table 4.2). The corresponding corner periods are also given in Table 4.2.

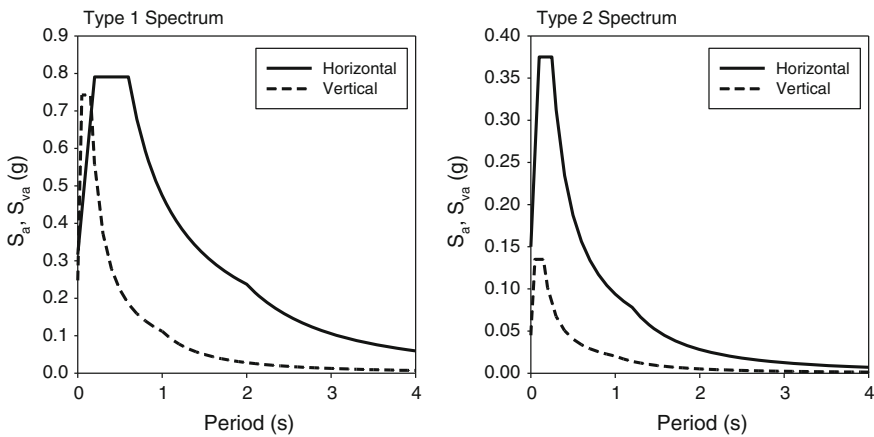


Fig. 4.3 Type 1 (left panel) and Type 2 (right panel) Eurocode 8 spectra for Example 4.1

Example 4.2 Eurocode 8 suggests an importance factor of $I = 1.2$ for the design of school buildings. What is the corresponding return period and exceedance probability in 50 years for design seismic action?

Solution

The first expression in Eq. (4.1) gives the exceedance probability for $I = 1.2$ whereas the second term in the same equation is used to compute the corresponding return period. These calculations are done in the following line by assuming $k = 3$:

$$1.2 = \left(\frac{P_L}{10}\right)^{-1/3} \Rightarrow P_L = 5.787 \% \approx 5.8 \%$$

$$1.2 = \left(\frac{475}{T_L}\right)^{-1/3} \Rightarrow T_L = 870.8 \text{ years} \approx 871 \text{ years}$$

4.2.2 Elastic Design Spectrum Based on NEHRP Provisions and ASCE 7 Standards

NEHRP provisions used PGA maps of 475-year return period (i.e., 10 % exceedance probability in 50 years) for creating the 5 %-damped design spectrum until 1997. The basis of design was to provide life safety under design ground motions. After 1997, the design objective has become avoiding structural collapse under the maximum considered earthquake (MCE) ground motion (BSSC 1997, 2000, 2003). The MCE ground motion, in probabilistic sense, is defined with an exceedance probability of 2 % in 50 years (i.e., 2475-year return period). The corresponding MCE spectrum is described by $T = 0.2$ s and $T = 1.0$ s spectral acceleration ordinates. They are determined from the USGS¹ National Seismic Hazard Mapping project that provides hazard curves for a pre-determined set of spectral acceleration ordinates for a grid of locations and/or polygons for the entire U.S. The spectral acceleration amplitudes at $T = 0.2$ s and $T = 1.0$ s, having 2 % exceedance probability in 50 years are extracted from the corresponding hazard curves. As discussed in Chap. 2, the mean annual exceedance rate for this process is $\gamma \approx 0.0004$ that corresponds to the reciprocal of target return period, $T_R = 2475$ years. The 2475-year spectral accelerations at $T = 0.2$ s and $T = 1.0$ s that are determined from this approach represent a rock site of NEHRP site class B (see Table 4.3 for NEHRP site class definitions). USGS also runs deterministic seismic hazard assessment because the NEHRP provisions (e.g., BSSC 1997, 2000, 2003) as well as ASCE 7 standards (ASCE 1998, 2002, 2005) calculate the MCE ground motion as the lesser of deterministic and probabilistic ground motion. The deterministic MCE ground motion is computed as 150 % of the median spectral acceleration in the aforementioned editions of NEHRP and ASCE 7 provisions. In the 2009 edition of NEHRP provisions (BSSC 2009) and 2010 ASCE 7 standard (i.e., ASCE 7-10; ASCE 2010), deterministic MCE has started to be calculated as median + sigma (84th percentile) spectral acceleration assuming that the spectral acceleration is log-normally distributed. These two seismic codes have also introduced other modifications to the definition of elastic design spectrum and they are discussed later in this section. An illustration of USGS maps used for the computation of MCE spectrum is presented in Fig. 4.4.

The use of spectral acceleration ordinates at $T = 0.2$ s and $T = 1.0$ s has multiple advantages in the computation of MCE spectrum. The soil response changes at short- and long-period spectral ordinates. Softer soil deposits amplify the long-period spectral ordinates of small amplitude motions with respect to bedrock motions. In contrast, soft soil deposits de-amplify short-period spectral ordinates with increasing ground-motion amplitudes due to nonlinear soil behavior. This genuine soil behavior is captured to an extent, by the separate specification of short- ($T = 0.2$ s) and long-period ($T = 1.0$ s) spectral ordinates while

¹ USGS stands for United States Geological Survey.

Table 4.3 NEHRP site class definitions and suggested site amplification factors for spectral accelerations at $T = 0.2$ s (S_S) and $T = 1.0$ s (S_I) of $V_{S30} = 760$ m/s

Site class	Values of site coefficient F_a^a				
	MCE spectral acceleration at $T = 0.2$ s determined from USGS maps of site class B				
	$S_S \leq 0.25$ g	$S_S = 0.50$ g	$S_S = 0.75$ g	$S_S = 1.0$ g	$S_S \geq 1.25$ g
A ($V_{S30} > 1500$ m/s)	0.8	0.8	0.8	0.8	0.8
B (760 m/s $< V_{S30} \leq 1500$ m/s)	1.0	1.0	1.0	1.0	1.0
C (360 m/s $< V_{S30} \leq 760$ m/s)	1.2	1.2	1.1	1.0	1.0
D (180 m/s $< V_{S30} \leq 360$ m/s)	1.6	1.4	1.2	1.1	1.0
E ($V_{S30} < 180$ m/s)	2.5	1.7	1.2	0.9	0.9

Site class	Values of site coefficient F_v^a				
	MCE spectral acceleration at $T = 1.0$ s determined from USGS maps of site class B				
	$S_I \leq 0.10$ g	$S_I = 0.20$ g	$S_I = 0.30$ g	$S_I = 0.40$ g	$S_I \geq 0.50$ g
A ($V_{S30} > 1500$ m/s)	0.8	0.8	0.8	0.8	0.8
B (760 m/s $< V_{S30} \leq 1500$ m/s)	1.0	1.0	1.0	1.0	1.0
C (360 m/s $< V_{S30} \leq 760$ m/s)	1.7	1.6	1.5	1.4	1.3
D (180 m/s $< V_{S30} \leq 360$ m/s)	2.4	2.0	1.8	1.6	1.5
E ($V_{S30} < 180$ m/s)	3.5	3.2	2.8	2.4	2.4

^a Use linear interpolation for intermediate S_S and S_I values for the computation of F_a and F_v

computing the MCE spectrum. Table 4.3 shows the site amplification factors (F_a and F_v) provided by NEHRP provisions for spectral acceleration ordinates of $T = 0.2$ s and $T = 1.0$ s. The site factors vary in terms of site classes and amplitudes of spectral accelerations at rock conditions of NEHRP site class B. It should be noted that the distance-dependent decay rates of short- and long-period spectral ordinates differ from each other. In general, short-period spectral ordinates decay faster than their long-period counterparts with increasing distance. Thus, the use of spectral accelerations at $T = 0.2$ s and $T = 1.0$ s would partially map this effect onto computed MCE spectrum.

The 2003 edition of NEHRP provisions as well as the 2005 ASCE 7 standard (ASCE 7-05; ASCE 2005) proposed a third spectral period that defines the commencement of displacement plateau in MCE. This spectral period (T_L) depends on magnitude and it is given as a separate USGS map in the above codes. Figure 4.5 shows an illustrative map of T_L developed for California. T_L values differ for each seismic region in the US by considering the dominant magnitude distribution.

The computation of elastic design spectrum (S_a) suggested by NEHRP 2003 provisions and ASCE 7 (2005) standard is described in the following expressions:

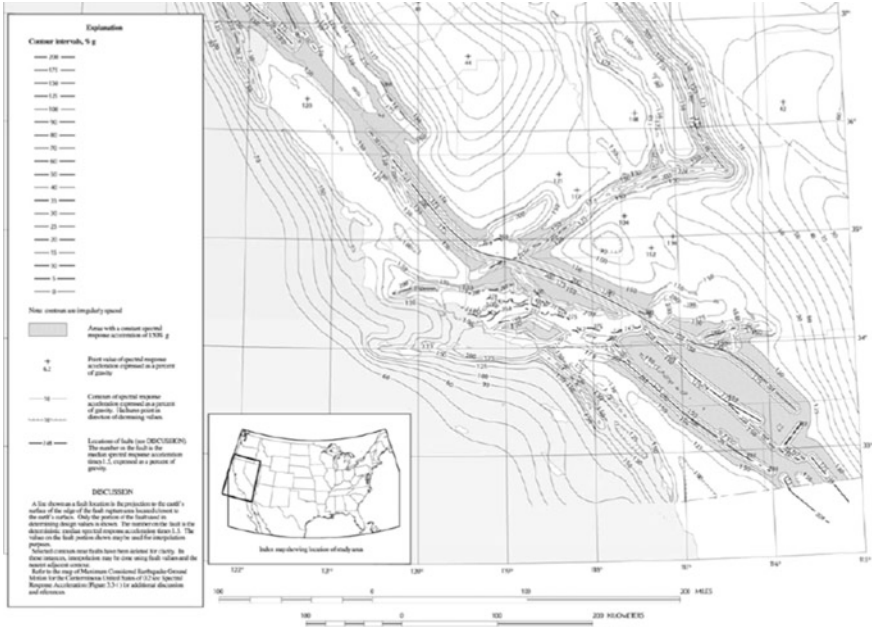


Fig. 4.4 A sample USGS spectral acceleration contour map for $T = 0.2$ s used in the computation of NEHRP (BSSC 2003) and ASCE 7-05 (ASCE 2005) MCE spectrum. Contours are in %g (modified from 2003 NEHRP provisions)

$$\begin{aligned}
 S_{DS} &= \frac{2}{3} S_{MS}; & S_{MS} &= F_a S_S \\
 S_{D1} &= \frac{2}{3} S_{M1}; & S_{M1} &= F_v S_1 \\
 S_a &= 0.6 \frac{S_{DS}}{T_0} T + 0.4 S_{DS}; & T_0 &= 0.2 \frac{S_{D1}}{S_{DS}}; & 0 \leq T \leq T_0 \\
 S_a &= S_{D1}; & T_s &= \frac{S_{D1}}{S_{DS}}; & T_0 < T \leq T_s \\
 S_a &= \frac{S_{D1}}{T}; & T_s < T; & T \leq T_L \\
 S_a &= \frac{S_{D1}}{T}; & T^2 &\leq T_L
 \end{aligned} \tag{4.4}$$

where

- S_S the MCE spectral acceleration at $T = 0.2$ s for NEHRP site class B determined from USGS spectral acceleration maps
- S_1 the MCE spectral acceleration at $T = 1.0$ s for NEHRP site class B determined from USGS spectral acceleration maps
- S_{MS} the MCE spectral acceleration at $T = 0.2$ s modified for the specific NEHRP site class of concern

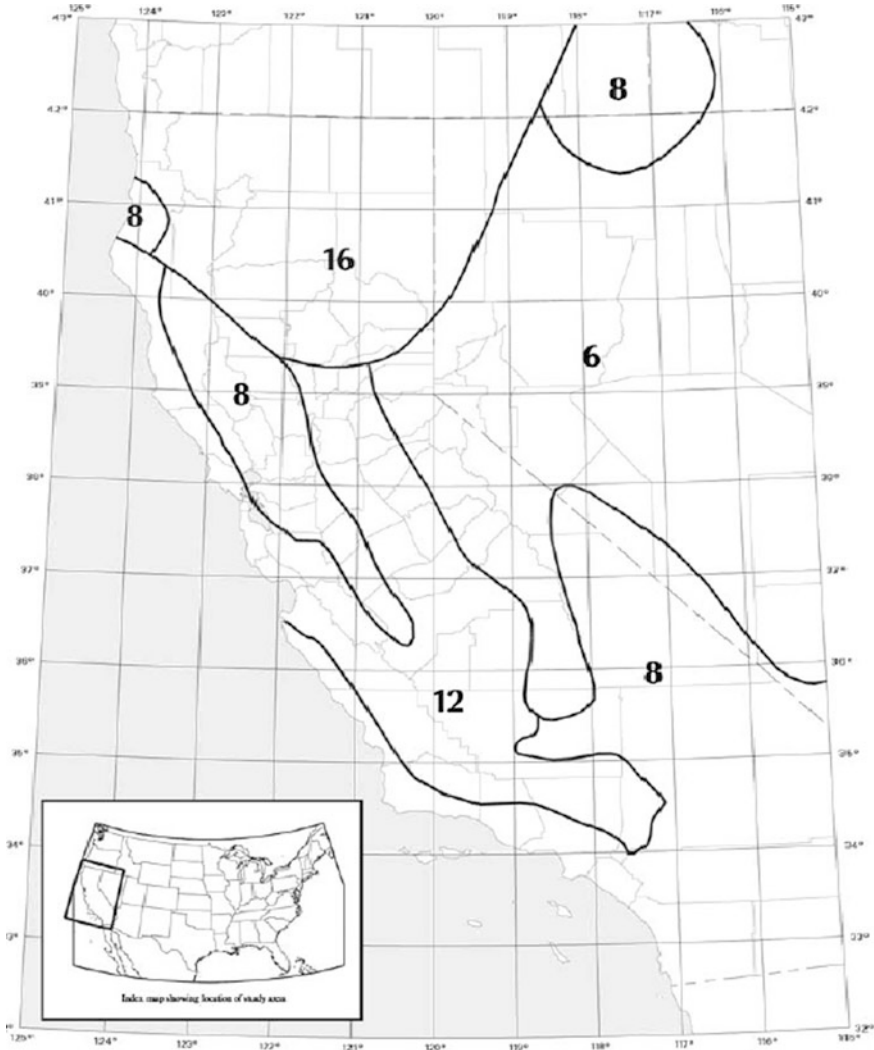
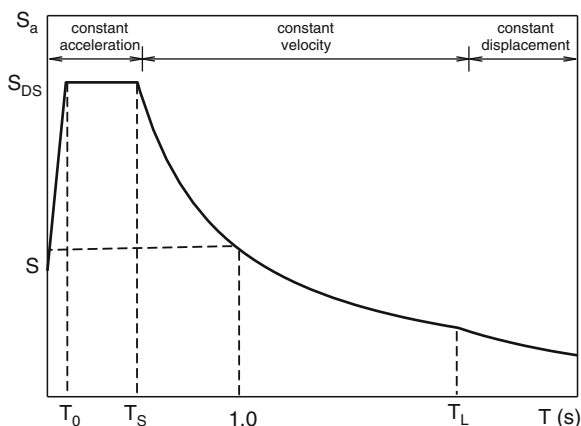


Fig. 4.5 T_L distribution in the conterminous US provided by USGS (modified from 2003 NEHRP provisions)

- S_{MI} the MCE spectral acceleration at $T = 1.0$ s modified for the specific NEHRP site class of concern
- S_{DS} the design spectral acceleration at $T = 0.2$ s
- S_{DI} the design spectral acceleration at $T = 1.0$ s

Figure 4.6 shows the spectral shape of elastic design spectrum computed from the expressions given in Eq. (4.4). T_S and T_L describe the boundaries for constant-acceleration, constant-velocity and constant-displacement spectral regions. Note

Fig. 4.6 Elastic design spectrum shape used in NEHRP and ASCE 7 codes



that the design spectrum is $2/3$ of MCE spectral ordinates. The $2/3$ factor represents the margin of safety against collapse. This concept assumes that buildings designed in accordance with the Code requirements have a safety factor of $3/2$ against collapse. In other words, well-designed buildings can resist a ground shaking that is 1.5 times larger than the design ground motion. Thus, although MCE spectrum is reduced by $2/3$ for design seismic action, the structure is not supposed to collapse under the MCE ground motion.

Consideration of the design earthquake by MCE ground motion is replaced by the risk-targeted maximum considered earthquake (MCE_R) approach in the 2009 version of NEHRP provisions (BSSC 2009) and ASCE 7-10 standards (ASCE 2010). The risk-targeted MCE (MCE_R) considers the probability distribution of ground motions (seismic hazard) and probability of structural failure. The structure is designed by using spectral accelerations that provide a uniform collapse probability of 1 % in 50 years by these codes. This concept is entirely different than the uniform hazard spectrum (UHS) approach implemented in the previous versions of these codes. The risk targeted spectrum accounts for the probabilistic natures of structural response and ground motion whereas UHS merely considers the variability in ground motions. These standards also implement maximum direction of ground motions for design as spectral ordinates of maximum direction is more meaningful in the design process. The use of maximum-direction ground motion in design reduces the probability of structural failure in the direction of the stronger ground-motion component. The other new development in the 2009 edition of NEHRP provisions and ASCE 7-10 is a more transparent consideration of probabilistic and deterministic seismic hazard maps while creating the design spectrum. More specifically, USGS provides the probabilistic and deterministic maps separately for spectral acceleration ordinates at $T = 0.2$ s and $T = 1.0$ s from which the engineer can compute the design spectral ordinates through the procedure described in the following paragraphs.

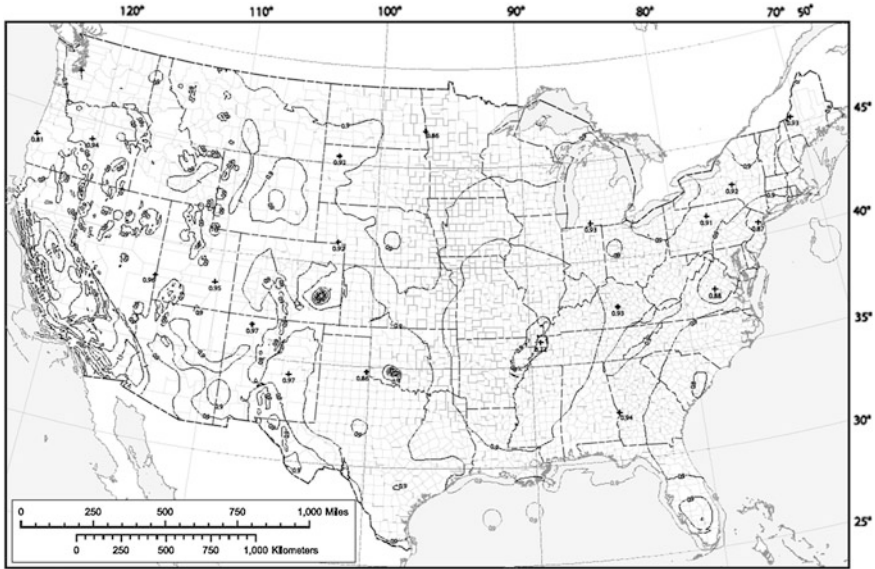


Fig. 4.7 C_{RS} contour map for the conterminous US in the 2009 version of NEHRP provisions. The same map is also used in ASCE 7-10 (ASCE 2010)

There are three steps in determining MCE_R and corresponding design acceleration spectral ordinates in ASCE 7-10 and 2009 NEHRP provisions. The first step considers the probabilistic USGS maps for target risk of structural collapse. The below expressions are used for this purpose

$$S_S = C_{RS}S_{SUH}; \quad S_1 = C_{R1}S_{1UH} \tag{4.5}$$

where

S_{SUH} Mapped uniform-hazard 5 %-damped NEHRP site class B spectral response acceleration at $T = 0.2$ s having an exceedance probability of 2 % in 50 years

S_{1UH} Mapped uniform-hazard 5 %-damped rock NEHRP site class B spectral response acceleration at $T = 1.0$ s having an exceedance probability of 2 % in 50 years

C_{RS} Mapped value of the risk coefficient at $T = 0.2$ s

C_{R1} Mapped value of the risk coefficient at $T = 1.0$ s

S_S Adjusted spectral acceleration at $T = 0.2$ s for NEHRP site class B to achieve risk-targeted design spectrum with 1 % probability of collapse in 50 years

S_1 Adjusted spectral acceleration at $T = 1.0$ s for NEHRP site class B to achieve risk-targeted design spectrum with 1 % probability of collapse in 50 years

Note that S_S and S_1 values determined from Eq. (4.5) represent uniform risk spectral accelerations at $T = 0.2$ s and $T = 1.0$ s, respectively. This is the major modification with respect to the previous editions of NEHRP and ASCE 7 standards. These two parameters correspond to the mapped MCE spectral ordinates in

the previous editions of NEHRP and ASCE 7. The new S_S and S_I spectral accelerations consider the probability of structural failure by modifying the uniform hazard spectral ordinates of USGS with the risk coefficients C_{RS} and C_{RI} . Figure 4.7 illustrates the mapped C_{RS} values for the conterminous US. It should also be noted that the spectral accelerations S_{SUH} and S_{IUH} obtained from USGS maps are modified for maximum direction.

In the second step, the deterministic hazard maps of USGS are used to obtain the deterministic spectral accelerations at $T = 0.2$ s (S_{SD}) and $T = 1.0$ s (S_{ID}). The deterministic spectral ordinates consider the maximum direction and they correspond to 180 % of median ground motion estimates (simplification for median + sigma, 84th percentile spectral acceleration). As in the case of previous NEHRP and ASCE 7 codes, the lesser of deterministic and probabilistic (obtained from first step) spectral ordinates are taken into account for the computation of uniform collapse design spectrum. The choice of lesser spectral ordinates from deterministic and probabilistic hazard is to cap the unreasonably large ground motions in the vicinity of active faults. A sample deterministic USGS contour map used in the computation of S_{SD} is given in Fig. 4.8.

The third step adjusts the short-period ($T = 0.2$ s) and $T = 1.0$ s spectral accelerations for specific site conditions. Site factors F_a and F_v that are given in Table 4.3 for different acceleration levels and site classes modify the final S_S and S_I values that are determined from the probabilistic versus deterministic ground-motion comparisons described in the second step. Equation (4.6) shows the expressions used for this adjustment where S_{MS} and S_{M1} are the short- and long-period site-adjusted and risk-targeted (MCE_R) spectral ordinates, respectively. This step is the same as that in the 2003 versions of NEHRP provisions (BSSC 2003) and ASCE 7-05 (ASCE 2005) except that the resulting spectral accelerations represent MCE_R .

$$S_{MS} = F_a S_S; \quad S_{M1} = F_v S_I \quad (4.6)$$

The design ground motions are 2/3 of MCE_R ground motions. The expressions used in the computation of elastic design spectrum (S_a) are similar to the 2003 NEHRP provisions and ASCE 7-05. They are given in Eq. (4.7) for completeness.

$$\begin{aligned} S_{DS} &= \frac{2}{3} S_{MS}; & S_{D1} &= \frac{2}{3} S_{M1} \\ S_a &= 0.6 \frac{S_{DS}}{T_0} T + 0.4 S_{DS}; & T_0 &= 0.2 \frac{S_{D1}}{S_{DS}}; & 0 \leq T \leq T_0 \\ S_a &= S_{D1}; & T_S &= \frac{S_{D1}}{S_{DS}}; & T_0 < T \leq T_S \\ S_a &= \frac{S_{D1}}{T}; & T_S &< T \leq T_L \\ S_a &= \frac{S_{D1} T_L}{T^2}; & T &> T_L \end{aligned} \quad (4.7)$$



Fig. 4.8 Deterministic USGS contour map for short-period spectral acceleration ($T = 0.2$ s) that is given separately in the 2009 NEHRP provisions and ASCE 7-10. Contours are in %g (modified from the 2009 edition of NEHRP provisions)

The parameters S_{DS} and S_{DI} are uniform-collapse design spectral accelerations at $T = 0.2$ s and $T = 1.0$ s, respectively. The corner periods T_S and T_L separate the constant-acceleration, constant-velocity and constant-displacement spectral ordinates. The long-period transmission period, T_L , is determined from the USGS maps as explained in the computation of 2003 NEHRP and ASCE 7-05 design spectra.

ASCE 7-05 (ASCE 2005) and previous versions of NEHRP provisions describe vertical seismic load effects by a period-independent fraction of horizontal design spectrum. For example, ASCE 7-05 determines vertical seismic force effects as 20 % of short-period design acceleration S_{DS} . This approach carries some similarities with the one implemented in Eurocode 8. The 2009 provisions of NEHRP and ASCE 7-10 (ASCE 2010) abandoned this method and defined a separate

Table 4.4 Vertical-to-horizontal spectral ratios for the computation of vertical design spectrum of the 2009 NEHRP provisions and ASCE 7-10 (ASCE 2010)

MCE _R spectral ordinates at $T = 0.2$ s (S_S) ^a	Site class A, B	Site class C	Site class D, E
$S_S \geq 2.0$ g	0.9	1.3	1.5
$S_S = 1.0$ g	0.9	1.1	1.3
$S_S = 0.6$ g	0.9	1.0	1.1
$S_S = 0.3$ g	0.8	0.8	0.9
$S_S \leq 0.2$ g	0.7	0.7	0.7

^a Use linear interpolation for intermediate S_S values

vertical design spectrum that is analogous to horizontal design spectrum. The vertical design spectrum in these codes uses period-dependent scaling functions that depend on S_{DS} and coefficient C_V representing the vertical-to-horizontal spectral ratio. The coefficient C_V is a function of site class and short-period spectral acceleration S_S that implies its implicit dependency on earthquake magnitude and distance.

The vertical design spectrum S_{va} , is defined for 4 period intervals in the 2009 NEHRP provisions and ASCE 7-10. These expressions are given in Eq. (4.8):

$$\begin{aligned}
 S_{va} &= 0.3C_V S_{DS}; & T \leq 0.025 \text{ s} \\
 S_{va} &= 20C_V S_{DS}(T - 0.025) + 0.3C_V S_{DS}; & 0.025 \text{ s} < T \leq 0.05 \text{ s} \\
 S_{va} &= 0.8C_V S_{DS}; & 0.05 \text{ s} < T \leq 0.15 \text{ s} \\
 S_{va} &= 0.8C_V S_{DS} \left(\frac{0.15}{T} \right)^{0.75} & 0.15 \text{ s} < T \leq 2.0 \text{ s}
 \end{aligned} \tag{4.8}$$

C_V is defined in Table 4.4 in terms of S_S (short period MCE_R at $T = 0.2$ s) and site classes (see Table 4.3 for the description of site classes). The computed vertical spectrum should not be less than one half of the corresponding horizontal design spectrum, S_a . For periods longer than 2 s, the ordinates of vertical design spectrum requires special studies according to the 2009 NEHRP provisions and ASCE 7-10 standard. In any case, one half of the corresponding horizontal spectral ordinates are set as minimum limit for vertical design spectrum of $T > 2$ s.

Example 4.3 For a given site, the short-period ($T = 0.2$ s) and $T = 1$ s MCE spectral accelerations are $S_S = 1.32$ g and $S_I = 0.46$ g according to the USGS contour maps that are provided for the 2003 edition of NEHRP provisions and ASCE 7-05 standard. The site class is NEHRP C according to the V_{S30} value that is measured as 420 m/s in the site. The long-period transition period is $T_L = 6$ s for the given location and it is also determined from the USGS maps. Compute the horizontal design spectrum by following the steps in these codes.

Solution

The given S_S and S_I values represent NEHRP B site conditions and they should be adjusted for NEHRP C. This is done by using F_a and F_v values given in Table 4.3.

S_S value is greater than 1.25 g and Table 4.3 suggests $F_a = 1$ for NEHRP site class C. S_I is between 0.4 and 0.5 g. Linear interpolation is required to compute the F_v value corresponding to $S_I = 0.46$ g. This computation is performed below:

$$F_v = 1.4 + \frac{(1.3 - 1.4)}{(0.5 - 0.4)}(0.46 - 0.4) = 1.34$$

After the computation of F_a and F_v , one can compute the elastic design spectrum for NEHRP 2003 or ASCE 7-05 using Eq. (4.4).

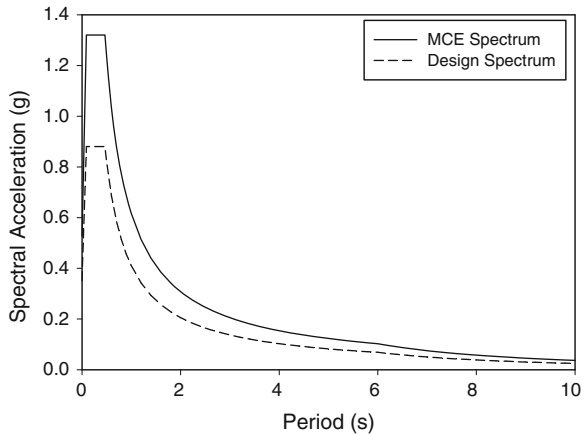
$$S_{MS} = 1.00 \times 1.32 = 1.32 \text{ g}; \quad S_{M1} = 1.34 \times 0.46 = 0.616 \text{ g}$$

$$S_{DS} = \frac{2}{3} \times 1.32 = 0.88 \text{ g}; \quad S_{D1} = \frac{2}{3} \times 0.616 = 0.411 \text{ g}$$

$$T_S = \frac{0.411}{0.88} = 0.467 \text{ s}; \quad T_S = 0.2 \times \frac{0.411}{0.88} = 0.09 \text{ s}$$

The MCE and design spectra for the given site of interest are presented in Fig. 4.9.

Fig. 4.9 MCE and elastic design spectra for the site of interest in Example 4.3



Example 4.4 For the same site in Example 4.3, the short-period ($T = 0.2$ s) and the long-period ($T = 1.0$ s) probabilistic and deterministic spectral acceleration ordinates are given below. They are determined from the updated USGS maps used in the 2009 NEHRP provisions and ASCE 7-10.

$$S_{SUH} = 1.31 \text{ g}$$

$$S_{IUH} = 0.55 \text{ g}$$

$$S_{SD} = 1.50 \text{ g}$$

$$S_{ID} = 0.60 \text{ g}$$

The mapped short-period and $T = 1.0$ s risk coefficients are $C_{RS} = 0.99$ and $C_{RI} = 0.96$, respectively. The long-period transition period is not changed and it is

$T_L = 6$ s for the region of interest. Determine the horizontal MCE_R and design spectra using the approach described in the 2009 NEHRP provisions and ASCE 7-10.

Solution

Following Eq. (4.5) and comparing probabilistic and deterministic spectral ordinates, S_S and S_I are determined as given below in order to create risk-targeted spectrum with 1 % probability of collapse in 50 years:

$$S_S = 0.99 \times 1.31 = 1.30 \text{ g} < 1.5 \text{ g} \quad \Rightarrow \quad S_S = 1.30 \text{ g}$$

$$S_I = 0.96 \times 0.55 = 0.53 \text{ g} < 0.6 \text{ g} \quad \Rightarrow \quad S_I = 0.53 \text{ g}$$

F_a and F_v values can now be determined for adjusting above spectral ordinates for NEHRP C site class. Similar to Example 4.3, Table 4.3 is used for this calculation. Since S_S is greater than 1.25 g, $F_a = 1.0$ for NEHRP C site class. S_I is also greater than 0.5 g and $F_v = 1.3$ according to Table 4.3. Therefore, from Eq. (4.6):

$$S_{MS} = 1.00 \times 1.30 = 1.30 \text{ g}; \quad S_{M1} = 1.30 \times 0.53 = 0.689 \text{ g}$$

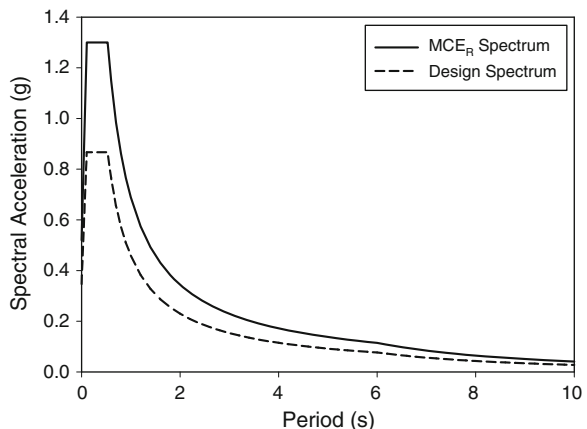
The above values are site class adjusted risk-targeted $T = 0.2$ s (S_{MS}) and $T = 1$ s (S_{M1}) spectral accelerations for 1 % probability of collapse in 50 years. The corresponding spectral ordinates and corner periods for elastic design spectrum are given below by using Eq. (4.7):

$$S_{DS} = \frac{2}{3} \times 1.30 = 0.867 \text{ g}; \quad S_{D1} = \frac{2}{3} \times 0.689 = 0.459 \text{ g}$$

$$T_S = \frac{0.459}{0.867} = 0.529 \text{ s}; \quad T_5 = 0.2 \times \frac{0.459}{0.867} = 0.106 \text{ s}$$

These values are used in the rest of the expressions given in Eq. (4.7) to compute the elastic design spectrum ordinates according to the 2009 edition of NEHRP provisions and ASCE 7-10. Figure 4.10 shows the MCE_R and design spectra for the subject site.

Fig. 4.10 Horizontal MCE_R and design spectra of Example 4.4



Example 4.5 What is the corresponding vertical design spectrum for the site given in Example 4.4. Use the vertical design spectrum equations given in NEHRP 2009 provisions and ASCE 7-10 for consistency with the horizontal elastic design spectrum in Example 4.4.

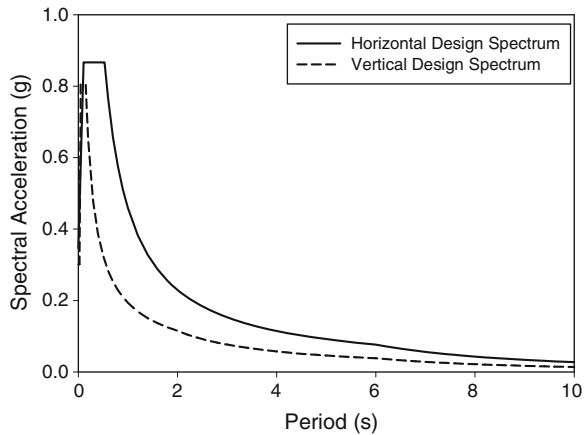
Solution

The computed S_S value is 1.3 g in Example 4.4. The corresponding vertical-to-horizontal spectral ratio, C_V , is 1.16. It is computed from the linear interpolation of NEHRP site class C C_V values listed for $S_S = 1.0$ g and $S_S \geq 2.0$ g. This calculation is shown below:

$$C_V = 1.1 + \frac{(1.3 - 1.1)}{(2.0 - 1.0)}(1.3 - 1.0) = 1.16.$$

The computed C_V and S_{DS} (0.867 g; given in Example 4.4) are inserted into Eq. (4.8) to obtain the vertical design spectrum of the project site in Example 4.4. For periods greater than 2.0 s, one half of the horizontal design spectrum ordinates are used that is imposed as the minimum requirement in the 2009 NEHRP provisions and ASCE 7-10 standard. The vertical design spectrum is given in Fig. 4.11. This figure also shows the horizontal design spectrum of the project site for comparison purposes.

Fig. 4.11 Vertical design spectrum and corresponding horizontal design spectrum for the project site given in Example 4.4



4.2.3 Effect of Damping on Linear Elastic Design Spectrum

The discussions in the previous sections indicate that linear elastic design spectrum in seismic codes is usually defined for a standard viscous damping ratio of 5%. This ratio represents viscous damping in reinforced concrete systems with cracked

Table 4.5 Damping scaling factors provided in the recent NEHRP provisions and ASCE 7 standards

Damping, ξ (%)	Seismically isolated structures	Structures with supplemental damping devices
2	0.8	0.8
5	1.0	1.0
10	1.2	1.2
20	1.5	1.5
30	1.7	1.8
40	1.9	2.1
50	2.0	2.4

sections under gravity loading. Viscous damping ratio however is different in other systems, such as steel, prestressed concrete and masonry (see Table 3.1). Spectral ordinates with different viscous damping are also necessary for designing base isolated buildings and structures with supplemental damping. Eurocode 8 implements Eqs. (4.9) and (4.10) to adjust the 5 %-damped elastic design spectral ordinates for other damping values. In these expressions η is the damping scaling factor for modifying 5 %-damped spectral acceleration ordinates, $S_a(\xi = 5\%)$. ξ represents the target damping value in per cent, and $S_a(\xi)$ is the spectral acceleration ordinate with target damping value ξ .

$$S_a(\xi) = \frac{1}{\eta} S_a(\xi = 5\%) \quad (4.9)$$

$$\eta = \sqrt{\frac{5 + \xi}{10}}. \quad (4.10)$$

The NEHRP (BSSC 2009) provisions and ASCE 7 standards (ASCE 2005, 2009) provide alternative damping scaling factors for buildings of supplemental damping and base isolation. These values are listed in Table 4.5. The reciprocals of the suggested damping scaling factors in Table 4.5 should be multiplied with the 5 %-damped elastic spectral acceleration ordinates to obtain the corresponding spectral accelerations at target damping ξ . This computational phase is already given in Eq. (4.9). The suggested damping scaling factors show some slight variations with respect to those suggested by Eurocode 8 towards higher damping.

4.2.4 Structure Importance Factor (I)

The parameter I , as implemented in Eurocode 8 in Eq. (4.1), is the so-called importance factor that generally takes values between 1 and 1.5 according to the structural system. The structure importance factor I indirectly accounts for the level of risk in design. I is greater than unity for structures that are expected to

perform better against design seismic action. More specifically, the seismic design forces are increased by I if the structural damage is less tolerable against seismic action. Eurocode 8 imposes an importance factor of $I = 1.4$ for emergency facilities (hospitals, fire and police stations, emergency centers, etc.), and $I = 1.2$ for schools, stadiums, theatres, concert halls, power and water stations, etc. with respect to the reference ordinary buildings where $I = 1$. Accordingly, these structures are designed for higher lateral strength, and they are expected to sustain lesser damage under the design earthquake. The associated importance factors in ASCE 7 are 1.5 for emergency facilities and 1.25 for buildings which house large numbers of people, with reference to the ordinary buildings. Both ASCE 7 and Eurocode impose larger importance factors for emergency facilities ($I = 1.4\text{--}1.5$) as they are expected to remain functional after the design earthquake.

Importance factors also reflect the reliability of a structure that is described by the expected target performance under the design ground motion with a given return period. For example, the target performance of an ordinary building ($I = 1$) is “no collapse” under the design ground motion with a return period of 475 years ($T_R = 475$ years) in Eurocode 8. However the target performance of an emergency facility, such as a hospital ($I = 1.5$) is “limited damage”, or continued functionality under the same design ground-motion with $T_R = 475$ years. In fact, this condition approximately corresponds to “no collapse” performance under a design ground motion with a return period of 2475 years ($T_R = 2475$ years). In other words, the linear elastic design spectrum of $T_R = 475$ years approximately corresponds to the linear elastic design spectrum for $T_R = 2475$ years when the latter is divided by $I = 1.5$ in Eurocode 8. This concept is explicitly introduced in Eurocode 8 by providing approximate relationships between importance factor and return period or exceedance probability. These expressions are already given in Eq. (4.1).

4.3 Reduction of Elastic Forces: Inelastic Design Spectrum

We have discussed earlier in Chap. 3 that linear elastic acceleration spectrum, or linear elastic seismic force demands can be reduced if inelastic response is permitted. The reduced inelastic acceleration response spectrum $S_{ai}(T)$ can be directly obtained from the linear elastic acceleration response spectrum $S_a(T)$ through

$$S_{ai}(T) = \frac{S_a(T)}{R_\mu(T)} \quad (4.11)$$

by invoking Eq. (3.65a). R_μ is the ductility reduction factor in the above equation, which was introduced in Sect. 3.6.4. It is a function of both period and the ductility factor (see Figs. 3.35 and 3.36).

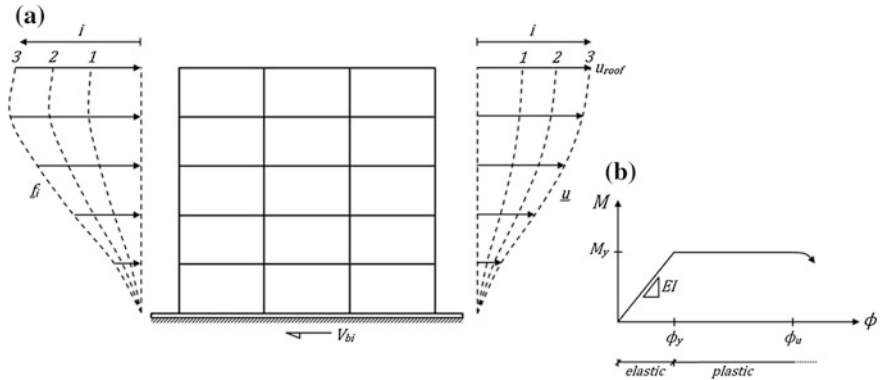


Fig. 4.12 An inelastic frame subjected to increasing static lateral forces (pushover analysis), **a** incremental lateral forces and corresponding incremental lateral displacements; **b** idealized inelastic force-deformation (moment-curvature) characteristics of the yielding member ends

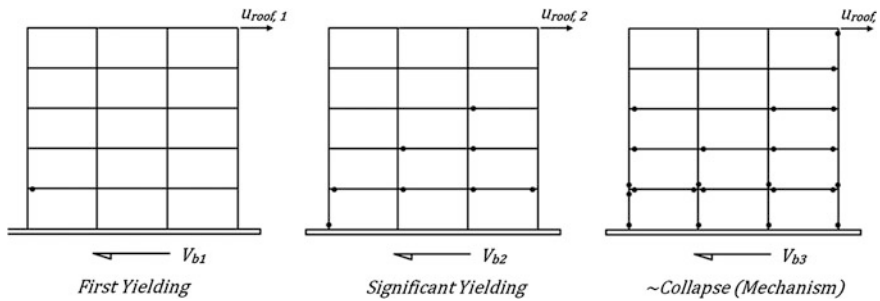


Fig. 4.13 Plastic hinge distribution in an inelastic frame subjected to increasing static lateral forces (pushover analysis) at three different loading states

The force reduction concept of SDOF systems introduced earlier in [Chap. 3](#) can also be applied to the MDOF systems which can be idealized as equivalent SDOF systems. Let's consider a frame in [Fig. 4.12](#) with inelastic deformation capacity, subjected to an increasing lateral force distribution (static pushover analysis, see [Sect. 5.5](#)).

For each force distribution \underline{f}_i , there is a corresponding displacement distribution \underline{u}_i obtained from nonlinear static analysis. The distribution of \underline{f}_i can be taken similar to the distribution of equivalent static first mode force distribution given by [Eq. \(5.50\)](#) with $n = 1$, but applied incrementally in small lateral load steps. The sum of lateral forces in \underline{f}_i is the base shear force V_{bi} where $V_{bi} = \underline{1}^T \cdot \underline{f}_i$, and the roof displacement at top is $u_{roof,i}$ at the i th load step.

When the loading increments are applied progressively on the inelastic structure, internal moments at critical sections will eventually reach their yield capacities as shown in [Fig. 4.13](#) with black dots, and these sections will enter the

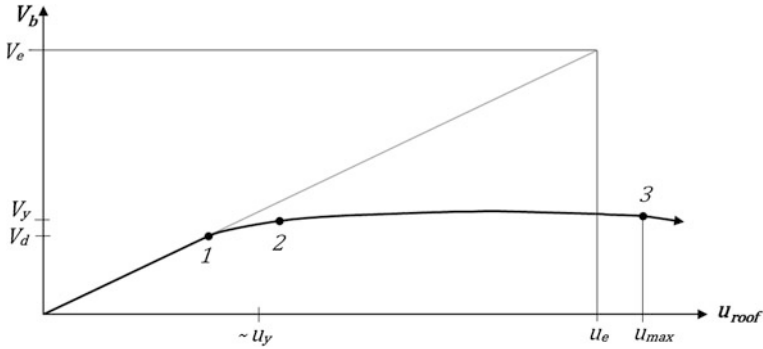


Fig. 4.14 Capacity curve of the inelastic frame obtained from pushover analysis

post-elastic response region. As lateral load increments are further applied, such sections will not be able to develop additional resistance and they redistribute these additional internal forces to other sections while exhibiting plastic deformation. Hence, the number of plastic end regions (plastic hinges) increases with increasing lateral loads, accompanied by the reduction of the overall lateral stiffness of the system. The state of plastic hinge distribution at three different lateral load states is depicted in Fig. 4.13.

If we plot V_b versus u_{roof} , we obtain a capacity curve which resembles the force-displacement relation of an equivalent SDOF inelastic system. Capacity curve for the frame in Fig. 4.13 is shown in Fig. 4.14, and the lateral load states indicated in Fig. 4.8 are also marked on the capacity curve.

Various strength levels are indicated on the capacity curve in Fig. 4.14. V_e is the base shear force demand from linear elastic structure by the earthquake ground motion, which is expressed by a linear elastic spectrum. V_y is the yield base shear force or the base shear capacity whereas V_d is the presumed design base shear of the frame structure.

We may now introduce two ratios among these strength levels.

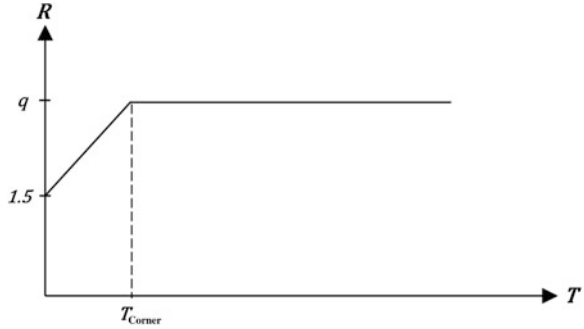
$$\frac{V_e}{V_y} = R_\mu : \quad \text{Ductility reduction factor} \quad (4.12)$$

$$\frac{V_y}{V_d} = R_{ov} : \quad \text{Overstrength reduction factor} \quad (4.13)$$

Ductility reduction factor R_μ in Eq. (4.12) that is defined for an inelastic MDOF system is identical to the ductility reduction factor introduced in Eq. (4.11), and previously introduced in Chap. 3 for an inelastic SDOF system. The similarity between Fig. 4.14 for an inelastic MDOF system and Fig. 3.34 for an ideal inelastic (elasto-plastic) SDOF system is also evident.

The actual yield base shear force (yield strength) V_y of a system that is designed for a design base shear force of V_d , is usually larger than V_d (i.e. $V_y > V_d$) because

Fig. 4.15 Earthquake force reduction factor in Eurocode 8



of the overstrength inherent in design. The overstrength reduction factor R_{ov} describes this deviation from the target strength. Various factors contributing to overstrength are;

- material strength reduction factors ($f_{cd} = \frac{f_{ck}}{\gamma_c}$ for concrete, etc.);
- minimum dimensions;
- minimum reinforcement ratio in RC members;
- minimum strength of materials;
- detailing requirements;
- redundancy (redistribution of internal forces from the yielded to non-yielded members in indeterminate systems).

We can simply combine R_μ and R_{ov} in Eqs. (4.12) and (4.13) into a single reduction factor.

$$R_\mu \times R_{ov} = \frac{V_e}{V_y} \cdot \frac{V_y}{V_d} = \frac{V_e}{V_d} = R \quad (4.14)$$

$R(T)$ is called the *earthquake response reduction factor*. In Eurocode 8, $R(T)$ is denoted by the symbol q called the *behavior factor*, defined by a bi-linear spectral curve shown in Fig. 4.15.

Accordingly, the reduced (inelastic) design spectrum S_{aR} is defined by

$$S_{aR}(T) = \frac{S_{ae}(T)}{R(T)} \quad (4.15)$$

which is similar to Eq. (4.11).

When Fig. 4.15 is compared with Fig. 3.36, we may observe that R represents the ductility capacity for an equivalent inelastic SDOF system, and T_{Corner} is the corner period where equal displacement rule starts to be valid. q factors in Eurocode 8 and R factors in ASCE 7 include both ductility and overstrength as shown in Eq. (4.14).

Response reduction factors are commonly employed in all seismic design codes for approximating the ratio of linear elastic force demand to design strength. They account for the type of structural system and its regularity in elevation. Different response reduction factors are assigned in different national or regional seismic

Table 4.6 Comparison of ASCE R factors and Eurocode q factors for similar structural systems

Structural system	Eurocode 8		ASCE 7	
	DCM	DCH	Intermediate	Special
RC frame	4	6	5	8
RC dual system	4	6	5.5	7
RC coupled wall	3.6	5.4	–	–
Steel frame	4	6.5	4.5	8
Steel frame with diagonal bracing	4	4	–	7
Steel frame with eccentric bracing	4	6	–	8

codes to various building types, depending on the local design and construction practices and seismic response characteristics.

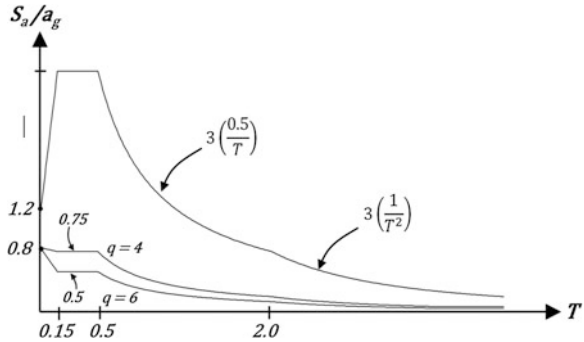
R (or q) factors are described in Eurocode 8 and ASCE 7 for various structural systems and for two different ductility levels; one for ordinary ductility (ductility class *Medium* in EC8 and *Intermediate* in ASCE 7) and the other for enhanced ductility (ductility class *High* in EC8 and *Special* in ASCE 7). These ductility levels are imposed by capacity design requirements in both Codes and they are discussed in the following chapter. A comparison of ASCE R factors and Eurocode 8 q factors for similar structural systems are presented in Table 4.6. These factors are based on judgment and engineering practice as well as experimental and analytical verifications. The difference between the Eurocode 8 q factors and the ASCE 7 R factors is the consequence of regional differences seismic hazard. Seismic intensity levels (PGA or S_a) accommodated in design in the US are higher compared to Europe. Hence larger reduction factors are employed in order to achieve similar economy in design. Lower seismic hazard in Europe permits lower reduction factors while maintaining economy in design. Accordingly seismic damage risk is lower in Europe compared to USA in similar code conforming buildings.

The reduced design spectra in the Eurocode 8 for $q = 4$ (RC frame, Medium ductility) and $q = 6$ (RC frame, High ductility) are shown in Fig. 4.16, together with the linear elastic design spectrum.

4.3.1 Minimum Base Shear Force

Seismic codes generally impose a minimum value for the design base shear force which is effective at long periods and for large response reduction factors. The basic idea behind specifying a minimum base shear force is to provide a minimum lateral resistance for seismic safety. Design base shear forces can practically reduce to very low values for flexible structures with high ductility. As an example, consider a building with a fundamental period of 2 s, designed in Europe for high ductility ($q = 6$), on stiff soil. Its design spectral acceleration can be calculated as $0.125 a_g$. However the minimum spectral acceleration in Eurocode 8

Fig. 4.16 Reduced earthquake design spectra in the Eurocode (2004) for linear elastic ($q = 1$), medium ($q = 4$) and high ductility ($q = 6$) RC frames



is suggested as $0.2 a_g$. Therefore the design spectral acceleration, hence the design base shear force should be increased accordingly.

ASCE 7 directly specifies the minimum design base shear force as 1 % of the building weight ($0.01 W$) for simple analysis procedures (see Sect. 6.7). When more rigorous analysis is employed in design, this minimum value can be reduced by a factor of 0.85 (see Sect. 6.6).

Exercises

1. Discuss the major differences between Eurocode 8 and NEHRP provisions while establishing the horizontal and vertical design spectrum.
2. A residential building will be designed in a highly seismic region. The short-period ($T = 0.2$ s) and $T = 1.0$ s spectral accelerations from probabilistic and deterministic USGS maps are given below:

$$S_{SUH} = 0.86 \text{ g}$$

$$S_{IUH} = 0.34 \text{ g}$$

$$S_{SD} = 0.78 \text{ g}$$

$$S_{ID} = 0.43 \text{ g}$$

The short-period and $T = 1.0$ s risk coefficients are $C_{RS} = 0.93$ and $C_{RI} = 0.83$, respectively for the site of interest. The long-period transition period is read as $T_L = 4$ s.

- (a) Compute the 5 % damped horizontal and vertical design spectra by following the procedure implemented in NEHRP 2009 and ASCE 7-10 codes.
- (b) Use the PGA of horizontal design spectrum computed in part (a) and determine the Eurocode 8 horizontal and vertical design spectra for the same site. (Hint: Assume that the PGA value of part (a) corresponds to 475-year return period).
- (c) Compare the design spectra computed in parts (a) and (b). The comparisons should be done for spectral periods of $T \leq 5.0$ s.

3. An equivalent SDOF system with an effective mass of 100 tons and an effective lateral stiffness of 20,000 kN/m is designed for the linear elastic design spectrum given in the figure, by using a force reduction factor of $R = 4$ and the importance factor $I = 1$. The actual lateral strength of the system is measured as 400 kN after the system is designed. Determine R_μ and R_{ov} .

Answer $R_\mu = 2.45$ and $R_{ov} = 1.63$.

4. An ordinary building with a moment resisting reinforced concrete frame structure for lateral resistance is designed on stiff soil. Determine the design acceleration spectrum if:
- (a) The building is in Naples city center (EC8 Type 1, ductility class “high”).
 - (b) The building is in San Francisco city center (ASCE 7, ductility class “special”).

Chapter 5

Response of Building Frames to Earthquake Ground Motions

Abstract We introduce seismic response analysis for multi degree of freedom building frame systems, particularly for plane frames in this chapter. The equations of motion are first developed for plane frames under external forces and earthquake ground excitation. Static condensation procedure is employed for defining the dynamic degrees of freedom, hence for reducing the total number of degrees of freedom. Then free vibration analysis is conducted leading to natural vibration modes and frequencies. Modal properties are exploited through mode superposition analysis for obtaining dynamic frame response under base excitation. Mode superposition procedure is specialized into the equivalent static response spectrum analysis under modal spectral forces with modal combination rules. Chapter concludes with two special applications, nonlinear static (pushover) analysis and analysis of base isolated buildings.

5.1 Introduction

Plane frames are multi degree of freedom (MDOF) systems where more than one displacement coordinate is necessary for defining the position of the system during motion.

The minimum number of displacement coordinates required to define the deflected shape of a structural system properly at any time t during motion is the number of “degrees of freedom”, DOF. They are the independent coordinates (displacement $u(t)$, rotation $\theta(t)$, etc.) that change with time.

The simplest idealization of MDOF systems are either a mass-spring-damper system connected in series, or a shear frame. A mass-spring-damper system is simply a series of N rigid mass blocks constrained to translate in the horizontal direction only, connected to each other with intermediate springs and dampers. A shear frame on the other hand is a single-bay, N -story frame consisting of flexible columns and dampers in each story with fully rigid girders, where the story masses are assigned to the girders. Since the girders are rigid, there are no rotations at the

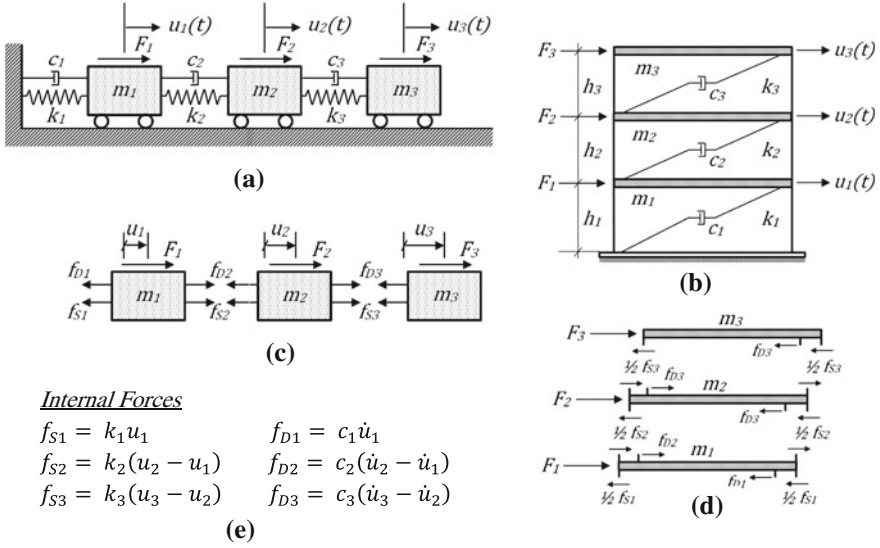


Fig. 5.1 **a** A 3-DOF mass-spring-damper system; **b** a 3-DOF (3 story) shear frame; **c** free body diagrams of the mass blocks; **d** free body diagrams of the rigid girders; **e** internal elastic and damping force expressions

joints and transverse displacements at both ends of a girder are identical. Accordingly only one degree of freedom u_i is sufficient for each story i , which is along the girder where the mass m_i is assigned. Each story i has a total lateral stiffness k_i that is composed of the sum of column shear stiffnesses, i.e. $k_i = \sum 12EI/h_i^3$ in that story.

Two different 3-DOF systems represented with both idealizations are shown in Fig. 5.1. These two idealizations are indeed analogous to each other as verified in the following section where we will develop the equations of motion of the two 3-DOF systems in parallel.

5.2 Equations of Motion Under External Forces

We will assign arbitrary values to u_1, u_2 and u_3 , at time t such that $u_1 < u_2 < u_3$ for brevity. Since all u_i are time dependent, they also have associated values of \dot{u}_i and \ddot{u}_i at time t . The springs k_i in the mass-spring-damper system in Fig. 5.1a, or flexible columns in the shear frame in Fig. 5.1b develop internal elastic forces f_{Si} in relation to the difference of consecutive displacements \ddot{u}_i and \ddot{u}_{i-1} . Similarly, the dampers c_i develop internal damping forces f_{Di} in relation to the difference of consecutive velocities \dot{u}_i and \dot{u}_{i-1} . These internal forces act as the forces of action and reaction with equal magnitude and opposite direction on the masses m_i connected by the associated springs k_i and dampers c_i in Fig. 5.1a and b according to

the Newton's first law. Free-body diagrams of the masses are given in Fig. 5.1c and d for the mass-spring-damper and the shear frame systems respectively, where the internal forces are given in Fig. 5.1e in terms of relative displacements and relative velocities. The equation of motion for each mass m_i can be expressed in the horizontal direction through direct equilibrium by employing Newton's second law $\sum F_x = m\ddot{u}_x$ and force-displacement/velocity relations in Fig. 5.1e.

$$\begin{aligned} m_1 : F_1 - k_1 u_1 + k_2(u_2 - u_1) - c_1 \dot{u}_1 + c_2(\dot{u}_2 - \dot{u}_1) &= m_1 \ddot{u}_1 \\ m_2 : F_2 - k_2(u_2 - u_1) + k_3(u_3 - u_2) - c_2(\dot{u}_2 - \dot{u}_1) + c_3(\dot{u}_3 - \dot{u}_2) &= m_2 \ddot{u}_2 \\ m_3 : F_3 - k_3(u_3 - u_2) - c_3(\dot{u}_3 - \dot{u}_2) &= m_3 \ddot{u}_3 \end{aligned} \quad (5.1)$$

Equation (5.1) can be rearranged and expressed in matrix form.

$$\begin{aligned} \begin{bmatrix} m_1 & 0 & 0 \\ 0 & m_2 & 0 \\ 0 & 0 & m_3 \end{bmatrix} \begin{Bmatrix} \ddot{u}_1 \\ \ddot{u}_2 \\ \ddot{u}_3 \end{Bmatrix} + \begin{bmatrix} c_1 + c_2 & -c_2 & 0 \\ -c_2 & c_2 + c_3 & -c_3 \\ 0 & -c_3 & c_3 \end{bmatrix} \begin{Bmatrix} \dot{u}_1 \\ \dot{u}_2 \\ \dot{u}_3 \end{Bmatrix} \\ + \begin{bmatrix} k_1 + k_2 & -k_2 & 0 \\ -k_2 & k_2 + k_3 & -k_3 \\ 0 & -k_3 & k_3 \end{bmatrix} \begin{Bmatrix} u_1 \\ u_2 \\ u_3 \end{Bmatrix} = \begin{Bmatrix} F_1 \\ F_2 \\ F_3 \end{Bmatrix} \end{aligned} \quad (5.2)$$

or,

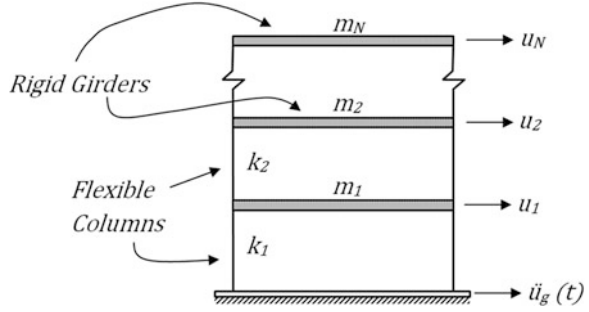
$$\underline{m}\ddot{\underline{u}} + \underline{c}\dot{\underline{u}} + \underline{k}\underline{u} = \underline{F}(t). \quad (5.3)$$

It should be noted that the mass matrix in Eq. (5.2) is indicating no coupling between the story masses. It is a lumped mass matrix where the entire mass of a story is assigned to the associated translational DOF of that story. Moreover, the stiffness matrix in Eq. (5.2) is tri-diagonal, hence the lateral stiffness of a story is coupled with the lateral stiffnesses of the story below and above only (close-coupling). These are the inherent properties of the idealized MDOF systems in Fig. 5.1.

5.3 Equations of Motion Under Earthquake Base Excitation

We will develop the equation of motion of an MDOF system subjected to an earthquake base excitation $\ddot{u}_g(t)$ by employing an N-story shear frame shown in Fig. 5.2. The equation of motion under base excitation has the same form with Eq. (3.5) for a SDOF system, where the scalar displacement variables u, \dot{u} and \ddot{u} for a SDOF system are replaced with the vectorial displacement variables

Fig. 5.2 An N-story shear frame subjected to the ground excitation $\ddot{u}_g(t)$



\underline{u} , $\dot{\underline{u}}$ and $\ddot{\underline{u}}$ for a MDOF system given in Eqs. (5.2) and (5.3). Similarly, the scalar mass, stiffness and damping property terms of a SDOF system are replaced with the associated matrix quantities of a MDOF system defined in Eq. (5.2). Replacement of the scalar quantities in Eq. (3.5) with the vector/matrix quantities in Eq. (5.2) leads to,

$$\underline{m}\ddot{\underline{u}}^{total} + \underline{c}\dot{\underline{u}} + \underline{k}\underline{u} = \underline{0}. \quad (5.4)$$

where

$$\ddot{\underline{u}}^{total} = \ddot{\underline{u}} + \ddot{u}_g \cdot \underline{l} \quad \text{and} \quad \underline{l} = \left\{ \begin{array}{c} 1 \\ 1 \\ \vdots \\ 1 \end{array} \right\}. \quad (5.5)$$

The vector \underline{l} is transmitting the ground displacement u_g to the story DOF's above as rigid body displacements. It is called the *influence vector*. For shear frames, $\underline{l} = \underline{1}$ since a unit displacement at the ground is transmitted equally to all DOF's defined at the stories above.

When $\ddot{\underline{u}}^{total}$ and \underline{l} are substituted from Eq. (5.5) into Eq. (5.4), we obtain,

$$\underline{m}\ddot{\underline{u}} + \underline{c}\dot{\underline{u}} + \underline{k}\underline{u} = -\underline{m}\ddot{u}_g. \quad (5.6)$$

Here,

$$\underline{m} = \begin{bmatrix} m_1 & 0 & \cdots & 0 \\ 0 & m_2 & \cdots & 0 \\ \vdots & \vdots & \ddots & \vdots \\ 0 & 0 & \cdots & m_N \end{bmatrix} \quad (5.7)$$

and

$$\underline{k} = \begin{bmatrix} (k_1 + k_2) & -k_2 & & & & \\ -k_2 & (k_2 + k_3) & -k_3 & & & \\ & & \ddots & & & \\ & & & \ddots & & \\ & & & & -k_{N-1}(k_{N-1} + k_N) & -k_N \\ & & & & -k_N & k_N \end{bmatrix} \quad (5.8)$$

are the mass and stiffness matrices for the N-story shear frame, respectively. Each stiffness coefficient k_i in Eq. (5.8) represents the total lateral stiffness of the i th story that is composed of the column shear stiffnesses as indicated above:

$$k_i = \sum 12 \left(\frac{EI}{h^3} \right)_i. \quad (5.9)$$

The displacement vector is composed of the N lateral story displacements (degrees of freedom).

$$\underline{u}(t) = \begin{Bmatrix} u_1(t) \\ u_2(t) \\ \vdots \\ u_N(t) \end{Bmatrix}. \quad (5.10)$$

There is no analytical method for obtaining the coefficients of the damping matrix \underline{c} in Eq. (5.6) from the damping properties of structural members. There is a practical approach for obtaining the damping matrix of a MDOF system in structural dynamics, called Rayleigh damping. The construction of damping matrix is not required however for linear elastic systems, as explained in the following section.

5.4 Static Condensation

In seismic response analysis, only those degrees of freedom along which inertial forces act are considered in the equations of motion. These degrees of freedom are the ones for which a mass is assigned, and they are called the *dynamic degrees of freedom*. Usually they are the translational degrees of freedom which define the lateral motion of the mass of a floor slab in a building system. The remaining *static degrees of freedom* are necessary for calculating the internal forces under gravity loads, such as the nodal rotations of joints and axial shortening of columns. However they can be eliminated from the dynamic equations of motion by a method called static condensation, which leads to a significantly reduced number of degrees of freedom compared to the original system.

We can eliminate the static degrees of freedom during dynamic analysis by static condensation. Let's define the displacements along dynamic DOF's by \underline{u}_d

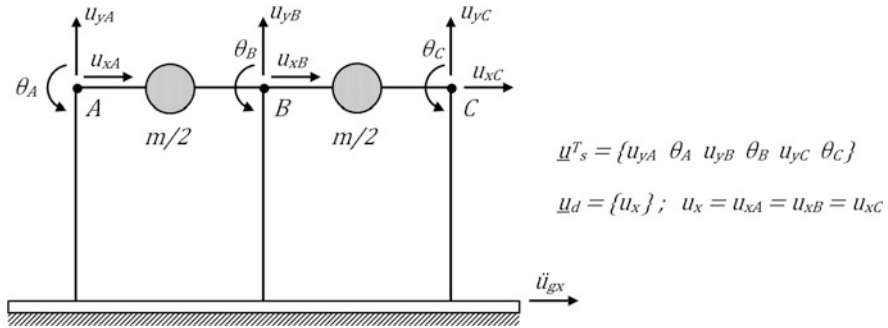


Fig. 5.3 Dynamic and static DOF's of a single story, multi-bay frame

and those along static DOF's by \underline{u}_s . The dynamic and static DOF's of a single story, multi-bay frame with axially rigid girders are sketched in Fig. 5.3.

Accordingly, the vector of inertial forces acting on dynamic DOF's is \underline{f}_d whereas $\underline{f}_s = \underline{0}$ since no dynamic forces act on the static DOF's. Then the stiffness equation between forces and displacements under dynamic excitation becomes,

$$\begin{Bmatrix} \underline{f}_d \\ \underline{0} \end{Bmatrix} = \begin{bmatrix} \underline{k}_{dd} & \underline{k}_{ds} \\ \underline{k}_{sd} & \underline{k}_{ss} \end{bmatrix} \begin{Bmatrix} \underline{u}_d \\ \underline{u}_s \end{Bmatrix}. \quad (5.11)$$

The second row of Eq. (5.11) can be expanded as

$$\underline{k}_{sd}\underline{u}_d + \underline{k}_{ss}\underline{u}_s = \underline{0} \quad (5.12)$$

which yields

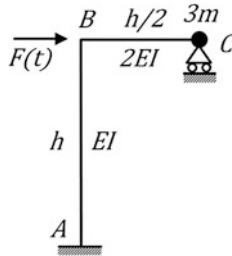
$$\underline{u}_s = -\underline{k}_{ss}^{-1}\underline{k}_{sd}\underline{u}_d. \quad (5.13)$$

Substituting \underline{u}_s from Eq. (5.13) into the first row of Eq. (5.11) gives

$$\underline{f}_d = (\underline{k}_{dd} - \underline{k}_{ds} \cdot \underline{k}_{ss}^{-1} \cdot \underline{k}_{sd})\underline{u}_d \equiv \underline{k}_d\underline{u}_d. \quad (5.14)$$

The term in the parenthesis in Eq. (5.14) is called the *condensed stiffness matrix* \underline{k}_d which has a size equal to the number of dynamic degrees of freedom. Static condensation reduces the size of the matrix equation of motion enormously. The 2D frame in Fig. 5.3 has a total of 9 DOF's whereas it reduces to a 1 DOF system after static condensation.

Example 5.1 The frame ABC is composed of column AB of length h and beam BC of length $h/2$. Column AB and beam BC has no mass whereas a point mass of $3m$ is attached to point C. AB and BC are axially rigid, with flexural rigidities of EI and $2EI$ respectively. Determine the equation of motion.



Solution

This is a 3 DOF system, with rotations θ_B and θ_C , and translation u along BC. The element stiffness matrices of AB and BC can be expressed in terms of the global DOF's.

$$\underline{k}_{AB} = \frac{EI}{h^3} \begin{bmatrix} 12 & 6h \\ 6h & 4h^2 \end{bmatrix}; \quad \underline{u}_{AB} = \begin{Bmatrix} u \\ \theta_B \end{Bmatrix}; \quad \underline{k}_{BC} = \frac{4EI}{h} \begin{bmatrix} 4 & 2 \\ 2 & 4 \end{bmatrix}; \quad \underline{u}_{BC} = \begin{Bmatrix} \theta_B \\ \theta_C \end{Bmatrix}$$

\underline{k}_{AB} and \underline{k}_{BC} can be assembled for the global DOF's to obtain the global stiffness matrix \underline{k} .

$$\underline{k} = \frac{EI}{h} \begin{bmatrix} 12/h^2 & 6/h & 0 \\ 6/h & 20 & 8 \\ 0 & 8 & 16 \end{bmatrix}; \quad \underline{u} = \begin{Bmatrix} u \\ \theta_B \\ \theta_C \end{Bmatrix}.$$

Hence, the equation of motion becomes,

$$\begin{bmatrix} 3m & 0 & 0 \\ 0 & 0 & 0 \\ 0 & 0 & 0 \end{bmatrix} \begin{Bmatrix} \ddot{u} \\ \ddot{\theta}_B \\ \ddot{\theta}_C \end{Bmatrix} + \begin{bmatrix} 12/h^2 & 6/h & 0 \\ 6/h & 20 & 8 \\ 0 & 8 & 16 \end{bmatrix} \begin{Bmatrix} u \\ \theta_B \\ \theta_C \end{Bmatrix} = \begin{Bmatrix} F \\ 0 \\ 0 \end{Bmatrix}.$$

u is the only dynamic degree of freedom whereas θ_B and θ_C are the static degrees of freedom since no mass and external dynamic force are defined along these two rotational degrees of freedom. Applying static condensation by using Eq. (5.14), we obtain the equation of motion for the condensed 1-DOF system.

$$3m \ddot{u} + \frac{39EI}{4h^3} u = F.$$

5.5 Undamped Free Vibration: Eigenvalue Analysis

When the force term on the right-hand-side of Eq. (5.3) or (5.6) is zero and the damping is ignored, we obtain the undamped free vibration equation:

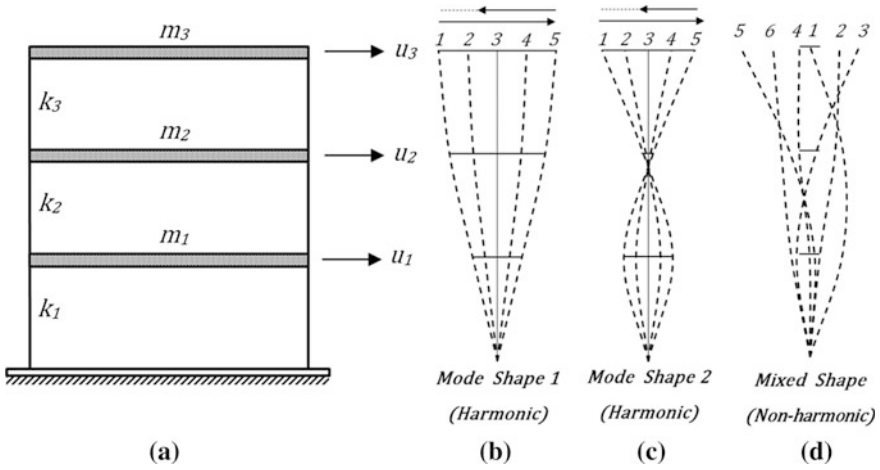


Fig. 5.4 A 3-story shear frame in free vibration: **a** Shear frame properties; **b** and **c** harmonic free vibrations with special initial shapes; **d** non-harmonic free vibration where the initial shape degenerates. Numbers on top indicate time sequence of deflections

$$m\ddot{u} + ku = 0. \tag{5.15}$$

Free vibration can be induced by the initial conditions at $t = 0$.

$$u(0) = u_0; \quad \dot{u}(0) = v_0. \tag{5.16}$$

If we can impose a “special” initial shape u_0 , then we observe harmonic free vibration (simple harmonic motion) with a fixed displacement profile along the height. A fixed profile indicates fixed proportionality of the story displacements with respect to each other. Vibration with a fixed displacement profile is identical to an idealized single degree of freedom response which was previously discussed in Sect. 3.1.2 and shown below in Fig. 5.4b and c. These special displacement profiles are the *natural mode shapes*, and their corresponding harmonic vibration frequencies are the *natural frequencies of vibration*. There are N such mode shapes for an N -DOF system. Typical displacement profiles representing such mode shapes are illustrated in Fig. 5.4b and c for a three story shear frame. When free vibration is induced with a non-special, or general initial displacement shape, then the displacement profile of this initial shape cannot be retained during free vibrations, and a modality does not develop as shown in Fig. 5.4d.

We have to carry out eigenvalue analysis for determining the natural mode shapes and natural vibration frequencies.

5.5.1 Vibration Modes and Frequencies

At a given mode, the displacement vector varies harmonically with time whereas its profile shape remains “fixed”. Then, we can express the modal displacement vector as the product of a harmonic function of time and a shape function.

$$\underline{u}_n(t) = q_n(t) \cdot \underline{\phi}_n. \quad (5.17)$$

Here, $\underline{\phi}_n$ describes the displacement profile along the height, or the mode shape whereas $q_n(t)$ is the time dependent amplitude of this profile. Their product in Eq. (5.17) gives the modal displacement shape for a mode n at any time t during free vibration. This assumption is analogous to the method of “separation of variables” in solving partial differential equations.

Since free vibration motion with a mode shape is harmonic, we can assume a general harmonic function for $q_n(t)$.

$$q_n(t) = A_n \cos \omega_n t + B_n \sin \omega_n t. \quad (5.18)$$

When $q_n(t)$ is substituted from Eq. (5.18) into Eq. (5.17) and the displacement vector in Eq. (5.17) is differentiated twice with respect to time, an expression for acceleration vector is obtained.

$$\underline{\ddot{u}}_n(t) = \ddot{q}_n(t) \cdot \underline{\phi}_n = -\omega_n^2 q_n(t) \cdot \underline{\phi}_n \equiv -\omega_n^2 u_n(t). \quad (5.19)$$

In Eq. (5.19), ω_n^2 and $\underline{\phi}_n$ are the eigenvalue and eigenvector of the n th mode, which have to be determined through an inverse solution procedure. In structural dynamics, ω_n is called the *modal vibration frequency* and $\underline{\phi}_n$ is called the *modal vector*.

Substituting \underline{u} and $\underline{\ddot{u}}$ from Eqs. (5.17) and (5.19) respectively into the equation of free vibration motion (5.15), we obtain

$$\left(-\omega_n^2 \underline{m} \underline{\phi}_n + \underline{k} \underline{\phi}_n \right) q_n(t) = \underline{0}. \quad (5.20)$$

Here, $q_n = 0$ is not an acceptable solution for Eq. (5.20), because it implies no vibration (trivial solution). Therefore,

$$-\omega_n^2 \underline{m} \underline{\phi}_n + \underline{k} \underline{\phi}_n = \underline{0} \quad (5.21a)$$

or

$$\left(\underline{k} - \omega_n^2 \underline{m} \right) \cdot \underline{\phi}_n = \underline{0}. \quad (5.21b)$$

This is a set of N -homogeneous algebraic equations. $\underline{\phi}_n = \underline{0}$ is also a trivial solution (no deformation) for Eq. (5.21a, b). A non-trivial solution is possible only if the determinant of $\left(\underline{k} - \omega_n^2 \underline{m} \right)$ is zero (*Cramer's Rule*):

$$\left| \underline{k} - \omega_n^2 \underline{m} \right| = 0. \quad (5.22)$$

Equation (5.22) is equivalent to an Nth order algebraic equation with N roots. The ω_n^2 values are the roots, or the eigenvalues ($n = 1, 2, \dots, N$). If ω_n^2 is known for a mode n , then we can determine the corresponding shape vector $\underline{\phi}_n$ from Eq. (5.21a, b).

5.5.1.1 Summary

For an N-DOF structural system, there are N pairs of eigenvalues and eigenvectors ($\omega_n^2, \underline{\phi}_n$), $n = 1, 2, \dots, N$. Their values are related to the mass and stiffness properties of the system. The system can vibrate in a simple harmonic motion independently at each mode, with the displacement profile $\underline{\phi}_n$ at the associated angular frequency ω_n .

Example 5.2 Two different 2-DOF systems are given in Fig. 5.5a and b, which are dynamically identical. Determine its eigenvalues and eigenvectors.

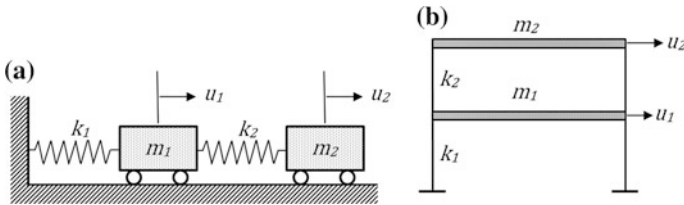


Fig. 5.5 Two different 2-DOF systems which are dynamically identical

Solution

The equation of motion for free vibration, from Eq. (5.15), can be written as

$$\begin{bmatrix} m_1 & 0 \\ 0 & m_2 \end{bmatrix} \begin{Bmatrix} \ddot{u}_1 \\ \ddot{u}_2 \end{Bmatrix} + \begin{bmatrix} k_1 + k_2 & -k_2 \\ -k_2 & k_2 \end{bmatrix} \begin{Bmatrix} u_1 \\ u_2 \end{Bmatrix} = \begin{Bmatrix} 0 \\ 0 \end{Bmatrix}. \quad (1)$$

Then Eq. (5.22) is applied to the given problem.

$$\det(\underline{k} - \omega_n^2 \underline{m}) = \begin{vmatrix} (k_1 + k_2 - \omega_n^2 m_1) & -k_2 \\ -k_2 & k_2 - \omega_n^2 m_2 \end{vmatrix} = 0. \quad (2)$$

A closed form solution cannot be obtained from Eq. (2). This is possible however if we make a simplification in the parameters. Let $k_1 = k_2 = k$, and $m_1 = m_2 = m$. Then Eq. (3) can be obtained from Eq. (2), which is called the *characteristic equation*.

$$\omega_n^4 - 3 \frac{k}{m} \omega_n^2 + \left(\frac{k}{m}\right)^2 = 0 \quad (3)$$

Equation (3) is a quadratic algebraic equation in ω_n^2 where $n = 1, 2$. The roots of the quadratic equation are ω_1^2 and ω_2^2 , which are the eigenvalues (note that the roots are not ω_1 and ω_2). Solution of Eq. (3) yields the following roots:

$$\omega_1^2 = \frac{3 - \sqrt{5} k}{2} \frac{k}{m} \quad \rightarrow \quad \omega_1 = 0.618 \sqrt{\frac{k}{m}} \quad (4)$$

$$\omega_2^2 = \frac{3 + \sqrt{5} k}{2} \frac{k}{m} \quad \rightarrow \quad \omega_2 = 1.618 \sqrt{\frac{k}{m}}. \quad (5)$$

The eigenvectors will be determined from Eq. (5.21b). For the given problem,

$$\begin{bmatrix} (2k - \omega_n^2 m) & -k \\ -k & k - \omega_n^2 m \end{bmatrix} \begin{Bmatrix} \phi_{n1} \\ \phi_{n2} \end{Bmatrix} = \begin{Bmatrix} 0 \\ 0 \end{Bmatrix}; \quad n = 1, 2 \quad (6)$$

$$\text{From row 1 :} \quad (2k - \omega_n^2 m) \phi_{n1} - k \phi_{n2} = 0 \quad (7)$$

$$\text{From row 2 :} \quad -k \phi_{n1} + (k - \omega_n^2 m) \phi_{n2} = 0. \quad (8)$$

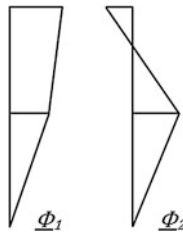
We cannot find a unique solution for ϕ_{n1} and ϕ_{n2} from Eqs. (7) and (8) because they are a set of homogeneous equations. We can rather express ϕ_{n2} in terms of ϕ_{n1} for both $n = 1$ and $n = 2$.

$$\phi_{n2} = \frac{2k - \omega_n^2 m}{k} \phi_{n1}. \quad (9)$$

Let $\phi_{11} = 1$ in Eq. (9) for $n = 1$. Then we substitute ω_1^2 into Eq. (9) and determine $\phi_{12} = 1.618$. Next, let $\phi_{21} = 1$. Then we substitute ω_2^2 into Eq. (9) and determine $\phi_{22} = -0.618$. Accordingly, the modal vectors, or the eigenvectors for the two modes are determined as,

$$\underline{\phi}_1 = \begin{Bmatrix} 1.0 \\ 1.618 \end{Bmatrix}; \quad \underline{\phi}_2 = \begin{Bmatrix} 1.0 \\ -0.618 \end{Bmatrix}. \quad (10)$$

The mode shapes for the 2DOF system in Fig. 5.5b are plotted below.



Example 5.3 Identify the degrees of freedom of the system given in Fig. 5.6a. Then determine its eigenvalues and eigenvectors.

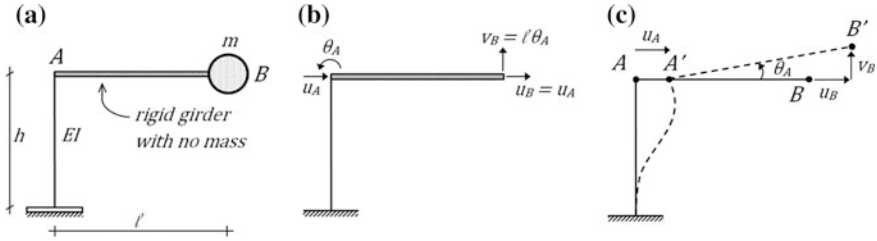


Fig. 5.6 2 DOF System

Solution

The frame has 2 DOF's, which are defined at the top end A of the cantilever column and shown in Fig. 5.6b. Although this is correct and consistent for static analysis, we have to transfer these DOF's to point B for dynamic analysis since the point mass is assigned to the B end of the rigid girder. The original (u_A, θ_A) and the transformed (new) degrees of freedom (u_B, v_B) are shown in Fig. 5.6b. Note that these two sets of DOF's are dependent since $u_B = u_A$ (rigid body translation of AB) and $v_B = l\theta_A$ (rigid body rotation of AB). The kinematic relations between (u_B, v_B) and (u_A, θ_A) are sketched in Fig. 5.6c.

The stiffness equations for the first and second set of DOF's can be written as (determine as an exercise),

$$\begin{bmatrix} F_{hA} \\ M_A \end{bmatrix} = \frac{EI}{h} \begin{bmatrix} \frac{12}{h^2} & \frac{6}{h} \\ \frac{6}{h} & 4 \end{bmatrix} \begin{bmatrix} u_A \\ \theta_A \end{bmatrix} \quad \text{and} \quad \begin{bmatrix} F_{hB} \\ F_{vB} \end{bmatrix} = \frac{EI}{h} \begin{bmatrix} \frac{12}{h^2} & \frac{6}{hl} \\ \frac{6}{hl} & \frac{4}{l^2} \end{bmatrix} \begin{bmatrix} u_B \\ v_B \end{bmatrix}. \quad (1a, b)$$

Then the mass and stiffness matrices for the second set of DOF's are,

$$\underline{m} = \begin{bmatrix} m & 0 \\ 0 & m \end{bmatrix} \quad \underline{k} = \frac{EI}{h} \begin{bmatrix} \frac{12}{h^2} & \frac{6}{hl} \\ \frac{6}{hl} & \frac{4}{l^2} \end{bmatrix}. \quad (2a, b)$$

Let's assume $l = h$ for simplicity. Then $\det(\underline{k} - \omega_n^2 \underline{m}) = 0$ gives,

$$m^2 \lambda_n^2 - \frac{16EI}{h^3} m \lambda_n + \frac{12(EI)^2}{h^6}. \quad (3)$$

In Eq. (3), $\lambda_n = \omega_n^2$. The two roots of the quadratic Eq. (3) can be determined as

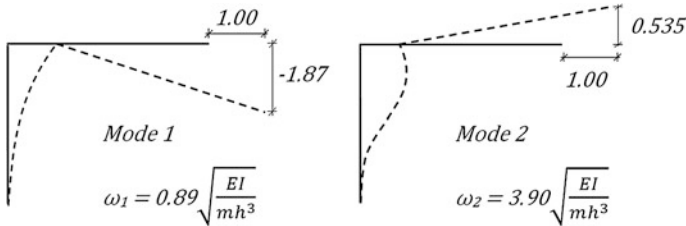
$$\lambda_1 \equiv \omega_1^2 = 0.789 \left(\frac{EI}{mh^3} \right) \quad \text{and} \quad \lambda_2 \equiv \omega_2^2 = 15.211 \left(\frac{EI}{mh^3} \right).$$

Substituting ω_1^2 and ω_2^2 into Eq. (5.21a, b) and solving the homogeneous set of linear equations, we can obtain the two eigenvectors.

$$n = 1 : \phi_{11} = 1; \quad \phi_{12} = -1.869$$

$$n = 2 : \phi_{21} = 1; \quad \phi_{22} = 0.535$$

The mode shapes are sketched below.



5.5.2 Normalization of Modal Vectors

Let $\underline{\phi}_n^T m \underline{\phi}_n = M_n$ where M_n is called the n th modal mass. If we divide $\underline{\phi}_n$ by $\sqrt{M_n}$; then

$$\frac{1}{\sqrt{M_n}} \underline{\phi}_n^T m \frac{1}{\sqrt{M_n}} \underline{\phi}_n = 1. \tag{5.23}$$

The scaled modal vector $\left(\frac{1}{\sqrt{M_n}} \underline{\phi}_n\right)$ is now normalized with respect to the modal mass M_n . This is practical in numerical applications because it reduces the amount of arithmetical computations. Most of the computational software directly calculates mass normalized modal vectors in earthquake engineering practice.

Example 5.4 Consider Example 5.2. Calculate the mass normalized modal vectors.

$$M_1 = \{ 1.0 \quad 1.618 \} \begin{bmatrix} m & 0 \\ 0 & m \end{bmatrix} \begin{Bmatrix} 1.0 \\ 1.618 \end{Bmatrix} = 3.618m$$

$$M_2 = \{ 1.0 \quad -0.618 \} \begin{bmatrix} m & 0 \\ 0 & m \end{bmatrix} \begin{Bmatrix} 1.0 \\ -0.618 \end{Bmatrix} = 1.382m$$

The mass parameter m can be neglected in both M_n terms since m is arbitrary. Then,

$$\underline{\phi}_1 = \frac{1}{\sqrt{3.618}} \begin{Bmatrix} 1.0 \\ 1.618 \end{Bmatrix} = \begin{Bmatrix} 0.526 \\ 0.851 \end{Bmatrix} \text{ and}$$

$$\underline{\phi}_2 = \frac{1}{\sqrt{1.382}} \begin{Bmatrix} 1.0 \\ -0.618 \end{Bmatrix} = \begin{Bmatrix} 0.851 \\ -0.576 \end{Bmatrix}$$

are the normalized modal vectors. It can be verified that the normalized modal vectors satisfy

$$\underline{\phi}_1^T \underline{m} \underline{\phi}_1 = 1 \quad \text{and} \quad \underline{\phi}_2^T \underline{m} \underline{\phi}_2 = 1.$$

Hence, $M_n = 1$ for both mass-normalized modal vectors.

5.5.3 Orthogonality of Modal Vectors

Let's consider two modes n and m , with $(\omega_n^2, \underline{\phi}_n)$ and $(\omega_m^2, \underline{\phi}_m)$. From Eq. (5.21a),

$$\underline{k} \underline{\phi}_n = \omega_n^2 \underline{m} \underline{\phi}_n \quad (5.24a)$$

and

$$\underline{k} \underline{\phi}_m = \omega_m^2 \underline{m} \underline{\phi}_m. \quad (5.24b)$$

Pre-multiplying Eq. (5.24a) with $\underline{\phi}_m^T$ and Eq. (5.24b) with $\underline{\phi}_n^T$ respectively,

$$\underline{\phi}_m^T \underline{k} \underline{\phi}_n = \omega_n^2 \underline{\phi}_m^T \underline{m} \underline{\phi}_n \quad (5.25a)$$

and

$$\underline{\phi}_n^T \underline{k} \underline{\phi}_m = \omega_m^2 \underline{\phi}_n^T \underline{m} \underline{\phi}_m. \quad (5.25b)$$

Now, transposing both sides of Eq. (5.25b) and considering that $\underline{k}^T = \underline{k}$ and $\underline{m}^T = \underline{m}$ due to the symmetry of both matrices,

$$\underline{\phi}_m^T \underline{k} \underline{\phi}_n = \omega_m^2 \underline{\phi}_m^T \underline{m} \underline{\phi}_n. \quad (5.26)$$

Finally, subtracting Eq. (5.26) from Eq. (5.24a),

$$0 = (\omega_n^2 - \omega_m^2) \underline{\phi}_m^T \underline{m} \underline{\phi}_n. \quad (5.27)$$

Since $\omega_n^2 \neq \omega_m^2$ in general,

$$\underline{\phi}_m^T \underline{m} \underline{\phi}_n = 0. \quad (5.28)$$

This is the condition of orthogonality of modal vectors with respect to the mass matrix. A similar orthogonality condition with respect to the stiffness matrix follows from Eq. (5.26).

$$\underline{\phi}_m^T \underline{k} \underline{\phi}_n = 0. \quad (5.29)$$

Therefore modal vectors are orthogonal with respect to \underline{m} and \underline{k} .

Example 5.5 Consider Example 5.2. Verify orthogonality of modal vectors with respect to the mass matrix.

Solution

$$\underline{\phi}_1^T \underline{m} \underline{\phi}_2 = \{1.0 \quad 1.618\} \begin{bmatrix} m & 0 \\ 0 & m \end{bmatrix} \begin{Bmatrix} 1.0 \\ -0.618 \end{Bmatrix} = 0.$$

A similar orthogonality condition can also be verified for Example 5.3.

5.5.4 Modal Expansion of Displacements

Any displacement vector $\underline{u}(t)$ can be expressed as a linear combination of the orthogonal modal vectors $\underline{\phi}_n$:

$$\underline{u}(t) = q_1(t)\underline{\phi}_1 + q_2(t)\underline{\phi}_2 + \cdots + q_N(t)\underline{\phi}_N. \quad (5.30)$$

This equation implies that $\underline{\phi}_n$ ($n = 1, 2, \dots, N$) constitute an N -dimensional vector space where any arbitrary vector \underline{u} can be expressed as a linear combination of $\underline{\phi}_n$. The $q_n(t)$ terms in Eq. (5.30) are the modal amplitudes, or modal coordinates.

For a set of $\underline{\phi}_n$, we can determine q_n by employing the orthogonality property of modal vectors. Let's pre-multiply all terms in Eq. (5.30) by $\underline{\phi}_n^T \underline{m}$.

$$\underline{\phi}_n^T \underline{m} \underline{u} = q_1 \left(\underline{\phi}_n^T \underline{m} \underline{\phi}_1 \right) + \cdots + q_n \left(\underline{\phi}_n^T \underline{m} \underline{\phi}_n \right) + \cdots + q_N \left(\underline{\phi}_n^T \underline{m} \underline{\phi}_N \right). \quad (5.31)$$

All parentheses terms are zero due to modal orthogonality with respect to mass, except the $\left(\underline{\phi}_n^T \underline{m} \underline{\phi}_n \right)$ term. Then,

$$q_n(t) = \frac{\underline{\phi}_n^T \underline{m} \underline{u}}{\underline{\phi}_n^T \underline{m} \underline{\phi}_n}. \quad (5.32)$$

The denominator term is equal to 1 if the modes are mass normalized.

Example 5.6 Determine the modal expansion of $\underline{u} = \begin{Bmatrix} 1 \\ 1 \end{Bmatrix}$ in terms of the modal vectors determined in Example 5.4.

Solution

$$q_1 = \underline{\phi}_1^T \underline{m} \underline{u} = \{0.526 \quad 0.851\} \begin{bmatrix} 1 & 0 \\ 0 & 1 \end{bmatrix} \begin{Bmatrix} 1 \\ 1 \end{Bmatrix} = 1.377$$

$$q_2 = \underline{\phi}_2^T \underline{m} \underline{u} = 0.325.$$

Substituting into Eq. (5.30),

$$\underline{u} = 1.377 \begin{Bmatrix} 0.526 \\ 0.851 \end{Bmatrix} + 0.325 \begin{Bmatrix} 0.851 \\ -0.526 \end{Bmatrix} \equiv \begin{Bmatrix} 1.0 \\ 1.0 \end{Bmatrix}.$$

5.6 Solution of Equation of Motion Under Earthquake Excitation

We will reconsider the equation of motion of a MDOF system that was expressed by Eq. (5.6).

$$\underline{m}\ddot{\underline{u}} + \underline{c}\dot{\underline{u}} + \underline{k}\underline{u} = \underline{m}\underline{l}\ddot{u}_g(t). \quad (5.6)$$

\underline{u} can be expanded in terms of modal vectors by using Eq. (5.30).

$$\underline{u}(t) = \sum_{r=1}^N \underline{\phi}_r q_r(t). \quad (5.33)$$

Substituting $\underline{u}(t)$ from Eq. (5.33) into Eq. (5.6) and calculating the appropriate time derivatives in Eq. (5.6), we obtain

$$\sum_r \underline{m} \underline{\phi}_r \ddot{q}_r(t) + \sum_r \underline{c} \underline{\phi}_r \dot{q}_r(t) + \sum_r \underline{k} \underline{\phi}_r q_r(t) = -\underline{m}\underline{l}\ddot{u}_g. \quad (5.34)$$

Pre-multiplying each term in Eq. (5.34) by $\underline{\phi}_n^T$,

$$\sum_r \underline{\phi}_n^T \underline{m} \underline{\phi}_r \ddot{q}_r + \sum_r \underline{\phi}_n^T \underline{c} \underline{\phi}_r \dot{q}_r + \sum_r \underline{\phi}_n^T \underline{k} \underline{\phi}_r q_r = -\underline{\phi}_n^T \underline{m}\underline{l}\ddot{u}_g. \quad (5.35)$$

Only those terms with $r = n$ are non-zero due to the orthogonality of modes. Although this is theoretically valid for \underline{m} and \underline{k} , we can also assume the orthogonality of modal vectors with respect to \underline{c} .

$$\left(\underline{\phi}_n^T \underline{m} \underline{\phi}_n \right) \ddot{q}_n + \left(\underline{\phi}_n^T \underline{c} \underline{\phi}_n \right) \dot{q}_n + \left(\underline{\phi}_n^T \underline{k} \underline{\phi}_n \right) q_n = -\underline{\phi}_n^T \underline{m}\underline{l}\ddot{u}_g. \quad (5.36)$$

The terms in the first, second and third parentheses on the left hand side are the modal mass M_n , modal damping C_n and modal stiffness K_n , respectively. The term $\underline{\phi}_n^T \underline{m}\underline{l}$ on the right hand side is called the *modal excitation factor*, L_n

$$M_n = \underline{\phi}_n^T \underline{m} \underline{\phi}_n \quad (5.37)$$

$$C_n = \underline{\phi}_n^T \underline{c} \underline{\phi}_n \quad (5.38)$$

$$K_n = \underline{\phi}_n^T \underline{k} \underline{\phi}_n \quad (5.39)$$

$$L_n = \underline{\phi}_n^T \underline{m}\underline{l}. \quad (5.40)$$

When the parentheses terms in Eq. (5.36) are replaced with the definitions in Eqs. (5.37) to (5.40), a compact form is obtained.

$$M_n \ddot{q}_n + C_n \dot{q}_n + K_n q_n = -L_n \ddot{u}_g. \quad (5.41)$$

Dividing all terms by M_n and introducing the modal damping ratio and modal vibration frequency from Sect. 3.4.1 leads to a final normalized form.

$$\ddot{q}_n + 2\xi_n \omega_n \dot{q}_n + \omega_n^2 q_n = -\frac{L_n}{M_n} \ddot{u}_g. \quad (5.42)$$

Equation (5.42) is valid for all modes, $n = 1, 2, \dots, N$. This is equivalent to a SDOF system in the modal coordinate q_n .

Equations (5.36–5.42) describe the *modal superposition procedure* where the system of N-coupled equations of motion of the MDOF system in Eq. (5.6) is replaced with the N-uncoupled equations of motion of the equivalent SDOF systems in Eq. (5.42). This procedure provides significant advantages because working with coupled stiffness and mass matrices is much more difficult in applying numerical integration methods, compared to integrating the uncoupled equations of motion separately.

Now, let's recall the equation of motion of a SDOF system under base excitation \ddot{u}_g from Eq. (3.6). When Eq. (3.6) is normalized similar to the normalization of Eq. (5.41) into Eq. (5.42), we obtain

$$\ddot{u} + 2\xi_n \omega_n \dot{u} + \omega_n^2 u = -\ddot{u}_g. \quad (5.43)$$

The only difference between Eqs. (5.42) and (5.43) is the constant term $\frac{L_n}{M_n}$ term applied to the ground excitation \ddot{u}_g in the modal equation of motion. Therefore the solution procedures developed for SDOF systems under earthquake excitation in Chap. 3 are also valid for solving Eq. (5.42).

5.6.1 Summary: Modal Superposition Procedure

Modal superposition procedure for solving Eq. (5.6) is summarized below in a stepwise form.

1. Carry out eigenvalue analysis for Eq. (5.15) and determine the modal properties (ϕ_n, ω_n) for $n = 1, 2, \dots, N$. Calculate M_n and L_n .
2. Construct Eq. (5.41) or (5.42) for each mode n .
3. Solve Eq. (5.41) by using the methods developed for SDOF systems in Chap. 3 (\ddot{u}_g is scaled by $\frac{L_n}{M_n}$), and determine $q_n(t)$ for $n = 1, 2, \dots, N$.
4. Transform from modal coordinates back to physical coordinates by using Eq. (5.33).

5.6.2 Response Spectrum Analysis

The third step in the mode superposition analysis procedure above can also be performed by response spectrum analysis in a very simple manner. Let $S_d(T, \xi)$ be the displacement spectrum for $\ddot{u}_g(t)$. Then,

$$u_{n,max} = S_{dn} = S_d(T_n, \xi_n) \quad (5.44)$$

and

$$q_{n,max} = \frac{L_n}{M_n} S_{dn} \equiv \frac{L_n S_{an}}{M_n \omega_n^2} \quad (5.45)$$

Also

$$\ddot{q}_{n,max} = \frac{L_n}{M_n} S_{an} \quad (5.46)$$

where

$$S_{an} = \omega_n^2 S_{dn} \quad (5.47)$$

Accordingly,

$$\underline{u}_{n,max} = \underline{\phi}_n q_{n,max} \equiv \underline{\phi}_n \frac{L_n}{M_n} S_{dn} \equiv \underline{\phi}_n \frac{L_n P S_{an}}{\omega_n^2}. \quad (5.48)$$

In Eq. (5.48) above, $\underline{u}_{n,max}$ is the maximum value of the n th mode displacement vector \underline{u}_n . However since the time dependence is lost in Eq. (5.48), we cannot apply Eq. (5.33) directly and combine the maximum modal displacement for obtaining the maximum displacement distribution \underline{u}_{max} . Since all $q_{n,max}$ and accordingly $\underline{u}_{n,max}$ do not occur simultaneously,

$$\underline{u}_{max} \leq \underline{u}_{1,max} + \underline{u}_{2,max} + \cdots + \underline{u}_{N,max}$$

or

$$\begin{Bmatrix} u_1 \\ u_2 \\ \vdots \\ u_N \end{Bmatrix}_{max} \leq \begin{Bmatrix} u_{11} \\ u_{21} \\ \vdots \\ u_{N1} \end{Bmatrix}_{max} + \cdots + \begin{Bmatrix} u_{N1} \\ u_{N2} \\ \vdots \\ u_{NN} \end{Bmatrix}_{max}$$

5.6.3 Modal Combination Rules

Modal responses are independent from each other, and the maximum modal values r_n of a response parameter r (displacement, rotation, internal force, moment, etc.)

occur at different times, without any synchronization. Hence a statistical combination is necessary for obtaining the maximum combined response. The SRSS (Square Root of the Sum of Squares) rule provides good approximation for combining the modal maxima of displacement components.

$$u_{1,max} = (u_{11,max}^2 + u_{21,max}^2 + \cdots + u_{N1,max}^2)^{1/2} \quad (5.49)$$

or, in general

$$u_{j,max} = (u_{1j,max}^2 + u_{2j,max}^2 + \cdots + u_{Nj,max}^2)^{1/2}. \quad (5.50)$$

SRSS is equally applicable for estimating the maximum value of any force parameter (moment, shear, stress, etc.) or displacement parameter (curvature, rotation, displacement, strain, etc.) from the combination of the associated maximum modal values. Let r be a force or displacement parameter, and r_n ($n = 1, 2, \dots, N$) be its maximum n th mode value. Then,

$$r_{max} \approx (r_{1,max}^2 + r_{2,max}^2 + \cdots + r_{N,max}^2)^{1/2}. \quad (5.51)$$

SRSS is based on the assumption that the modal contributions to a response quantity are completely independent, hence orthogonal to each other. This method yields acceptable results when the modal frequencies are well-separated. However SRSS method creates significant errors when the structure has closely spaced modal frequencies, which usually occur in torsionally coupled frames. Practically, SRSS results are not acceptable if

$$0.9 < \frac{T_i}{T_j} < 1.1 \quad (5.52)$$

where T_i and T_j are the vibration periods of modes i and j . In this case, the cross-terms between the modes become important, which SRSS method does not consider.

An improved statistical combination method which reduces the errors arising from the SRSS method is the complete quadratic combination (CQC) method. What makes the CQC method more accurate compared to SRSS is that CQC method involves cross-modal coupling terms in its formulation.

$$r_{max} \approx \left(\sum_{n=1}^N r_n^2 + \sum_{i=1}^N \sum_{\substack{n=1 \\ i \neq n}}^N \rho_{in} r_i r_n \right)^{1/2}. \quad (5.53a)$$

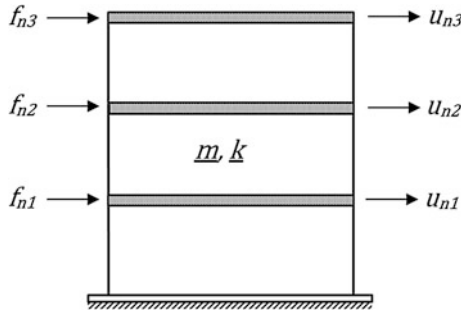
By definition, there is a cross-modal coefficient ρ_{in} in all terms in the CQC combination, and it is the function of modal damping ratios and vibration frequencies of the structure. If modal damping ratios are equal for all modes, i.e. $\xi_n = \xi$, then

$$\rho_{in} = \frac{\xi^2(1 + \beta_{in})^2}{(1 - \beta_{in})^2 + 4\xi^2\beta_{in}}; \quad \beta_{in} = \frac{\omega_i}{\omega_n}. \quad (5.53b)$$

CQC method reduces to the SRSS method theoretically for perfectly separated modes. However, this is not the case in reality and all modes are correlated to some extent. The significance of cross-modal terms increases as the modal frequencies are spaced closer.

5.6.4 Equivalent Static (Effective) Modal Forces

We can define an equivalent “static” lateral force vector \underline{f}_n for each mode n , which produces the modal spectral displacements $\underline{u}_{n,max}$ when they are applied to the MDOF system.



During maximum dynamic response at the n th mode, dynamic equilibrium requires

$$\underline{f}_n = \underline{k}\underline{u}_{n,max} \quad (5.54)$$

Substituting $\underline{u}_{n,max} = \underline{\phi}_n q_{n,max}$ from Eq. (5.44) into Eq. (5.54),

$$\underline{f}_n = \underline{k}\underline{\phi}_n q_{n,max} = \underline{k}\underline{u}_{n,max} \quad (5.55)$$

We can express the modal forces in a simpler form. Eq. (5.21) for free vibration can be written as

$$\underline{k}\underline{\phi}_n = \omega_n^2 \underline{m}\underline{\phi}_n \quad (5.56)$$

Multiplying each term by $q_{n,max}$ gives

$$\underline{k}\underline{\phi}_n q_{n,max} = \omega_n^2 \underline{m}\underline{\phi}_n q_{n,max} \quad (5.57)$$

Substituting the right hand side of Eq. (5.57) for the middle term in Eq. (5.55), we obtain

$$\underline{f}_n = \omega_n^2 \underline{m}\underline{\phi}_n q_{n,max} \quad (5.58)$$

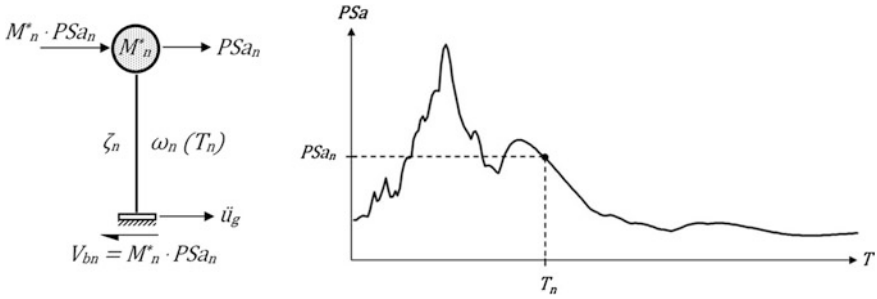


Fig. 5.7 SDOF representation of spectral modal response at mode n

This is a more practical expression since the diagonal matrix \underline{m} is easier to work with compared to the banded matrix \underline{k} having off-diagonal terms. Then, substituting $q_{n,max}$ from Eq. (5.45) into Eq. (5.58),

$$f_{-n} = \omega_n^2 \underline{m} \underline{\phi}_n \left[\frac{L_n S_{an}}{M_n \omega_n^2} \right]. \tag{5.59}$$

Finally, we obtain a simplified expression for the modal spectral force vector after rearranging Eq. (5.59).

$$f_{-n} = \frac{L_n}{M_n} \left(\underline{m} \underline{\phi}_n \right) S_{an}. \tag{5.60}$$

The total force at the base V_{bn} (modal base shear force) of the frame is equal to $\underline{1}^T f_{-n}$ where $\underline{1}$ is the unit vector.

$$V_{bn} = \underline{1}^T f_{-n} = \frac{L_n}{M_n} \left(\underline{1}^T \underline{m} \underline{\phi}_n \right) S_{an} \equiv \frac{L_n}{M_n} \left(\underline{\phi}_n^T \underline{m} \underline{1} \right) S_{an}. \tag{5.61}$$

Then,

$$V_{bn} = \frac{L_n^2}{M_n} S_{an} \equiv M_n^* S_{an} \tag{5.62}$$

where $M_n^* = \frac{L_n^2}{M_n}$ is the *effective modal mass*. With this definition, the spectral response at each mode under an earthquake base excitation which is expressed by its acceleration response spectrum can be represented on a simple sketch of an equivalent SDOF system as shown in Fig. 5.7.

Effective modal mass has an important practical aspect such that the sum of effective modal masses for all modes is equal to the total mass of the building system.

$$\sum_n^{modes} M_n^* = \sum_i^{stories} m_i. \tag{5.63}$$

This is exact for a shear frame, and quite accurate for an actual building frame structure. Effective modal mass can be directly calculated from the mass matrix and the n th mode vector.

$$M_n^* = \frac{\left(\underline{\phi}_n^T \underline{m} \underline{l}\right)^2}{\underline{\phi}_n^T \underline{m} \underline{\phi}_n} \tag{5.64}$$

Example 5.7 Consider the 2 story cantilever frame in Fig. 5.8a. The stiffness matrix for a frame member is given in Fig. 5.8b:

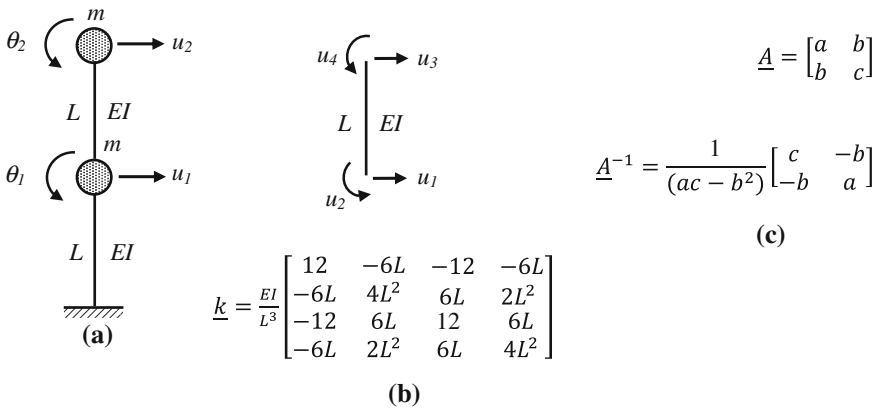


Fig. 5.8 2 story cantilever frame

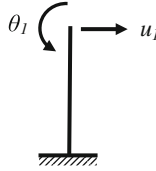
- (a) Determine the stiffness matrix of the system.
- (b) Apply static condensation for calculating the stiffness matrix of the reduced 2 DOF system. Inverse of a 2×2 matrix is given in Fig. 5.8c.
- (c) Calculate the eigenvalues and eigenvectors of the reduced system (in terms of EI , L and m).
- (d) Calculate the EQ moment diagrams for each mode in terms of mgL under the given response spectrum if $\frac{EI}{mL^3} = 116 \frac{r}{s^2}$

Solution

(a) *Stiffness Matrices*

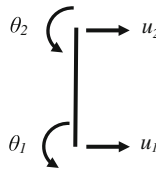
Global stiffness of the 1st story column;

$$\underline{k} = \frac{EI}{L^3} \begin{bmatrix} 12 & 6L \\ 6L & 4L^2 \end{bmatrix} ; \quad u = \begin{Bmatrix} u_1 \\ \theta_1 \end{Bmatrix}.$$



Global stiffness of the 2nd story column:

$$\underline{k} = \frac{EI}{L^3} \begin{bmatrix} 12 & -6L & -12 & -6L \\ -6L & 4L^2 & 6L & 2L^2 \\ -12 & 6L & 12 & 6L \\ -6L & 2L^2 & 6L & 4L^2 \end{bmatrix} \quad \underline{u} = \begin{Bmatrix} u_1 \\ \theta_1 \\ u_2 \\ \theta_2 \end{Bmatrix}$$



Mapping the two matrices on the global DOF's;

$$\underline{k}_{sys} = \frac{EI}{L^3} \begin{bmatrix} 24 & 0 & -12 & -6L \\ 0 & 8L^2 & 6L & 2L^2 \\ -12 & 6L & 12 & 6L \\ -6L & 2L^2 & 6L & 4L^2 \end{bmatrix} \quad \underline{u} = \begin{Bmatrix} u_1 \\ \theta_1 \\ u_2 \\ \theta_2 \end{Bmatrix}.$$

We should separate the dynamic DOF's (u_1, u_2) and static DOF's (θ_1, θ_2) for static condensation. This requires interchanging second and third rows and columns of \underline{k}_{sys} respectively, which gives;

$$\underline{k}_{sys} = \frac{EI}{L^3} \begin{bmatrix} 24 & -12 & 0 & -6L \\ -12 & 12 & 6L & 6L \\ 0 & 6L & 8L^2 & 2L^2 \\ -6L & 6L & 2L^2 & 4L^2 \end{bmatrix} \quad \underline{u} = \begin{Bmatrix} u_1 \\ u_2 \\ \theta_1 \\ \theta_2 \end{Bmatrix}.$$

(b) *Static Condensation*

$$\underline{k}_{sys} = \begin{bmatrix} \underline{k}_{dd} & \underline{k}_{ds} \\ \underline{k}_{sd} & \underline{k}_{ss} \end{bmatrix} \quad \text{and} \quad \underline{k}_d = (\underline{k}_{dd} - \underline{k}_{ds}\underline{k}_{ss}^{-1}\underline{k}_{sd}).$$

$\underline{k}_{ss} = \frac{EI}{L^3} \begin{bmatrix} 8L^2 & 2L^2 \\ 2L^2 & 4L^2 \end{bmatrix} = \frac{2EI}{L} \begin{bmatrix} 4 & 1 \\ 1 & 2 \end{bmatrix}$. Considering that $(ac - b^2) = 8 - 1 = 7$ from Fig. 5.8c,

$\underline{k}_{ss}^{-1} = \frac{L}{14EI} \begin{bmatrix} 2 & -1 \\ -1 & 4 \end{bmatrix}$. Then the condensed stiffness matrix is obtained from the above equation as

$$\underline{k}_d = \frac{EI}{L^3} \begin{bmatrix} 24 & -12 \\ -12 & 12 \end{bmatrix} - \left(\frac{EI}{L^3}\right)^2 * \frac{L}{14EI} \begin{bmatrix} 0 & -6L \\ 6L & 6L \end{bmatrix} \begin{bmatrix} 2 & -1 \\ -1 & 4 \end{bmatrix} \begin{bmatrix} 0 & 6L \\ -6L & 6L \end{bmatrix}, \text{ or}$$

$$\underline{k}_d = \frac{EI}{L^3} \begin{bmatrix} 24 & -12 \\ -12 & 12 \end{bmatrix} - \frac{EI}{7L^3} \begin{bmatrix} 72 & -54 \\ -54 & 72 \end{bmatrix} = \frac{EI}{7L^3} \begin{bmatrix} 96 & -30 \\ -30 & 12 \end{bmatrix}.$$

(c) *Eigenvalue Analysis*

$$(\underline{k}_d - \omega_n^2 \underline{m}) = \underline{0} \quad \underline{m} = m \begin{bmatrix} 1 & 0 \\ 0 & 1 \end{bmatrix}$$

$$\frac{EI}{7L^3} \begin{bmatrix} 96 & -30 \\ -30 & 12 \end{bmatrix} - \omega_n^2 m \begin{bmatrix} 1 & 0 \\ 0 & 1 \end{bmatrix} = \begin{Bmatrix} 0 \\ 0 \end{Bmatrix}, \text{ or,}$$

$$\begin{bmatrix} \frac{96EI}{7L^3} - \omega_n^2 m & \frac{-30EI}{7L^3} \\ \frac{-30EI}{7L^3} & \frac{12EI}{7L^3} - \omega_n^2 m \end{bmatrix} = \begin{Bmatrix} 0 \\ 0 \end{Bmatrix}.$$

$\det() = 0$ gives; $\left(\frac{96EI}{7L^3} - \omega_n^2 m\right) \left(\frac{12EI}{7L^3} - \omega_n^2 m\right) - \left(\frac{30EI}{7L^3}\right)^2 = 0$. Simplifying and rearranging,

$$1152 \left(\frac{EI}{7L^3}\right)^2 - \omega_n^2 m \left(108 \frac{EI}{7L^3}\right) + (\omega_n^2 m)^2 - 900 \left(\frac{EI}{7L^3}\right)^2 = 0$$

Let $\omega_n^2 m = \lambda_n$ and $\frac{EI}{7L^3} = a$. Substituting and solving the quadratic equation above,

$$\lambda_{1,2} = \frac{108a \mp \sqrt{10656a^2}}{2}; \quad \lambda_1 = 2.386a = \omega_1^2 m \text{ and } \lambda_2 = 105.614a = \omega_2^2 m.$$

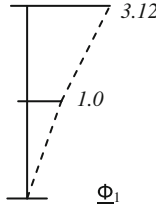
Accordingly, $\omega_1^2 = 0.341 \frac{EI}{mL^3}$ and $\omega_2^2 = 15.088 \frac{EI}{mL^3}$

$$\text{Then } \omega_1 = 0.584 \sqrt{\frac{EI}{mL^3}}; \quad \omega_2 = 3.884 \sqrt{\frac{EI}{mL^3}}.$$

Mode vector 1

$$\frac{EI}{7L^3} \begin{bmatrix} 93.614 & -30 \\ -30 & 9.614 \end{bmatrix} \begin{Bmatrix} \phi_{11} \\ \phi_{12} \end{Bmatrix} = \underline{0}$$

$$93.614\phi_{11} - 30\phi_{12} = 0$$

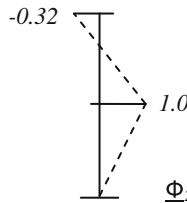


Let $\phi_{11} = 1.0$ Then $\phi_{12} = \frac{93.614}{30} = 3.12$. Hence $\underline{\Phi}_1 = \begin{Bmatrix} 1.00 \\ 3.12 \end{Bmatrix}$.

Mode vector 2

$$\frac{EI}{7L^3} \begin{bmatrix} -9.614 & -30 \\ -30 & -93.614 \end{bmatrix} \begin{Bmatrix} \phi_{21} \\ \phi_{22} \end{Bmatrix} = \underline{0}$$

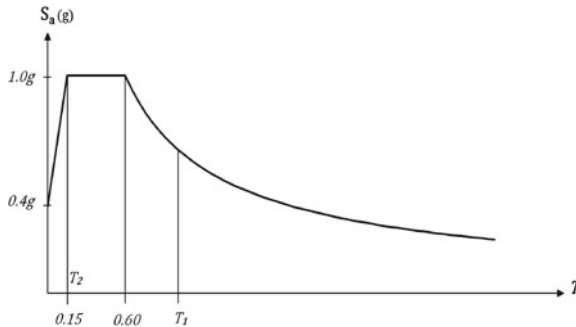
$$-9.614\phi_{21} - 30\phi_{22} = 0$$



Let $\phi_{21} = 1.0$. Then $\phi_{22} = -0.32$. Accordingly, $\underline{\Phi}_2 = \begin{Bmatrix} 1.00 \\ -0.32 \end{Bmatrix}$.

(d) EQ Moment Diagrams

When $\frac{EI}{mL^3} = 116r/s^2$, $T_1 = 1.0$ s and $T_2 = 0.15$ s. The spectral accelerations for the two modes are obtained from the acceleration response spectrum given below.



$$S_{a1} = 0.665 \text{ g} = 6.52 \text{ m/s}^2; \quad S_{a2} = 1.0 \text{ g} = 9.81 \text{ m/s}^2$$

The modal force vectors are expressed as $\underline{f}_n = \frac{L_n}{M_n} (\underline{m}\underline{\phi}_n) S_{an}$. Here,

$$L_1 = \underline{\phi}_1^T \underline{m} \underline{1} = 4.12m; \quad L_2 = 0.68m \text{ and } M_1 = 10.73m; \quad M_2 = 1.102m.$$

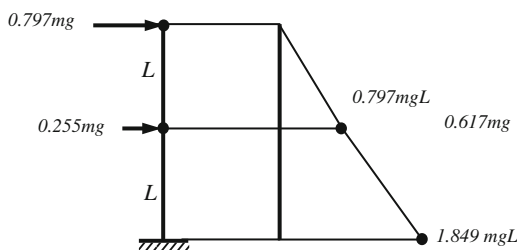
Hence, $\frac{L_1}{M_1} = 0.384$ and $\frac{L_2}{M_2} = 0.617$. Then the modal forces are,

$$\underline{f}_1 = 0.384m \begin{Bmatrix} 1.00 \\ 3.12 \end{Bmatrix} * 0.665g = mg \begin{Bmatrix} 0.255 \\ 0.797 \end{Bmatrix} \text{ and}$$

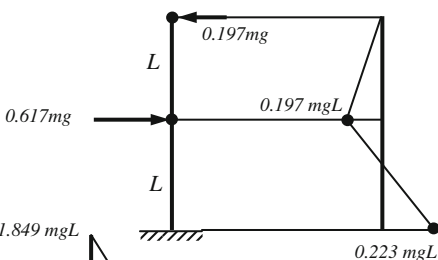
$$\underline{f}_2 = 0.617m \begin{Bmatrix} 1.00 \\ -0.32 \end{Bmatrix} * 1.0g = mg \begin{Bmatrix} 0.617 \\ -0.197 \end{Bmatrix}.$$

Since the system is statically determinate, we can calculate the moment distributions directly.

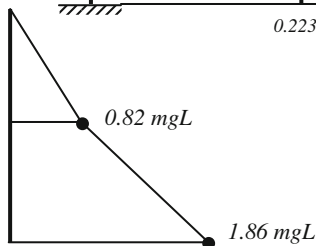
Moment diagram for Mode 1



Moment diagram for Mode 2



SRSS:



Example 5.8 Determine the maximum displacement distribution of the 3-story shear frame in Fig. 5.9a under the acceleration spectrum given in Fig. 5.9b. The results of eigenvalue analysis are also given below.

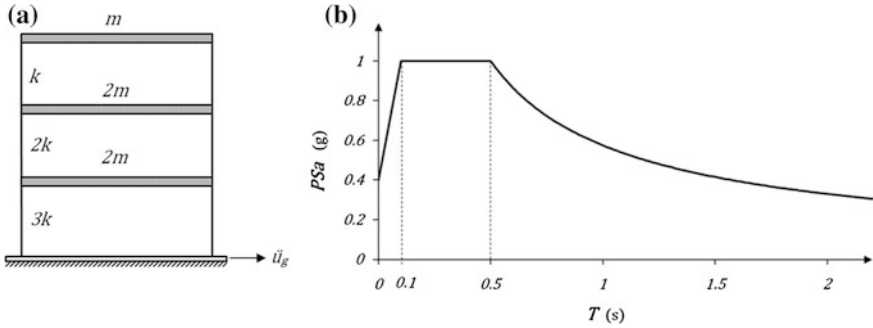


Fig. 5.9 3 story shear frame

$k = 140,000 \text{ kN/m}$ $m = 175,000 \text{ kg}$ k : total lateral stiffness for both columns

$$\underline{\phi}_1 = \begin{Bmatrix} 0.314 \\ 0.686 \\ 1.00 \end{Bmatrix} \quad \underline{\phi}_2 = \begin{Bmatrix} -0.50 \\ -0.50 \\ 1.00 \end{Bmatrix} \quad \underline{\phi}_3 = \begin{Bmatrix} 1.00 \\ -0.686 \\ 0.313 \end{Bmatrix}$$

$$\omega_1 = 15.84 \text{ r/s} \quad \omega_2 = 34.64 \text{ r/s} \quad \omega_3 = 50.50 \text{ r/s}$$

$$T_1 = 0.40 \text{ s} \quad T_2 = 0.18 \text{ s} \quad T_3 = 0.125 \text{ s}$$

Solution

When we enter the response spectrum with the modal period values, we determine the modal spectral acceleration values.

$$S_{a1} = S_{a2} = S_{a3} = 1.0 \text{ g.}$$

Then the modal masses and modal excitation factors are determined.

$$M_1 = \underline{\phi}_1^T \underline{m} \underline{\phi}_1 = 374700 \text{ kg} \quad M_2 = 350000 \text{ kg} \quad M_3 = 531000 \text{ kg}$$

$$L_1 = \underline{\phi}_1^T \underline{m} \underline{1} = 525350 \text{ kg} \quad L_2 = -175000 \text{ kg} \quad L_3 = 165550 \text{ kg}$$

$$\frac{L_1}{M_1} = 1.40 \quad \frac{L_2}{M_2} = -0.50 \quad \frac{L_3}{M_3} = 0.31$$

Let $q_{n,max} = q_n$ (drop the max index). q_n are obtained from Eq. (5.45) and maximum modal displacements are determined from Eq. (5.48).

$$q_1 = \frac{L_1 S_{a1}}{M_1 \omega_1^2} = 5.47 \text{ cm} \quad q_2 = -0.41 \text{ cm} \quad q_3 = 0.12 \text{ cm}$$

$$\underline{u}_1 = \underline{\phi}_1 q_1 = \begin{Bmatrix} 1.72 \\ 3.76 \\ 5.47 \end{Bmatrix}_{cm} \quad \underline{u}_2 = \begin{Bmatrix} -0.20 \\ -0.20 \\ 0.41 \end{Bmatrix}_{cm} \quad \underline{u}_3 = \begin{Bmatrix} 0.12 \\ -0.10 \\ 0.04 \end{Bmatrix}_{cm}$$

Finally, the modal spectral displacements are combined with the SRSS rule for obtaining the maximum story displacement distribution.

$$\underline{u} = \left\{ \begin{array}{l} \sqrt{1.72^2 + (-0.20)^2 + (0.12)^2} = 1.74 \\ \sqrt{3.76^2 + (-0.20)^2 + (-0.10)^2} = 3.77 \\ \sqrt{5.47^2 + 0.41^2 + 0.04^2} = 5.50 \end{array} \right\}_{cm}$$

It may be noted that $\underline{u} \approx \underline{u}_1$, i.e. the first mode displacements dominate the total displacement distribution. In particular,

$$u_{roof} \simeq \sqrt{5.47^2 + 0.41^2 + 0.04^2} = 5.50 \text{ cm.}$$

Example 5.9 A two story, one bay frame with six DOF's is given in Fig. 5.10a. All frame members have a length of L , moment of inertia of I and the modulus of elasticity is E . A uniform distributed vertical gravity load with intensity q is acting on the beams. Determine the design moments and shear forces in column AC and beam CD under gravity and earthquake loads. Design earthquake is defined with the reduced design spectrum given in Fig. 5.10b. Axial deformations in all frame members are neglected.

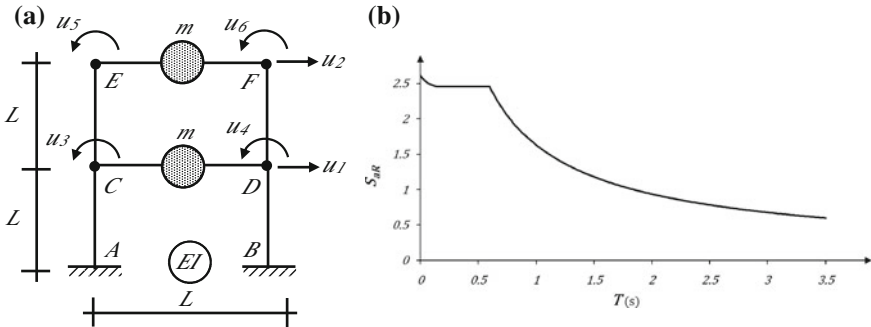


Fig. 5.10 a Frame structure. b Reduced design spectrum

Solution

The procedure summarized above will be implemented in the solution.

(a) *Static Condensation*

The 6 DOF system in Fig. 5.10a will be reduced to a 2 DOF dynamic system for eigenvalue and mode superposition analyses. Displacement vector \underline{u} of the unreduced 6 DOF system and the displacement vector \underline{u}_d of the reduced (condensed) 2 DOF system are given below. Hence, the condensed system DOF's are the lateral

DOF's along the floor levels where the story masses are defined and accordingly the inertial forces develop.

$$\underline{u} = \begin{Bmatrix} u_1 \\ u_2 \\ u_3 \\ u_4 \\ u_5 \\ u_6 \end{Bmatrix} \quad \underline{u}_d = \begin{Bmatrix} u_1 \\ u_2 \end{Bmatrix}. \quad (1)$$

The stiffness matrix of the 6 DOF system is

$$\underline{k}_{\text{sys}} = \frac{EI}{L^3} \begin{bmatrix} 48 & -24 & 0 & 0 & -6L & -6L \\ -24 & 24 & 6L & 6L & 6L & 6L \\ 0 & 6L & 12L^2 & 2L^2 & 2L^2 & 0 \\ 0 & 6L & 2L^2 & 12L^2 & 0 & 2L^2 \\ -6L & -6L & 2L^2 & 0 & 8L^2 & 12L^2 \\ -6L & 6L & 0 & 2L^2 & 2L^2 & 8L^2 \end{bmatrix} \quad (2)$$

$\underline{k}_{\text{sys}}$ can be partitioned as

$$\underline{k}_{\text{sys}} = \begin{bmatrix} \underline{k}_{dd} & \underline{k}_{ds} \\ \underline{k}_{sd} & \underline{k}_{ss} \end{bmatrix}$$

where the condensed stiffness matrix \underline{k}_d is expressed as $\underline{k}_d = \underline{k}_{dd} - \underline{k}_{sd}^T \underline{k}_{ss}^{-1} \underline{k}_{ds}$. Then,

$$\underline{k}_d = \frac{EI}{17L^3} \begin{bmatrix} 690 & -300 \\ -300 & 228 \end{bmatrix}$$

Similarly, the mass matrix for the condensed 2 DOF system is

$$\underline{m} = \begin{bmatrix} m & 0 \\ 0 & m \end{bmatrix}$$

(b) Eigenvalue Analysis

The equation $\det(\underline{k}_d - \omega^2 \underline{m}) = 0$ should be solved for determining the eigenvalues and eigenvectors. Here, we will assign numerical values to frame properties.

Let $EI = 660 \text{ kN m}^2$, $L = 2 \text{ m}$ and $m = 10 \text{ tons}$. Then, the eigenvalues are obtained as:

$$\omega_1^2 = 39.00 \text{ (rad/s)}^2; \omega_2^2 = 406.50 \text{ (rad/s)}^2 \text{ and } T_1 = 1.00 \text{ s}; T_2 = 0.31 \text{ s}.$$

The mode shapes are determined by solving the equation $(\underline{k}_d - \omega^2 \underline{m})\underline{\phi}_n = \underline{0}$. The solution gives;

$$\underline{\phi}_1 = \begin{Bmatrix} 0.49 \\ 1.00 \end{Bmatrix} \quad \text{and} \quad \underline{\phi}_2 = \begin{Bmatrix} -2.03 \\ 1.00 \end{Bmatrix} \quad (3)$$

(c) *Spectral Accelerations*

Spectral acceleration values for the modal periods are obtained from the reduced design spectrum given in Fig. 5.10b above:

Mode 1: $T_1 = 1.00$ s, $S_{aR,1} = 1.63$ m/s²

Mode 2: $T_2 = 0.31$ s, $S_{aR,2} = 2.45$ m/s².

(d) *Modal Force Vectors*

$$\underline{f}_{-n} = \frac{L_n}{M_n} (\underline{m}\underline{\phi}_{-n}) S_{aR,n} \quad \text{where} \quad L_n = \underline{\phi}_{-n}^T \underline{m} \underline{l}; \quad M_n = \underline{\phi}_{-n}^T \underline{m} \underline{\phi}_{-n} \quad \text{and} \quad \underline{l} = \begin{Bmatrix} 1 \\ 1 \end{Bmatrix}$$

When the respective values of $\underline{\phi}_{-n}$, \underline{m} and \underline{l} are substituted into these expressions, we find

$L_1 = 14.92$ tons; $L_2 = -10.32$ tons; $M_1 = 12.42$ tons; $M_2 = 51.29$ tons, and

$$\underline{f}_{-1} = \begin{Bmatrix} 9.63 \\ 19.58 \end{Bmatrix} \text{ kN}; \quad \underline{f}_{-2} = \begin{Bmatrix} 10.03 \\ -4.93 \end{Bmatrix} \text{ kN}. \quad (4)$$

(e) *Earthquake Analysis (Mode Superposition Procedure)*

The modal force vectors of the condensed 2 DOF system are first expressed for the uncondensed (original) 6 DOF system in view of the DOF's defined in Fig. 5.10a.

$$\underline{f}'_{-1} = \begin{Bmatrix} 9.63 \\ 19.58 \\ 0 \\ 0 \\ 0 \\ 0 \end{Bmatrix} \text{ kN}; \quad \underline{f}'_{-2} = \begin{Bmatrix} 10.03 \\ -4.93 \\ 0 \\ 0 \\ 0 \\ 0 \end{Bmatrix} \text{ kN}. \quad (5)$$

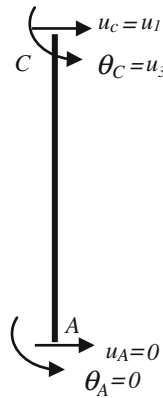
Then the modal displacement vectors are obtained by solving $\underline{f}'_{-n} = \underline{k}_{sys} \cdot \underline{u}_n$ where \underline{k}_{sys} is the 6×6 global system stiffness matrix in Eq. (2). Solution for $n = 1$ and $n = 2$ gives,

$$\underline{u}_1 = \begin{Bmatrix} 0.0247 \\ 0.0502 \\ -0.0099 \\ -0.0099 \\ -0.0057 \\ -0.0057 \end{Bmatrix}; \quad \underline{u}_2 = \begin{Bmatrix} 0.0025 \\ -0.0012 \\ 0.0001 \\ 0.0001 \\ 0.0011 \\ 0.0011 \end{Bmatrix}. \quad (6)$$

The units are meters and radians.

(f) *Earthquake Forces in Member AC*

Member forces are calculated from the member equilibrium equation;



$$\underline{f}_{AC,n} = \underline{k}_{AC} \cdot \underline{u}_{AC,n}$$

$$\underline{k}_{AC} = \frac{EI}{L^3} \begin{bmatrix} 12 & -6L & -12 & -6L \\ -6L & 4L^2 & 6L & 2L^2 \\ -12 & 6L & 12 & 6L \\ -6L & 2L^2 & 6L & 4L^2 \end{bmatrix}; \quad \underline{u}_{AC} = \begin{Bmatrix} u_A \\ \theta_A \\ u_C \\ \theta_C \end{Bmatrix} = \begin{Bmatrix} 0 \\ 0 \\ u_1 \\ u_3 \end{Bmatrix}$$

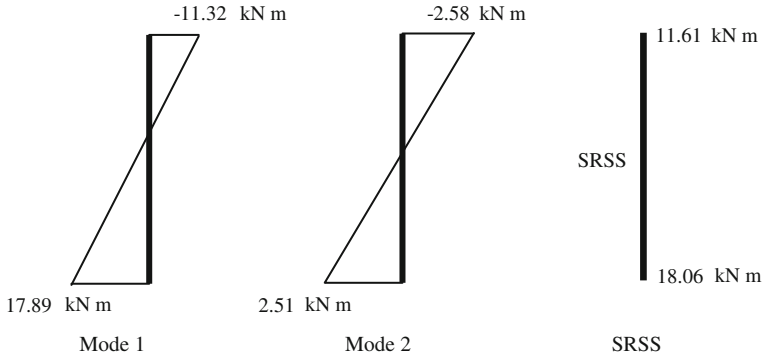
Mode 1

$$\underline{f}_{AC,1} = \begin{Bmatrix} V_A \\ M_A \\ V_C \\ M_C \end{Bmatrix} = \underline{k}_{AC} \begin{Bmatrix} 0 \\ 0 \\ u_1 \\ u_3 \end{Bmatrix} = \underline{k}_{AC} \begin{Bmatrix} 0 \\ 0 \\ 0.0247 \\ -0.0099 \end{Bmatrix} = \begin{Bmatrix} -14.61 \\ 17.89 \\ 14.61 \\ 11.32 \end{Bmatrix} \text{ kN and kN m}$$

Mode 2

$$\underline{f}_{AC,2} = \begin{Bmatrix} V_A \\ M_A \\ V_C \\ M_C \end{Bmatrix} = \underline{k}_{AC} \begin{Bmatrix} 0 \\ 0 \\ u_1 \\ u_3 \end{Bmatrix} = \underline{k}_{AC} \begin{Bmatrix} 0 \\ 0 \\ 0.0025 \\ 0.0001 \end{Bmatrix} = \begin{Bmatrix} -2.55 \\ 2.51 \\ 2.55 \\ 2.58 \end{Bmatrix} \text{ kN and kN m}$$

(g) Earthquake Moment Diagram AC



$$M_{AC,bot} = (17.89^2 + 2.51^2)^{1/2} = 18.06 \text{ kN m};$$

$$M_{AC,top} = (11.32 + 2.58^2)^{1/2} = 11.61 \text{ kN m}$$

(h) Earthquake Forces in Member CD

Member forces are calculated from the member equilibrium equation;

$$\underline{f}_{CD,n} = \underline{k}_{CD} \cdot \underline{u}_{CD,n}$$

$$\underline{k}_{CD} = \frac{EI}{L^3} \begin{bmatrix} 12 & 6L & -12 & 6L \\ 6L & 4L^2 & -6L & 2L^2 \\ -12 & -6L & 12 & -6L \\ 6L & 2L^2 & -6L & 4L^2 \end{bmatrix}; \quad \underline{u}_{CD} = \begin{Bmatrix} u_C \\ \theta_C \\ u_D \\ \theta_D \end{Bmatrix} = \begin{Bmatrix} 0 \\ u_3 \\ 0 \\ u_4 \end{Bmatrix}$$



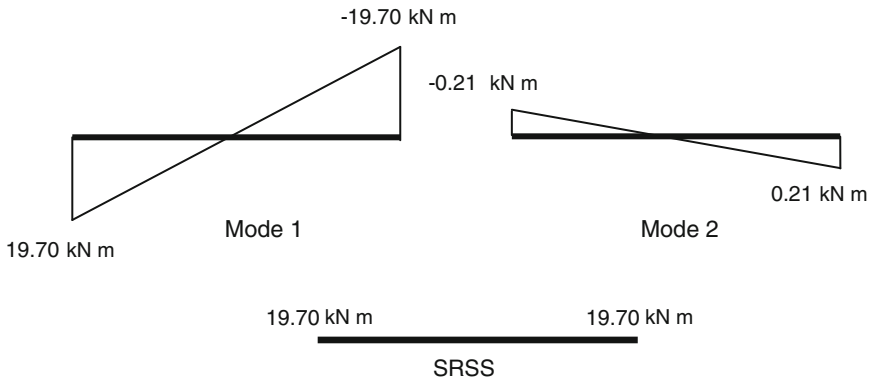
Mode 1

$$\underline{f}_{CD,1} = \begin{Bmatrix} V_C \\ M_C \\ V_D \\ M_D \end{Bmatrix} = \underline{k}_{CD} \begin{Bmatrix} 0 \\ u_3 \\ 0 \\ u_4 \end{Bmatrix} = \underline{k}_{CD} \begin{Bmatrix} 0 \\ -0.0099 \\ 0 \\ -0.0099 \end{Bmatrix} = \begin{Bmatrix} -19.70 \\ -19.70 \\ 19.70 \\ -19.70 \end{Bmatrix} \text{ kN and kN m}$$

Mode 2

$$\underline{f}_{CD,2} = \begin{Bmatrix} V_A \\ M_A \\ V_C \\ M_C \end{Bmatrix} = \underline{k}_{CD} \begin{Bmatrix} 0 \\ 0 \\ u_1 \\ u_3 \end{Bmatrix} = \underline{k}_{CD} \begin{Bmatrix} 0 \\ 0.0001 \\ 0 \\ 0.0001 \end{Bmatrix} = \begin{Bmatrix} 0.21 \\ 0.21 \\ -0.21 \\ 0.21 \end{Bmatrix} \text{ kN and kN m}$$

(i) Earthquake Moment Diagram CD



$$M_{CD,l} = (19.70^2 + 0.21^2)^{1/2} = 19.71 \text{ kN m ;}$$

$$M_{CD,r} = (19.70^2 + 0.21^2)^{1/2} = 19.71 \text{ kN m}$$

(j) Gravity Load Analysis

Let $q = 50 \text{ kN m}$. This value is consistent with the story mass of 10 tons, hence 10 g kN is distributed uniformly over the story girders of $L = 2 \text{ m}$. Fixed-end moments at beam ends are calculated from $M_{FEM} = qL^2/12 = 16.67 \text{ kN m}$.

Accordingly, the gravity force vector for global DOF's is

$$\underline{f}_G = \begin{Bmatrix} 0 \\ 0 \\ -16.67 \\ 16.67 \\ -16.67 \\ 16.67 \end{Bmatrix} \text{ kN m}$$

Displacement vector under gravity forces is determined by solving $\underline{f}_G = \underline{k}_{sys} \cdot \underline{u}_G$.

The global displacement vector and the member end displacements are obtained as,

$$\underline{u}_G = \begin{Bmatrix} 0 \\ 0 \\ -0.0036 \\ 0.0036 \\ -0.0072 \\ 0.0072 \end{Bmatrix}; \underline{u}_{AC} = \begin{Bmatrix} u_A \\ \theta_A \\ u_C \\ \theta_C \end{Bmatrix} \equiv \begin{Bmatrix} 0 \\ 0 \\ u_1 \\ u_3 \end{Bmatrix} = \begin{Bmatrix} 0 \\ 0 \\ 0 \\ -0.0036 \end{Bmatrix};$$

$$\underline{u}_{CD} = \begin{Bmatrix} u_C \\ \theta_C \\ u_D \\ \theta_D \end{Bmatrix} = \begin{Bmatrix} 0 \\ u_3 \\ 0 \\ u_4 \end{Bmatrix} = \begin{Bmatrix} 0 \\ -0.0036 \\ 0 \\ 0.0036 \end{Bmatrix}$$

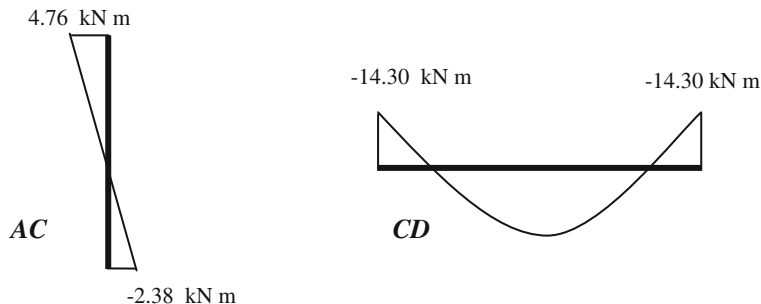
Then the member end forces under gravity loads are determined from

$$\underline{f}_{AC,G} = \underline{k}_{AC} \cdot \underline{u}_{AC} + \underline{F}_{ext} \quad \text{and} \quad \underline{f}_{CD,G} = \underline{k}_{CD} \cdot \underline{u}_{CD} + \underline{F}_{ext}$$

where $\underline{F}_{ext,AC} = \underline{0}$ (no span loading) and $\underline{F}_{ext,CD} = \begin{Bmatrix} 0 \\ 16.67 \\ 0 \\ -16.67 \end{Bmatrix}$ kN m. Then,

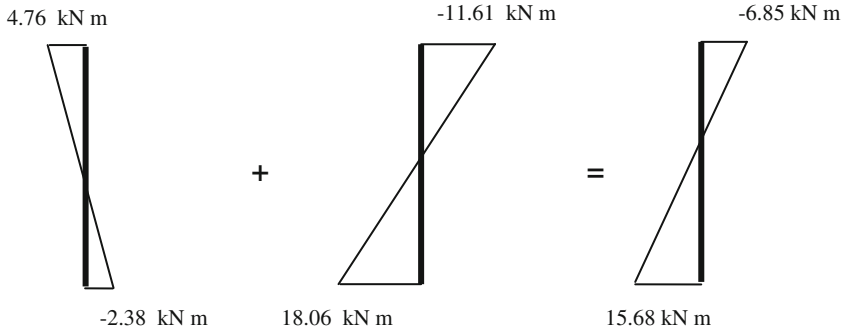
$$\underline{f}_{AC,G} = \begin{Bmatrix} 3.57 \\ -2.38 \\ -3.57 \\ -4.76 \end{Bmatrix} \quad \text{and} \quad \underline{f}_{CD,G} = \begin{Bmatrix} 0 \\ 14.30 \\ 0 \\ -14.30 \end{Bmatrix}$$

(k) Gravity Moment Diagrams of AC and CD

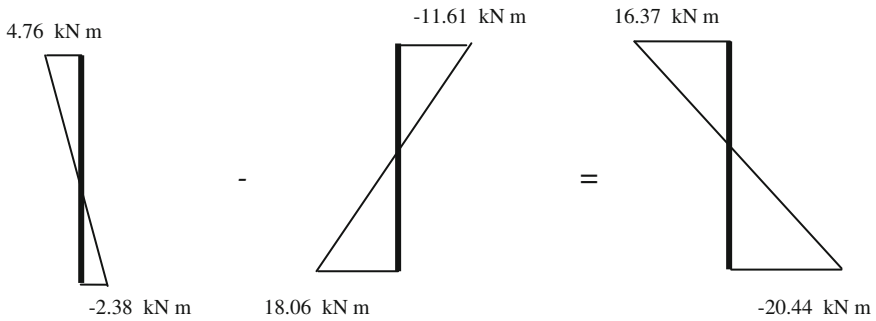


Combining the Internal Forces: $M_G \mp M_{EQ}$

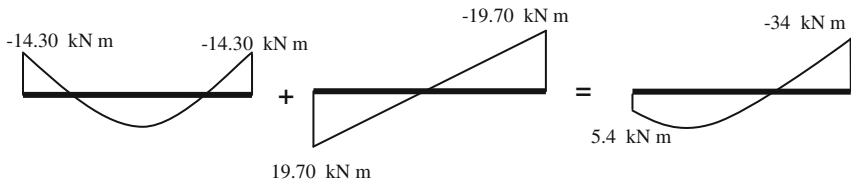
Member AC: $M_G + M_{EQ}$



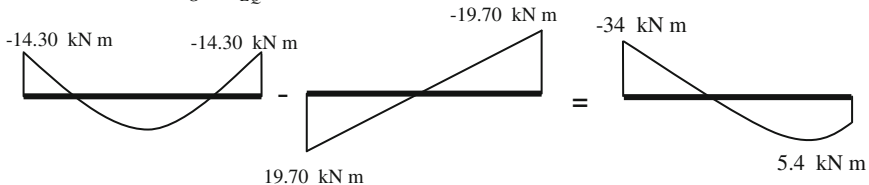
Member AC: $M_G - M_{EQ}$



Member CD: $M_G + M_{EQ}$



Member CD: $M_G - M_{EQ}$



It should be noted that the design moments in columns and the design shear forces in columns and beams are calculated differently in the capacity design procedure. This is explained in [Chap. 7](#).

Example 5.10 Calculate the modal force vectors for the frame in Example 5.8. Also calculate the effective modal masses, modal base shear forces, and modal moments at the top end of the first story columns. Combine these forces and moments by SRSS for calculating the total base shear force and first story column top moment.

Solution

(a) *Modal Forces*

$$\underline{f}_{-1} = \frac{L_1}{M_1} \left(\underline{m\phi}_{-1} \right) S a_1 = 1.40 \begin{bmatrix} 2m & 0 & 0 \\ 0 & 2m & 0 \\ 0 & 0 & m \end{bmatrix} \begin{Bmatrix} 0.314 \\ 0.687 \\ 1.00 \end{Bmatrix} .g$$

$$\underline{f}_{-1} = \begin{Bmatrix} 1509 \\ 3302 \\ 2408 \end{Bmatrix}_{\text{kN}} \quad \underline{f}_{-2} = \begin{Bmatrix} -858 \\ -858 \\ 858 \end{Bmatrix}_{\text{kN}} \quad \underline{f}_{-3} = \begin{Bmatrix} 1064 \\ -728 \\ 167 \end{Bmatrix}_{\text{kN}}$$

(b) *Effective modal masses*

From Eq. (5.64),

$$M_1^* = 736,550 \text{ kg} (84.2 \% M) \quad M_2^* = 87,500 \text{ kg} (10 \% M)$$

$$M_3^* = 51,275 \text{ kg} (5.8 \% M)$$

$$M_1^* + M_2^* + M_3^* \simeq 875,000 \text{ kg} (100 \% M)$$

M is the total mass where $M = 5 m = 5 \times 175,000 \text{ kg} = 875,000 \text{ kg}$. Therefore the sum of effective modal masses is equal to the total mass (inaccuracy is due to the decimal truncation in modal vectors).

(c) *Modal base shear forces*

$$V_{bn} = M_n^* S a_n$$

$$V_{b1} = 736,550 \text{ kg} \times 9.81 \frac{\text{m}}{\text{s}^2} = 7226 \text{ kN}; \quad V_{b2} = -858 \text{ kN}; \quad V_{b3} = 503 \text{ kN}$$

Note that $V_{bn} = \sum_{j=1}^3 f_{nj}$ for all $n = 1-3$.

$$V_b \simeq \sqrt{V_{b1}^2 + V_{b2}^2 + V_{b3}^2} = 7294 \text{ kN}.$$

d) *Modal column moments*

$M^{top} = \frac{1}{2}Vh$ where V is the shear force in the column and h is the story height. $V = \frac{1}{2}V_b$ at the first story columns. Then the modal column top moments at the first story are;

$$M_1^{top} = \frac{1}{2} \left(\frac{1}{2} \cdot 7226 \right) h = 1806h; \quad M_2^{top} = 214.5h; M_3^{top} = 126h$$

$$M^{top} \simeq \sqrt{(M_1^{top})^2 + (M_2^{top})^2 + (M_3^{top})^2} = 1823 h(\text{kN m}).$$

Example 5.11 Consider the frame given in Example 5.3. If the frame is subjected to the ground excitation defined by the acceleration spectrum given in Example 5.8, determine the displacement of the mass at end B, the base shear force and base moment at the support, and the top moment of the column. Let $EI = 4,000 \text{ kN m}^2$, $m = 4 \text{ tons}$ and $h = l = 4 \text{ m}$.

Solution $T_n = 2\pi/\omega_n$, which gives $T_1 = 1.786 \text{ s}$ and $T_2 = 0.407 \text{ s}$ from the results of Example 5.3. The corresponding spectral accelerations can be determined from the acceleration response spectrum of Example 5.6, as $S_{a1} = 0.34 \text{ g}$ and $S_{a2} = 1.0 \text{ g}$.

$$\begin{aligned} M_n &= \underline{\phi}_n^T \underline{m} \underline{\phi}_n; & M_1 &= 17.99 \text{ tons} & M_2 &= 5.145 \text{ tons} \\ L_n &= \underline{\phi}_n^T \underline{m} \underline{1}; & L_1 &= -3.48 \text{ tons} & L_2 &= 6.14 \text{ tons} \\ \frac{L_1}{M_1} &= -0.193 & \frac{L_2}{M_2} &= 1.193. \end{aligned} \quad (1)$$

(a) *Modal amplitudes*

$$q_n = \frac{L_n S_{a_n}}{M_n \omega_n^2}; \quad q_1 = -0.0522 \text{ m} \quad q_2 = 0.0492 \text{ m}. \quad (2)$$

(b) *Modal displacement vectors*

$$\underline{u}_n = \underline{\phi}_n q_n; \quad \underline{u}_1 = \left\{ \begin{array}{c} -0.0522 \\ 0.0976 \end{array} \right\}_m \quad \underline{u}_2 = \left\{ \begin{array}{c} 0.0492 \\ 0.0263 \end{array} \right\}_m \quad (3)$$

where

$$\underline{u}_n = \left\{ \begin{array}{c} u_{Bn} \\ v_{Bn} \end{array} \right\}; \quad n = 1, 2.$$

(c) *Displacements at the B end (SRSS combination)*

$$u_B = \sqrt{(-0.0522)^2 + (0.0492)^2} = 0.0717 \text{ m} \quad (\text{Both modes contribute})$$

$$v_B = \sqrt{(0.0976)^2 + (0.0263)^2} = 0.1011 \text{ m} \quad (\text{1st mode dominant})$$

(d) *Internal forces in column OA*

Let's denote the bottom end (fixed end) of the column by O. The end forces (lateral force and bending moment) of column OA can be determined both by the stiffness analysis of the column by using the modal end displacements, or by applying the equivalent static modal forces and calculating the associated modal internal forces. We will do both.

Stiffness analysis: Let's write the stiffness equation for column OA at the n th mode.

$$\begin{Bmatrix} F_O \\ M_O \\ F_A \\ M_A \end{Bmatrix}_n = \frac{EI}{h} \begin{bmatrix} \frac{12}{h^2} & -\frac{6}{h} & -\frac{12}{h^2} & -\frac{6}{h} \\ -\frac{6}{h} & 4 & \frac{6}{h} & 2 \\ -\frac{12}{h^2} & \frac{6}{h} & \frac{12}{h^2} & \frac{6}{h} \\ -\frac{6}{h} & 2 & \frac{6}{h} & 4 \end{bmatrix} \begin{Bmatrix} u_O \\ \theta_O \\ u_A \\ \theta_A \end{Bmatrix}_n \quad (4)$$

Note that $u_o = \theta_o = 0$ (fixed end), $u_A = u_B$ and $\theta_B = v_B/h$. Inserting the associated modal displacements from Eq. (3), together with EI and h values into Eq. (4),

$$\begin{Bmatrix} F_O \\ M_O \\ F_A \\ M_A \end{Bmatrix}_1 = \begin{Bmatrix} 2.55 \text{ kN} \\ -29.5 \text{ kN m} \\ -2.55 \text{ kN} \\ 19.3 \text{ kN m} \end{Bmatrix} \quad \text{and} \quad \begin{Bmatrix} F_O \\ M_O \\ F_A \\ M_A \end{Bmatrix}_2 = \begin{Bmatrix} -46.76 \text{ kN} \\ 86.95 \text{ kN m} \\ 46.76 \text{ kN} \\ 100.1 \text{ kN m} \end{Bmatrix}$$

Base shear force and base moment at O, and moment at A (SRSS combination):

$$V_b = \sqrt{(2.55)^2 + (46.76)^2} = 46.83 \text{ kN} \quad (\text{2nd mode dominant})$$

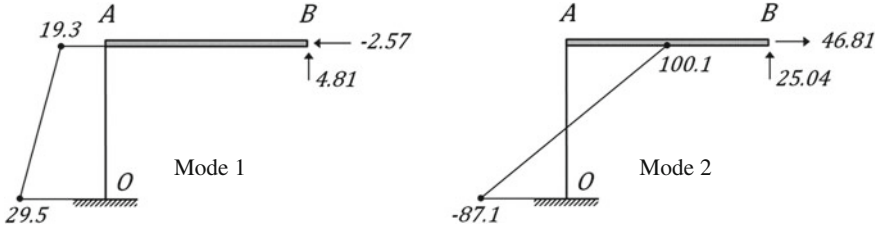
$$M_b = \sqrt{(29.5)^2 + (86.95)^2} = 91.82 \text{ kN m} \quad (\text{2nd mode dominant})$$

$$M_A = \sqrt{(19.3)^2 + (100.1)^2} = 101.94 \text{ kN m} \quad (\text{2nd mode dominant})$$

Equivalent static modal forces: From Eq. (5.60),

$$\underline{f}_{-n} = \frac{L_n}{M_n} (\underline{m} \underline{\phi}_n) \cdot S_{an} \quad ; \quad \underline{f}_{-1} = \begin{Bmatrix} -2.57 \\ 4.81 \end{Bmatrix}_{\text{kN}} \quad \text{and} \quad \underline{f}_{-2} = \begin{Bmatrix} 46.81 \\ 25.04 \end{Bmatrix}_{\text{kN}}$$

The modal forces and the associated modal moment diagrams of the column *OA* are shown on the frame below.



Modal base shear forces, base moments and moments at *A* can be calculated from statics. Then their SRSS combinations give the final values.

$$V_{b1} = -2.57, \quad V_{b2} = 46.81, \quad V_b = \sqrt{(2.57)^2 + (46.81)^2} = 46.88 \text{ kN}$$

$$M_{b1} = 29.5, \quad M_{b2} = -87.08, \quad M_b = \sqrt{(29.5)^2 + (87.08)^2} = 91.94 \text{ kN m}$$

$$M_{A1} = 19.3, \quad M_{A2} = 100.1, \quad M_A = \sqrt{(19.3)^2 + (100.1)^2} = 102.04 \text{ kN m}$$

These values are very close to the values calculated from stiffness analysis. The differences are due to truncation errors.

5.7 Limitations of Plane Frame (2D) Idealizations for 3D Frame Systems

We have developed the equations of motion and their solutions for 2D plane frame systems above. Employing plane frame models in seismic response analysis is indeed very instructive and simple. It is also a basic modeling approach in practice for ideal systems with perfectly symmetrical plan. However the actual 3D building systems under earthquake base excitation can be seldom modeled as 2D frame systems. The basic limitation for 2D modeling is symmetry both in mass and stiffness about both horizontal directions. A 3D frame plan having symmetrical stiffness distribution in both directions and uniformly distributed mass over the plan is shown in Fig. 5.11a. We may assume that the frame has 4 stories with similar floor plans. We may model this 3D frame with two different plane frames in the two orthogonal horizontal directions and analyze them separately. Each frame in the long and short horizontal directions are shown in Fig. 5.11b and c, respectively. The long frame ABCD represents the total stiffnesses and masses of parallel frames 123. Similarly, the short frame 123 represents the total stiffnesses and masses of

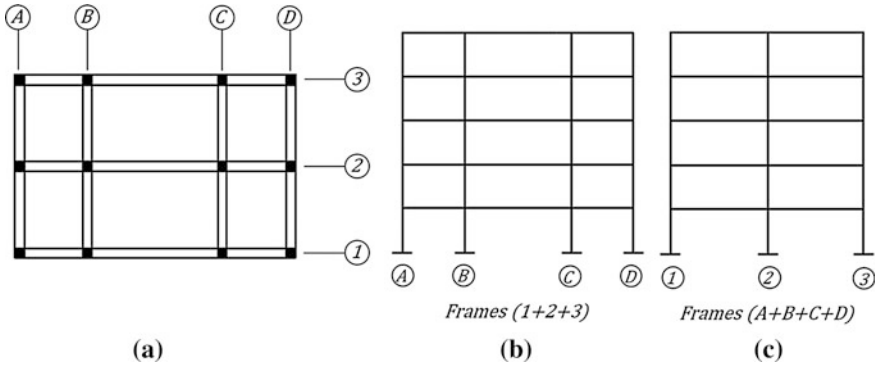


Fig. 5.11 2D representations of 3D frames with symmetrical distributions of stiffness and mass in plan

parallel frames ABCD. When symmetry is disturbed in one direction, then the other 2D representation is still valid. However 2D modeling of actual 3D structures is usually not possible in practice since asymmetry due to several causes is always introduced in design (accidental eccentricity, see Sect. 6.6.3).

Modeling and seismic analysis of 3D building structures with unsymmetrical distribution of stiffness is introduced in Chap. 6.

5.8 Nonlinear Static (Pushover) Analysis

Let's consider a simple, regular building structure, such as the one shown in Fig. 5.4. If the first vibration mode dominates seismic response under earthquake excitation, then an equivalent static lateral load analysis can be conducted with the first mode effective force vector f_{-1} ,

$$f_{-1} = \Gamma_1 \left(\frac{m\phi_{-1}}{M_1} \right) S_{a1}. \tag{5.65}$$

Equation (5.65) can be obtained from Eq. (5.53a, b) and $\Gamma_1 = \frac{L_1}{M_1}$. We can repeat Fig. 5.4 for the first mode in Fig. 5.12.

The building can be represented with a nonlinear structural model which permits flexural plastic hinge formation at member ends. A plastic hinge is a simplified representation of yielding member ends under flexural bending. Flexural yielding of a member section can be represented by the basic moment-curvature relationship shown in Fig. 5.13a. If the length of yielding sections at a member end is L_p , then the member-end curvatures ϕ along L_p can be converted to end rotation θ by assuming that curvature is approximately constant along the plastic hinge length L_p at the member end. Hence,

$$\theta \approx \phi \cdot L_p \tag{5.66}$$

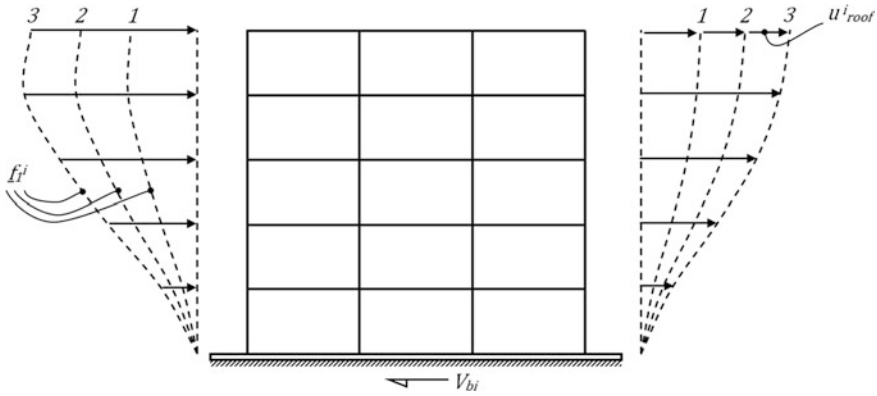


Fig. 5.12 Pushover analysis under incrementally applied first modal force vector f_{-1}

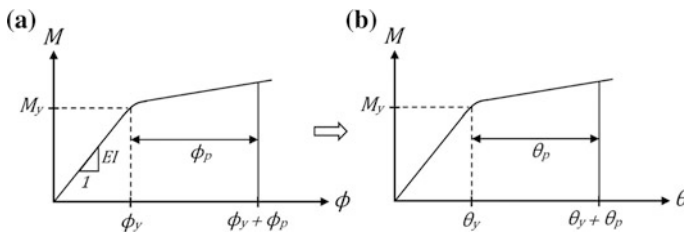


Fig. 5.13 Conversion of moment-curvature relationship into a moment-rotation relationship at a member end

The resulting moment-end rotation relationship is shown in Fig. 5.13b. In reinforced concrete frame members, L_p can be approximated as the half of effective member depth, i.e. $L_p = h/2$. This type of representation of the member-end yielding is called *lumped plasticity*. Since L_p is small compared to the member span length L , plastic hinges can be located at the member ends next to the joint in nonlinear modeling where maximum moments are expected to develop.

Then equivalent static lateral load analysis can be conducted incrementally under f_{-1} . During the incremental analysis, f_{-1} is applied in small increments as shown in Fig. 5.12.

$$\underline{f}_{-1}^i = \alpha_i \underline{f}_{-1}; \quad \alpha_i = 0.1, 0.2 \dots \tag{5.67}$$

α_i is sufficiently small, such as the fractions of 0.1. The base shear force at loading increment i is calculated from Eq. (5.62) for the first mode.

$$V_b^i = M_1^* \alpha_i S_{a1}. \tag{5.68}$$

The roof displacement shown in Fig. 5.7 can be obtained by using Eq. (5.48) for $n = 1$.

$$u_{roof} = \Gamma_1 \phi_{1N} S_{d1} = \Gamma_1 \phi_{1N} \frac{S_{a1}}{\omega_1^2}. \quad (5.69)$$

Here, ϕ_{1N} is the value of first mode eigenvector at the roof level N . Thus the roof displacement at the loading increment i becomes

$$u_{roof}^i = \Gamma_1 \phi_{1N} \alpha_i \frac{S_{a1}}{\omega_1^2}. \quad (5.70)$$

If V_b^i is plotted against u_{roof}^i , we obtain the capacity curve of the system which is responding in the first mode (equivalent SDOF system). We will investigate the capacity curve for linear elastic and nonlinear systems separately.

5.8.1 Capacity Curve for Linear Elastic Response

If the system is linear elastic, then the capacity curve is obtained as a straight line with the slope K_1 , as shown in Fig. 5.9a. We can convert the capacity curve in the $(V_b^i - u_{roof}^i)$ format to the $(S_{a1} - S_{d1})$ format by using the conversion equations:

$$\alpha_i S_{a1} = \frac{V_b^i}{M_1^*} \quad (5.71)$$

and

$$\alpha_i S_{d1} = \frac{u_{roof}^i}{\Gamma_1 \phi_{1N}}. \quad (5.72)$$

Equation (5.71) follows from Eq. (5.68), and Eq. (5.72) follows from Eq. (5.69), respectively.

Each point $(\alpha_i S_{a1} - \alpha_i S_{d1})$ can be plotted on the $(S_{a1} - S_{d1})$ plane to obtain the capacity curve in the acceleration-displacement format, as shown in Fig. 5.9b. It can be observed that the slope of this line is ω_1^2 , which follows from the $S_{a1} = \omega_1^2 S_{d1}$ relationship for an SDOF system.

5.8.2 Capacity Curve for Inelastic Response

When the elastic limit of the structural system is exceeded under lateral loads, inelastic response develops by the progressive yielding of member ends under increasing moments during incremental pushover analysis. Accordingly the

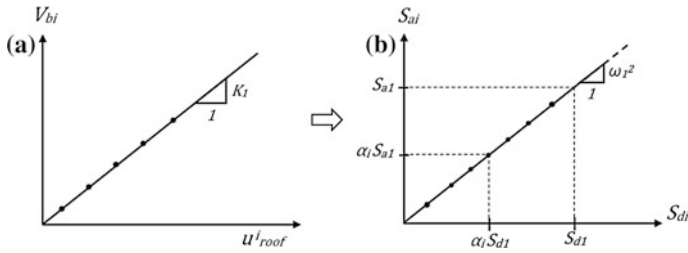


Fig. 5.14 Capacity curves for linear elastic response. **a** Base shear versus roof displacement; **b** response acceleration versus response displacement

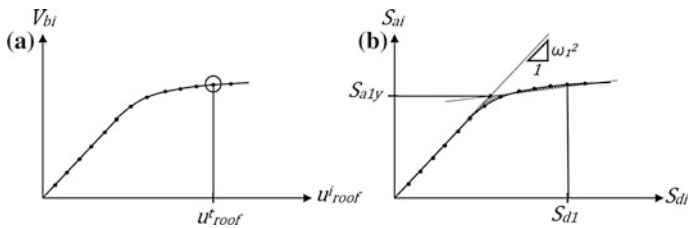


Fig. 5.15 Capacity curves for inelastic response. **a** Base shear versus roof displacement; **b** response acceleration versus response displacement

$(V_b^i - u_{roof}^i)$ relationship in Fig. 5.14a becomes a nonlinear curve as shown in Fig. 5.15a. This curve can be idealized with a bi-linear curve with the slope K_1 for the initial linear elastic segment, and βK_1 for the post-elastic segment where β is the strain hardening ratio of the capacity curve. The yield base shear force and the yield roof displacement can be identified from the intersection of two line segments of the idealized capacity curve.

This capacity curve can similarly be converted into the acceleration-displacement format by using the conversion equations, Eqs. (5.71) and (5.72). The resulting capacity curve and its idealized bi-linear representation are shown in Fig. 5.14b. In the bi-linear representation, the slope of the initial linear segment is ω_1^2 and the yielding segment is calculated such that the area between the actual and idealized curves are equal in the modal displacement range bounded by the linear elastic displacement S_{d1} .

5.8.3 Target Displacement Under Design Earthquake

Maximum internal forces and deformations of different members in a MDOF structural system usually develop at different instants of time under an earthquake ground excitation. If the structural system can be idealized as an equivalent SDOF

system responding at its first mode, then there is a single instant at which all internal forces and deformations become maximum. This is the time when the SDOF displacement is also maximum. If we can determine this maximum displacement, then we make the performance evaluation at the load step corresponding to this displacement. The maximum displacement demand of the equivalent SDOF system under an earthquake ground excitation is called the *target displacement*, and it is expressed in terms of the roof displacement in pushover analysis. We can use Eq. (5.69) for expressing the target roof displacement for a linear elastic system.

$$u_{roof}^t = \Gamma_1 \phi_{1N} S_{d1}^t = \Gamma_1 \phi_{1N} \frac{S_{a1}^t}{\omega_1^2}. \quad (5.73)$$

Here, S_{d1}^t is the target (maximum) value of spectral displacement and S_{a1}^t is the target value of spectral pseudo acceleration under an earthquake ground excitation. These values correspond to each other through $S_{d1}^t = \omega_1^2 S_{a1}^t$ and they are marked on Fig. 5.14 for a linear elastic system. In fact S_{a1}^t can be directly obtained from the acceleration spectrum of the ground motion, or the linear elastic design spectrum at $T = T_1$ as shown in Fig. 5.16.

When the response is inelastic, target modal displacement S_{d1}^t is either calculated by solving the nonlinear equation of motion of the bi-linear system in Fig. 5.9b under a ground excitation, or by using its inelastic spectrum as explained in Sect. 3.6. However if the ground motion is defined by a design spectrum, then S_{d1}^t is estimated by using the equal displacement rule.

$$u_{roof}^t = \Gamma_1 \phi_{1N} \frac{S_{a1}^t}{\omega_1^2} \quad T_1 \geq T_B. \quad (5.74a)$$

$$u_{roof}^t = \Gamma_1 \phi_{1N} \frac{S_{a1}^t}{\omega_1^2} C_1 \quad T_1 < T_B. \quad (5.74b)$$

$$C_1 = \frac{1 + (R_{y1} - 1) \frac{T_B}{T_1}}{R_{y1}}; \quad R_{y1} = \frac{S_{a1}^t}{S_{a1y}}. \quad (5.74c)$$

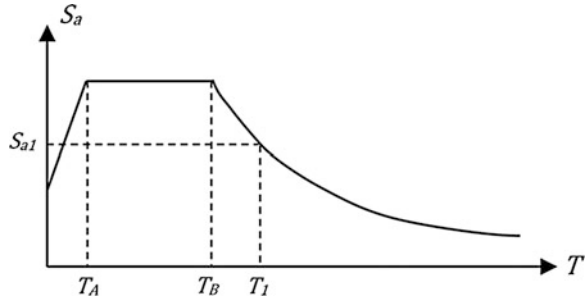
The yield pseudo acceleration S_{a1y} is shown in Fig. 5.15b.

5.8.3.1 Summary: Pushover Analysis

Nonlinear static (pushover) analysis procedure can be summarized with the following steps.

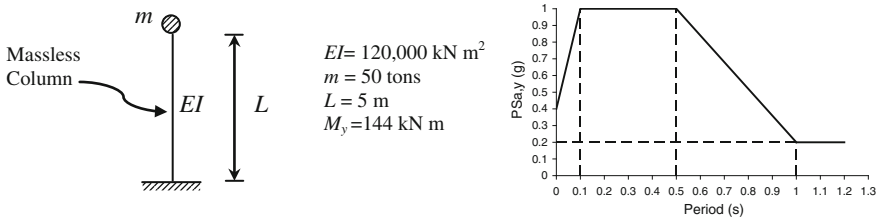
1. Eigenvalue analysis of the linear elastic system: Determine ω_1^2 and $\underline{\phi}_1$. Also calculate $T_1 = 2\pi / \omega_1$ and Γ_1 .
2. Determine S_{a1} at $T = T_1$ from the response spectrum. Calculate $f_{\underline{1}} = \Gamma_1 \left(\underline{m} \underline{\phi}_1 \right) S_{a1}$.

Fig. 5.16 Target modal displacement and the corresponding target acceleration of a linear elastic SDOF system



3. Prepare the nonlinear structural model of the system, with plastic hinges assigned at the ends of frame members defined by moment-rotation relationships.
4. Conduct incremental pushover analysis under $f_{-}^i = \alpha_i f_{-1}$; $\alpha_i = 0.1, 0.2, \dots$. Then plot the $(V_b^i - u_{roof}^i)$ curve, i.e. the capacity diagram.
5. Convert the capacity diagram into a modal capacity diagram $(S_{a1} - S_{d1})$ by using Eqs. (5.71) and (5.72).
6. Calculate the target roof displacement from Eqs. (5.74a) and (5.74b). Then go back to step 4 and retrieve all forces and displacements from the loading step producing the roof displacement closest to the target roof displacement.

Example 5.12 Determine the capacity curve and the target displacement of the cantilever structure by using nonlinear static analysis. Use the given spectrum. Assume that the plastic hinge develops at the base of the column with negligible length, and it is perfectly elasto-plastic.



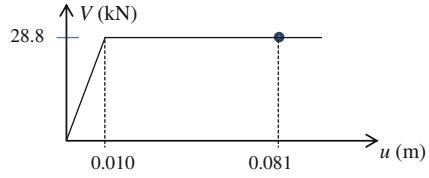
Solution

$$k = 3EI/L^3 = 2880 \frac{\text{kN}}{\text{m}}; \quad \omega = \sqrt{\frac{k}{m}} = \sqrt{\frac{2880}{50}} = 7.6 \frac{\text{rad}}{\text{s}}; \quad T = \frac{2\pi}{\omega} = 0.828 \text{ s}$$

$$S_a = \left(0.2 + \frac{0.8}{0.5}(1 - 0.828) \right) g = 4.66 \text{ m/s}^2$$

$$V_y = \frac{M_y}{L} = \frac{144}{5} = 28.8 \text{ kN}; \quad u_y = \frac{V_y}{k} = 0.01 \text{ m}$$

Target displacement: $T > T_B$, hence



$$u_{roof}^t = \Gamma_1 \phi_{1N} \frac{S_a}{\omega^2} = 1 \cdot 1 \cdot \frac{4.66}{(7.6)^2} = 0.081 \text{ m}$$

5.9 Seismic Response Analysis of Base Isolated Buildings

Seismic isolation system is a laterally soft but vertically stiff layer composed of seismic isolators, inserted between the base of the building structure and its foundation. Sometimes an isolation interface can be provided between the lower, laterally stiff and upper, laterally flexible parts of a building. Seismic isolation devices installed between the reinforced concrete ground story and steel upper structure are shown in Fig. 5.17.

5.9.1 General Principles of Base Isolation

A pair of fixed-base and a base isolated building is shown schematically in Fig. 5.17. The building structure itself has a lateral stiffness of k and an average damping ratio of ζ . The isolation layer on the other hand has a lateral stiffness k' and damping ratio ζ' where $k' \ll k$ and $\zeta' \gg \zeta$. The fixed-based building has a fundamental period of T , related to its lateral stiffness k and mass m . Fundamental vibration period T' of the base isolated building however is controlled by the low equivalent (secant) stiffness k' of the isolation layer, as explained in Sect. 5.9.2 below. Mass of the isolated building ($m + m'$) is also larger than the building mass m due to the added mass m' of the isolation layer. Accordingly its period is much longer than the period of the fixed-based building, i.e. $T' \gg T$. A similar situation also exists for damping. The overall damping of the isolated system is controlled by the high damping of the isolation layer. Hence, a base isolated building can be considered as a SDOF system in practice, with a vibration period T' and damping ratio ζ' , as shown in Example 5.13.



Fig. 5.17 Base isolation interface between concrete basement and steel upper structure of a building

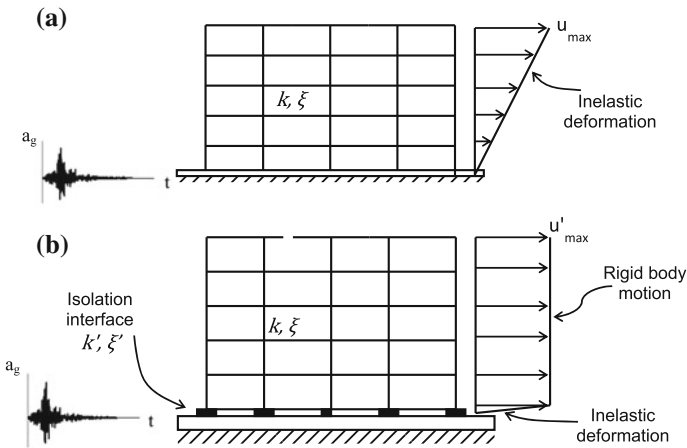


Fig. 5.18 a A fixed-based, and b a base isolated building

A fixed-based conventional building which is designed under reduced seismic design forces is expected to exhibit inelastic deformation response under a design level earthquake ground motion a_g (Fig. 5.18a). On the other hand, a building structure on an isolation layer displays rigid body motion with negligible lateral deformation. All inelastic seismic deformations are accommodated by the seismic isolators at the isolation layer as shown in Fig. 5.18b.

Seismic isolation modifies the dynamic characteristics of structures in two ways: Lengthening the vibration period, and increasing damping. Lengthening of vibration period to about 3 s reduces seismic forces on the structure significantly since most ground motions do not excite vibrating systems at such low

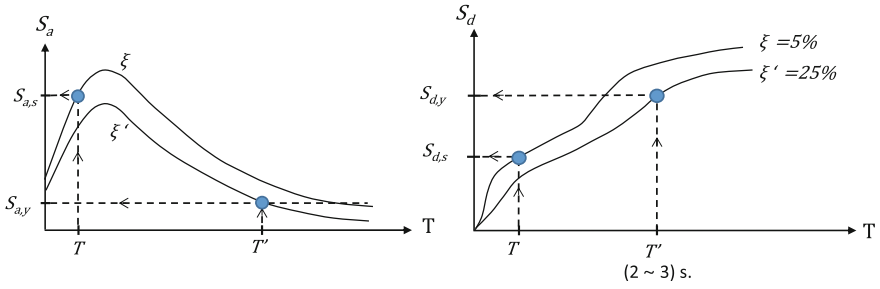


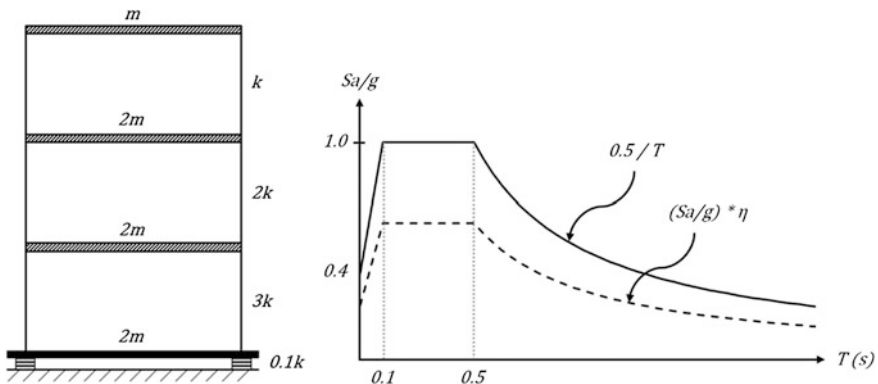
Fig. 5.19 Comparison of the spectral accelerations and displacements of a fixed-base (T, ξ) and a base isolated building (T', ξ'). Subscripts s are for the fixed-base structure and y for the isolated building, respectively

frequencies. However seismic displacements increase due to low lateral stiffness corresponding to long vibration periods of 2.5–3.0 s. Increased damping added by the isolators compensates the increase of displacements partly, but displacement control remains as a challenge. Seismic forces and displacements of a fixed-base and an isolated building are compared in Fig. 5.19. The reduction in the base shear force demand of the base isolated system compared to the fixed-base system is given by,

$$R = \frac{S_{a,s}}{S_{a,y}} \tag{5.75}$$

Example 5.13 The shear frame in Example 5.8 is base isolated with an elastic isolation system which has a lateral stiffness of $0.1k$ and a damping ratio of 0.20 . The mass of the foundation beam is also $2m$.

- (a) Calculate the modal periods and mode shapes.
- (b) Calculate modal displacements and modal base shear forces under the given design spectrum. Combine the displacements and base shears by SRSS for calculating the total base shear force and story displacements.



Solution

(a) Eigenvalue analysis gives,

$$\underline{\Phi}_1 = \begin{Bmatrix} 0.0278 \\ 0.0284 \\ 0.0290 \\ 0.0295 \end{Bmatrix} \quad \underline{\Phi}_2 = \begin{Bmatrix} 0.0290 \\ 0.0159 \\ -0.0152 \\ -0.0554 \end{Bmatrix} \quad \underline{\Phi}_3 = \begin{Bmatrix} -0.0230 \\ 0.0055 \\ 0.0378 \\ -0.0417 \end{Bmatrix}$$

$$\underline{\Phi}_4 = \begin{Bmatrix} 0.0268 \\ -0.0420 \\ 0.0188 \\ -0.0065 \end{Bmatrix}$$

$$T_1 = 1.885 \text{ s} \quad T_2 = 0.261 \text{ s} \quad T_3 = 0.161 \text{ s} \quad T_4 = 0.112 \text{ s}$$

(b) Spectral accelerations for all 4 modes have been obtained from the design spectrum reduced by $\eta = \sqrt{(5 + \xi)/10}$ for 20 % damping. It is assumed that damping in all modes is controlled by damping of the isolation layer. This is practically reasonable, however theoretically incorrect. Damping of the isolated system is 20 % at the isolation level and 5 % at the frame level. Such systems with two different damping sources have “non-classical” damping and their modal damping ratios cannot be calculated by the classical procedures of structural dynamics. Accordingly, assuming 20 % damping in all modes for brevity,

Modal displacements (meters)

$$\underline{u}_1 = \begin{Bmatrix} 0.1439 \\ 0.1474 \\ 0.1505 \\ 0.1526 \end{Bmatrix} \quad \underline{u}_2 = \begin{Bmatrix} 0.2163 \\ 0.1189 \\ -0.1135 \\ -0.4136 \end{Bmatrix} \quad 10^{-3} \quad \underline{u}_3 = \begin{Bmatrix} 0.1980 \\ -0.0471 \\ -0.3249 \\ 0.3584 \end{Bmatrix} \quad 10^{-4}$$

$$\underline{u}_4 = \begin{Bmatrix} 0.0638 \\ -0.1002 \\ 0.0449 \\ -0.0155 \end{Bmatrix} \quad 10^{-4}$$

Modal forces (kN)

$$\underline{F}_1 = \begin{Bmatrix} 559.58 \\ 573.05 \\ 585.30 \\ 296.77 \end{Bmatrix} \quad \underline{F}_2 = \begin{Bmatrix} 43.94 \\ 24.15 \\ -23.06 \\ -42.01 \end{Bmatrix} \quad \underline{F}_3 = \begin{Bmatrix} 10.57 \\ -2.51 \\ -17.34 \\ 9.57 \end{Bmatrix} \quad \underline{F}_4 = \begin{Bmatrix} 6.98 \\ -10.95 \\ 4.91 \\ -0.85 \end{Bmatrix}$$

Modal base shears at the isolation level

$$V_{b1} = 2014.79 \text{ kN}, V_{b2} = 3.03 \text{ kN}, V_{b3} = 0.28 \text{ kN}, V_{b4} = 0.09 \text{ kN}, \\ V_{b,SRSS} = 2014.8 \text{ kN}$$

Modal base shears above the isolation system (Frame modal base shears)

$$V'_{bf1} = 1455.1 \text{ kN}, V'_{bf2} = -40.9 \text{ kN}, V'_{bf3} = -10.3 \text{ kN}, \\ V_{bf4} = -6.3 \text{ kN}, V_{bf,SRSS} = 1455.7 \text{ kN}$$

When the base shear of the isolated frame is compared with the base shear force of the fixed-base frame from Example 5.9, the reduction in frame base shear can be calculated as,

$$R = \frac{7.294}{1.455} = 5.01.$$

It is evident from Example 5.13 that first mode strongly dominates lateral displacements and the base shears as expected. Then a simplified analysis can be justified. A SDOF system can be defined such that the entire lateral displacement response is accommodated by the isolation layer, and the entire mass of the superstructure (frame) and the foundation is moving as a rigid body on the isolation layer. Then the fundamental period can be calculated from,

$$T_1 = 2\pi\sqrt{\frac{\sum m}{k_b}} = 2\pi\sqrt{\frac{7m}{0.1k}} = 1.86 \text{ s}$$

which is very close to T_1 calculated from eigenvalue analysis. Similarly, the base shear force at the isolation layer is

$$V_b = (7m) \cdot S_a(T_1, \xi_b) = (7m) \cdot \frac{0.5}{1.86} g \cdot 0.632 = 2042 \text{ kN}$$

and the base shear force above the isolation system (frame base shear) is,

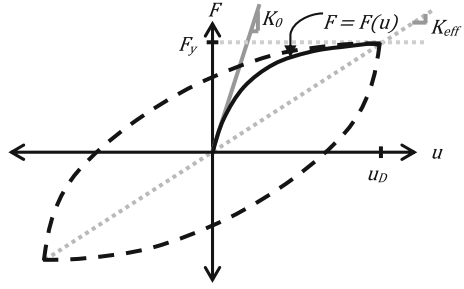
$$V_{bf} = (5m) \cdot S_a(T_1, \xi_b) = (5m) \cdot \frac{0.5}{1.86} g \cdot 0.632 = 1458 \text{ kN}.$$

These values are sufficiently close to the results of response spectrum analysis, i.e. 2015 kN and 1456 kN, respectively, calculated above.

5.9.2 Equivalent Linear Analysis of Base Isolation Systems with Inelastic Response

The isolation systems introduced above consist of a linear elastic flexible layer with high damping. Actually this is the equivalent linear idealization of a non-linear, stable hysteretic system with low yield strength and an approximate

Fig. 5.20 Hysteretic response of a typical isolation system



bi-linear hysteresis envelope. Let’s consider an isolation system which is composed of several isolators, and the lateral force-displacement relationship of the entire isolation system is expressed by the hysteresis envelope given in Fig. 5.20.

The initial stiffness K_0 is usually high for both the rubber and curved surface sliding isolator bearings. The yielding force is usually set to 5–10 % of the building weight, in order to produce the inelastic isolator displacements shown in Fig. 5.18b. Displacement of the isolation system u_D is the basic outcome of the equivalent linear analysis procedure. The analysis procedure is given below in terms of simple analysis steps. This is an iterative procedure since an inelastic system is converted into an equivalent linear SDOF system.

1. Assume T_{eff} (usually 2.5–3.0 s).
2. $K_{eff} = 4\pi^2 \frac{M}{T_{eff}^2}$ where M is the total mass of the superstructure.
3. $u_0 = \frac{F_y}{K_{eff}}$ where F_y is the yield strength of the isolation system (Fig. 5.15)
4. $u_i = \frac{M \cdot S_a(T_{eff}, \zeta_{eff})}{K_{eff}}$ where ζ_{eff} is the equivalent damping of the isolation system.
5. Check $(u_i - u_0)/u_i < 0.05$. If YES, then u_i is the design displacement of the isolator system.
6. If NO, then recalculate $K_{eff} = F(u_i)/u_i$ and $T_{eff} = 2\pi\sqrt{M/K_{eff}}$. Note that K_{eff} is the secant stiffness of the equivalent linear system (see Fig. 5.20).
7. Go to Step 4 and calculate u_{i+1} , then check convergence again.
8. Continue iterations (steps 4–6) until convergence is achieved.

Example 5.14 The shear frame in Example 5.13 is base isolated with an elastic-perfectly plastic isolation system which has an initial lateral stiffness of $3k$ and a damping ratio of 0.20. The lateral force capacity of the isolation system is $0.1W$. Determine the design displacement, effective stiffness, effective period and base shear force under the design spectrum given in Example 5.12, by the using equivalent linear analysis procedure.

Solution

The total mass of the isolated system is $M = 7m = 1,225,000$ kg, $W = Mg = 12,000$ kN and yield force $F_y = 0.1 W = 1,200$ kN. Damping reduction factor $1/\eta = 0.632$ from Eq. (4.10) for 20 % damping.

1. Let $T_{eff} = 2.5$ s.
 2. $K_{eff} = 4\pi^2 \frac{M}{T_{eff}^2} = 7,737,769$ N/m
 3. $u_0 = \frac{F_y}{K_{eff}} = 0.155$ m
 4. $S_a = (0.5/2.5)g$ $\eta = 1.23$ m/s² and $u_1 = \frac{M \cdot S_a}{K_{eff}} = 0.196$ m
 5. $\frac{u_1 - u_0}{u_1} = 0.21 > 0.05$. Continue with the updated equivalent stiffness and period.
 6. $K_{eff} = \frac{F(u_1)}{u_1} = 6,122,450 \frac{\text{kN}}{\text{m}}$ and $T_{eff} = 2\pi\sqrt{M/K_{eff}} = 2.81$ s
 7. $S_a = (0.5/2.81)g$ $\eta = 1.103$ m/s² and $u_2 = \frac{M \cdot S_a}{K_{eff}} = 0.221$ m
 8. $\frac{u_2 - u_1}{u_2} = 0.11 > 0.05$. Continue iteration with the updated equivalent stiffness and period.
 6. $K_{eff} = \frac{F(u_2)}{u_2} = 5,429,864 \frac{\text{kN}}{\text{m}}$ and $T_{eff} = 2\pi\sqrt{M/K_{eff}} = 2.984$ s
 7. $S_a = (0.5/2.984)g$ $\eta = 1.039$ m/s² and $u_3 = \frac{M \cdot S_a}{K_{eff}} = 0.234$ m
 8. $\frac{u_3 - u_2}{u_3} = 0.055 > 0.05$. Continue iteration with the updated equivalent stiffness and period.
 6. $K_{eff} = \frac{F(u_3)}{u_3} = 5,128,200 \frac{\text{kN}}{\text{m}}$ and $T_{eff} = 2\pi\sqrt{M/K_{eff}} = 3.07$ s
 7. $S_a = (0.5/3.07)g$ $\eta = 1.01$ m/s² and $u_4 = \frac{M \cdot S_a}{K_{eff}} = 0.241$ m
 8. $\frac{u_4 - u_3}{u_4} = 0.03 < 0.05$. Convergence is achieved.
- $$u_D = 0.241 \text{ m}, T_{eff} = 3.07 \text{ s}, K_{eff} = 5,128,200 \frac{\text{kN}}{\text{m}}.$$

Base shear force of the frame (above the foundation beam):

$$V'_b = (5m)S_a = 5 \cdot 175,000 \text{ kg} \cdot 1.01 \frac{\text{m}}{\text{s}^2} = 883.758 \text{ kN} \approx 884 \text{ kN}.$$

Reduction in base shear force (see Example 5.13): $R = \frac{7.294}{884} = 8.25$.

Note that this reduction is obtained only by the yielding of isolation system, not by the inelastic deformations (damage) of structural members as in ductile frames.

5.9.3 Critical Issues in Base Isolation

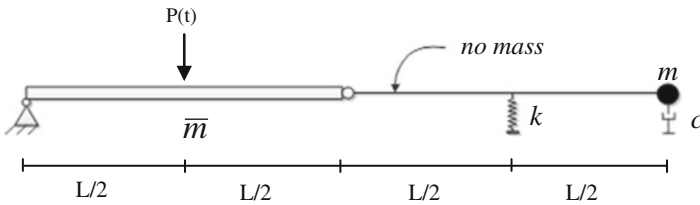
There are two critical issues in seismic isolation. One is the selection of design ground motions. Since ground motions are inherently uncertain, there is no guarantee that a future ground motion does not excite the isolated structure beyond its maximum expected displacement considered in design. This requires a rigorous seismological assessment of the construction site for selecting the design ground

motions appropriately (DSHA or PSHA). The second issue is the conformance of the produced isolation devices to the design specifications. This is a critical issue since any failure to satisfy design demands may lead to non-functioning of the isolation system during an earthquake and eventually lead to damage in the isolated structural system. This risk is handled by rigorous testing procedures applied to the isolators in advance. Once the risks taken by the uncertainty of ground motions and deficiencies or variations in production are minimized, seismic isolation is an ideal system for seismic protection since the “immediate occupancy” performance level under a strong earthquake can only be achieved by seismic isolation at the current state of knowledge and practice.

Exercises

1. A system that is composed of two rigid beams is given below. ($\bar{m}L = m$)

- (a) Determine the equations of motion. Use lumped-mass assumption.
- (b) Determine the eigenvalues and eigenvectors.



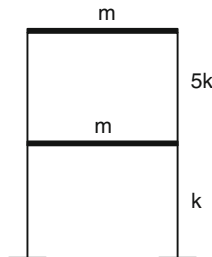
Answers

$$(a) \begin{bmatrix} \frac{\bar{m}L}{2} & 0 \\ 0 & m \end{bmatrix} \begin{bmatrix} \ddot{u}_1 \\ \ddot{u}_2 \end{bmatrix} + \begin{bmatrix} 0 & 0 \\ 0 & c \end{bmatrix} \begin{bmatrix} \dot{u}_1 \\ \dot{u}_2 \end{bmatrix} + \begin{bmatrix} 0.25k & 0.25k \\ 0.25k & 0.25k \end{bmatrix} \begin{bmatrix} u_1 \\ u_2 \end{bmatrix} = \begin{bmatrix} \frac{P}{2} \\ 0 \end{bmatrix}$$

$$(b) \omega_1 = 0 \quad \varphi_1 = \begin{bmatrix} 1 \\ -1 \end{bmatrix} \quad \omega_2 = \sqrt{\frac{3k}{4m}} \quad \varphi_2 = \begin{bmatrix} 1 \\ 0.5 \end{bmatrix}$$

2. For the frame with rigid girders given on the right

- (a) Determine the natural frequencies and mode shapes,
- (b) Show that the mode shapes are orthogonal with respect to the mass and stiffness matrices.



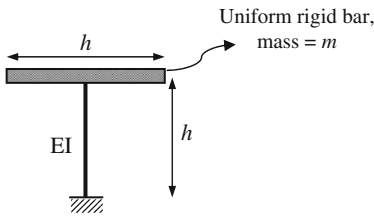
Answers

$$\omega_1 = 0.69\sqrt{\frac{k}{m}} \quad \varphi_1 = \begin{bmatrix} 0.905 \\ 1.0 \end{bmatrix}$$

$$\omega_2 = 3.24\sqrt{\frac{k}{m}} \quad \varphi_2 = \begin{bmatrix} -1.106 \\ 1.0 \end{bmatrix}$$

3. For the MDOF system given below,

- (a) Determine the equation of free vibration.
- (b) Determine eigenvalues and eigenvectors for $h = 1 \text{ m}$, $EI = 1 \text{ kN/m}^2$ and $m = 1 \text{ ton}$.
- (c) Normalize the eigenvectors with respect to mass.
- (d) Prove that the eigenvectors are orthogonal with respect to mass matrix.



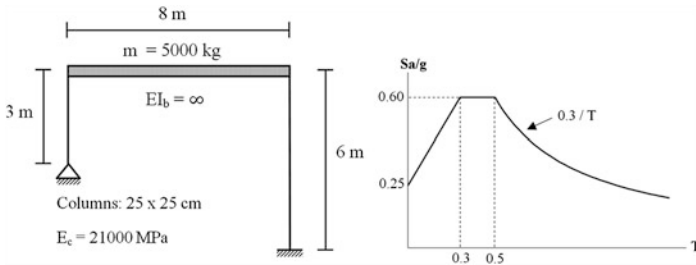
Frame Element:

$$k = \frac{EI}{h^3} \begin{bmatrix} 12 & -6h & -12 & -6h \\ -6h & 4h^2 & 6h & 2h^2 \\ -12 & 6h & 12 & 6h \\ -6h & 2h^2 & 6h & 4h^2 \end{bmatrix}$$

Answers

- (a) $\begin{bmatrix} m & 0 \\ 0 & \frac{mh^2}{12} \end{bmatrix} \begin{Bmatrix} \ddot{u} \\ \ddot{\theta} \end{Bmatrix} + \frac{EI}{h^3} \begin{bmatrix} 12 & 6h \\ 6h & 4h^2 \end{bmatrix} \begin{Bmatrix} u \\ \theta \end{Bmatrix} = \begin{Bmatrix} 0 \\ 0 \end{Bmatrix}$
- (b) $\omega_1 = 1.58 \text{ rad/s}$; $\omega_2 = 7.58 \text{ rad/s}$

4. Determine the moment diagram of all members of the linear elastic frame below under the given acceleration response spectrum. Ignore the mass of columns.



Answers

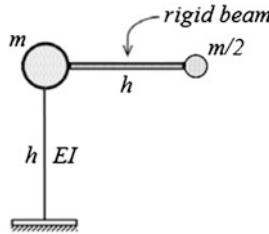
Left column, $M_{\text{bot}} = 0$, $M_{\text{top}} = 58.86 \text{ kN m}$; right column, $M_{\text{bot}} = -29.60 \text{ kN m}$, $M_{\text{top}} = -29.60 \text{ kN m}$

5. If the frame in Problem 4 has an elasto-plastic behavior with a base shear capacity of $W/6$, calculate its maximum displacement for a ductility factor of 5.

Answer

$$u_{\max} = 0.0359 \text{ m}$$

6. (a) Determine the eigenvectors and eigenvalues of the system given below.
 (b) Normalize the eigenvectors with respect to modal mass.
 (c) Prove that the eigenvectors are orthogonal with respect to the mass matrix.



Answer

Choosing u and v as the translation DOF's at the tip of the cantilever;

(a) $\omega_1^2 = 1.072 \left(\frac{EI}{mh^3} \right); \omega_2^2 = 14.928 \left(\frac{EI}{mh^3} \right)$

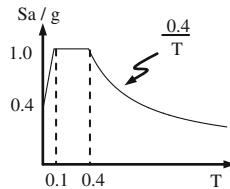
(b) $\underline{\phi}_1 = \begin{bmatrix} 0.577 \\ 1 \end{bmatrix}; \underline{\phi}_2 = \begin{bmatrix} 0.577 \\ -1 \end{bmatrix}$

7. A five story shear building is given, where the lateral stiffnesses are k , the masses are m and the heights are h meters for all stories. The first two eigenvalues and eigenvectors are given below.

$$\underline{\phi}_1 = \begin{Bmatrix} 0.334 \\ 0.641 \\ 0.895 \\ 1.078 \\ 1.173 \end{Bmatrix}$$

$$\underline{\phi}_2 = \begin{Bmatrix} -0.895 \\ -1.173 \\ -0.641 \\ 0.334 \\ 1.078 \end{Bmatrix}$$

$$\begin{aligned} m &= 0.259 \text{ ton} \\ w_1 &= 5.7 \text{ rad/s} \\ w_2 &= 16.6 \text{ rad/s} \\ g &= 9.81 \text{ m/s}^2 \end{aligned}$$



- (a) Determine the modal force vectors ($n = 1, 2$) for the earthquake spectrum given.
 (b) Determine the story displacements by using the first two modes and SRSS combination.
 (c) Determine the end moments of first story columns.

Answers

$$(a) \underline{f}_1 = \begin{bmatrix} 0.33 \\ 0.63 \\ 0.88 \\ 1.06 \\ 1.15 \end{bmatrix} \text{ kN} \quad \underline{f}_2 = \begin{bmatrix} 0.76 \\ 1.00 \\ 0.55 \\ -0.29 \\ -0.92 \end{bmatrix} \text{ kN}$$

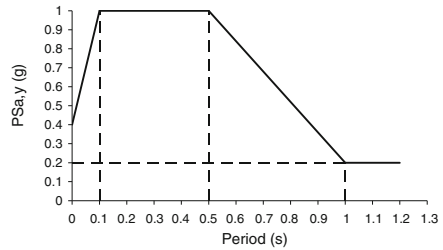
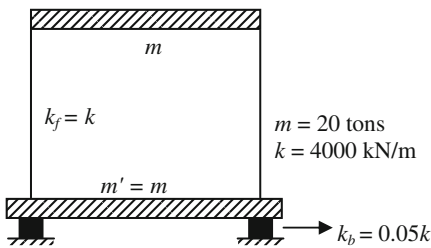
$$(b) \underline{u} = \begin{bmatrix} 0.0406 \\ 0.0765 \\ 0.1053 \\ 0.1266 \\ 0.1283 \end{bmatrix} \text{ m}$$

$$(c) M_{top} = M_{bot} = 1.052 h(\text{kN m})$$

8. Calculate the base shear forces and displacements of the isolated system by using

- (a) Complete mode superposition, calculate each mode separately.
- (b) Rigid structure approximation.
- (c) Compare and discuss the results.

Note k_f is the total lateral stiffness of the frame. It is assumed that the isolation system has the same damping with the frame, represented by the given acceleration spectrum.



Answers

Degrees of freedom: $u_1 = u_b$ (base), $u_2 = u_t$ (superstructure):

$$(a) \underline{u}_1 = \begin{Bmatrix} 0,3924 \\ 0,4022 \end{Bmatrix} m \quad \underline{u}_2 = \begin{Bmatrix} 3,076 * 10^{-4} \\ -3 * 10^{-4} \end{Bmatrix} m \quad \underline{u}_{total} = \begin{Bmatrix} 0,3927 \\ -0,4019 \end{Bmatrix} m$$

$$\underline{f}_1 = \begin{Bmatrix} 38,75 \\ 39,72 \end{Bmatrix} kN \quad \underline{f}_2 = \begin{Bmatrix} 2,49 \\ -2,43 \end{Bmatrix} kN \quad \underline{f}_{total} = \begin{Bmatrix} 41,24 \\ 37,29 \end{Bmatrix} kN$$

$$V_1 = 78.47 \text{ kN} \quad V_2 = 0.0615 \text{ kN} \quad V_b = 78.53 \text{ kN}$$

(b) $u_t = u_b$ (rigid structure) $\underline{u}' = \begin{Bmatrix} 0.3974 \\ 0.3974 \end{Bmatrix} m$ $V'_b = 78.48 \text{ kN}$.

(c) Structural displacements and base shears obtained from parts a and b are very close, therefore it can be concluded that rigid structure approximation is quite reasonable in terms of estimating the response of a base-isolated structure.

9. The single story frame given in Problem 8 is base isolated by a system which has an elastic-perfectly plastic hysteresis envelope. The lateral force capacity of the isolation system is $0.1 W$, and the damping ratio is 0.25. Determine the design displacement, effective stiffness and effective period under the design spectrum given in Problem 7, by using equivalent linear analysis.

Answer

$$u = 0.118 \text{ m}, T_{\text{eff}} = 2.23 \text{ s}, K_{\text{eff}} = 320 \text{ kN/m}.$$

Chapter 6

Analysis Procedures and Seismic Design Principles for Building Structures

Abstract Seismic analysis procedures and design principles are developed for building structures in this Chapter. Dynamic degrees of freedom are defined at each story by using the rigid diaphragm assumption, leading to a diagonal mass matrix. Stiffness matrix is derived for 3D buildings with unsymmetrical stiffness distribution in plan, leading to a coupled stiffness matrix. The effect of unsymmetrical stiffness distribution on the mode shapes is discussed, with emphasis on torsional coupling. Modal response spectrum analysis and equivalent lateral load procedure are introduced in the general seismic code format. Basic design principles and performance requirements for buildings are reviewed. Structural irregularities given in seismic codes and their effect on analysis procedure selection are discussed. The concept of seismic deformation control associated with interstory drift limits, second order effects and pounding is explained.

6.1 Introduction

The analysis procedures introduced in [Chap. 5](#) were developed for simple plane frames since the basic concepts of eigenvalue analysis and forced vibration analysis under earthquake excitation can be explained more clearly on simple, idealized structural systems. The actual buildings in engineering practice however are more complicated. Their mass and stiffness properties are spatially distributed, hence 3D structural models are required for their analysis. Usually the distribution of stiffness and/or mass in plan are not symmetrical about the horizontal axes in building structures which complicates dynamic analysis due to torsional coupling. The analysis procedures in seismic codes intend to consider all conceivable uncertainties related to the building characteristics and calculated response. They also exploit building properties which may lead to simplifications in analytical models and dynamic analysis procedures. Rigid floor diaphragm is the most prominent property of buildings which cause enormous reduction in the number of dynamic degrees of freedom.

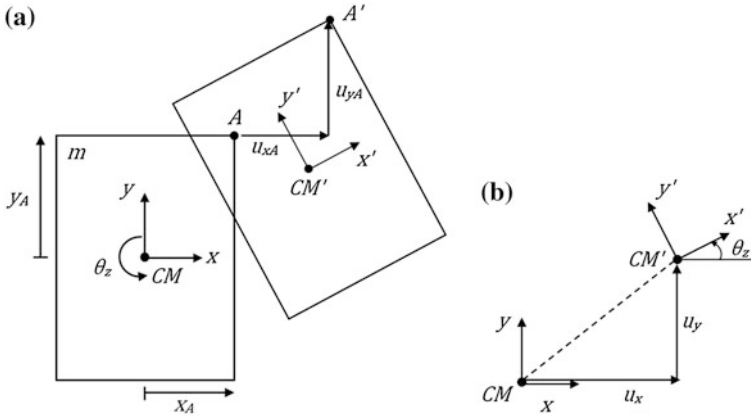


Fig. 6.1 a Motion of a rigid slab in its own plane, b Motion of the centre of mass

6.2 Rigid Floor Diaphragms and Dynamic Degrees of Freedom in Buildings

When the floor slabs act as rigid diaphragms in their own plane, then the motion of each slab during an earthquake can be defined by three dynamic degrees of freedom defined at its centre of mass. On the other hand, almost the entire mass of a building is confined to the slabs (concrete slab, cover, beams, live loads, hung ceilings, etc.). Only the columns and walls are not a part of the slab system; however their masses can be distributed evenly to the adjacent slabs at top and bottom. Accordingly, the inertial forces which act on the story masses during an earthquake can be defined on the slabs, at their centres of mass.

Let's consider a rigid slab diaphragm with mass m moving in its own plane. Two consecutive positions of the rigid slab are shown in Fig. 6.1a with the local coordinate axes $x - y$ and $x' - y'$, respectively. The horizontal motion of the centre of mass in the plane of motion is sketched in Fig. 6.1b. The horizontal motion of the corner point A (u_{xA}, u_{yA}) can be expressed in terms of the translational motion of the centre of mass (u_x, u_y), rotation of the rigid slab θ_z about its centre of mass, and the position of A with respect to the centre of mass (x_A, y_A).

$$u_{xA} = u_x - \theta_z \cdot y_A \tag{6.1a}$$

$$u_{yA} = u_y + \theta_z \cdot x_A \tag{6.1b}$$

Hence, the motion of the floor slab in the horizontal plane can be expressed in terms of two translational and one rotational component of motion of its centre of mass.

u_x, u_y and θ_z defined at the mass center of each floor are considered as the *dynamic degrees of freedom* ($3 \times N$ for an N -story 3D frame) whereas all other

DOF's are identified as the *static degrees of freedom* because a mass is not assigned to them (column and beam end rotations, slab edge rotations). Hence rigid diaphragm assumption leads to static condensation in building frames. It is assumed here that vertical deformations are very small compared to lateral deformations since structural systems are usually very stiff in the vertical direction. Therefore the vertical component of floor motion can be ignored.

Dynamic forces do not act on static DOF's. Accordingly, the dynamic displacement vector in an N-story 3D building structure with rigid floor diaphragms takes the form,

$$\underline{u}_d^T = \{ | u_{x1} \quad u_{y1} \quad u_{01} | u_{x2} \quad u_{y2} \quad u_{02} | \dots | u_{xN} \quad u_{yN} \quad u_{0N} | \}. \quad (6.2)$$

The rigid floor diaphragm assumption should be verified according to seismic code requirements. When the ratio of the area of floor cutouts to the total floor area is larger than a limit (generally 1/3), or the slab is not stiff enough in its own plane to transmit the lateral inertial forces to vertical elements between the stories without in-plane deformations (such as the large span steel truss roofs or timber slabs), then the simplified definition of inertial force resultants at the slab centre of mass is not permitted.

6.3 Equations of Motion for Buildings Under Earthquake Base Excitation

The equation of motion for the statically condensed system with rigid diaphragms under x or y direction of ground motion is obtained from Eq. (5.6)

$$\underline{m} \ddot{\underline{u}}_d + \underline{k}_d \underline{u}_d = -\underline{m} \underline{l}_i \ddot{u}_{gi} : i = x \text{ or } y \quad (6.3)$$

where

$$\underline{l}_x^T = \{ | 1 \quad 0 \quad 0 | 1 \quad 0 \quad 0 | \dots | 1 \quad 0 \quad 0 | \} \quad (6.4a)$$

and

$$\underline{l}_y^T = \{ | 0 \quad 1 \quad 0 | 0 \quad 1 \quad 0 | \dots | 0 \quad 1 \quad 0 | \} \quad (6.4b)$$

are the influence vectors in the x and y directions, in accordance with Eq. (6.2).

6.3.1 Mass Matrix

Mass matrix contains two translational masses, both m_i in the x and y directions, and a rotational mass I_i about the z axis for each story i . Hence, m_i is the mass of the i th story, and I_i is the mass moment of inertia of the i th slab about the z axis

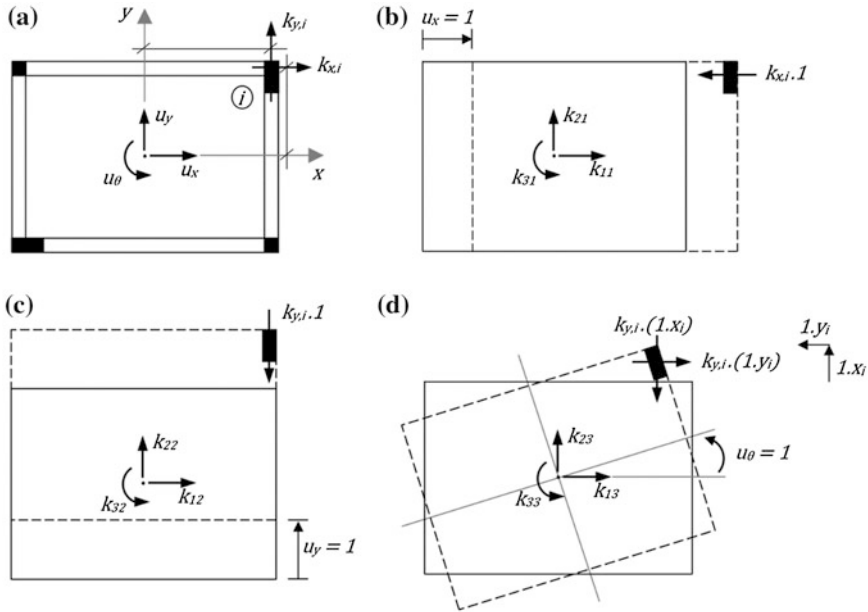


Fig. 6.2 Stiffness coefficients of a single story building with unsymmetrical distribution of stiffness. **a** Story plan, **b** stiffness coefficients for $u_x = 1$, **c** stiffness coefficients for $u_y = 1$, **d** stiffness coefficients for $u_\theta = 1$

$$k_{xy} = 0; \quad k_{yy} = \sum_1^k k_{yi}; \quad k_{\theta y} = \sum_1^k (k_{yi} \cdot x_i). \quad (6.6b)$$

Finally, we impose a unit rotational displacement in the z direction ($u_x = 0$, $u_y = 0$, $u_\theta = 1$). Column i develops resistance in both directions in proportion to the relative top displacements of $(-1 \cdot y_i)$ and $(1 \cdot x_i)$ in the x and y directions respectively, due to unit rotation $u_\theta = 1$ (Fig. 6.2d). The equilibrium of forces and moments in the three directions give,

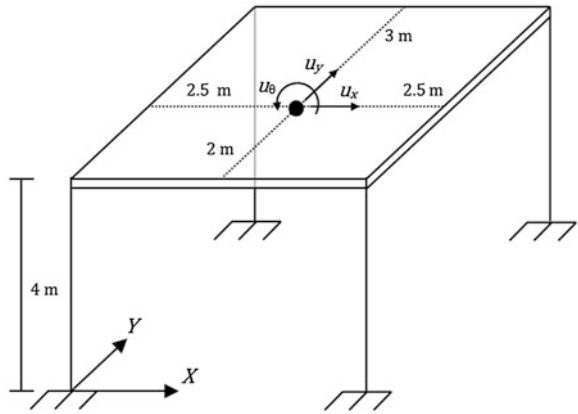
$$k_{x\theta} = \sum_1^k (-k_{xi} \cdot y_i); \quad k_{y\theta} = \sum_1^k (k_{yi} \cdot x_i); \quad k_{\theta\theta} = \sum_1^k (k_{xi} \cdot y_i^2 + k_{yi} \cdot x_i^2). \quad (6.6c)$$

Combining all stiffness coefficients, we obtain the condensed stiffness matrix as

$$\underline{k} = \begin{bmatrix} \sum_1^k k_{xi} & 0 & \sum_1^k (-k_{xi} \cdot y_i) \\ 0 & \sum_1^k k_{yi} & \sum_1^k (k_{yi} \cdot x_i) \\ \sum_1^k (-k_{xi} \cdot y_i) & \sum_1^k (k_{yi} \cdot x_i) & \sum_1^k (k_{xi} \cdot y_i^2 + k_{yi} \cdot x_i^2) \end{bmatrix}. \quad (6.7)$$

Example 6.1 The slab in the system shown below is a rigid diaphragm in its plane and also out of plane. The mass of the slab is 20 tons, and its centre of mass is

Fig. 6.3 Single story space frame



located as shown. Ignore the mass of columns. Determine the mass and stiffness matrices for the degrees of freedom shown.

$E = 20 \times 10^6 \text{ kN/m}^2$, Columns: $0.4 \times 0.4 \text{ m}^2$, $I_{CM} = 88.33 \text{ ton m}^2$. (use parallel axes theorem)

Solution

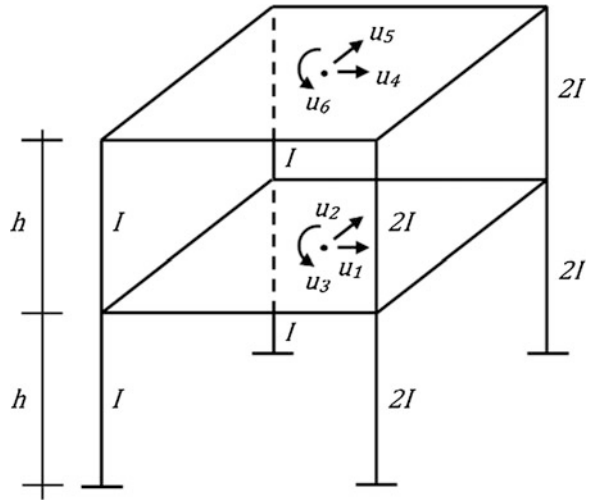
Each column has a lateral stiffness of $k = 12EI/h^3$ in both directions since rotations at the top of columns are constrained by the out of plane rigidity of the slab. Calculating I and substituting E , I and h into k , we find $k = 8,000 \text{ kN/m}$. Accordingly, mass and stiffness matrices of the single story building are obtained as,

$$\underline{m} = \begin{bmatrix} 20 & 0 & 0 \\ 0 & 20 & 0 \\ 0 & 0 & 88.33 \end{bmatrix}; \quad \underline{k} = \begin{bmatrix} 32,000 & 0 & -16,000 \\ 0 & 32,000 & 0 \\ -16,000 & 0 & 408,000 \end{bmatrix}; \quad \underline{u} = \begin{Bmatrix} u_x \\ u_y \\ u_\theta \end{Bmatrix}$$

Units of masses are tons and ton-m^2 , units of stiffness coefficients are kN/m , kN and kN-m . It can be observed that there is no stiffness coupling between x and y translations, which is always the case if the torsional inertias of the columns are ignored. Further, there is no stiffness coupling between y translation and rotation, indicating symmetry in the y direction which is obvious from the figure. There is stiffness coupling however between x translation and rotation, hence stiffness distribution along the x direction is not symmetrical (Fig. 6.3).

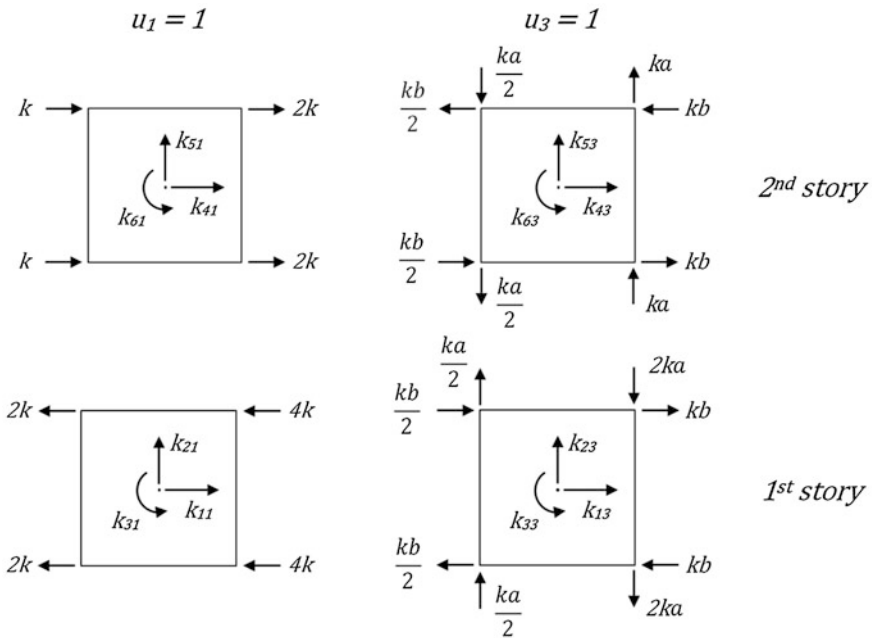
Example 6.2 The slabs in the two story building frame shown in Fig. 6.4 are rigid diaphragms in their plane and also out of plane. Determine the mass and stiffness matrices for the degrees of freedom shown. Story masses are m_1 and m_2 . The dimensions of the slabs are a (horizontal) and b (transverse).

Fig. 6.4 2 story space frame



Solution

Coefficients of the stiffness matrix can be determined by the direct stiffness method, by imposing a unit displacement/rotation to u_i while maintaining u_j ($j \neq i$) zero. Free body diagrams for u_1 and u_3 are given below where the stiffness coefficients can be determined from equilibrium. Note that $k = 12EI/h^3$.



Then the stiffness matrix can be calculated as,

$$\underline{k} = \begin{bmatrix} 12k & 0 & 0 & -6k & 0 & 0 \\ 0 & 12k & 2ka & 0 & -6k & -ak \\ 0 & 2ak & 3k(a^2 + b^2) & 0 & -ak & -1.5k(a^2 + b^2) \\ -6k & 0 & 0 & 6k & 0 & 0 \\ 0 & -6k & -ka & 0 & 6k & ak \\ 0 & -ak & -1.5k(a^2 + b^2) & 0 & ak & 1.5k(a^2 + b^2) \end{bmatrix}$$

The mass matrix and the displacement vector are,

$$\underline{m} = \begin{bmatrix} m_1 & 0 & 0 & 0 & 0 & 0 \\ 0 & m_1 & 0 & 0 & 0 & 0 \\ 0 & 0 & m_1(a^2 + b^2)/12 & 0 & 0 & 0 \\ 0 & 0 & 0 & m_2 & 0 & 0 \\ 0 & 0 & 0 & 0 & m_2 & 0 \\ 0 & 0 & 0 & 0 & 0 & m_2(a^2 + b^2)/12 \end{bmatrix};$$

$$\underline{u} = \begin{Bmatrix} u_1 \\ u_2 \\ u_3 \\ u_4 \\ u_5 \\ u_6 \end{Bmatrix}.$$

6.4 Free Vibration (Eigenvalue) Analysis

When the right hand side of Eq. (6.3) is zero during free vibration, we obtain the eigenvalue problem.

$$\underline{m} \ddot{\underline{u}}_d + \underline{k}_d \underline{u}_d = \underline{0} \quad (6.8)$$

Solution procedures of the eigenvalue problem for plane frames were given in Sect. 5.5. Similar procedures are also valid for the 3D building frames. The solution of eigenvalue problem provides the eigenvalues ω_n^2 and the eigenvectors $\underline{\phi}_n$ of the condensed system. The eigenvector $\underline{\phi}_n$ contains two translational components ϕ_{xin} and ϕ_{yin} , and one rotational component $\phi_{\theta in}$ at each floor i of a 3D building, as defined in Eq. (6.9).

$$\underline{\phi}_n^T = \{ | \phi_{x1n} \quad \phi_{y1n} \quad \phi_{\theta 1n} | \phi_{x2n} \quad \phi_{y2n} \quad \phi_{\theta 2n} | \dots | \phi_{xNn} \quad \phi_{yNn} \quad \phi_{\theta Nn} | \} \quad (6.9)$$

In a 2D plane structure oriented in the x direction, ϕ_{yin} and $\phi_{\theta in}$ components in ϕ_n are zero.

Example 6.3 Determine the eigenvalues and eigenvectors of the single story building with unsymmetrical stiffness given in Example 6.1. Normalize the eigenvectors with respect to mass.

Solution

Since stiffness and mass distributions are symmetrical in the y direction, we obtain an uncoupled equation of motion in this direction along u_y .

$$m \ddot{u}_y + \left(\sum_1^4 k_{yi} \right) u_y = 0$$

The motion in the y direction is governed by a SDOF equation of motion where $\omega_n^2 = 1600 \text{ (r/s)}^2$. The corresponding components of the modal vector are $\phi_{xn} = 0$; $\phi_{yn} = 1$; $\phi_{\theta n} = 0$. We do not yet know which mode is n . The remaining two coupled equations governing the motion in x and θ directions are,

$$\begin{bmatrix} 20 & 0 \\ 0 & 88.33 \end{bmatrix} \begin{Bmatrix} \ddot{u}_x \\ \ddot{u}_\theta \end{Bmatrix} + 1000 \begin{bmatrix} 32 & -16 \\ -16 & 408 \end{bmatrix} \begin{Bmatrix} u_x \\ u_\theta \end{Bmatrix} = \begin{Bmatrix} 0 \\ 0 \end{Bmatrix}.$$

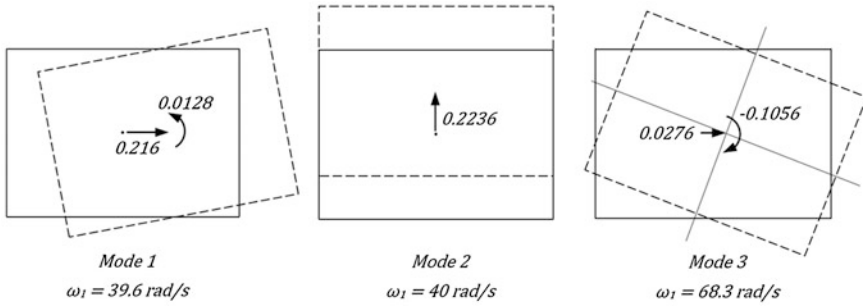
Determinant $(\underline{k} - \omega_n^2 \underline{m}) = 0$ gives the characteristic equation, yielding the roots 1552.4 (r/s)^2 and 4665 (r/s)^2 , and the respective eigenvectors $\begin{Bmatrix} \phi_{xn} \\ \phi_{\theta n} \end{Bmatrix} = \begin{Bmatrix} 1 \\ 0.0595 \end{Bmatrix}$ and $\begin{Bmatrix} \phi_{xn} \\ \phi_{\theta n} \end{Bmatrix} = \begin{Bmatrix} 1 \\ -3.8312 \end{Bmatrix}$. When we order the eigenvectors from smallest to largest, and expand the corresponding eigenvector to 3 DOF's, we obtain

$$\begin{aligned} \omega_1 &= 39.4 \text{ rad/s} \\ \omega_2 &= 40.0 \text{ rad/s} \\ \omega_3 &= 68.3 \text{ rad/s} \end{aligned} \quad \underline{\phi}_1 = \begin{Bmatrix} 1 \\ 0 \\ 0.0595 \end{Bmatrix} \quad \underline{\phi}_2 = \begin{Bmatrix} 0 \\ 1 \\ 0 \end{Bmatrix} \quad \underline{\phi}_3 = \begin{Bmatrix} 1 \\ 0 \\ -3.8312 \end{Bmatrix}$$

The eigenvectors can be normalized with respect to mass. Modal masses can be calculated by using Eq. (5.37) as $M_1 = 21.5$, $M_2 = 20$ and $M_3 = 1316.5$ tons. Applying mass normalization, we obtain

$$\underline{\phi}_1 = \begin{Bmatrix} 0.216 \\ 0 \\ 0.0128 \end{Bmatrix} \quad \underline{\phi}_2 = \begin{Bmatrix} 0 \\ 0.2236 \\ 0 \end{Bmatrix} \quad \underline{\phi}_3 = \begin{Bmatrix} 0.0276 \\ 0 \\ -0.1056 \end{Bmatrix} \quad \text{with } \underline{u} = \begin{Bmatrix} u_x \\ u_y \\ u_\theta \end{Bmatrix}$$

Note that each modal vector consists of three components for the single story building, the first one is translation in x , the second one is translation in y , and the third one is rotation θ about the centre of mass. The first and third mode vectors indicate torsional coupling of x translation and rotation. The second mode vector is uncoupled, and indicates pure translation in the y direction since the system is symmetrical about the y axis. The shapes of the three eigenvectors in plan are shown below.



6.4.1 The Effect of Building Symmetry on Mode Shapes

The mode shapes in Eq. (6.9) define a general deformation profile in the xyz space for the n th mode, in terms of ϕ_{xin} , ϕ_{yin} and rotational component $\phi_{\theta in}$ at each floor i of the 3D building. The modes in a 3D building are usually obtained in groups of three, which are ordered according to their vibration frequencies ω_n or periods T_n .

When the building is symmetrical about both axes, then these group of three modes are completely uncoupled. One mode is totally oriented in the x direction, the other in the y direction and the third in the rotation direction about the z axis. Then ϕ_{xin} is non-zero while ϕ_{yin} and $\phi_{\theta in}$ are zero for the symmetrical mode in the x direction, and vice versa for the other two modes in y and θ directions in Eq. (6.9). Such uncoupled shapes for the first group of three modes are shown in Fig. 6.5. The amplitudes of mode shapes are completely arbitrary. It is only assumed that the first mode with the longest period T_1 develops in the x direction, the second mode develops in the y direction, and the third mode develops in the rotational θ direction. Note that all three shapes are similar to the first mode shape of a 2D building. Accordingly, the shapes of the second group of three uncoupled modes are expected to be similar to the second mode shape of a 2D building. A common terminology in earthquake engineering is to label these group of first three modes as 1X, 1Y, 1 θ , then the group of second three modes as 2X, 2Y, 2 θ , and so on.

When symmetry is violated, which usually is the case in actual 3D building structures, the mode shapes become coupled in the three directions. Accordingly, ϕ_{xin} , ϕ_{yin} and $\phi_{\theta in}$ in Eq. (6.9) are all non-zero in a particular mode n although one may dominate the other two.

Let's consider the j th floor of a building, shown in Fig. 6.6. The mass is assumed to be uniformly distributed over the slab, hence it is symmetrical about both axes. Thus the centre of mass CM is at the geometric centroid. However the stiffness distribution of the lateral load resisting members (columns and walls) is not uniform.

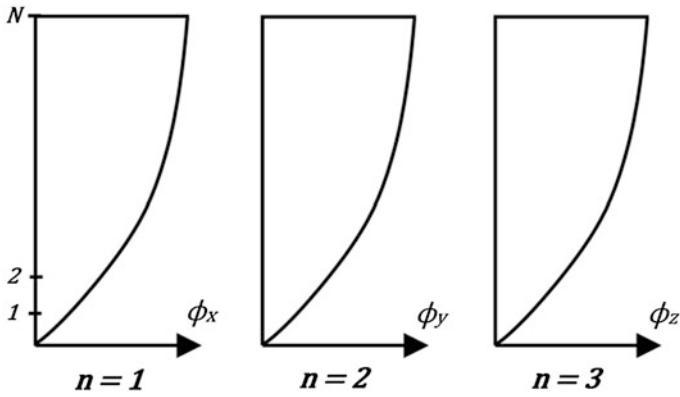


Fig. 6.5 First three uncoupled mode shapes of a purely symmetrical building structure

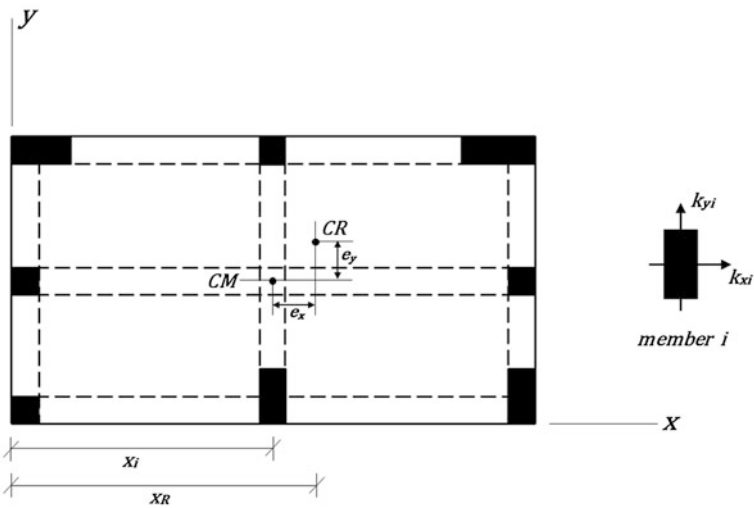


Fig. 6.6 A floor plan with unsymmetrical distribution of lateral stiffness in both directions

The location of the centre of rigidity CR , defined by the coordinates x_{CR} and y_{CR} from the coordinate center can be calculated from the first moment of stiffnesses about the origin.

$$x_{CR} = \frac{\sum x_i \cdot k_{yi}}{\sum k_{yi}}; \quad y_{CR} = \frac{\sum y_i \cdot k_{xi}}{\sum k_{xi}}. \tag{6.10}$$

Accordingly, the eccentricities in the x and y directions direction are

$$e_x = x_{CR} - x_{CM}; \quad e_y = y_{CR} - y_{CM}. \tag{6.11}$$

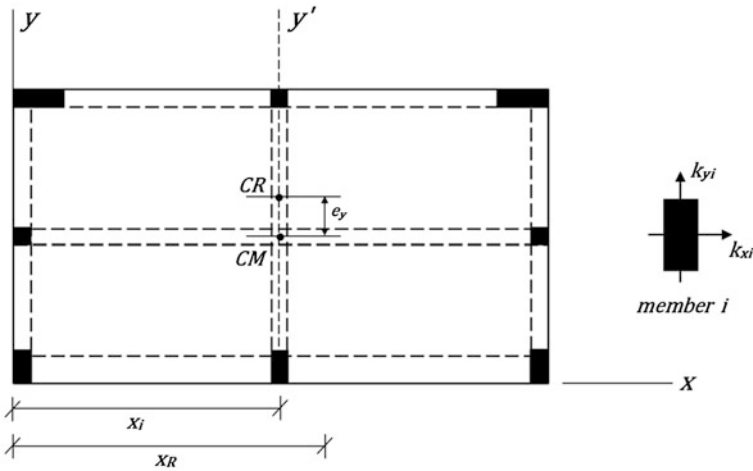


Fig. 6.7 A floor plan with unsymmetrical distribution of lateral stiffness in the x direction

If the centroid of the coordinate system is at the mass center CM such as in Fig. 6.2a, then e_x and e_y in Eq. (6.11) directly define the location of the center of rigidity CR . When e_x and e_y are zero, then the coupling terms in the stiffness matrix in Eq. (6.7) are also zero in accordance with Eqs. (6.10) and (6.11), leaving out a diagonal stiffness matrix for the j th story. A diagonal stiffness matrix for a story reveals that lateral stiffness is symmetrical about both horizontal axes in that story. Hence torsional coupling does not exist.

If there is stiffness coupling in all floors of a 3D building in both directions, i.e. both e_x and e_y are not zero in all stories, then all components of the modal vectors of size $3N$ in Eq. (6.9) are non-zero. This is a system with two-way unsymmetry. If there is stiffness coupling in one direction only, unsymmetry is one-way. Then some components of the modal vectors in Eq. (6.9) are non-zero. Let's consider Fig. 6.7 with $e_x = 0$ and $e_y \neq 0$. This system is symmetrical in the y direction about y' axis through the CM , and unsymmetrical in the x direction. The first two mode shapes of this system are given schematically in Fig. 6.8. The plan-wise motion of a typical floor is also shown in Fig. 6.9. In the first mode, each floor translates in the x direction and rotates about the z axis simultaneously while translation in the y direction is zero. In the second mode, there is pure translation in the y direction; hence x translation and rotation about the z axis is zero. Accordingly x -translation is coupled with rotation θ while y -translation is uncoupled with rotation.

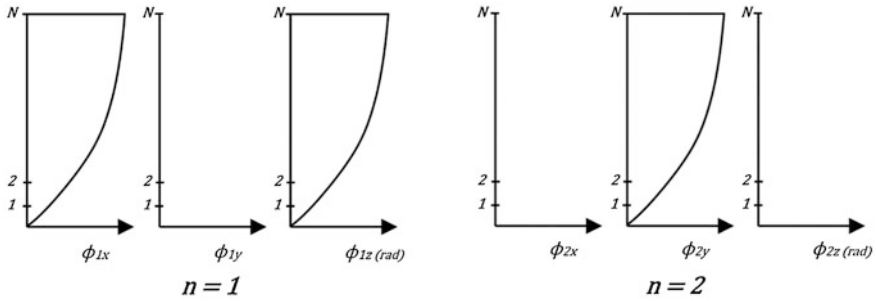


Fig. 6.8 First two coupled mode shapes of the unsymmetrical building structure in x direction

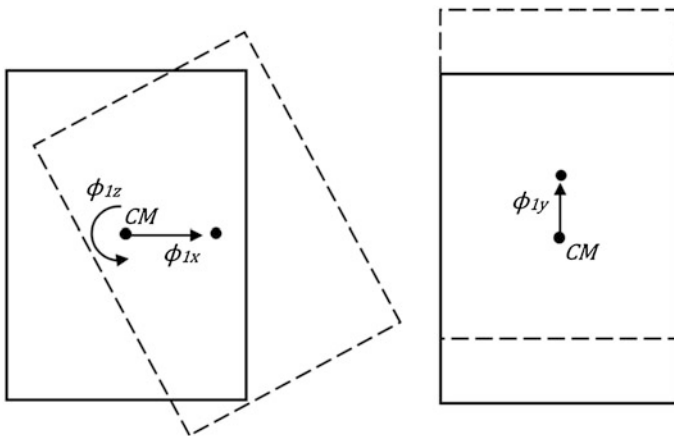


Fig. 6.9 Plan view of the first two coupled mode shapes of the unsymmetrical building in x direction

6.5 Analysis Procedures for Buildings in Seismic Codes

Analysis procedures in seismic design codes prescribe calculation of seismic design forces and deformations. Although the analytical development of the procedures introduced in this Chapter is theoretically similar to the procedures discussed in Chap. 5, their format is presented in conformance with the general code notation.

There are two basic linear elastic analysis procedures in seismic design codes. They are carried out under the design earthquake represented by an inelastic (reduced) design spectrum $S_{aR}(T)$ discussed in Chap. 4. The first one is the *modal response spectrum analysis procedure* and the second one is the *equivalent static lateral load procedure*, which is derived from the first one as a special case. Equivalent static lateral load procedure is applicable to simple, regular structures.

6.6 Modal Response Spectrum Analysis

A modal superposition analysis is carried out for the condensed system with dynamic degrees of freedom, under the reduced design earthquake S_{aR} by using a sufficient number of modes. This method is applicable to all buildings without any restrictions.

Modal forces are calculated for each mode under the reduced design spectrum by using Eq. (5.60).

$$\underline{f}_n = \frac{L_{ni}}{M_n} \left(\underline{m} \underline{\phi}_n \right) S_{aR,ni}. \quad (6.12)$$

L_{ni} in Eq. (6.12) for a 3D building is,

$$L_{ni} = \underline{\phi}_n^T \underline{m} \underline{l}_i; \quad i = x \text{ or } y \quad (6.13)$$

and $S_{aR,ni}$ is the ordinate of the reduced design spectrum at T_n where the earthquake is acting in direction $i = x$ or y .

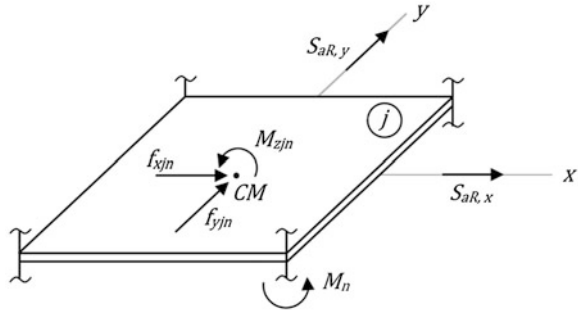
The force vector \underline{f}_n contains two lateral force components f_{xin} and f_{yin} , and one rotational moment $M_{\theta in}$ at each floor i of a 3D building, as shown in Eq. (6.14).

$$\underline{f}_n^T = \{ | f_{x1n} \quad f_{y1n} \quad M_{\theta 1n} | f_{x2n} \quad f_{y2n} \quad M_{\theta 2n} | \dots | f_{xNn} \quad f_{yNn} \quad M_{\theta Nn} | \}. \quad (6.14)$$

Note that the modal force vector in Eq. (6.14) and the modal vector in Eq. (6.9) are consistent in their components along the dynamic DOF's. In a 2D plane frame oriented in the x direction, f_{yin} and $M_{\theta in}$ components in \underline{f}_n are zero. Furthermore, when a building with purely symmetrical stiffness in both lateral directions ($e_x = e_y = 0$) is excited by a ground motion in the x or y directions, torsional moments $M_{\theta in}$ in Eq. (6.14) do not develop because there is no coupling between translational and rotational modal components in a purely symmetrical building (see Fig. 6.5). However when a building with an unsymmetrical distribution of stiffness ($e_x \neq 0$ and/or $e_y \neq 0$) is excited by a ground motion in x or y directions, torsional moments $M_{\theta in}$ in Eq. (6.14) develop because of the coupling between translational and rotational components (see Fig. 6.8). This coupling phenomenon is also called “*torsional coupling*” in earthquake engineering because torsional moments are not directly caused by a rotational ground excitation, but indirectly caused by translational ground excitation.

Then \underline{f}_n in Eq. (6.12) is applied to the “uncondensed” building structure with all static and dynamic DOF's activated, and all internal modal member forces and displacements at the n th mode are calculated from equivalent static modal analysis. Two horizontal force resultants and one torsion moment are applied at the centre of mass of the j th floor slab of a 3D structure as shown in Fig. 6.10.

Fig. 6.10 Modal force components at the n th mode, acting at the mass centre of the j th floor slab



Finally, the modal results are combined by SRSS or CQC formulation. For example, the design moment at the top end of the front right corner column in Fig. 6.10 is calculated by SRSS in the following equation.

$$M = \sqrt{(M_1)^2 + (M_2)^2 + \dots + (M_N)^2}. \quad (6.15)$$

6.6.1 Summary of Modal Response Spectrum Analysis Procedure

The modal response spectrum analysis procedure in seismic codes can be summarized with the following steps.

1. Prepare a complete structural model of your structure.
2. Condense the static DOF's (Eq. 5.14).
3. Carry out eigenvalue analysis of the condensed structure (Eq. 6.8) and determine ω_n (or T_n) and $\underline{\phi}_n$ for each mode n .
4. Calculate modal spectral accelerations from the design spectrum $S_{aR,n}$ (Eq. 4.15) for a selected R factor.
5. Calculate the modal forces $\underline{f}_{-n} = \frac{I_n}{M_n} (\underline{m} \underline{\phi}_n) S_{aR,n}$ from (Eq. 6.14).
6. Apply \underline{f}_{-n} to the complete (uncondensed) structural model by expanding \underline{f}_{-n} to the complete force vector \underline{f}'_{-n} and determine internal modal member forces and deformations r_n from $\underline{f}'_{-n} = \underline{k}' \cdot \underline{u}'_{-n}$ where \underline{k}' is the full (uncondensed) stiffness matrix and \underline{u}'_{-n} includes all DOF's.
7. Combine the modal results by SRSS: $r_{EQ} = \sqrt{(r_1)^2 + \dots + (r_n)^2 + \dots + (r_N)^2}$, or by CQC.
8. Further combine gravity and earthquake analysis results: $r_{design} = r_{gravity} \mp r_{EQ}$.

6.6.2 The Minimum Number of Modes

The total effective mass of the N_{min} modes considered in the mode superposition analysis should be larger than 90 % of the total mass, according to the seismic codes, separately in the x and y directions. This requirement is verified from the following inequalities.

$$x \text{ direction} : \sum_{n=1}^{N_{min}} M_n^* = \sum_{n=1}^{N_{min}} \frac{L_{xn}^2}{M_n} \geq 0.90 \sum_{i=1}^N m_i \quad (6.16)$$

$$y \text{ direction} : \sum_{n=1}^{N_{min}} M_n^* = \sum_{n=1}^{N_{min}} \frac{L_{yn}^2}{M_n} \geq 0.90 \sum_{i=1}^N m_i \quad (6.17)$$

In Eqs. (6.16) and (6.17), N is the number of stories and m_i is the story mass. Also,

$$L_{xn} = \sum_{i=1}^N m_i \phi_{xin}; \quad L_{yn} = \sum_{i=1}^N m_i \phi_{yin} \quad (6.18)$$

and,

$$M_n = \sum_{i=1}^N (m_i \phi_{xin}^2 + m_i \phi_{yin}^2 + I_i \cdot \phi_{\theta in}^2) \equiv \underline{\phi}_n^T \underline{m} \underline{\phi}_n. \quad (6.19)$$

It should be noticed that Eqs. (6.18) and (6.19) are the expanded scalar forms of Eqs. (5.40) and (5.37) respectively, where

$$L_{xn} = \underline{\phi}_n^T \underline{m} L_x; \quad L_{yn} = \underline{\phi}_n^T \underline{m} L_y; \quad M_n = \underline{\phi}_n^T \underline{m} \underline{\phi}_n \quad (6.20)$$

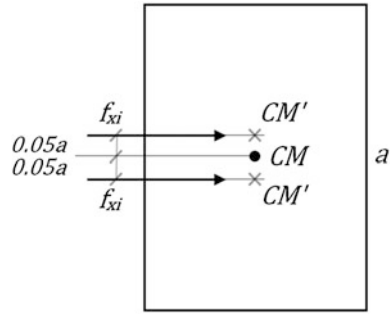
and $L_x = \{1 \ 0 \ 0; 1 \ 0 \ 0; \dots\}^T$; $L_y = \{0 \ 1 \ 0; 0 \ 1 \ 0; \dots\}^T$ are the influence vectors in the x and y directions, respectively. L_x and L_y transmit the motion of the ground in the x and y directions to the respective translational dynamic DOF's of the structure above as rigid body motion components.

The minimum number of modes as related to the ratio of total mass in Eqs. (6.16–6.20) has no theoretical basis, and it is only a practical assumption. It is merely an indication, which is approximately expressing the ratios of modal base shear forces to the total base shear force.

6.6.3 Accidental Eccentricity

The centre of rigidity or the centre of mass of the original structure at any story may be shifted because of several reasons, and accordingly creates an additional eccentricity which is not accounted for in the structural modeling of the system. This phenomenon is called *accidental torsion* in seismic design. The probable causes of accidental torsion are:

Fig. 6.11 Shifting of the centre of mass in order to account for accidental torsion in the x direction



- Non-synchronized cracking or yielding of lateral load resisting vertical members (columns and shear walls) in a story, leading to unsymmetrical stiffness loss during a strong earthquake excitation.
- Unsymmetrical distribution of non-structural members which carry a part of the story shear forces (partition walls, window frames, etc.).
- Shift in the centre of rigidity due to imperfections in construction.
- Shift in the centre of mass due to a concentrated live load mass.

Seismic design codes account for accidental torsion indirectly, by imposing an additional eccentricity to the applied inertial lateral force resultants. This is achieved by shifting the centre of mass at each story in the direction perpendicular to the earthquake direction by an additional eccentricity equal to 5 % of the floor dimension in the transverse direction. The shift is imposed in the x and y directions separately, and in both (\pm) senses. The shift at the i th floor in the x direction is shown in Fig. 6.11.

Example 6.4 The single story building given in Examples 6.1 and 6.3 is designed under the linear elastic acceleration spectrum (unreduced) given below.

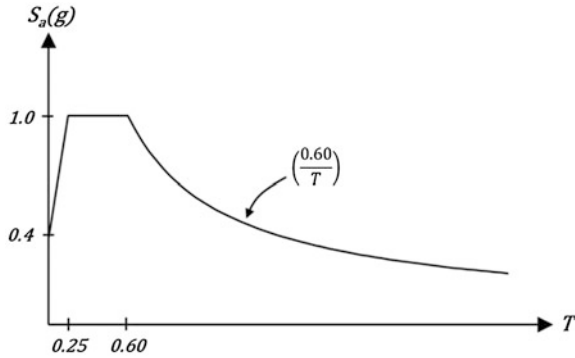
- Calculate the elastic modal displacements (center of mass) and modal forces under seismic forces acting in the x -direction only.
- Determine the design forces for columns under the same excitation. Assume that the columns share the weight of the slab equally. There is no live load, and the design load combination is DL + EQ. Use $R = 4$ in design.

$E_c = 20\text{e}6 \text{ kN/m}^2$, Columns: $0.4 \times 0.4 \text{ m}^2$, $I_G = 88.33 \text{ ton m}^2$.

Free vibration properties of the system are repeated below.

$$\omega_1 = 39.4 \text{ rad/s} \quad \phi_1 = \begin{Bmatrix} 0.216 \\ 0 \\ 0.0128 \end{Bmatrix} \quad \phi_2 = \begin{Bmatrix} 0 \\ 0.2236 \\ 0 \end{Bmatrix} \quad \phi_3 = \begin{Bmatrix} 0.0276 \\ 0 \\ -0.1056 \end{Bmatrix}$$

$$\underline{u} = \begin{Bmatrix} u_x \\ u_y \\ u_\theta \end{Bmatrix}$$

**Solution**

$$T = \langle 0.1595 \quad 0.157 \quad 0.092 \rangle \text{ s}$$

(a) Modal Displacements

$$S_{a1} = S_a(T_1) \cdot g = 1 * 9.81 = 9.81 \text{ m/s}^2$$

$$S_{a2} = S_a(T_2) \cdot g = 1 * 9.81 = 9.81 \text{ m/s}^2$$

$$S_{a3} = S_a(T_3) \cdot g = 0.77 * 9.81 = 7.53 \text{ m/s}^2$$

$$\underline{m} = \begin{bmatrix} 20 & 0 & 0 \\ 0 & 20 & 0 \\ 0 & 0 & 88.33 \end{bmatrix} \text{ ton; ton m}^2$$

$$\mathcal{L}_{xn} = \underline{\phi}_n^T \cdot \underline{m} \cdot \underline{l}_x \quad \underline{l}_x = \{ 1 \quad 0 \quad 0 \}^T$$

$$\mathcal{L}_{x1} = 4.44 \text{ tons}, \quad \mathcal{L}_{x2} = 0 \quad \mathcal{L}_{x3} = -0.551 \text{ tons}$$

$$u_{x1} = \frac{\mathcal{L}_{x1}}{M_1} \cdot \phi_{x1} \cdot \frac{PSa_1}{\omega_1^2} = 4.44 * 0.222 * \frac{9.81}{39.4^2} = 6.23 * 10^{-3} \text{ m}, \quad u_{x2} = 0,$$

$$u_{x3} = \frac{\mathcal{L}_{x3}}{M_3} \cdot \phi_{x3} \cdot \frac{PSa_3}{\omega_3^2} = -0.551 * -0.02755 * \frac{7.53}{68.3^2} = 2.45 * 10^{-5} \text{ m}$$

$$u_{\theta 1} = \frac{\mathcal{L}_{x1}}{M_1} \cdot \phi_{\theta 1} \cdot \frac{PSa_1}{\omega_1^2} = 4.44 * 0.0131 * \frac{9.81}{39.4^2} = 3.677 * 10^{-4} \text{ rad}, \quad u_{\theta 2} = 0,$$

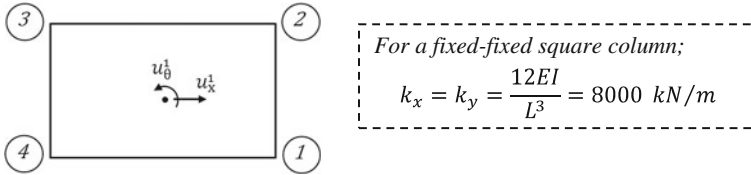
$$u_{\theta 3} = \frac{\mathcal{L}_{x3}}{M_3} \cdot \phi_{\theta 3} \cdot \frac{PSa_3}{\omega_3^2} = -0.551 * 0.1056 * \frac{7.53}{68.3^2} = -9.4 * 10^{-5} \text{ rad}$$

$$\underline{u}_1 = \begin{Bmatrix} 6.23 * 10^{-3} \text{ m} \\ 0 \\ 3.677 * 10^{-4} \text{ rad} \end{Bmatrix}, \quad \underline{u}_2 = 0, \quad \underline{u}_3 = \begin{Bmatrix} 2.45 * 10^{-5} \text{ m} \\ 0 \\ -9.4 * 10^{-5} \text{ rad} \end{Bmatrix}$$

Modal Forces: $f_{-n} = \frac{L_n}{M_n} (\underline{m} \cdot \underline{\phi}_n) P S a_n$

$$\underline{f}_{-1} = \begin{Bmatrix} 191.65 \\ 0 \\ 50.40 \end{Bmatrix}; \quad \underline{f}_{-3} = \begin{Bmatrix} 2.29 \\ 0 \\ -38.73 \end{Bmatrix} \quad \begin{matrix} \text{(Force-kN)} \\ \\ \text{(Moment-kN m)} \end{matrix}$$

(b) Design Forces in Columns



The superscript 1 in the figure indicates the 1st floor. Since there is only one floor, we can drop this index.

Mode 1 ($u_x = 6.23 \times 10^{-3} \text{ m}$; $u_\theta = 3.677 \times 10^{-4} \text{ rad}$)

Column 1

$$u_x = u_x + u_\theta * 2^m = 6.23 \times 10^{-3} + 3.677 \times 10^{-4} * 2 = 6.9654e - 3 \text{ m}$$

$$u_y = u_\theta * 2.5^m = 3.677 \times 10^{-4} * 2.5 = 9.1925e - 4 \text{ m}$$

$$f_x = 6.9654e - 3 * 8000 = 55.7232 \text{ kN}(\rightarrow); f_y = 9.1925e - 4 * 8000 = 7.354 \text{ kN}(\uparrow)$$

Column 2

$$M_x = F_y \cdot \frac{L}{2} = 7.354 * 2 = 14.708 \text{ kN m} \quad M_y = F_x \cdot \frac{L}{2} = 55.7232 * 2 = 111.446 \text{ kN m}$$

$$u_x = u_x - u_\theta * 3 = 6.23 \times 10^{-3} - 3.677 \times 10^{-4} * 3 = 5.1269e - 3 \text{ m}$$

$$u_y = u_\theta * 2.5 = 9.1925e - 4 \text{ m}$$

$$f_x = 5.1269e - 3 * 8000 = 41.01 \text{ kN}(\rightarrow); \quad M_x = 7.354 * 2 = 14.708 \text{ kN m}$$

$$f_y = 9.1925e - 4 * 8000 = 7.354 \text{ kN}(\uparrow); \quad M_y = 41.01 * 2 = 82.02 \text{ kN m}$$

Column 3

$$u_x = u_x - u_\theta * 3 = 5.1269e - 3 \text{ m} \quad f_x = 41.01 \text{ kN}(\rightarrow) \quad M_x = 14.708 \text{ kN m}$$

$$u_y = -u_\theta * 2.5 = -9.1925e - 4 \text{ m} \quad f_y = -7.354 \text{ kN}(\downarrow) \quad M_y = 82.02 \text{ kN m}$$

Column 4

$$u_x = u_x^1 - u_\theta^1 * 2 = 6.9654e - 3 \text{ m} \quad f_x = 55.7232 \text{ kN} (\rightarrow) \quad M_x = 14.708 \text{ kN m}$$

$$u_y = -u_\theta^1 * 2.5 = -9.1925e - 4 \text{ m} \quad f_y = -7.354 \text{ kN} (\downarrow) \quad M_y = 111.446 \text{ kN m}$$

Mode 3 ($u_x = 2.45 * 10^{-5}$ m; $u_\theta = -9.4 * 10^{-5}$ rad)

Column 1

$$u_x = u_x - u_\theta * 2 = 2.45 * 10^{-5} - 9.4 * 10^{-5} * 2 = -1.635 * 10^{-4} \text{ m}$$

$$u_y = -u_\theta * 2.5 = -9.4 * 10^{-5} * 2.5 = -2.35 * 10^{-4} \text{ m}$$

$$f_x = -1.635 * 10^{-4} * 8000 = -1.308 \text{ kN}(\leftarrow) \quad M_x = 1.88 * 2 = 3.76 \text{ kN m}$$

$$f_y = -2.35 * 10^{-4} * 8000 = -1.88 \text{ kN}(\downarrow) \quad M_y = 1.308 * 2 = 2.616 \text{ kN m}$$

Column 2

$$u_x = u_x + u_\theta * 3 = 2.45 * 10^{-5} + 9.4 * 10^{-5} * 3 = 3.065 * 10^{-4} \text{ m}$$

$$u_y = -u_\theta * 2.5 = -2.35 * 10^{-4} \text{ m}$$

$$f_x = 3.065 * 10^{-4} * 8000 = 2.452 \text{ kN}(\rightarrow) \quad M_x = 1.88 * 2 = 3.76 \text{ kN m}$$

$$f_y = -2.35 * 10^{-4} * 8000 = -1.88 \text{ kN}(\downarrow) \quad M_y = 2.452 * 2 = 4.904 \text{ kN m}$$

Column 3

$$u_x = u_x + u_\theta^3 * 3 = 3.065e - 4 \text{ m} \quad f_x = 2.452 \text{ kN}(\rightarrow) \quad M_x = 3.76 \text{ kN m}$$

$$u_y = u_\theta * 2.5 = 2.35e - 4 \text{ m} \quad f_y = 1.88 \text{ kN}(\uparrow) \quad M_y = 4.904 \text{ kN m}$$

Column 4

$$u_x = u_x^3 - u_\theta^3 * 2 = -1.635e - 4 \text{ m} \quad f_x = -1.308 \text{ kN}(\rightarrow) \quad M_x = 3.76 \text{ kN m}$$

$$u_y = u_\theta^3 * 2.5 = 2.35e - 4 \text{ m} \quad f_y = 1.88 \text{ kN}(\uparrow) \quad M_y = 2.616 \text{ kN m}$$

Combining the internal forces with SRSS:

Column 1

$$f_x = \sqrt{55.7232^2 + 1.308^2} = 55.74 \text{ kN}; \quad f_y = \sqrt{7.354^2 + 1.88^2} = 7.59 \text{ kN}$$

$$M_x = \sqrt{14.708^2 + 3.76^2} = 15.18 \text{ kN m}; \quad M_y = \sqrt{111.446^2 + 2.616^2} = 111.47 \text{ kN m}$$

Column 2

$$f_x = \sqrt{41.01^2 + 2.452^2} = 41.08 \text{ kN}; \quad f_y = \sqrt{7.354^2 + 1.88^2} = 7.59 \text{ kN}$$

$$M_x = \sqrt{14.708^2 + 3.76^2} = 15.18 \text{ kN m}; \quad M_y = \sqrt{82.02^2 + 4.904^2} = 82.16 \text{ kN m}$$

Column 3

$$f_x = \sqrt{44.01^2 + 2.452^2} = 41.08 \text{ kN}; \quad f_y = \sqrt{7.354^2 + 1.88^2} = 7.59 \text{ kN}$$

$$M_x = \sqrt{14.708^2 + 3.76^2} = 15.18 \text{ kN m}; \quad M_y = \sqrt{82.02^2 + 4.904^2} = 82.16 \text{ kN m}$$

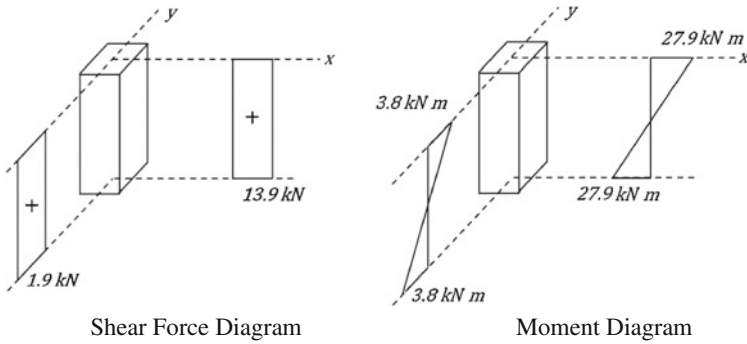
Column 4

$$f_x = \sqrt{1.308 + 55.7232^2} = 55.74 \text{ kN}; \quad f_y = \sqrt{7.354^2 + 1.88^2} = 7.59 \text{ kN}$$

$$M_x = \sqrt{14.708^2 + 3.76^2} = 15.18 \text{ kN m}; \quad M_y = \sqrt{111.446^2 + 2.616^2} = 111.47 \text{ kN m}$$

Columns 1 and 4 are the most critical!

Design shear forces (Reduce by R = 4): $F_x = \frac{55.74}{4} = 13.9 \text{ kN}$; $F_y = \frac{7.59}{4} = 1.9 \text{ kN}$
Design moments (Reduce by R = 4): $M_x = \frac{15.18}{4} = 3.8 \text{ kN m}$; $M_y = \frac{111.47}{4} = 27.9 \text{ kN m}$



Axial load for column 1

Slab weight = $20 * 9.81 = 196.2 \text{ kN}$
 Columns share slab weight equally $\rightsquigarrow N_{\text{①}} = 49.05 \text{ kN}$

Design will be conducted under

$N = 49.05 \text{ kN}$		$N = 49.05 \text{ kN}$	
$M_x = 3.8 \text{ kN m}$	and	$M_y = 27.9 \text{ kN m}$	
$F_y = 1.9 \text{ kN}$		$F_x = 13.9 \text{ kN}$	
$\underbrace{\hspace{10em}}_{\text{For y direction}}$		$\underbrace{\hspace{10em}}_{\text{For x direction}}$	

6.7 Equivalent Static Lateral Load Procedure

Let's consider the effective modal forces and the resulting modal displacements at the first mode of a building in Fig. 6.12, as discussed in Sect. 5.6.4.

The modal force vector f_{-n} under the reduced design spectrum S_{aR} was given in Eq. (6.12). Then the base shear force at the 1st mode can be obtained from Eq. (5.62).

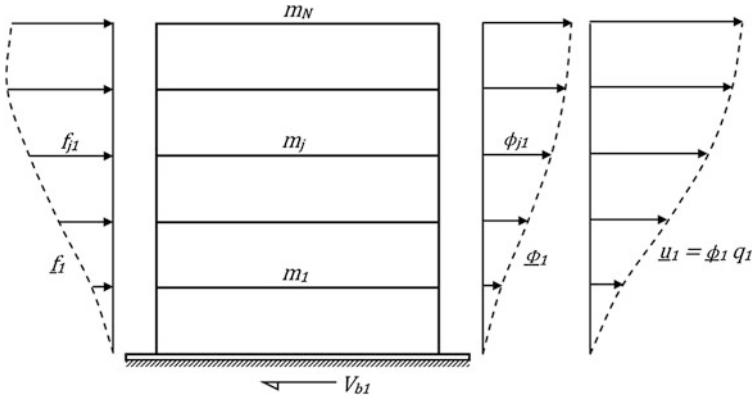


Fig. 6.12 Modal forces and resulting modal displacements at the first mode of a building

$$V_{b1} = M_1^* S_{aR,1} \equiv \frac{L_1^2}{M_1} S_{aR,1}. \tag{6.21}$$

The j th component of \underline{f}_{-1} in Eq. (6.12) and Fig. 6.8 can be expressed in scalar form as

$$f_{j1} = \frac{L_1}{M_1} (m_j \phi_{j1}) S_{aR,1}. \tag{6.22}$$

When we multiply and divide the RHS by L_1 and rearrange;

$$f_{j1} = \frac{L_1^2}{M_1} \cdot \frac{1}{L_1} (m_j \phi_{j1}) S_{aR,1}. \tag{6.23}$$

Substituting V_{b1} from Eq. (6.21) into Eq. (6.23), we obtain

$$f_{j1} = V_{b1} \frac{m_j \phi_{j1}}{L_1} \tag{6.24}$$

where

$$L_1 = \phi_1^T \underline{m} \underline{1} \equiv \sum_{i=1}^N m_i \phi_{i1}. \tag{6.25}$$

Note that L_1 in Eq. (6.25) is identical to its definitions in Eq. (6.20) for $n = 1$ in the x and y directions, respectively. Finally, substituting L_1 from Eq. (6.25) into Eq. (6.24),

$$f_{j1} = V_{b1} \frac{m_j \phi_{j1}}{\sum_{i=1}^N m_i \phi_{i1}}. \tag{6.26}$$

Multiplying and dividing the RHS by the gravitational acceleration g gives,

$$f_{j1} = V_{b1} \frac{w_j \phi_{j1}}{\sum_{i=1}^N w_i \phi_{i1}} \quad (6.27)$$

where $w_i = m_i g$ is the weight of the i th floor.

When the first mode (in the direction of earthquake excitation) is dominant on total dynamic response, then

$$V_b \cong V_{b1} \equiv M_1^* S_{aR,1} \quad (6.28)$$

from Eq. (6.21). Similarly, from Eq. (6.27), considering that $V_b \cong V_{b1}$,

$$f_j \cong f_{j1} = V_b \frac{w_j \phi_{j1}}{\sum_{i=1}^N w_i \phi_{i1}}. \quad (6.29)$$

The components of the first mode vector ϕ_1 in the direction of earthquake excitation can be approximated with a linear variation over the building height in simple buildings with regular height wise distribution of mass and stiffness.

$$\phi_{j1} = \alpha H_j. \quad (6.30)$$

H_j is the height of the j th floor from the base and α is an arbitrary constant representing the slope of linear distribution. Substituting ϕ_{j1} from Eq. (6.28) into Eq. (6.27), we obtain

$$f_j = V_b \frac{w_j H_j}{\sum_{i=1}^N w_i H_i} \quad (6.31)$$

6.7.1 Base Shear Force in Seismic Codes

It was proposed in Eq. (6.28) that $V_b \cong M_1^* S_{aR,1}$ in simple regular buildings where the effective modal mass of the first mode is $M_1^* = \frac{L_1^2}{M_1}$. If we replace M_1^* with the total mass $M^* = \sum m_i$, then we approximately account for the masses of higher modes. Hence,

$$V_b = M \cdot S_{aR,1} \equiv \frac{W S_{ae}(T_1)}{g R(T_1)} \quad (6.32)$$

where $W = \sum_{i=1}^N w_i$; $w_i = g_i + nq_i$; g_i is the dead load, q_i is the live load and n is the live load reduction factor for dynamic mass. W is also called the “seismic weight” of the building. The minimum value of the base shear force in seismic codes was introduced in Sect. 4.3.1.

Live load is reduced by the n factor in calculating the lateral earthquake forces which are based on the weight (mass) of the building during the earthquake. It is considered that the entire live load assumed in gravity design (factored dead load and live load combination) has a small probability of existence during an earthquake. Accordingly the mass of the live load is reduced by $n < 1$ to prevent overdesign. This factor mostly depends on how long the live load mass can be permanent in a building. Typical values in design codes are 0.3 for residences and offices, 0.6 for schools, dormitories, concert halls, restaurants and shops.

6.7.2 Estimation of the First Mode Period T_1

The first mode period T_1 is required in calculating the reduced base shear force from Eq. (6.32). T_1 can be calculated by an approximate procedure, called Rayleigh's method. Let F_f be a lateral force distributions and d_f be the resulting lateral story displacements, obtained by static analysis. Then

$$T_1 = 2\pi \left[\frac{\sum_{i=1}^N m_i d_i^2}{\sum_{i=1}^N F_i d_i} \right]^{1/2}. \quad (6.33)$$

F_f can have any distribution. However using f_j in Eq. (6.31) for F_f increases accuracy.

For building frames with free standing heights H less than 40 m, a simpler approximate equation is employed in Eurocode 8.

$$T_1 = C_t \cdot H^{3/4}. \quad (6.34a)$$

C_t is 0.075 for concrete frames, and 0.085 for steel frames. A similar approximate equation suggested in ASCE 7 is

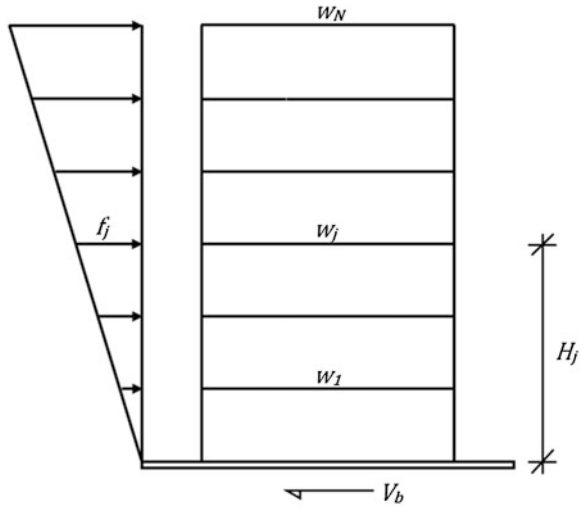
$$T_1 = C_t \cdot H^x. \quad (6.34b)$$

C_t is 0.0466 and x is 0.9 for concrete moment resisting frames whereas C_t is 0.0724 and x is 0.8 for steel moment resisting frames. These values are purely empirical, estimated from the eigenvalue analysis results of several building frames. A comparison can be made for a typical 8 story concrete moment resisting frame. Assuming that its height is 25 m, Eurocode 8 gives 0.84 s for the first mode period. The corresponding value in ASCE 7 is also 0.84 s.

ASCE 7 proposes an even simpler equation for moment resisting frames with the number of stories N less than 12:

$$T_1 = 0.1N. \quad (6.34c)$$

Fig. 6.13 Earthquake force distribution in the code for equivalent static lateral load procedure



6.7.3 Lateral Force Distribution in Seismic Codes

The distribution of lateral forces along the stories, given in Eq. (6.31), is slightly modified in the codes, and expressed by Eq. (6.35).

$$f_j = (V_b) \frac{w_j H_j}{\sum_{i=1}^N w_i H_i} \tag{6.35}$$

The lateral force distribution in seismic codes for the Equivalent Static Lateral Load Procedure is shown in Fig. 6.13.

Example 6.5 Determine the equivalent static lateral load distribution for the 3-story frame in Example 5.8. Let $R = 1$ for a consistent comparison with the modal force vectors obtained in Example 5.10.

Solution

The total weight W is 5 mg where $m = 175$ tons. $S_{ae}(T_1) = 1.0 g$ since $T_1 = 0.40$ s. Also, $R(T_1) = 1.0$. When these terms are substituted into Eq. (6.32), base shear is calculated as;

$V_b = 8583.75$ kN. Let $H_i = ih$ for $i = 1 - 3$. Also $w_i = m_i g$. Then, from Eq. (6.35),

$$f_1 = (8584) \frac{2}{9} = 1907 \text{ kN}; \quad f_2 = (8584) \frac{4}{9} = 3815 \text{ kN};$$

$$f_3 = (8584) \frac{3}{9} = 2851 \text{ kN}.$$

When these results are compared with the results of Example 5.10, it can be observed that the results of equivalent static lateral load procedure are 17.7 %

higher than that of mode superposition procedure. This is considered as a tradeoff for using a simpler procedure.

6.8 Basic Design Principles and Performance Requirements for Buildings

Seismic design is inherently based on inelastic structural response since seismic forces are usually severe enough to force the conventionally and economically designed structures into the inelastic response range, as discussed in [Chap. 3](#). When inelastic response is expected to develop under intensive seismic forces, engineers should normally conduct nonlinear analysis in order to calculate the true design forces and deformations. However nonlinear procedures are too rigorous and not practical for design purposes. Furthermore, nonlinear analysis procedures require inelastic structural models where the member force capacities are already defined. Hence analytical procedures based on linear elastic response are difficult to abandon at the current state of practice, at least at the preliminary design stage.

The dilemma between inevitable inelastic seismic response and practicality of traditional linear elastic analysis procedures in design has been overcome by a major assumption: Approximate reduction of elastic forces in order to account for the expected inelastic response. Although it is well known that seismic structural design is an iterative process due to the natural interaction between structural properties (basically the vibration period) and ground motion characteristics (basically the spectral acceleration), an a priori specification of seismic design forces by the codes is essential for common design practice. Practically, we should start the design process by specifying design forces acting on the linear elastic structure in order to produce a preliminary design.

Reduction of elastic forces in order to represent the inelastic design forces is furnished by the response reduction factors (R or q) in seismic design codes, which were introduced in [Chap. 4](#). The definition of response reduction factor in Eurocode 8 is quite informative: “It is an approximation of the ratio of the seismic forces that the structure would experience if its response was completely elastic, to the seismic forces that may be used in design with a conventional elastic analysis model, still ensuring a satisfactory response of the structure”. This approach is too simple however, which should be supplemented with further proportioning and detailing requirements in design.

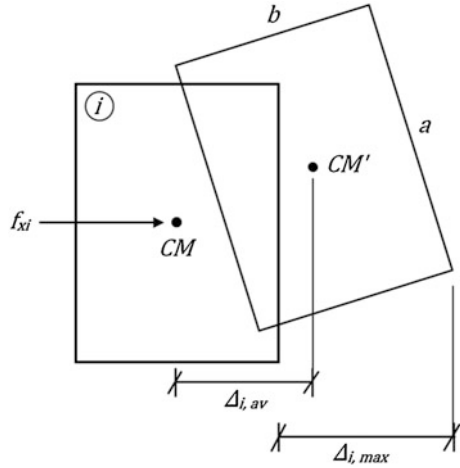
Although the calculation of member design forces and deformation demands are based on linear elastic models, reducing the linear elastic seismic forces to design forces through response reduction factors makes inelastic response of the designed structure inevitable under the actual ground motions with the accepted return periods (usually 475 years, or 10 % probability of being exceeded in

50 years). Then providing member force capacities (moments, shears, stresses, etc.) which satisfy the design force demands is just not sufficient for a satisfactory seismic performance. When such an event occurs, inelastic response and associated damage inevitably develops in the structural system.

The fundamental performance criterion in seismic design is the *no-collapse requirement* under the design seismic action. Simply, structural damage due to the formation of inelastic deformations should not lead to global or local collapse of the building structure, hence life safety of the building occupants can be ensured. An indirect consequence of the “life safety objective” under design seismic action is the *limited damage objective* under a more frequent, but lower intensity seismic action, i.e. the one with a shorter return period (95 years in EC8, or 10 % probability of being exceeded in 10 years). If the design satisfies life safety objective, it is believed that the structure would undergo minimal or no damage under a more frequent seismic action, not leading to the interruption of its use. Both of these objectives can only be verified via nonlinear analysis. However basic seismic design principles explained in the following paragraphs help maintaining these objectives enormously since they are based on engineering judgment and past experience from damaging earthquakes.

- (a) *Simplicity* A simple structural system increases the reliability of the structural model and the results of analysis. The uncertainties naturally involved in design are much less in a simple structure.
- (b) *Uniformity* Uniform distribution of mass and resistance of structural members both in plan and elevation allows a uniform distribution of inelastic deformations under design seismic action. Accordingly, uniformity prevents accumulation of damage which may initiate collapse. Basic features of uniformity are symmetry, continuity of lateral load resisting system and redundancy.
- (c) *Balanced spatial distribution of stiffness and strength* A balanced distribution of lateral and torsional stiffness and strength against bi-directional ground excitation and rotational vibrations reduce the risk of non-uniform damage accumulation. This is achieved by close modal vibration periods in the two lateral directions, and a rotational period shorter than the lateral periods of vibration (torsionally stiff system).
- (d) *Rigid floor diaphragms* Sufficient rigidity in floor diaphragms ensures uniform distribution of inertial forces to vertical members (columns and walls) in a story. In-plane deformations of floor diaphragms under the internal shears transferred by vertical members should be negligibly small.
- (e) *Strong foundations* The foundations should be strong enough to transmit the inertial forces to the ground without imposing additional deformations to the structure above.

Fig. 6.14 Definition of the interstory drift terms for torsional irregularity in x direction



6.9 Structural Irregularities

Violation or relaxation of basic design principles stated above, which is inevitable in practice due to architectural preferences or several other constraints, create irregularities in the structural system. Irregularities are penalized in design, either by enforcing more rigorous structural models and analysis procedures, or by reducing the response modification factors, increasing the design forces and imposing reduced deformation limits.

Structural irregularities are treated in two general categories: Horizontal (in plan) and vertical (along elevation).

6.9.1 Irregularities in Plan

The basic types of horizontal irregularities are the torsional irregularity and discontinuities in floor diaphragms.

Torsional irregularity is a result of large eccentricity between the centers of mass and stiffness in a story. It leads to non-uniform distribution of inelastic deformation demands in a story. Torsional irregularity is defined to exist if the maximum interstory drift ratio $\Delta_{i,max}$ is more than 1.2 times the average interstory drift ratio $\Delta_{i,average}$ in any story. Maximum and average interstory drift ratios are defined in Fig. 6.14 for the i th story floor slab.

Typical examples of diaphragm discontinuities are re-entrant corners and diaphragm cutouts shown in Fig. 6.15. If the plan dimension of the re-entrant corner is larger than a percentage of the plan dimension in the same direction, then a plan irregularity develops. This proportion varies from 15 to 20 % in different seismic

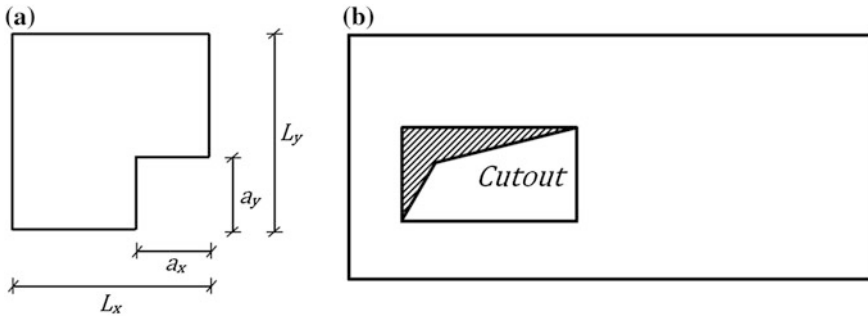


Fig. 6.15 **a** Re-entrant corners and **b** diaphragm cutouts creating plan irregularity

codes. Similarly, plan irregularity exists if the area of diaphragm cutouts is larger than a ratio of the total floor area. This ratio varies from 1/3 to 1/2 in different seismic codes.

6.9.2 Irregularities in Elevation

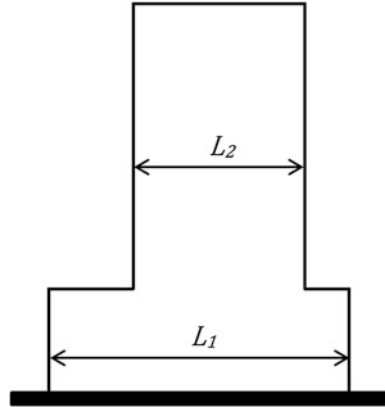
Significant variations of mass, stiffness, strength and floor size between adjacent stories are considered as vertical irregularities in seismic design. The main criterion for a vertically regular building is the continuity of lateral load resisting system from the foundation to the top. Usually a gradual reduction of mass, stiffness, strength and floor size is permitted from bottom to top along the building height, but the opposite has a negative impact on seismic performance.

Soft or weak story irregularity is the most critical type of vertical irregularity since soft story failures caused many building collapses during the past earthquakes, as discussed in [Chap. 7](#) for reinforced concrete buildings. If the stiffness and/or strength of a story is less than a proportion of that at the story above, then it is considered as a soft story. This proportion varies from 60 to 80 % in different seismic codes. Soft or weak story usually develops at the ground story of apartment buildings where the ground story is taller.

Vertical irregularity is also detected from the results of lateral load analysis. When the average interstory drift ratio $\Delta_{i, average}$ at the i th story is more than twice of this value calculated at the story above or below, then a vertical irregularity exists.

Significant reduction in the floor size or horizontal dimension of the lateral load resisting system between adjacent stories shown in [Fig. 6.16](#) causes vertical irregularity. When the L_1/L_2 ratio in [Fig. 6.16](#) exceeds a limit, then vertical irregularity develops. This limit is 1.3 in ASCE 7 and 1.25 in Eurocode 8. However Eurocode 8 increases the limit to 2.0 if the discontinuity occurs in the lower part of the building (15 % of the height).

Fig. 6.16 Vertical irregularity in the plan dimension of the lateral load resisting system



6.9.3 Selection of the Analysis Procedure

Analysis procedure selection is mainly based on structural irregularities present in the building system. Modal superposition procedure can be employed for all buildings whereas equivalent static lateral load procedure is subjected to certain restrictions because this procedure is based on a deformation configuration dominated by the first vibration mode. The deformation configurations of irregular buildings are more complicated however, hence higher mode contributions cannot be ignored.

The selection criteria depend on vertical and horizontal irregularities separately.

- (a) *There are no irregularities in plan and elevation* Both procedures can be employed. A planar structural model can be used separately in both orthogonal directions.
- (b) *Vertical irregularity is present* Only the modal superposition procedure can be employed. The response reduction factor can be reduced ($0.8q$ in EC8). If horizontal irregularity is not present additionally, then a planar structural model can be used separately in both orthogonal directions.
- (c) *Horizontal irregularity is present* Modal superposition procedure can be employed. Equivalent static lateral load procedure can also be employed if there is no additional vertical irregularity. However a spatial (3D) structural model is required for analysis in both orthogonal directions.

There is a further height or fundamental period limitation for the equivalent static lateral load procedure. This simpler procedure is not permitted for buildings having $T_1 > 4T_C$ or $T_1 > 2$ s (Eurocode 8), for most buildings having $T_1 > 3.5T_S$ (ASCE 7) and for buildings taller than 25 m (Turkish Earthquake Code). Higher modes shall be effective in the seismic response of such buildings.

6.9.3.1 Amplification of Accidental Eccentricity in Equivalent Static Lateral Load Procedure

When torsional irregularity defined in Sect. 6.9.1 exists, accidental eccentricity calculated according to Sect. 6.6.3 (5 % of dimension) is amplified as an additional punishment for using the simple equivalent static lateral force procedure in the US seismic code ASCE 7. The amplification coefficient D_i is given by,

$$D_i = \left(\frac{\Delta_{i,max}/\Delta_{i,average}}{1.2} \right)^2 \quad (6.36)$$

$\Delta_{i,max}$ and $\Delta_{i,average}$ were defined in Fig. 6.12. Eurocode 8 does not apply this amplification.

6.10 Deformation Control in Seismic Codes

Buildings designed under reduced seismic forces may undergo large inelastic deformations under the actual design ground motions with return periods of $T_R = 475$ years or ground motions with longer return periods. Large deformations may cause severe damage in architectural components, and also lead to significant second order (P-delta) effects in the vertical structural members. Moreover, two adjacent buildings may pound each other if they are not separated sufficiently by seismic joints. Hence, these deformations should be controlled for proper damage limitation.

6.10.1 Interstory Drift Limitation

Interstory drift δ_j is the difference between the lateral displacements of two adjacent floors j and $j - 1$. When it is divided, or normalized with the story height h_j , it is called the *interstory drift ratio* of the j th story, Δ_j as shown in Fig. 6.17.

Seismic codes impose limitations on interstory drift for preventing excessive relative deformations of the stories. The basic reason for limiting interstory drift is to prevent extensive damage and fall out of non-structural components such as infill walls, partition walls or window frames which occupy an entire bay of a story. Since these non-structural components do not have the ductile deformation characteristics of the frame members, they cannot cope with the in-plane frame deformations during an earthquake and sustain severe damage under excessive interstory deformations of the ductile frame. Although such damage cannot be totally prevented due to the fragile behavior of non-structural components, their disintegration from the frame can be prevented by imposing limitations on interstory drift.

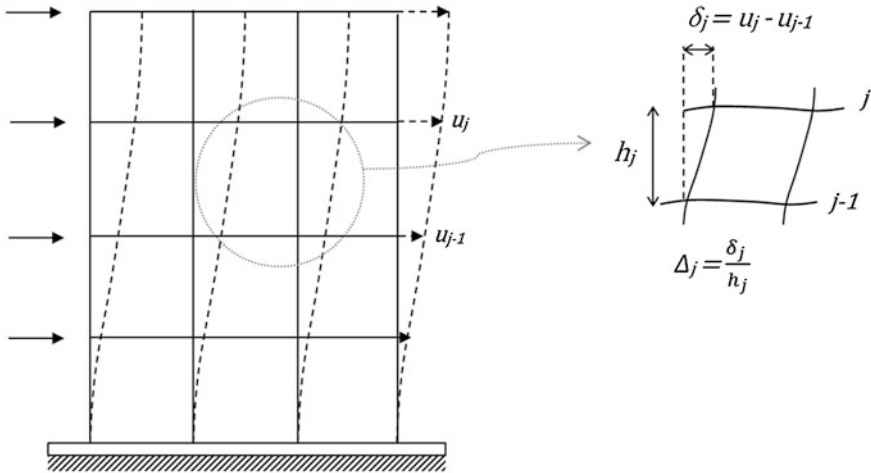


Fig. 6.17 Interstory drift δ_j and interstory drift ratio Δ_j in a building frame under the action of lateral seismic forces

ASCE 7 limits the interstory drift ratio to 2.5 % under earthquake forces which are “not” reduced by the response reduction factor. Accordingly, the interstory drift deformations obtained under the reduced design earthquake forces (design spectrum) are re-multiplied by a C_d factor, and checked for the 2.5 % limit of interstory drift ratio at each story j .

$$C_d \Delta_j \leq 0.025. \quad (6.37)$$

This limit is usually quite high for most buildings and it never controls seismic design. Unlike ASCE 7, Eurocode 8 always has a strict drift limitation under a serviceability earthquake ($T_R = 95$ years) and the interstory drifts are calculated from the equal displacement rule (i.e. the deformations obtained under the reduced design earthquake forces are re-multiplied by the q factor, not from a C_d factor that is much less than R). When converted from the serviceability to the design earthquake, the limiting interstory drift ratio in Eurocode 8 is 0.01 for buildings with brittle partitions, 0.015 for ductile partitions and 0.02 for buildings without partitions in contact with the frame. Accordingly, drift limits in EC8 control the sizing of frame members more than the strength demands and the q -factors.

Infill wall damages from two earthquakes are shown in Fig. 6.18. The ductile building frame in Fig. 6.18a was totally undamaged after the 2011 Van, Turkey earthquake. However there was significant damage in masonry infills since the infill material was unable to cope with the frame deformations (Sucuoğlu 2013). Building frame of the State building in Padang, Indonesia was also undamaged after the 2009 Padang earthquake, but the infill wall panels were completely destroyed. The State building could not function after the earthquake and continued its emergency operations at the tents in the building yard.

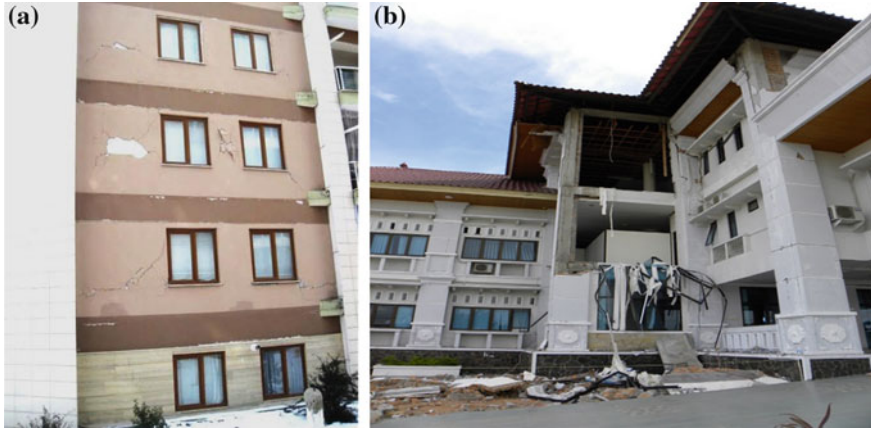


Fig. 6.18 Infill wall and panel damages in undamaged frames after the **a** 2011 Van, Turkey, and **b** 2009 Padang, Indonesia earthquakes

Drift limitation is more important for emergency facilities (hospitals, emergency centers, police and fire stations, etc.) compared to the ordinary buildings after an earthquake. Because non-structural damages prevent their use mainly due to psychological reasons. People affected from the earthquake do not simply enter buildings with exposed damage. Hence more stringent drift requirements are necessary for these buildings. This issue is usually overlooked in seismic codes and an increased importance factor in design is accepted sufficient.

6.10.2 Second Order Effects

Second order, or $P-\Delta$ effects are generated due to the interaction of vertical forces P with the lateral seismic deformations Δ to produce additional overturning moments $P\Delta$ on the structure. Let's consider an intermediate story in Fig. 6.19 where all lateral load resisting members in that story are represented by a single vertical flexural member which is shown in Fig. 6.19a. P is the entire vertical load acting on this story, h is the story height, M is the total overturning moment, V is the total lateral force exerted on this story by the stories above, and M_b is the overturning moment reaction at the base of the story. We will consider two cases separately, without and with considering the $P-\Delta$ effects.

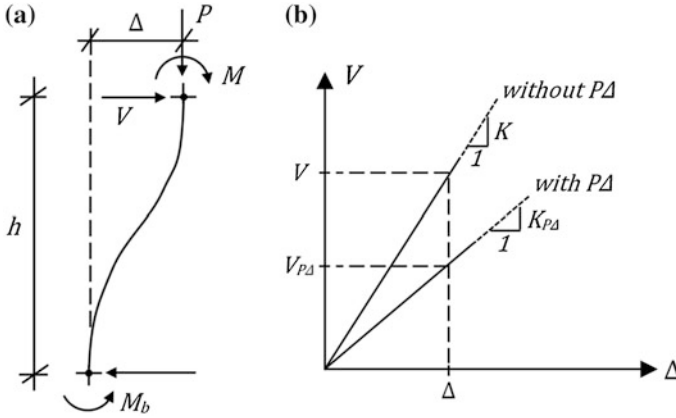


Fig. 6.19 a Forces acting on a column which undergoes lateral deformation, b Stiffness change due to second order effects

6.10.2.1 Without Considering P-Δ Effects

Moment equilibrium about the story base gives,

$$Vh + M = M_b. \tag{6.38}$$

6.10.2.2 With Considering P-Δ Effects

Moment equilibrium about the base includes the $P\Delta$ term.

$$Vh + M + P\Delta = M_b. \tag{6.39}$$

Equal overturning stability of the two cases, i.e. with and without $P-\Delta$ effects requires the equality of overturning moments M_b at the bottom of the story in Eqs. (6.38) and (6.39). This is possible only if the total lateral force V in Eq. (6.39) is replaced with a reduced term $V_{P\Delta}$. Then the equality leads to,

$$V_{P\Delta} = V(1 - \theta) \tag{6.40}$$

where

$$\theta = P\Delta/Vh. \tag{6.41}$$

Here, θ is called the *drift sensitivity coefficient*. It is simply the ratio of the second order overturning moment $P\Delta$ to the first order overturning moment Vh in Fig. 6.19a. Therefore at a lateral drift of Δ , the overturning stability of the system with $P-\Delta$ effects can be maintained the same as the system without $P-\Delta$ effects only if the total lateral force V is reduced by $(1 - \theta)$ according to Eq. (6.40). The

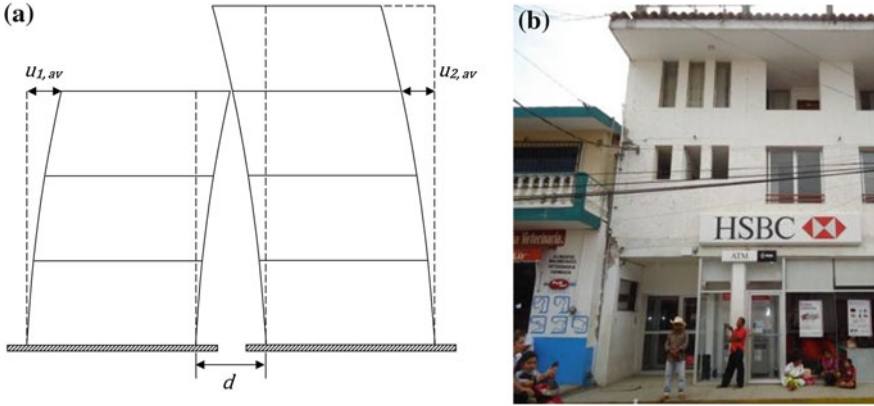


Fig. 6.20 **a** Building separations for preventing pounding, **b** Pounding damage

lateral stiffness of the system with $P-\Delta$ effects also reduces by $(1 - \theta)$, as depicted in Fig. 6.19b.

$$K_{P\Delta} = K(1 - \theta). \tag{6.42}$$

$P-\Delta$ effects can be indirectly and approximately compensated in design by increasing the seismic forces, and accordingly the lateral stiffness by a ratio $1/(1 - \theta)$ in view of Fig. 6.19b. In seismic codes, second order effects can be ignored in design if $\theta < 0.1$ in all stories. If $0.1 < \theta < 0.2$, $P-\Delta$ effects can be approximately accounted for by increasing the seismic design forces by the factor $1/(1 - \theta)$ at a story. If $\theta > 0.2$, an exact second order analysis is required. Finally, $\theta > 0.3$ is not permitted at any story.

6.10.3 Building Separations

Two adjacent buildings may deform toward each other during earthquake induced vibrations as shown in Fig. 6.20a. These two building blocks should be separated by at least a distance d equal to the maximum value of SRSS combination of the average displacements at the adjacent story levels. Usually maximum value of d occurs at the possible pounding level which is the roof level of the shorter building in Fig. 6.20. According to Eurocode 8 and the Turkish Earthquake Code,

$$d > \alpha \sqrt{(u_{1,av}^2 + u_{2,av}^2)max} \tag{6.43a}$$

where u_i is the elastic displacement under the (reduced) design earthquake, amplified by the q factor (equal displacement rule). The value of α is 0.7 if the story levels are equal, or 1.0 if story levels are not equal in the adjacent buildings according to Eurocode 8. According to ASCE 7, the minimum separation is calculated for individual building blocks as,

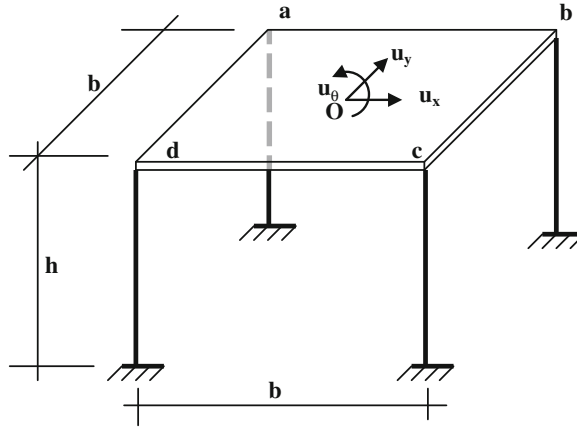
$$d > \frac{C_d \delta_{xe}}{I} \tag{6.43b}$$

Here, C_d is the deflection amplification factor (5.5 for special moment resisting frames), δ_{xe} is the elastic displacement at level x under the design earthquake (reduced by R), and I is the structure importance factor.

Pounding is a major hazard during strong earthquakes. An example of pounding damage is shown in Fig. 6.20b.

Exercises

1. Figure shows a uniform slab supported on four columns rigidly attached to the slab and fixed at the base. The slab has a total mass m and it is rigid both in plane and out of plane. Each column is of circular cross section, and their second moment of cross-sectional area about any diametrical axis is as noted below. With DOFs selected as u_x , u_y and u_θ at the center of mass of the slab, and using influence coefficients:
 - (a) Formulate the mass and stiffness matrices in terms of m and the lateral stiffness $k = 12 EI/h^3$ of the right columns; h is the height. Moment of inertia of the left columns is $2I$ and of the right columns is I .
 - (b) Formulate the equations of motion for ground motion in the x -direction.
 - (c) Solve the equation of motion for ground acceleration given as $\ddot{u}_{gx}(t) = a_0 \cos \bar{\omega}t$ in the x -direction (system is initially at rest).

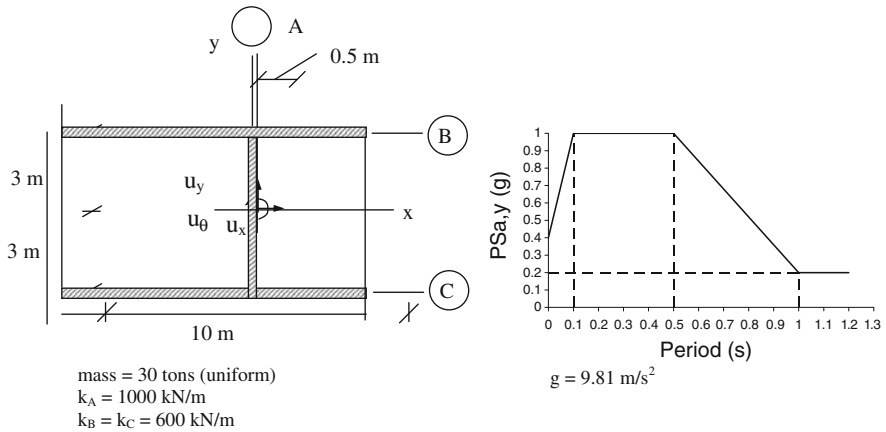


Answers

$$(a) K = k \begin{bmatrix} 6 & 0 & 0 \\ 0 & 6 & -b \\ 0 & -b & 3b^2 \end{bmatrix}$$

$$(b) u(t) = \frac{a_0}{(\omega_n^2 - \bar{\omega}^2)} (\cos \omega_n t - \cos \bar{\omega} t)$$

2. A single story 3-DOF frame with an unsymmetrical plan about the y axis is given below, with its eigenvalues and eigenvectors. It is excited by the given spectrum in the y direction. Damping is 5 % for all modes.

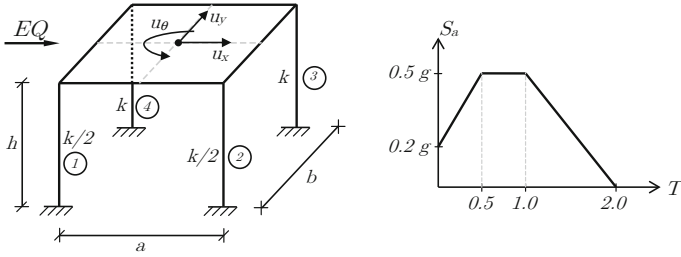


- Write the equation of motion for the coupling degrees of freedom under the excitation in y direction $\ddot{u}_{gy}(t)$.
- Calculate the modal vectors and frequencies.
- Calculate the modal displacements of the mass center and combine them with SRSS and CQC separately. Also calculate the displacements of the mass center by using the equivalent static lateral load procedure in the y direction. Discuss the results.
- Calculate the base shear in y direction by SRSS, CQC and equivalent static lateral load procedure.

Answers

- $\underline{m} = \begin{bmatrix} 30 & 0 \\ 0 & 340 \end{bmatrix}$, $\underline{k} = \begin{bmatrix} 1000 & 500 \\ 500 & 11,050 \end{bmatrix}$, $\underline{p} = - \begin{bmatrix} 30 \\ 0 \end{bmatrix} \ddot{u}_{gy}$
- $\omega_1 = 5.29 \text{ rad/s}$, $\omega_2 = 6.15 \text{ rad/s}$, $\phi_2 = \begin{Bmatrix} -0.134 \\ -0.037 \end{Bmatrix}$, $\phi_1 = \begin{Bmatrix} -0.123 \\ 0.040 \end{Bmatrix}$
- $\underline{u}_{SRSS} = \begin{bmatrix} 0.0423 \text{ m} \\ 0.0129 \text{ rad} \end{bmatrix}$, $\underline{u}_{CQC} = \begin{bmatrix} 0.0483 \text{ m} \\ 0.0109 \text{ rad} \end{bmatrix}$, $\underline{u}_{EQL} = \begin{bmatrix} 0.0602 \text{ m} \\ -0.0027 \text{ rad} \end{bmatrix}$
- $V_{b,SRSS} = 41.39 \text{ kN}$, $V_{b,CQC} = 46.18 \text{ kN}$, $V_{b,EQL} = 58.86 \text{ kN}$

3. A single story eccentric 3D frame is given below. The degrees of freedom u_x , u_y and u_θ are defined at the centroid of the slab. The slab is rigid both in-plane and out-of-plane. Its mass is 100 tons. $a = b = 4 \text{ m}$, $h = 3 \text{ m}$ and $k = \frac{12EI}{h^3} = 400 \text{ kN/m}$ in both directions.



The slab is rigid both in-plane and out-of-plane. Determine,

- (a) The eigenvalues and eigenvectors
- (b) Shear forces and bending moments in columns 1 and 4, if the frame is subjected to the reduced design spectrum given in the figure above, in the x direction.

Answers

- (a) $\omega_1 = 3.32 \text{ rad/s}$
 $\omega_2 = 3.46 \text{ rad/s}$
 $\omega_3 = 6.08 \text{ rad/s}$
 $\underline{\phi}_1 = \begin{Bmatrix} 0.0981 \\ 0 \\ 0.0118 \end{Bmatrix}$ $\underline{\phi}_2 = \begin{Bmatrix} 0 \\ 1 \\ 0 \end{Bmatrix}$ $\underline{\phi}_3 = \begin{Bmatrix} 0.0193 \\ 0 \\ -0.0601 \end{Bmatrix}$ $\underline{u} = \begin{Bmatrix} u_x \\ u_y \\ u_\theta \end{Bmatrix}$
- (b) Column 1 (SRSS):
 $f_x = 12.78 \text{ kN}$, $f_y = 6.30 \text{ kN}$, $M_x = 9.43 \text{ kN m}$, $M_y = 19.17 \text{ kN m}$

Chapter 7

Seismic Design of Reinforced Concrete Structures

Abstract Seismic design is based on inherent ductile response, which is manifested by capacity design principles in reinforced concrete buildings. Ductility in reinforced concrete materials and members are discussed in this chapter. The effect of confinement for increasing compressive strain capacity of concrete is explained. Seismic design requirements for providing ductile response of beams, columns and slender shear walls under earthquake loads are evaluated in detail. Strong column-weak beam principle and its implementation in seismic design codes is elaborated. Strength design of non-ductile members, namely beam-column joints and squat shear walls in seismic codes are described. Chapter concludes with a comprehensive design example of a 5-story concrete frame.

7.1 Introduction

Seismic design procedures in earthquake codes mainly comprise of the following steps:

1. Calculate lateral earthquake forces for linear elastic response.
2. Reduce linear elastic forces to account for inelastic response.
3. Apply reduced forces to the structural model, carry out structural analysis and determine the internal seismic design forces acting on structural members as well as interstory drifts.
4. Combine internal seismic design forces with the internal forces from gravity loads (Use load combinations in the relevant design code).
5. Design structural members under these combined design forces.
6. Check the calculated interstory drifts with the permitted drift limits.

In Step 1, lateral earthquake forces are calculated from a linear elastic design spectrum which represents design ground motion intensity. The linear elastic spectrum is reduced in Step 2 with the response reduction factor (R or q) in order to account for the inelastic deformation capacity (ductility) of the system. Then a

structural model is constructed in Step 3, and response spectrum analysis is carried out under the reduced acceleration spectrum (inelastic design spectrum). The internal seismic design forces determined in Step 3 are combined with the results of gravity analysis in Step 4. Finally structural members are designed under these combined force demands in Step 5. Hence, this is a “*force-based*” design procedure since the design of structural members is based on internal forces which indirectly account for the inelastic deformation capacity of the conceived structural system. This deformation capacity has to be “assumed” in advance, depending on the ductility level selected for design (medium or high in EC8, ordinary or special in ASCE7). Excessive lateral deformations are not permitted however, which are checked in Step 6 in terms of interstory drift ratios. When seismic forces are low, interstory drift limits may control design.

The basis for the design of RC members and systems are the compulsory concrete design standards under non-seismic conditions. These are Eurocode 2 in Europe and ACI 318 in the USA. Seismic design rules for reinforced concrete structures are implemented by imposing additional requirements by the seismic codes to the conventional design under non-seismic loads.

Seismic design of structural systems is essentially based on an inherent ductile response under strong ground excitation. Ductility can be defined as the “capacity of undergoing large plastic deformations without reduction in strength”, both at the material, component and system levels. Although ductility is not expressed explicitly in the seismic analysis procedures recommended by seismic design codes, reduction of elastic earthquake forces which was discussed in [Chap. 4](#) relies on the premise of a ductile seismic response.

Systems with medium or ordinary ductility levels are composed of members with certain longitudinal and lateral reinforcement arrangement as well as confinement and anchorage requirements at critical sections in order to ensure a minimum required ductile response under design earthquake forces. This is considered as equivalent to $q = 4$ in Eurocode 8 and $R = 5$ in ASCE 7 for reinforced concrete structures.

Special additional detailing rules are applied for high or special ductility, leading to larger reduction in elastic forces ($q = 6$ in Eurocode 8 and $R = 7-8$ in ASCE 7). Special ductility level in RC systems which are composed of ductile beams, columns and shear walls and strong connections is provided by employing the “Capacity Design Principles”.

7.2 Capacity Design Principles

Capacity design in Eurocode 8 is defined as follows: “Design method in which elements of the structural system are chosen and suitably designed and detailed for energy dissipation under severe deformations while all other structural elements are provided with sufficient strength so that the chosen means of energy dissipation can be maintained”.

A dissipative structure is able to dissipate energy by means of ductile hysteretic behavior and/or by other mechanisms at the dissipative zones, which are the predetermined parts of a dissipative structure where the dissipative capabilities are mainly located. These are also called critical regions.

Capacity design has two major implications, one at the member level, and the other at the system level.

Member level Flexural failure mode is ensured by suppressing shear failure (capacity shear principle in beams, columns, walls and connections).

System level The spreading of plastic regions that undergo flexural yielding follows a hierarchy for obtaining a more ductile system response (strong column–weak beam principle at the connections).

An overview of the capacity design of concrete structures, detailing and dimensioning according to Eurocode 8 is discussed extensively in Fardis (2009).

7.3 Ductility in Reinforced Concrete

Ductility or deformation capacity of reinforced concrete systems is provided by the ductility of its constituent materials (steel and concrete), ductility of its members (beams, columns and walls), and the overall ductility of the structural system under seismic actions. These are discussed separately below. However it should be noted that a ductile reinforced concrete response can be obtained only if the dominant failure mode of the structural components is flexure. Therefore brittle failure modes such as shear, diagonal tension and compression should be prevented whereas ductility in flexure should be enhanced for obtaining a ductile system response under strong seismic excitations.

7.3.1 Ductility in Reinforced Concrete Materials

A ductile flexural member behavior can be achieved by employing materials with ductile stress–strain behavior at the critical sections where bending moments are maximum. One of the two constituents of reinforced concrete is steel, which is inherently ductile. Typical stress–strain relationships for structural steel are shown in Fig. 7.1 for (a) the hot rolled and (b) cold worked reinforcing bars where the horizontal axis is strain. It is observed that both types of structural steel have large plastic strain capacity, exceeding 12 %.

The other constituent material, plain concrete does not possess such ductile uniaxial stress–strain behavior (see curve with $\sigma_2 = 0$ in Fig. 7.2). However when the conditions of stress change from uniaxial ($\sigma_2 = 0$) to triaxial ($\sigma_2 > 0$), both stress and strain capacities of concrete enhance significantly with the increasing lateral pressure, as shown in Fig. 7.2.

Fig. 7.1 Stress–strain relationships for structural steel. Modulus of elasticity $E_s = 2 \times 10^5$ MPa

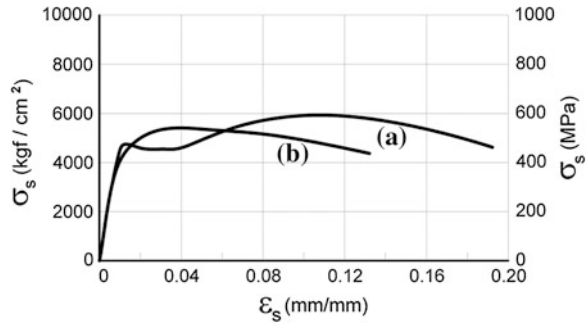
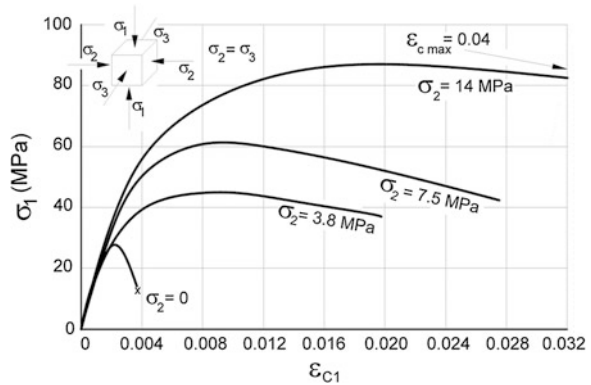


Fig. 7.2 Stress–strain relationships for concrete under uniaxial ($\sigma_2 = 0$) and triaxial ($\sigma_2 > 0$) stress



Triaxial stress state in reinforced concrete members can be provided with confinement reinforcement. When concrete is subjected to axial stress σ_1 , passive lateral pressure σ_2 developed by the lateral tie reinforcement (Fig. 7.3a) provides significant increase in strength and enormous increase in the strain capacity of concrete. The improvement is strongly related with the tie spacing “s” (Fig. 7.3b, c).

Strength and deformation capacities of concrete fibers in the core region of columns increase with the amount of lateral confinement reinforcement (Fig. 7.4). Confinement is most effective in circular columns since lateral pressure develops uniformly in all radial directions whereas a rectangular tie is more effective at the corners as shown in Fig. 7.3a.

7.3.2 Ductility in Reinforced Concrete Members

Reinforced concrete members, namely beams, columns and shear walls may either fail in flexure by reaching the yielding at a cross section, or they may fail in shear or diagonal tension under the applied internal forces (bending moment, shear

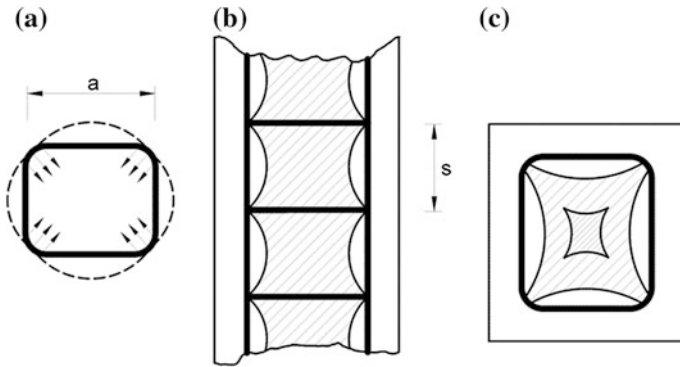
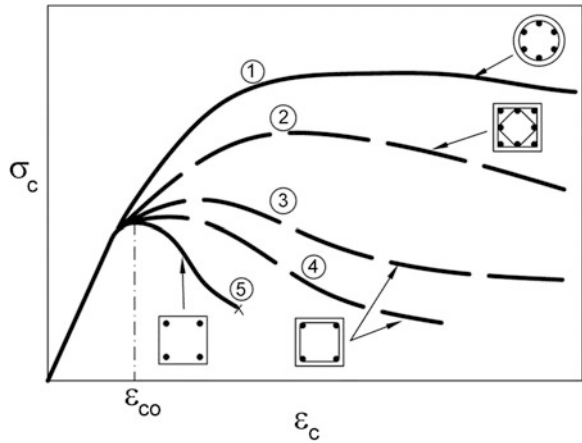


Fig. 7.3 Confinement of concrete in rectangular sections. **a** Lateral confinement pressure provided with lateral ties; **b** confined concrete along elevation; **c** confined concrete along cross section

Fig. 7.4 Stress–strain relations for unconfined (curve 5) and confined (curves 1–4) reinforced concrete sections



force, axial force) during an earthquake. Shear failure is brittle since it is accompanied with no deformation capacity once the shear capacity is exceeded. Flexure failure on the other hand is generally ductile. After the yield moment is attained under bending, the tension steel may continue to elongate in the plastic range until it ruptures or the concrete in compression crushes. This leads to large plastic rotation capacities, hence large ductility capacity at member ends where yielding occurs.

Seismic design rules for obtaining a ductile flexural behavior in reinforced concrete beams, columns and shear walls are discussed separately below.

7.4 Seismic Design of Ductile Reinforced Concrete Beams

Ductility in reinforced concrete beams is sensitive to the level of shear stress, ratio of tensile reinforcement, ratio of compression reinforcement, and ratio of lateral reinforcement for the confinement of concrete.

7.4.1 Minimum Section Dimensions

Minimum dimensions are imposed for providing the space required for reinforcing detailing to ensure ductile flexural behavior.

- Minimum beam width is 200 mm (Eurocode 8) and 250 mm (ACI 318).
- Beam width is limited with the adjoining column dimension perpendicular to the beam axis (ACI 318).
- The width to depth ratio shall not be less than 0.3 (ACI 318).
- Maximum beam depth is 1/4 of the beam clear span (ACI 318).

The last item controls lateral buckling phenomenon and prevents deep beam behavior which may induce flexure-shear failure mode at large deformations.

7.4.2 Limitations on Tension Reinforcement

Longitudinal tension reinforcement ratio at both support and span sections should satisfy the following limits:

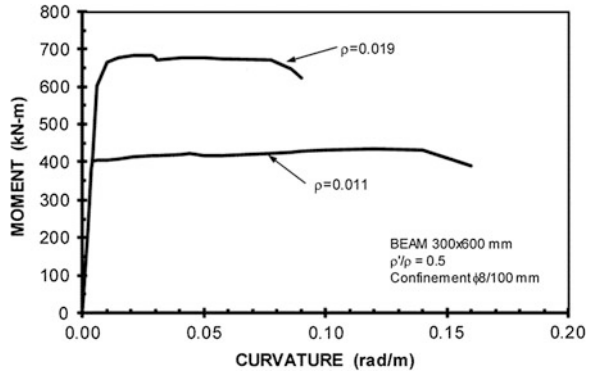
$$\rho_{\min} \leq \rho \leq \rho_{\max} \quad (7.1a)$$

$$\rho_{\min} = \frac{0.5f_{ctm}}{f_{yk}} \text{ (Eurocode 8) and } 200/f_y \text{ (ACI 318, psi);} \quad (7.1b)$$

$$\rho_{\max} = 0.025 \text{ (ACI 318).}$$

Eurocode 8 defines ρ_{\max} with a rigorous equation. The minimum tensile reinforcement ratio controls cracking of concrete in service conditions whereas the maximum ratio controls ductility of the section. Let us consider the moment-curvature relationships of two beam sections in Fig. 7.5 with identical lateral reinforcement and compression reinforcement ratio that ensure flexural failure mode. The only difference is the ratio of tension reinforcement. It can be observed that ductility reduces with increase in tension reinforcement, and 0.02 appears as a reasonable upper limit for a ductile response.

Fig. 7.5 The effect of tension reinforcement ratio on the moment-curvature ductility of beams



7.4.3 Minimum Compression Reinforcement

The ratio of bottom reinforcement to top reinforcement at the support regions of beams should be at least 0.5 in seismic zones with high intensity, and 0.3 in seismic zones with lower intensity. This is indeed the ratio of compression steel to tension steel (ρ'/ρ) at the support regions.

Compression reinforcement is known to be increasing the ductility of a beam cross section significantly. Moment-curvature relations for beam sections with minimum tension and lateral reinforcement, but with different compression reinforcement ratios are shown in Fig. 7.6. It is evident that $\rho'/\rho > 0.5$ is a reasonable lower limit to ensure ductility. Furthermore, when the direction of earthquake excitation reverses which also lead to a moment reversal at the beam support, the compression reinforcement serves as the tension reinforcement.

7.4.4 Minimum Lateral Reinforcement for Confinement

The under-reinforced beams are ductile under monotonically increasing moments. However when a beam undergoes moment reversals during a strong earthquake and plastic regions (plastic hinges) form at the critical end regions, confinement of these regions are necessary in order to prevent crushing of concrete and buckling of longitudinal bars. The absence of confined end regions results in strength degradation (reduction of yield moment under moment reversals), which leads to extensive damage accumulation in the yielding regions (Fig. 7.7, Acun and Sucuoğlu 2010).

The length of the confined regions at both ends should not be less than twice the depth of the beam $2h_w$ (ACI 318). Special seismic ties shall be used in these regions, with spacing s being the lesser of 225 mm, 1/4 of the beam depth,

Fig. 7.6 The effect of compression reinforcement on the moment-curvature ductility of beams

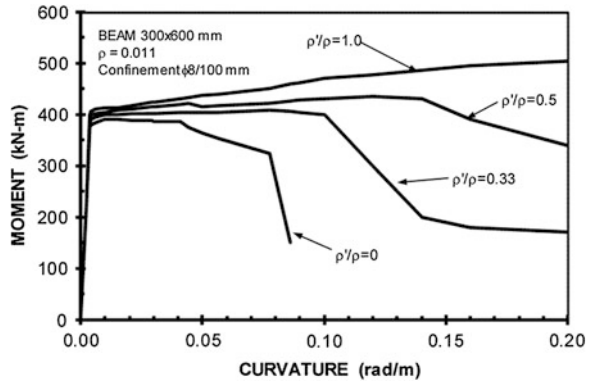
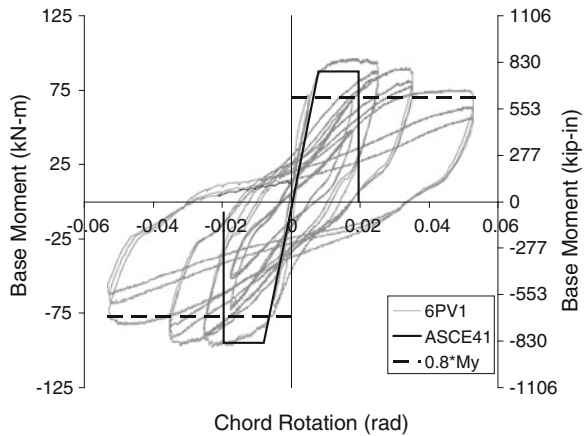


Fig. 7.7 The effect of confinement reinforcement on the moment-rotation ductility



or 8 times the smallest longitudinal bar diameter (Eurocode 8 and ACI 318). The first tie spacing from the column face should be less than 50 mm ($s_o < 50$ mm) for capturing the first shear crack on the beam end. Detailing of the confined regions of a typical ductile beam is given in Fig. 7.8.

7.4.5 Shear Design of Beams

Shear failure is suppressed by calculating the design shear force from flexural capacity, but not from analysis. The shear forces due to gravity loading are also taken into account. This is called *capacity shear* in earthquake resistant design.

Let us consider the free body diagram of a beam carrying uniformly distributed gravity loading ($g + q$) along its span. When the earthquake moments act on the

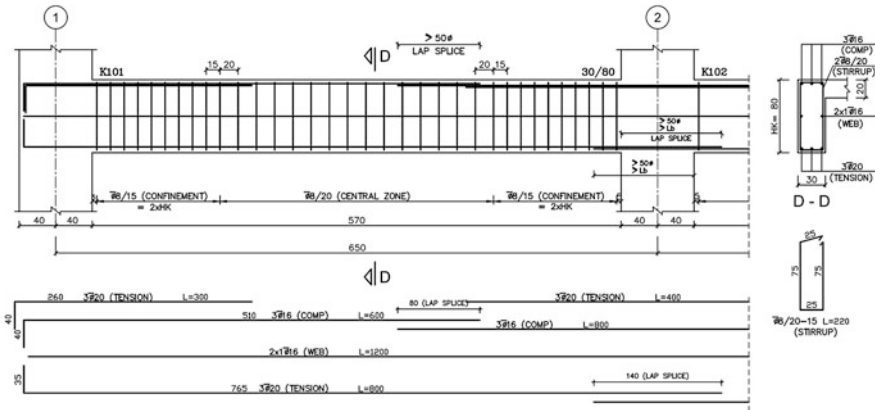


Fig. 7.8 Reinforcement detailing of a typical beam

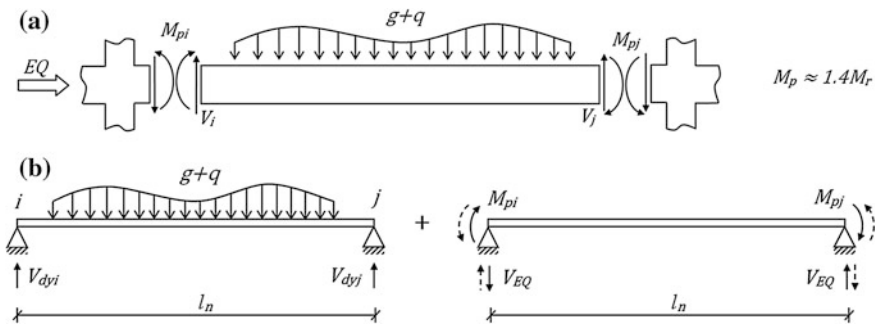


Fig. 7.9 a Free body diagram of a beam under gravity loads and earthquake moments at flexural capacity; b superposition of gravity and earthquake shear forces at beam ends

beam, we will assume that both end-sections i and j reach their flexural capacities (with strain hardening) under double flexure (Fig. 7.9a).

Then the shear forces (capacity shear) acting at both ends can be calculated from Fig. 7.9b by using the principle of superposition. From equilibrium;

$$V_{ei,j} = V_{dyi,j} \mp V_{EQ} \quad \text{where } V_{EQ} = \frac{M_{pi} + M_{pj}}{l_n}. \quad (7.2)$$

V_e is the design shear force in Eq. (7.2). The top and bottom plastic moment capacities M_{pi} and M_{pj} should consider strain hardening of tension steel shown in Fig. 7.1. This corresponds to an approximate 25 % increase in the yield moment capacities on average. V_e is theoretically the maximum shear force that can

develop in a beam under extreme earthquake excitation which may exceed the design earthquake intensity (which was reduced with R). The shear capacity V_r supplied in design should exceed the capacity shear force V_e which requires

$$V_e < V_r. \quad (7.3)$$

The shear capacity of the beam section V_r is calculated according to the relevant concrete design standards. Further, possible compression strut failure due to over-reinforcing in shear is prevented by the requirement

$$V_e \leq 0.22 b_w d f_{cd} \text{ (ACI 318, metric)}. \quad (7.4)$$

Reinforcement detailing of a typical beam designed according to modern seismic code requirements is shown in Fig. 7.8.

7.5 Seismic Design of Ductile Reinforced Concrete Columns

Ductility of a reinforced concrete columns is sensitive to the level of axial load, ratio of longitudinal reinforcement, ratio of lateral reinforcement for the confinement of concrete and the shear forces acting on the column. Each parameter is governed with a different design rule.

7.5.1 Limitation on Axial Stresses

Moment–curvature relationship for reinforced concrete column sections is highly sensitive to the level of axial load. Moment capacity and stiffness increases with axial load up to $N/N_o = 0.4$, but ductility decreases as shown in Fig. 7.10. Therefore the level of axial load or axial stress has to be limited such that ductile section response is ensured.

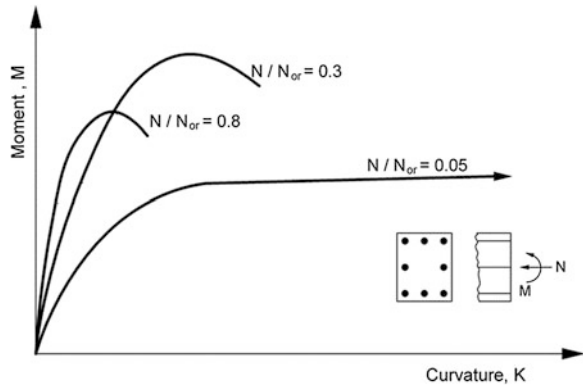
There are two requirements for limiting axial stresses in columns. The first one controls the minimum cross section dimensions in rectangular columns:

$$A_c = bd \geq 75000 \text{ mm}^2; \quad b \geq 250 \text{ mm (Eurocode 8)}. \quad (7.5)$$

The second one controls the maximum axial stress in columns.

$$\frac{N_d}{A_c f_{cd}} \leq 0.65; \quad f_{ck} \geq 20 \text{ MPa (Eurocode 8)}. \quad (7.6)$$

Fig. 7.10 The effect of axial load on the moment–curvature response of rectangular columns



7.5.2 Limitation on Longitudinal Reinforcement

A ductile flexural column response requires that the minimum and maximum longitudinal reinforcement ratios are 1 and 4 %, respectively. A longitudinal reinforcement ratio larger than 0.04 may produce flexure-compression failure mode, which is not ductile.

$$0.01 \leq \rho_t \leq 0.04. \tag{7.7}$$

7.5.3 Minimum Lateral Reinforcement for Confinement

Lateral ties which confine concrete in compression increases the compressive strain capacity of concrete as discussed in Sect. 7.2. This increase in the strain capacity of concrete also improves the curvature ductility of the cross section significantly. Moment-curvature relationships of two typical rectangular column sections are shown in Fig. 7.11. Two columns are identical except the amount of lateral reinforcement. The lower curve is for a column with inadequate lateral reinforcement, which represents typical non-seismic design detailing. It has an extremely brittle response with almost no deformation capacity after yielding. The upper curve is for a column with minimum lateral reinforcement according to seismic codes. Even minimum lateral reinforcement improves the curvature ductility of the column cross section enormously.

Minimum lateral reinforcement is required for the critical end regions of columns where yielding is expected to occur. These regions are called the confinement regions at both ends and their length should not be less than the larger of 450 mm, 1/6 of the column clear length, or the larger dimension of the column section (Eurocode 8).

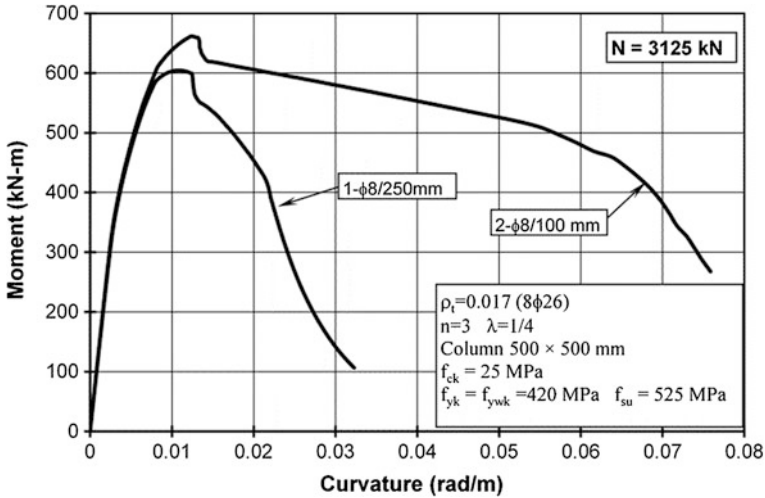


Fig. 7.11 The effect of confinement on the moment–curvature response of rectangular columns

Minimum diameter of the tie reinforcement is 6 mm and the minimum vertical spacing s is the lesser of 175 mm or 1/2 of the smaller section dimension (Eurocode 8). The maximum lateral distance a (see Fig. 7.3a) between the legs of tie reinforcement should be less than 25 tie diameters. Cross ties are added to satisfy this requirement if necessary.

The minimum area of lateral reinforcement should satisfy the larger value in Eq. (7.8a, b) for $N_d > 0.20 A_c f_{ck}$ in ACI 318 (metric). N_d is the axial force under gravity loads. If N_d is less, 2/3 of the value calculated from Eq. (7.8a, b) is used.

$$A_{sh} \geq 0.30 s b_k \left[\frac{A_c}{A_{ck}} - 1 \right] \frac{f_{ck}}{f_{ywk}} \quad \text{or} \quad A_{sh} \geq 0.075 s b_k \frac{f_{ck}}{f_{ywk}}. \quad (7.8a)$$

The minimum lateral reinforcement in Eq. (7.8a, b) maintains the flexural strength of a column after cover spalling, following the formation of a plastic hinge at the considered section. Eurocode 8 requires a minimum volume of transverse confining reinforcement within the critical regions, defined by the mechanical volumetric ratio ω_{wd} :

$$\omega_{wd} = \frac{\text{volume of confining hoops}}{\text{volume of concrete core}} \cdot \frac{f_{yd}}{f_{cd}}. \quad (7.8b)$$

f_{yd} and f_{cd} are the design strengths of confining steel and concrete, respectively.

7.5.4 Strong Column-Weak Beam Principle

The implementation of capacity design at the system level was manifested in Sect. 7.2 as “the spreading of plastic regions that undergo flexural yielding follows a hierarchy for obtaining a more ductile system response”. Flexural plastic hinges inevitably form at the ends of frame members under design ground motions which are reduced with $R > 1$.

A plastic hinge formed on a beam is less critical than a plastic hinge on a column or shear wall, because vertical members may lose their stability under gravity loads when plastic hinges form. Accordingly, plastic hinge hierarchy requires formation of plastic hinges first on beams, then at the base of first story columns. A plastic hinging hierarchy can be imposed in design by proportioning the flexural capacities of beam and column ends joining at a connection. This is called the *strong column–weak beam principle*, which is expressed by Eq. (7.9) and explained in Fig. 7.12. The constant λ is a safety factor in Eq. (7.9), which is 1.2 in ASCE 7 and 1.3 in Eurocode 8.

$$(M_{r,bot} + M_{r,top}) \geq \lambda (M_{r,i} + M_{r,j}) \quad (7.9)$$

Strong column-weak beam principle leads to a ductile collapse strategy under increasing lateral earthquake forces. Let us consider the three story and single bay frame in Fig. 7.13a, which obeys strong column-weak beam design. It is loaded with increasing lateral forces until collapse, similar to the static pushover analysis introduced in Sect. 5.5. If we plot the base shear force versus roof displacement, we obtain the capacity curve in Fig. 7.13b. The progress of plastic hinges at different stages of loading are marked on both figures. It can be observed that the frame exhibits significant ductility before collapse under lateral forces.

Formation of plastic hinging at the column (or wall) bases is inevitable at the later stages of loading since they effectively become cantilever columns after all the beams spanning to the column yield, as shown in Fig. 7.13c.

If columns are weaker than beams, then a soft story may develop. Plastic hinges form at the first story columns first where the moments are maximum (Fig. 7.14a). When plastic hinges develop both at the bottom and top ends of the first story columns, a soft story forms since the instantaneous lateral stiffness becomes very low, even zero when there is no strain hardening (Fig. 7.14b). Then lateral deformations increase quickly under increasing lateral loads, and the frame loses its stability under gravity loads. This is a catastrophic collapse (pan-caking). Most collapses and life losses in buildings during strong earthquakes are due to soft story formation.

Two examples of soft story damage and collapse are shown below in Fig. 7.15.

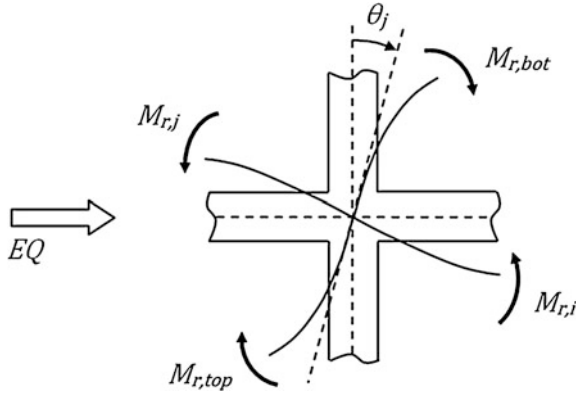


Fig 7.12 Moment capacities of member ends joining at a beam–column connection

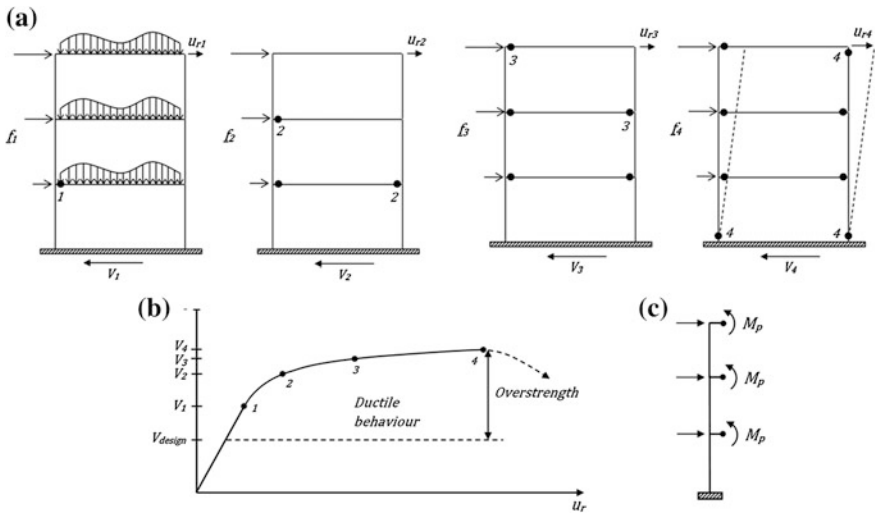


Fig. 7.13 **a** Plastic hinge hierarchy in a frame with strong columns and weak beams under increasing lateral loads; **b** capacity curve of the frame in (a); **c** free body diagram of a column when all connecting beams yield. Further increase in lateral loads will lead to yielding at the column base

7.5.5 Shear Design of Columns

The design shear force is also calculated from capacity shear, but not from analysis as discussed in the shear design of beams. Further, there is no span loading on columns. Let us consider a column which reaches its flexural capacity (with strain hardening) at both top and bottom ends under double flexure (Fig. 7.16a). From equilibrium:

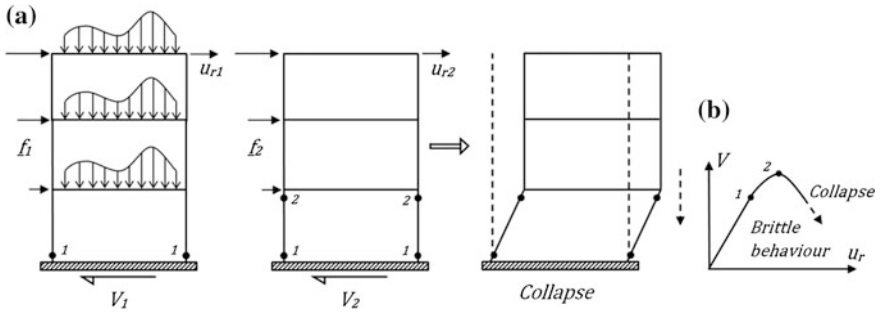


Fig. 7.14 a Plastic hinge hierarchy in a frame with weak columns and strong beams under increasing lateral loads; b capacity curve of the frame in (a)



Fig. 7.15 Soft story collapses from a 1971 San Fernando Earthquake, USA on the left, b 2003 Bingöl earthquake, Turkey on the right

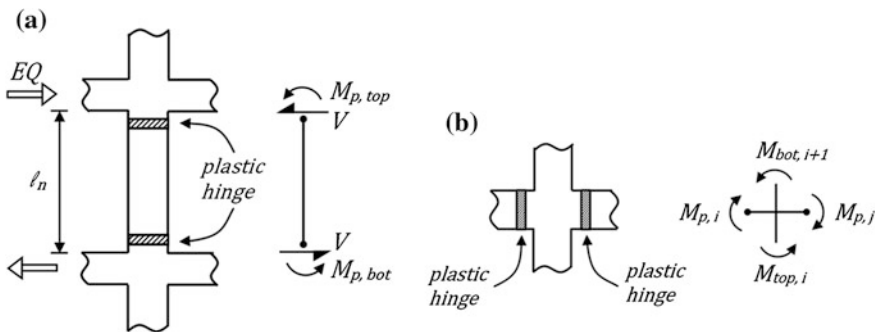


Fig. 7.16 A column under double flexure. a Yielding at column ends: weak column–strong beam; b yielding at beam ends: strong column–weak beam

$$V_e = \frac{M_{p,top} + M_{p,bot}}{l_n} \quad (7.10)$$

where V_e is the design shear force, $M_{p,top}$ and $M_{p,bot}$ are the plastic moment capacities with strain hardening at the top and bottom ends, respectively.

Equation (7.10) is valid when columns are weaker than beams. In capacity design however, columns are stronger than beams. Hence beam ends yield before column ends around a connection (Fig. 7.16b). In this case, equilibrium of moments around the connection requires

$$M_{top,i} + M_{bot,i+1} \simeq M_{p,i} + M_{p,j}. \quad (7.11)$$

Hence, the plastic column end moments in Eq. (7.10) is replaced with the moments distributed to column ends in accordance with the proportions obtained from linear elastic analysis under lateral loads.

$$M_{top,i} = (M_{p,i} + M_{p,j}) \cdot \frac{M_{top,i}^{analysis}}{M_{top,i}^{analysis} + M_{bot,i+1}^{analysis}} \quad (7.12)$$

$$M_{bot,i+1} = (M_{p,i} + M_{p,j}) \cdot \frac{M_{bot,i}^{analysis}}{M_{bot,i}^{analysis} + M_{top,i-1}^{analysis}} \quad (7.13)$$

Clearly, this replacement reduces the column design shear force in Eq. (7.10).

The shear capacity V_r supplied in design should exceed the capacity shear force V_e .

$$V_e < V_r. \quad (7.14)$$

The shear capacity of the column section V_r is calculated according to reinforced concrete design standards. Possible compression strut failure due to over-reinforcing in shear is prevented by the requirement

$$V_e \leq 0.22 A_w f_{cd} \quad (\text{ACI 318, metric}). \quad (7.15)$$

A_w is the shear area in the earthquake direction.

Example 7.1 A 2 story, 2 bay frame is given in Fig. 7.17 with the gravity and earthquake forces. The results of analysis under gravity and earthquake loads are also provided separately. Determine the design moments and design shears for the left beam, left column and center column at the first story. Assume that columns are stronger than beams around a joint, and flexural capacity moments in beams are 1.4 times the design moments.

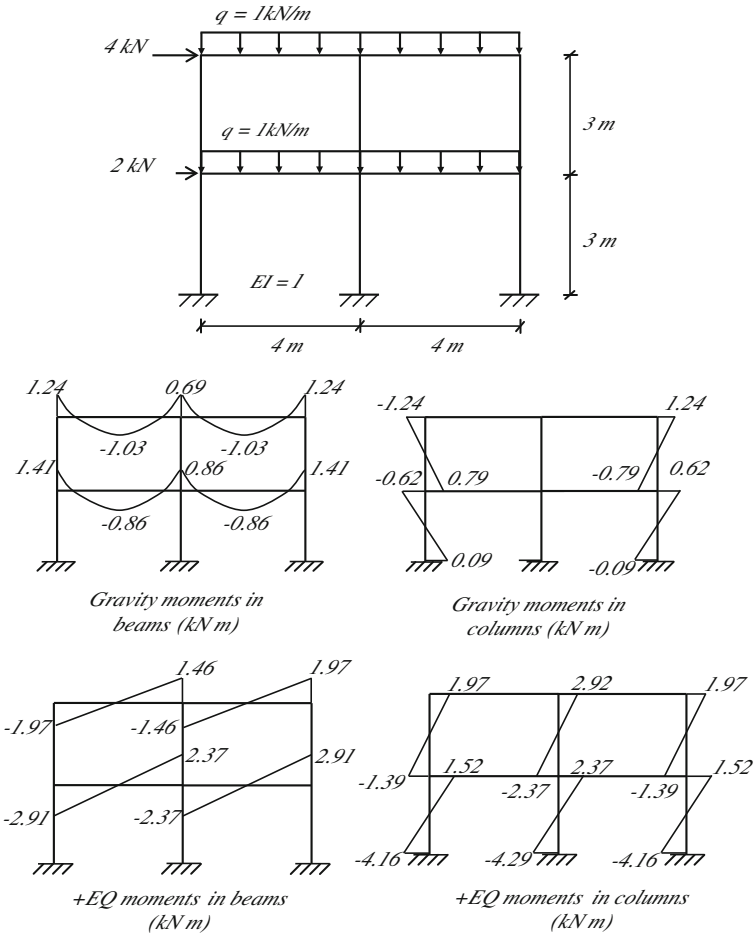


Fig. 7.17 2 story, 2 bay frame

Solution

1st Story Left Beam

Design moments from 1.0G + 1.0EQ load combination.

$$M_{di} = 1.41 - 2.91 = -1.5 \text{ kN m} \quad M_{dj} = 0.86 + 2.37 = 3.23 \text{ kN m}$$

Design moments from 1.0GR - 1.0EQ load combination.

$$M_{di} = 1.41 - (-2.91) = 4.32 \text{ kN m}$$

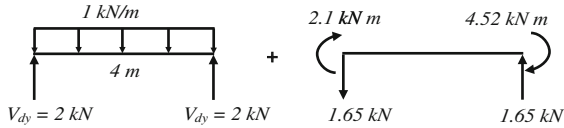
$$M_{dj} = 0.86 - 2.37 = -1.51 \text{ kN m}$$

The design shear force for the beam:

$$(EQ \text{ acting from left}): V_e = V_{dy} + (M_{pi} + M_{pj})/l_n$$

$$M_{pi} = 1.4 * M_{di} = 1.4 * 1.5 = 2.1 \text{ kN m}$$

$$M_{pj} = 1.4 * M_{dj} = 1.4 * 3.23 = 4.52 \text{ kN m}$$



$$V_e = 2 + 1.65 = 3.65 \text{ kN}$$

$$(EQ \text{ acting from right}): V_e = V_{dy} + (M_{pi} + M_{pj})/l_n$$

$$M_{pi} = 1.4 * M_{di} = 1.4 * 4.32 = 6.05 \text{ kN m}$$

$$M_{pj} = 1.4 * M_{dj} = 1.4 * 1.51 = 2.11 \text{ kN m}$$

$$V_e = 2 + 2.04 = 4.04 \text{ kN (design shear force)}$$

1st Story Left Column

Design moments for the column are calculated from 1.0GR + 1.0EQ load combination.

$$M_{db} = 0.09 + (-4.16) = -4.07 \text{ kN m (Bottom end design moment)}$$

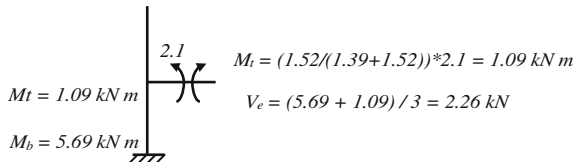
$$M_{dt} = -0.62 + 1.52 = 0.9 \text{ kN m (Top end design moment)}$$

Design shear force for the column is calculated from:

$$V_e = (M_b + M_t)/l_n$$

$$M_b = 1.4 * M_{db} = 1.4 * 4.07 = 5.69 \text{ kN m (Bottom end moment capacity)}$$

Column top end moment capacity is calculated from the distribution of the capacities of the beam ends connecting to the same joint that the column connects to, according to the ratio of EQ analysis moments of bottom end of upper story column and top end of lower story column from Eq. (7.12).



1st Story Middle Column:

The design moments for the column are calculated from 1.0G + 1.0EQ combination.

$$M_{db} = 0 + (-4.29) = -4.29 \text{ kN m (Bottom end design moment)}$$

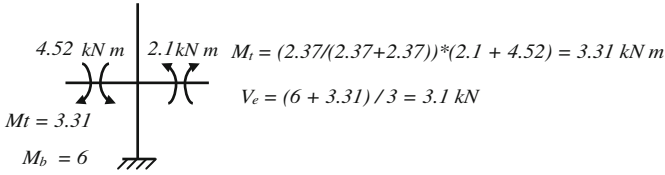
$$M_{dt} = 0 + 2.37 = 2.37 \text{ kN m (Top end design moment)}$$

The design shear force for the column is calculated from:

$$V_e = (M_b + M_t)/l_n$$

$$M_b = 1.4 * M_{db} = 1.4 * 4.29 = 6 \text{ kN m (Bottom end moment capacity)}$$

Column top end moment capacity is calculated with the same method described above, from Eq. (7.12).



7.5.6 Short Column Effect

Short columns may lead to brittle shear failure even if the original column is designed for capacity shear. Short columns form due to shortening of clear length from l_n to l'_n by architectural interventions such as parapet walls (Fig. 7.18). Then the shear force which develops in the short column V'_e can be estimated from Eq. (7.16) by replacing l_n with l'_n in Eq. (7.10).

$$V'_e = \frac{M_{p,top} + M'_p}{l'_n} \quad (7.16)$$

M'_p is the plastic moment capacity of the column at the bottom of clear length. Since $l'_n < l_n$, naturally $V'_e > V_e$. Such increase in the shear force usually reverses the design inequality in Eq. (7.14) which causes shear failure during an earthquake.

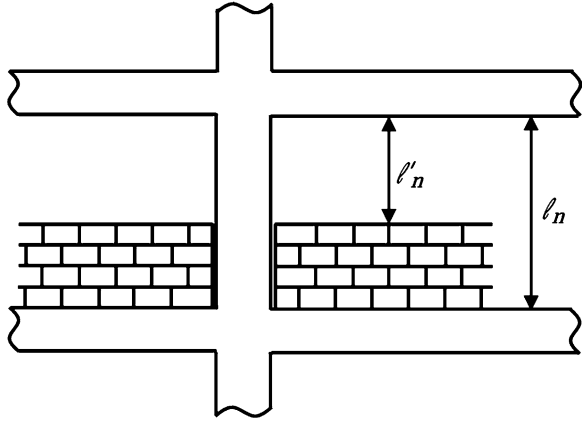
Furthermore, the lateral stiffness of a short column is much larger than the original column.

$$\left[k'_h \approx \frac{12EI}{(l'_n)^3} \right] \gg \left[k_h \approx \frac{12EI}{l_n^3} \right] \quad (7.17)$$

Accordingly, a short column attracts larger internal shear forces compared to its original state even if M_p is small in Eq. (7.14), and reaches its shear capacity easily.

Short column formation can be prevented by separating the parapet walls or architectural obstacles from the columns which reduce their effective clear lengths. Otherwise, short columns which develop intentionally should be designed for the revised shear force V'_e calculated from Eq. (7.16).

Fig. 7.18 Short column formation



A short column failure during the 1999 Düzce earthquake is shown in Fig. 7.19.

Reinforcement detailing of a typical column designed according to modern seismic code requirements is shown in Fig. 7.20. Field application of column reinforcement is also shown at the inset of the same figure.

7.6 Seismic Design of Beam-Column Joints in Ductile Frames

A beam-column joint is a part of the column where the beams join. Joints are considered as brittle components in seismic design. Accordingly, shear strength of a joint should be larger than the maximum shear force acting on the joint during an earthquake for an acceptable design. A typical interior joint is shown in Fig. 7.21.

Beam-column joints in a ductile frame are classified into two types in seismic design. If beams are connecting to the joint from all four sides, and if the width of these beams is at least $3/4$ of the width of the column that they are joining to, then such a joint is classified as a *confined joint* (b_{w1} and b_{w2} both larger than $3/4 b$; b_{w3} and b_{w4} both larger than $3/4 h$ in Fig. 7.21b). Only some interior joints can satisfy this condition. All other joints which do not satisfy the above condition are classified as *unconfined joints*. The contribution of concrete to joint shear strength is larger in confined joints compared to unconfined joints, as given in Sect. 7.6.2.

7.6.1 Design Shear Force

Design shear force acting along a joint can be calculated with the aid of Fig. 7.21a. Design shear force is not calculated from analysis, but it is calculated from the



Fig. 7.19 Short column failures in a school building after the 1999 Düzce earthquake. Picture on the right shows detailed shear damage from one of the short columns

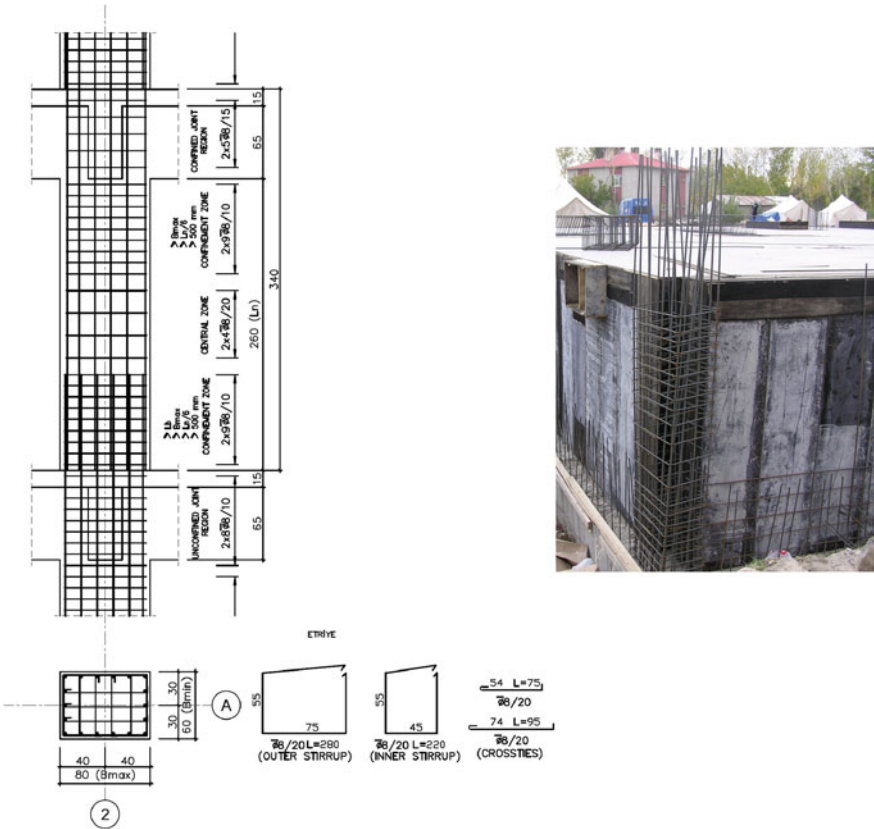


Fig. 7.20 Detailing of a ductile column and the photograph of a column reinforcement cage in the field (dimensions in cm)

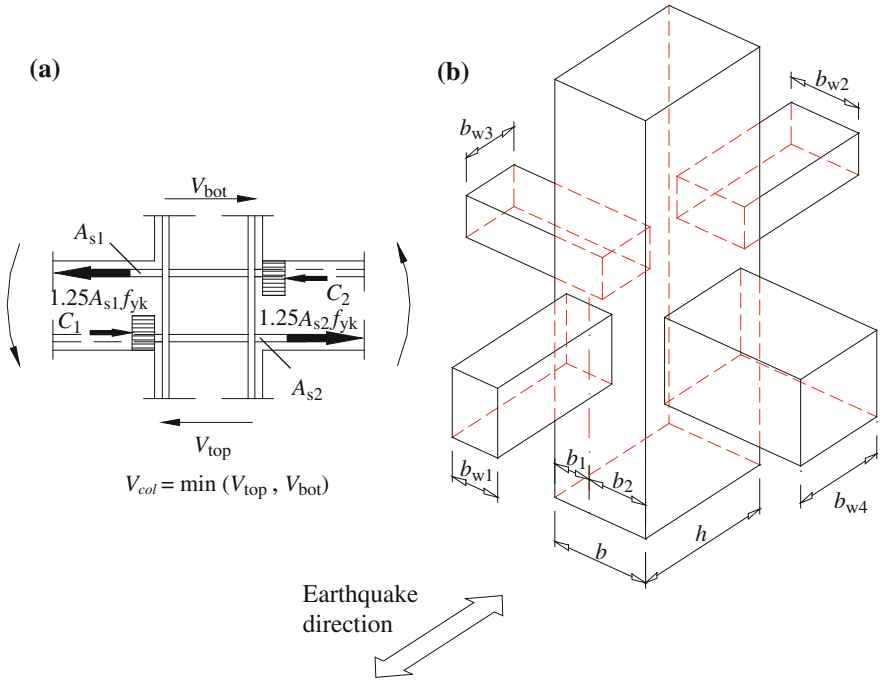


Fig. 7.21 A typical beam–column joint. **a** Equilibrium of horizontal (shear) forces acting on an interior joint; **b** confinement conditions of a joint determined by the spanning beams

flexural capacities of the beams spanning into the joint according to capacity design principles. Since the frame design is based on the strong column–weak beam principle, it is assumed that maximum shear force in the joint develops with the flexural yielding of beams in the earthquake direction connecting from both sides. These beam ends are in opposite bending directions under lateral earthquake effects, hence top longitudinal reinforcement on the left beam end and bottom longitudinal reinforcement on the right beam end yields under the bending directions shown in Fig. 7.21a. If a horizontal cross section is taken from the middle of joint in Fig. 7.21a, we can calculate the joint shear along this section from equilibrium. Considering that the compression in concrete is equal to the tension in the reinforcement at a section in bending, the design shear force simply becomes (Eurocode 8):

$$V_e = 1.2f_{yd}(A_{s1} + A_{s2}) - V_{col} \quad (7.18)$$

where f_{yd} is the design yield strength of longitudinal reinforcement and V_{col} is the smaller shear force in the connecting columns at top and bottom. The smaller value is taken because column shear acts against the shear imposed by the beams. $A_{s2} = 0$ when the joint is at the exterior frame. The factor 1.2 in Eq. (7.18) accounts for the overstrength of reinforcing bars due to strain hardening, which leads to larger shear stresses at the joint.

7.6.2 Design Shear Strength

The nominal joint design shear strength V_r is given in Eq. (7.19a, b) for confined and unconfined joints respectively in ACI 318 and TEC 2007.

$$V_r = 0.60 b_j h f_{cd}, \quad (7.19a)$$

$$V_r = 0.40 b_j h f_{cd}. \quad (7.19b)$$

It can be noticed that the contribution of joint lateral reinforcement to joint shear strength is not given explicitly in Eq. (7.19a, b). Lateral reinforcement requirements in joints are controlled by the minimum reinforcement conditions. In confined joints, 50 % of the column lateral reinforcement at the column confinement region should be continued into the joint region, however maximum spacing is 150 mm. 100 % of the column lateral reinforcement at the column confinement region should be provided in the joint region for unconfined joints. Larger amount of horizontal reinforcement is placed in unconfined joints since the contribution of concrete is less, as discusses above. The minimum horizontal bar diameter is 8 mm in both types of joints. Details of a confined and an unconfined joint reinforcement are shown in Fig. 7.21.

A joint design is acceptable for shear if

$$V_e < V_r. \quad (7.20)$$

Otherwise the width of the column (hence the size of the joint) or the depth of the beam (for reducing longitudinal reinforcement) should be increased.

Eurocode 8 does not require a design shear calculation at the joint, but provides 50 and 100 % of the column lateral reinforcement at the column confinement region for unconfined and confined joints, respectively. This is similar to ACI 318 detailing requirements. The maximum spacing of hoops in confined joints is also 150 mm.

7.7 Comparison of the Detailing Requirements of Modern and Old Seismic Codes

The detailing of beams, columns and beam-column joints have been improved significantly in the recent seismic codes compared to the older (pre-1980) codes. A comparison of the detailing of typical beam-column-joint assemblages with respect to the old and recent codes are shown in Fig. 7.22. It is evident that there is no lateral reinforcement in the joints, and no confined regions at the ends of beams and columns. Seismic performance of non-ductile beams, columns and beam-column joints which were designed according to the old code regulations are shown in Fig. 7.23. Joint shear strengths were too low to resist the shear forces transmitted by beams. Further, the lower end of the column failed in shear, which is not acceptable in capacity design.

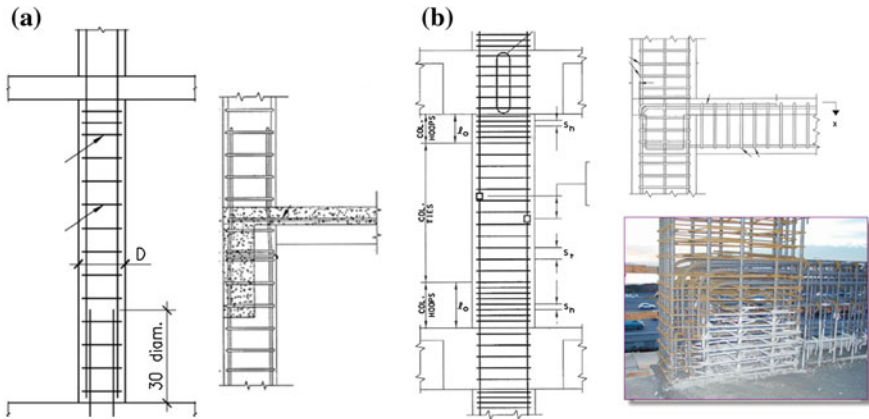


Fig. 7.22 Typical reinforcement details of beams and beam-column joints in **a** older and **b** modern construction

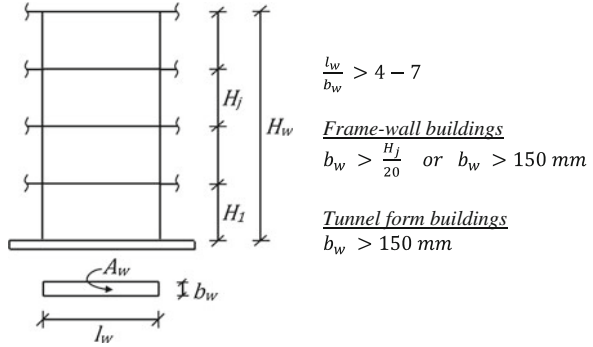


Fig. 7.23 Joint failures observed in non-ductile reinforced concrete buildings due to strong ground shaking (from Moehle et al. 2004)

7.8 Seismic Design of Ductile Concrete Shear Walls

Shear walls mainly serve as the major component of a building for resisting lateral loads applied during an earthquake. Their lateral stiffnesses compared to typical columns are very large due to their large size in the direction of earthquake forces. A typical shear wall is shown in Fig. 7.24. A large column qualifies as a shear wall if length to thickness ratio of its cross section is larger than $4 \sim 7$, depending on the design code employed. The minimum thickness is either 150 mm or $1/20$ of the clear story height (Eurocode 8). In buildings where the entire lateral load resisting system are composed of shear walls (tunnel form buildings in particular),

Fig. 7.24 A typical shear wall and minimum dimensions



minimum thickness may be reduced to 150 mm. The thickness of a shear wall may be reduced along the wall height, depending on the design requirements.

Shear walls are classified into two types regarding their deformation behavior. The classification is based on the height to length ratio, or the aspect ratio of the wall.

$$\frac{H_w}{l_w} > 2.0 : \text{Slender walls—Flexural behavior governs.}$$

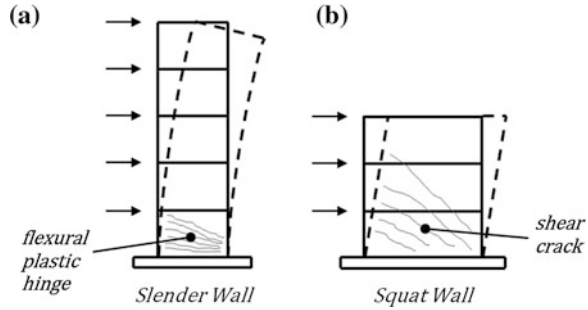
$$\frac{H_w}{l_w} \leq 2.0 : \text{Squat walls—Shear behavior governs.}$$

The deformation behavior of slender (flexure dominant) and squat (shear dominant) walls are shown in Fig. 7.25. Slender walls deform similar to cantilever columns under lateral forces, hence flexural deformations dominate wall deformations. A slender wall reaches its lateral strength capacity with flexural yielding at its base region, with the formation of horizontal flexural cracks accompanied with the yielding of longitudinal tension steel (Fig. 7.25a). Shear deformations dominate the deformation of squat walls. A squat wall reaches its lateral strength capacity with the formation of a family of diagonal cracks under diagonal tensile stresses, accompanied with the yielding of web reinforcing bars which are crossing these cracks (Fig. 7.25b).

7.8.1 Seismic Design of Slender Shear Walls

The behavior of slender walls is similar to ductile columns except the bending moment distribution (Fig. 7.26). A column bends in double curvature under lateral forces and reaches its lateral capacity with the formation of plastic hinges forming at the beam ends connecting to the column when the columns is stronger than the beam (Figs. 7.15b and 7.25a). Slender shear walls on the other hand usually bend in single curvature because the flexural capacities of the connecting beams are too small to change the sign of moment distribution along the wall height (Fig. 7.25b).

Fig. 7.25 Deformation behaviors of **a** a slender shear wall; **b** a squat shear wall



Maximum bending at the base cannot exceed the plastic moment capacity $M_{p,base}$ of the base section.

7.8.1.1 Reinforcement Detailing in Ductile Shear Walls

Ductility capacity of a shear wall is therefore controlled by the ductility capacity of its plastic zone at the base. The height of this zone is H_{cr} and it is defined in Eurocode 8 as,

$$H_{cr} = l_w \text{ or } H_{cr} = \frac{H_w}{6} \text{ (larger of the two), but } H_{cr} \leq 2l_w.$$

Along H_{cr} , confined end regions are provided at the edges of the wall section at each end region (Fig. 7.27). The minimum length l_u of the confined end regions in plan along H_{cr} are defined as; $l_u \geq 1.5b_w$ or $l_u \geq 0.15l_w$ in Eurocode 8 (larger governs). Confined end regions are also formed above H_{cr} , but their length is reduced. The minimum ratio of total longitudinal reinforcement within the confined end zones to the total wall area ($\rho_u = A_s/A_w$) is 0.005 along H_{cr} . The details of lateral confinement reinforcement at the confined end regions are similar to the details given for column confinement region in Sect. 7.5.3.

The reason for confining the end regions of walls along the plastic hinge regions is similar to that of columns, but also this is more economical for the effectiveness of vertical flexural reinforcement. When ultimate moment develops at a wall section, the vertical reinforcement in the confined region at the tension side is much more effective than the vertical reinforcement distributed along the web because of its lever arm from the neutral axis (Fig. 7.27). On the other hand, the end region at the compression side is subjected to high compressive stresses and strains. Confining the concrete in this region increases the compressive strain capacity of concrete, accordingly it increases the curvature capacity of the section along the critical height H_{cr} where plastic hinge develops at the wall base.

Uniform layers of horizontal and vertical reinforcement are placed in the web between the confined end regions, at both faces. The ratio of minimum web reinforcement is 0.0025 in both vertical and horizontal reinforcement, with a maximum spacing of 250 mm (ACI 318).

Fig. 7.26 Moment and curvature distributions along **a** a column; **b** a slender shear wall

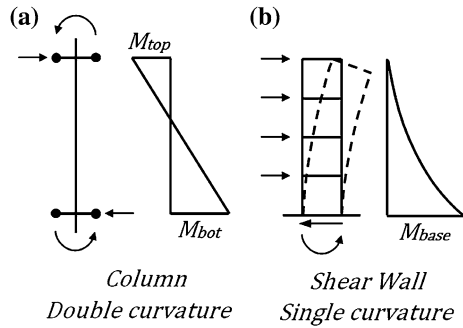
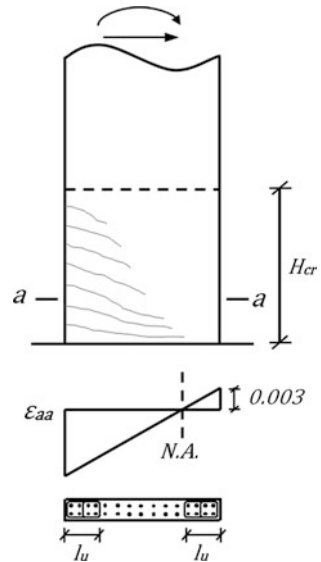


Fig. 7.27 Strain distributions along the wall length within H_{cr} and reinforcement detailing



7.8.1.2 Flexural Design of Slender Shear Walls

Design moment distribution in ductile slender walls under earthquake loading is defined in Fig. 7.28. Moment diagram obtained from analysis usually reaches its maximum at the base and decreases with height. In wall-frame systems, moment diagram changes sign at upper stories because of the interaction of the wall with the frame. When beams are spanning into the shear wall, moment diagram displays discontinuities at the floor levels due to the resisting moments of the beams with opposite sign, however these moments are very small compared to the wall moments and they can be ignored in the wall moment distribution.

Design moments are obtained from analysis moments by drawing a chord from the base moment to the zero moment at the wall top, and then shifting this chord up by the distance H_{cr} as shown in Fig. 7.28. The reason for increasing the design

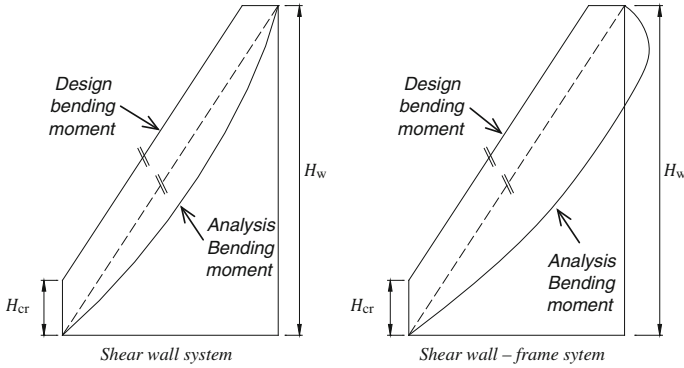


Fig. 7.28 Design moment distributions along the wall length

moments at the support region (along H_{cr}) is the increase of tensile forces due to *tension shift*.

Tension shift is essential in the curtailment of longitudinal reinforcement in deep beams and shear walls. Let us consider the cantilever shear wall in Fig. 7.29a under the effect of lateral forces. Horizontal reinforcement (stirrups) at the web is activated with the formation of a diagonal shear crack, and ultimate capacity of the shear wall is reached with the yielding of tensile steel. A free body diagram of the wall above the shear crack is shown in Fig. 7.29b, where T_2 is the tension in longitudinal steel at section 2, C_1 is the compression at section 1, z is the moment arm, V_s is the shear force carried by stirrups crossing the diagonal crack and V_b is the base shear at section 1. Moment equilibrium about the base requires

$$M_1 = zT_2 + 0.5zV_s \quad (7.21)$$

where M_1 is the internal resisting moment at section 1, or at the base. Also, from the equilibrium of the vertical cantilever part 1–2 in Fig. 7.29b,

$$M_1 = M_2 + zV_2 + \frac{z}{2}F_{1-2} \quad (7.22)$$

Here, V_2 and M_2 are the internal shear and moment at section 2, respectively and F_{1-2} is the portion of external lateral force acting on the wall between sections 1 and 2. T_2 can be obtained from Eqs. (7.21) and (7.22).

$$T_2 = \frac{1}{z}(M_2 + zV_2 + 0.5zF_{1-2} - 0.5zV_s) \equiv \frac{M_2}{z} + (V_2 + 0.5F_{1-2} - 0.5V_s). \quad (7.23)$$

In Eq. (7.23), $0.5V_s$ is small compared to $(V_2 + 0.5F_{1-2})$ where V_s is the force in the stirrup crossing the diagonal crack, whereas V_2 is the total shear at section 2. Hence it can be ignored. Accordingly, Eq. (7.23) reduces to

$$T_2 = \frac{M_1}{z} \quad (7.24)$$

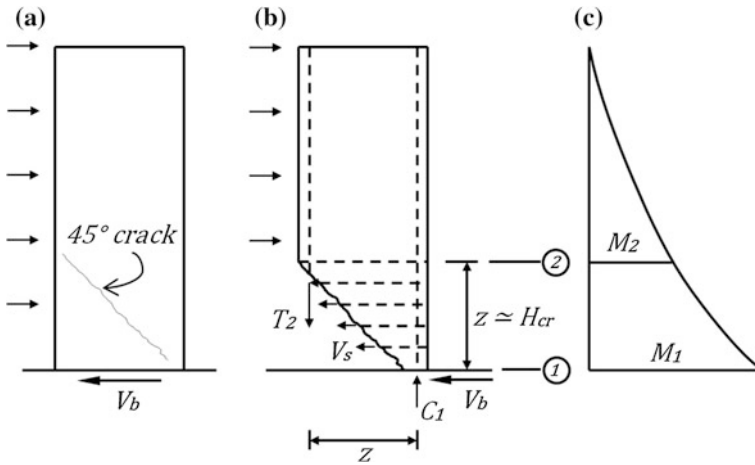


Fig. 7.29 a External forces acting on the wall; b internal forces acting along the diagonal crack; c moment diagram of the wall

with the aid of Eq. (7.22). Hence, tension at section 2 is not related to the moment at section 2 as in a homogeneous, uncracked wall but it is calculated from the larger moment at section 1.

The moment capacity of a shear wall can be simply calculated by ignoring the contribution of vertical reinforcement in the web by using Eq. (7.25), with the aid of Fig. 7.27.

$$M_r = A_s f_y l_w \left(1 + \frac{N_d}{A_s f_y} \right) \left(1 - \frac{c}{l_w} \right). \tag{7.25}$$

A_s is the area of vertical reinforcement in the confined region at the tension side, c is the depth of neutral axis, N_d is the axial compressive force acting on the wall section under vertical loads and f_y is the yield strength of vertical steel in Eq. (7.25). M_r should exceed the design moments calculated according to Fig. 7.27 at all sections. The moment capacity of shear walls usually satisfy the strong column-weak beam principle defined for columns in Sect. 7.5.4.

7.8.1.3 Shear Design of Slender Shear Walls

Design shear in ductile walls is calculated from analysis, but it is modified by the plastic moment capacity of the base.

$$V_e = \beta_v \frac{(M_p)_b}{(M_d)_b} V_d. \tag{7.26}$$

M_d and V_d are the moment and shear calculated from analysis under vertical loads and linear elastic earthquake forces ($R_a = 1$), and β_v is the dynamic magnification



Fig. 7.30 Shear wall damage at the ground story of a modern concrete building during the 2010 Chile earthquake (M 8.8)

factor for taking into account the higher mode effects. Its value is 1.5 for frame-wall systems in Eurocode 8. At the wall base, M_d cannot exceed the plastic moment capacity M_p . Hence the shear force distribution calculated from analysis is scaled by $\left(\frac{M_p}{M_d}\right)$ at the wall base. If a detailed analysis is not conducted, then $M_p \simeq 1.25M_r$ can be assumed.

An acceptable shear design should satisfy $V_e \leq V_r$ for diagonal tension, and $V_e \leq 0.22A_w f_{cd}$ for diagonal compression where

$$V_r = A_w(0.65f_{ctd} + \rho_{sh}f_{ywd}) \quad (7.27)$$

Here, f_{cd} and f_{ctd} are the compressive and tensile design strength of concrete, ρ_{sh} is the ratio of horizontal web reinforcement and f_{ywd} is the design strength of horizontal reinforcement.

A shear wall with insufficient shear design is shown in Fig. 7.30. Although the ground shaking was strong, capacity design should have prevented shear failure if the design was fully conforming to the seismic code regulations.

An example of a slender wall detailing which is designed according to the requirements discussed above is shown in Fig. 7.31.

7.8.2 Seismic Design of Squat Shear Walls

Squat walls cannot exhibit ductile response. Hence, H_{cr} and confined end regions are not defined for these walls. Design moments are calculated from analysis. However bending is never critical for squat walls since their moment capacity is always much larger than the design moments.

Design shear is calculated from analysis with $R_a = 1$, but not modified with capacity as in the slender walls. Hence $V_e = V_d(R_a = 1)$. Then an acceptable shear design is achieved if $V_e \leq V_r$ for diagonal tension, and $V_e \leq 0.22A_w f_{cd}$ for diagonal compression where V_r is given by Eq. (7.24).

Fig. 7.32 A squat shear wall failed during the 2011 Van Earthquake



7.9 Capacity Design Procedure: Summary

A summary of the capacity design procedure is given below in an algorithmic form. Then a case study is presented for the seismic design of a 5 story concrete frame.

1. Analyze the system under gravity and reduced earthquake forces acting in both lateral directions, combined according to the design code employed.
2. Design the beams for flexure under the analysis moments M_d and design for shear under capacity shear V_e .
3. Calculate column moments from strong column-weak beam inequality. Perform flexural design under these moments and shear design under capacity shear.
4. Design shear walls for flexure under design moment distribution with tension shift, and design for shear under capacity shear V_e .
5. Check the shear capacity of joints for capacity shear.

Example 7.2 Seismic Design of a 5 Story Reinforced Concrete Frame. Typical floor plan of a 5-story reinforced concrete frame building and all member dimensions are given in Fig. 7.33 below. Floor plan and member dimensions are the same in all stories. Linear elastic design spectrum is given for semi-stiff soil conditions. Design Frame 3 according to the code requirements. Concrete grade is C25 and steel grade is S420. Ductility level is “enhanced” ($R = 8$). The earthquake direction is Y.

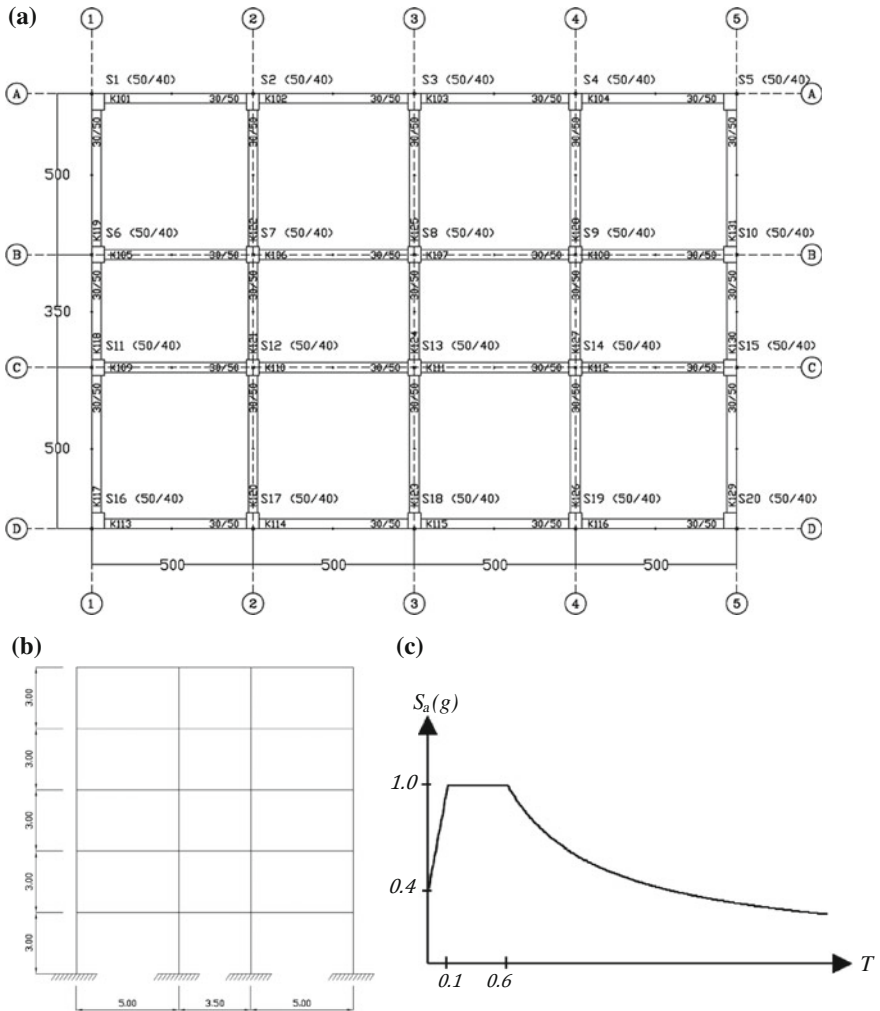


Fig. 7.33 a Plan view (units in centimeters); b Frame-3 elevation view (units in meters); c Linear elastic design spectrum

Solution

Story masses

Columns are 50×40 cm; beams are 30×50 cm; slab thickness is 12 cm.

Finishing on slabs 1.5 kN/m^2 (except the roof slab). Live load on slabs is 2 kN/m^2 .

Dead loads (*DL*), live loads (*LL*) and story masses which are calculated consistently with the gravity loads are given in the table below.

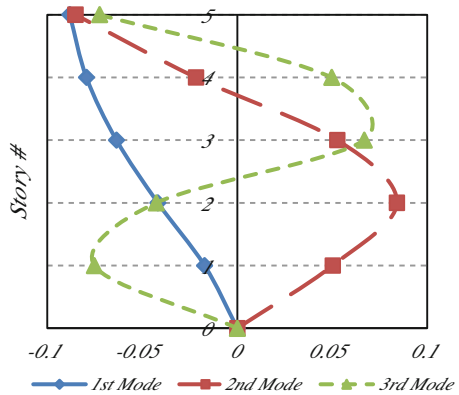
Dead load (kN)				Live load (kN)	Story masses (tons) (<i>DL</i> + 0.3 <i>LL</i>)	
Columns	Beams	Slab	Finishing	Slab		
60.0	125.6	202.2	101.2	135	1st Story	53.7
60.0	125.6	202.2	101.2	135	2nd Story	53.7
60.0	125.6	202.2	101.2	135	3rd Story	53.7
60.0	125.6	202.2	101.2	135	4th Story	53.7
30.0	125.6	202.2	0	135	5th Story	42.9

Eigenvalue analysis

Eigenvalues (modal periods) and mass normalized eigenvectors (mode shapes) are calculated from eigenvalue analysis, by using the structural model in the Y direction.

Mode	1	2	3	4	5
Period (s)	0.505	0.160	0.089	0.060	0.046

Mass normalized eigenvectors				
Mode 1	Mode 2	Mode 3	Mode 4	Mode 5
-0.0173	0.0502	-0.0753	-0.0823	0.0579
-0.0418	0.0840	-0.0427	0.0446	-0.0774
-0.0636	0.0526	0.0668	0.0383	0.0767
-0.0794	-0.0217	0.0497	-0.0802	-0.0542
-0.0882	-0.0852	-0.0725	0.0495	0.0237



Response spectrum analysis and equivalent lateral forces

(a) *Minimum number of modes*

Mode	Mass participation ratio (%)	Cumulative (%)
1	83.2	83.2
2	10.5	93.7
3	4.0	97.7
4	1.8	99.5
5	0.5	100.0

First two modes are sufficient for the response spectrum analysis according to Sect. 6.4.1.

(b) Modal forces and base shear forces

Effective modal masses (M_n^*) (tons)		Spectral accelerations (m/s^2)		
M_1^*	M_2^*	$S_a(T_1)$	$S_a(T_2)$	
214.33	27.17	9.81	9.81	
Modal forces ($f_n = \Gamma_n * m^* * \phi_n^* * S_{a,n}$) (kN)		Base shear forces (kN)		
Mode 1	Mode 2	Mode 1	Mode 2	V_{IB} (kN) (SRSS)
16.64	17.24			
40.34	28.84			
61.34	18.05	262.83	33.31	265.05
76.57	-7.46			
67.93	-23.36			

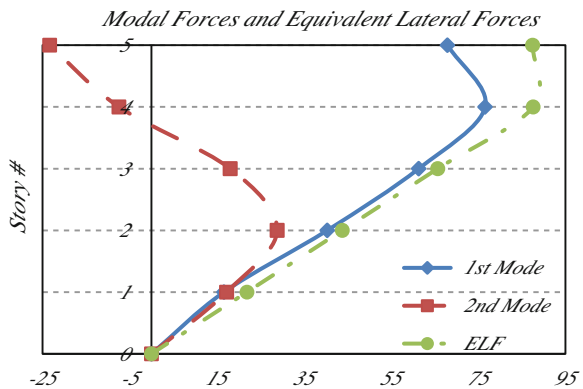
(c) Equivalent lateral forces

We will also calculate the equivalent lateral forces for comparison with modal forces.

Total weight	2547.26	kN
Period	0.505	s
$S(T)$	1	
$A(T)$	9.81	m/s^2
Base shear	318.40	kN for $R = 8$
Minimum shear check	101.89	$(0.1 * A_0 * I^* W) < 318.4$ OK

Equivalent lateral force procedure gives 20 % larger base shear force compared to response spectrum analysis.

Story	F_i (kN)
1	21.90
2	43.80
3	65.70
4	87.59
5	87.47



(d) *Minimum base shear check*

In some earthquake codes, base shear calculated from response spectrum analysis should not be less than a ratio β of the base shear calculated from equivalent lateral load procedure.

$V_{IB} = 265.05 \text{ kN}$ (Calculated from response spectrum analysis)

$V_t = 318.40 \text{ kN}$ (Calculated from equivalent lateral load procedure)

$B = 0.8.$

Check: $\beta * V_t = 254.72 \text{ kN} < V_{IB} = 265.05 \text{ kN}$

Therefore, there is no need for base shear correction in mode superposition analysis.

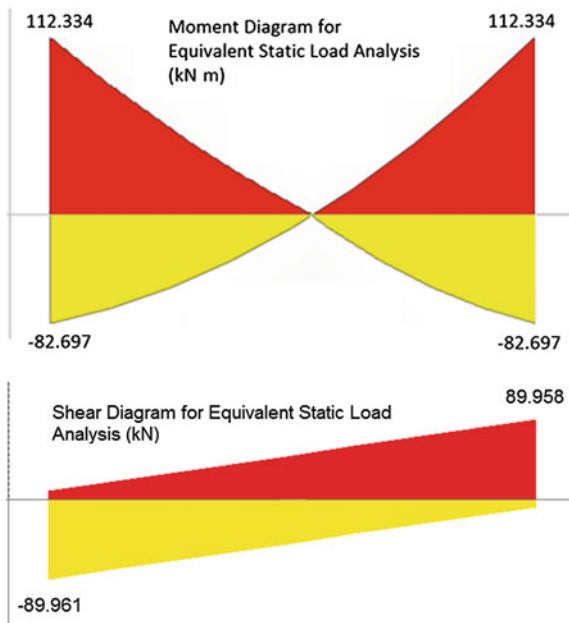
Design

Response spectrum analysis is conducted under the modal forces given above and member forces and displacements are obtained by SRSS combination. Also member forces are obtained with the equivalent static lateral load method for comparison. The most critical members according to the internal forces acting on them ($DL + LL \mp EQ/R$) are designed.

Beam design

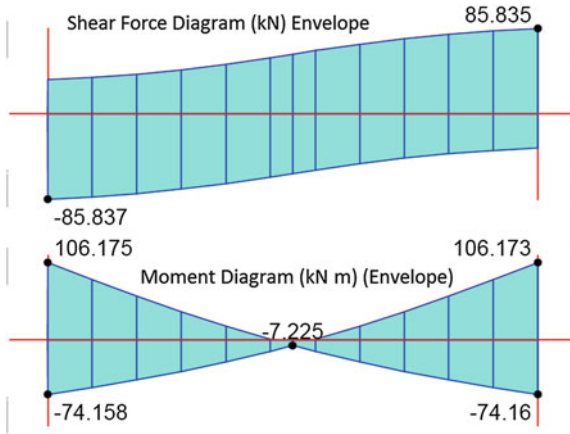
Beam Moment and Shear Diagrams from Equivalent Lateral Load Analysis:

The most critical member: K224 (Second Story, Middle Bay Beam)



(Lateral forces are applied in both \pm directions, envelope moment diagram is presented).

Moment and Shear Diagrams from Response Spectrum Analysis:
 The most critical member: K224 (Second Story, Middle Bay Beam).
 Envelope moment and shear diagrams are presented.



Flexural design of the most critical beam (slab contribution is ignored)

		i End	j End		
Positive direction	M_d (kN m)	106.175	106.173	106	74
	$A_{s,req}$ (mm ²)	685	685	←————→	
	$A_{s,min}$ (mm ²)	348	348		
Negative direction	M_d (kN m)	74.16	74.16	74	106
	$A_{s,req}$ (mm ²)	455	455	←————→	
	$A_{s,min}$ (mm ²)	348	348		

	Support	Span
$A_{s,top}$ (mm ²)	3φ14 + 2φ16 (864 mm ²)	3φ14 (462 mm ²)
$A_{s,bottom}$ (mm ²)	3φ16 (604 mm ²)	3φ16 (604 mm ²)
M_r (kN m)	134.96	95.8

Shear design of the most critical beam

		i End	j End	
	V_{dy} (kN)	25.72 (from gravity load analysis)		
$(M_p \approx 1.4M_r)$	(+) M_p (kN m)	188.95	134.17	←————→
$(M_p \approx 1.4M_r)$	(-) M_p (kN m)	134.17	188.95	
Positive direction	V_c (kN)	133.72		134 $M_p \approx 1.4 M_r$ 189
Negative direction	V_e (kN)	131.15		

Shear reinforcement provided

	Support	Span
$A_{s,w}$	8φ/110 mm	8φ/200 mm

Shear capacity of the Beam

$V_w = (A_{s,w}/s) * f_{yw} * d$	V_w (kN)	85.84
$V_c = 0.8 * (0.65 * f_{cd} * b_w * d * (1 + \gamma(N_d/A_c)))$	V_c (kN)	103.29
$V_r = V_c + V_w$	V_r (kN)	189.13
	0.22 $b_w d f_{cd}$ (kN)	522.5
	$V_e < V_r; V_e < 0.22 b_w d f_{cd}$ —OK	

Column design

The most critical member: S13 (First Story, Middle column)

Column flexural design (Loads on the most critical column from combinations)

Design load on the column, from analysis	N_d (kN m)	803.56	
	M_d (kN m)	120.2	
$\rho_1 = 0.01$	$A_{s,req}$ (mm ²)	2000	
	$A_{s,provided}$ (mm ²)	2010.62	10 ϕ 16
	M_r (kN m)	266.2	

Minimum longitudinal reinforcement ratio governs column design.

Strong column—weak beam check for the most critical connection

Columns	M_{ra} (kN m)	266.2
	M_{ri} (kN m)	266.2
Beams	M_{ri} (kN m)	134.96
	M_{rj} (kN m)	95.8
$(M_{ra} + M_{ri}) \geq 1.2 * (M_{ri} + M_{rj})$	Check	1.92 > 1.2 OK

Column shear design

Most critical column: Second story middle columns

M_u calculations for the top end

ΣM_p (kN m)	323.12
M_u (kN m)	191.22

M_u calculations for the bottom end

ΣM_p (kN m)	323.12
M_u (kN m)	158.81

Shear force in Column

$V_c = (M_a + M_u)/l_n$	V_c (kN)	100.01
-------------------------	------------	--------

Shear Reinforcement provided

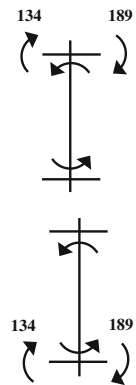
Region	End	Middle
$A_{s,w}$	8 ϕ /7	8 ϕ /19

Confined region length for column top and bottom

500 mm

Shear Capacity of the Column

V_w (kN)	249.01
V_c (kN)	162.35
V_r (kN)	411.36
$0.22b_wdf_{cd}$ (kN)	733.33
$V_e < V_r; V_e < 0.22b_wdf_{cd}$ —OK	



Beam-column connection shear check

Connection check for column S13 (First Story, Middle Column):

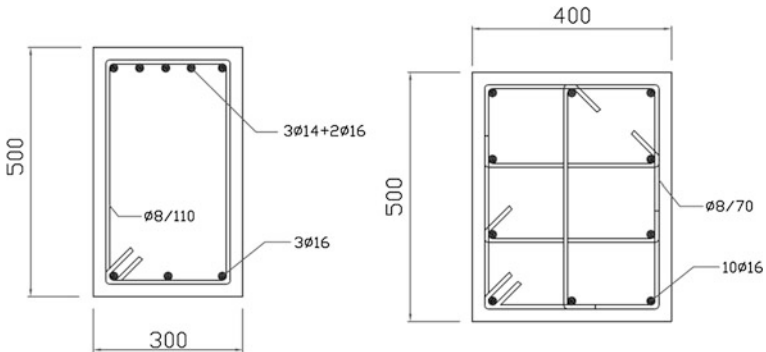
Confinement check			
Beam dimensions		Column dimensions	
b_{w1}	0.3 m	b	0.4 m
b_{w2}	0.3 m	h	0.5 m
b_{w3}	0.3 m		
b_{w4}	0.3 m		
<i>Check</i>			
b_{w1} and $b_{w2} \geq 3/4b$ (Satisfied)			
b_{w3} and $b_{w4} < 3/4 h$ (Not Satisfied)			

Therefore the joint is unconfined.

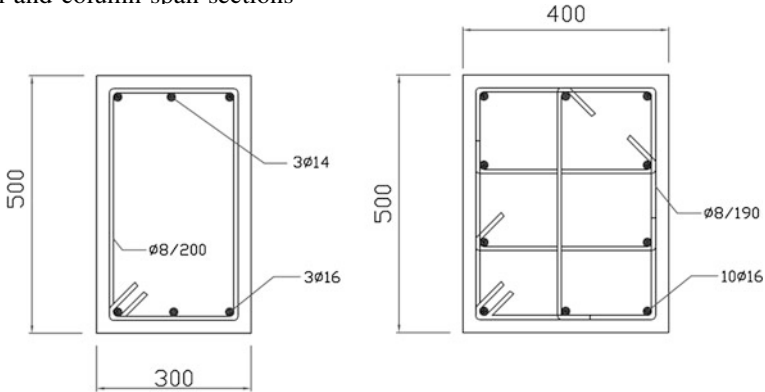
<i>Shear Force on the Joint</i>			
$V_e = 1.25f_{yk}(A_{s1} + A_{s2}) - V_{kol}$			
A_{s1}	864 mm ²	A_{s2}	603 mm ²
f_{yk}	420 Mpa	V_{kol}	90.5 kN
$V_e = 679.7$ kN			
<i>Joint shear force limit</i>			
$V_e \leq 0.45 b_j h f_{cd}$			
b_j	0.4 m	h	0.5 m
$V_e < 1500$ kN (Satisfied)		f_{cd}	16.67 MPa

Beam and column cross-sections (units in mm)

Beam and column support sections

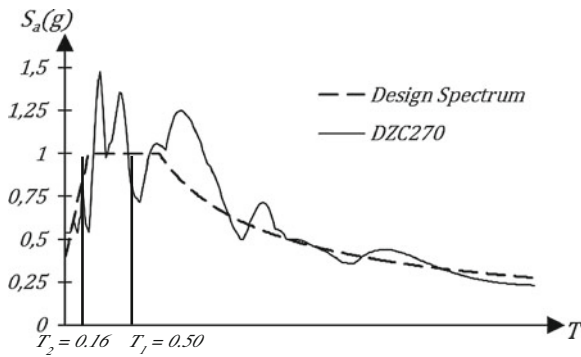


Beam and column span sections

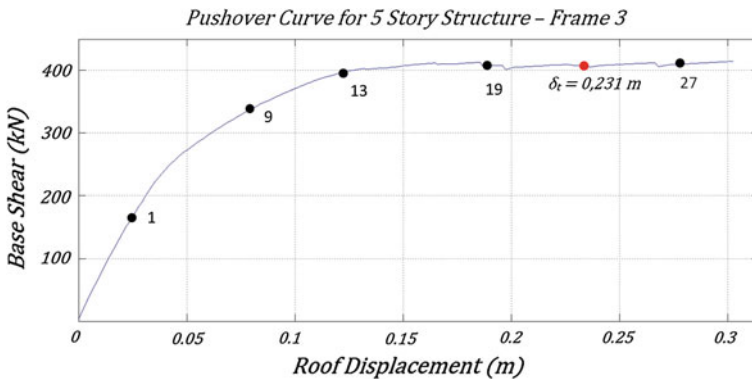


Pushover analysis

Frame is modeled using the design parameters and pushover analysis is conducted. Capacity curve and plastic hinge pattern is determined.

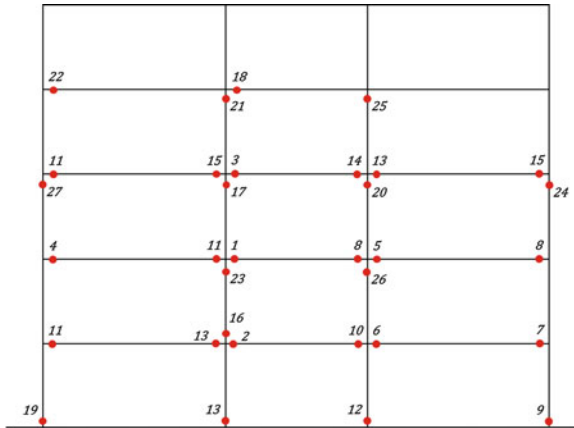


(a) Capacity curve



Target roof displacement (δ_t) is calculated as 0.231 m by using the design spectrum. If the actual response spectrum of the DZC270 is employed, then the target roof displacement demand is 0.158 m. The difference is due to the difference of spectral ordinates at T_1 , which is observed on the spectrum figure above. It will be evident from the foregoing analysis in the next paragraph that this target displacement is quite close to the maximum roof displacement obtained from non-linear response history analysis under DZC270.

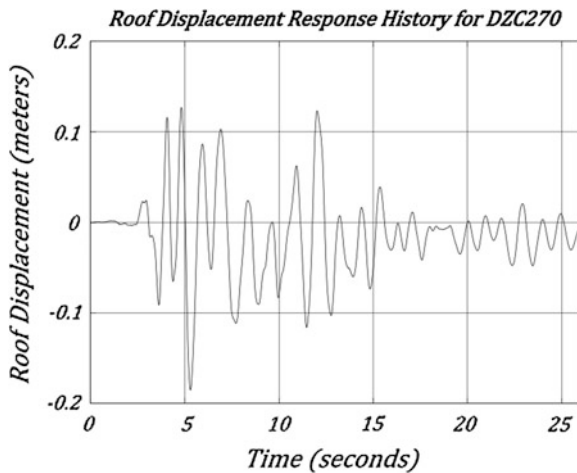
(b) Plastic hinge pattern



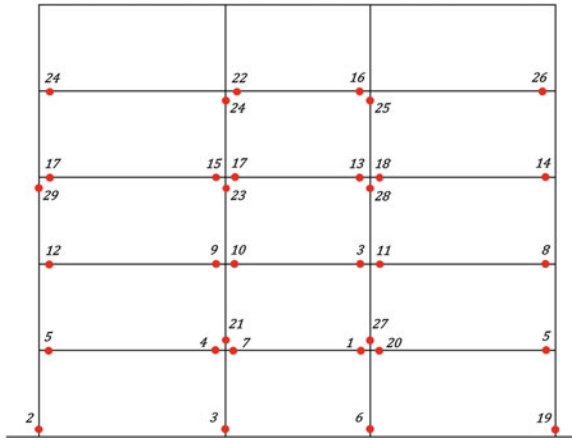
Response history analysis under DZC270

Frame is dynamically analyzed under DZC270 recorded during the 1999 Düzce Earthquake. Roof displacement history and plastic hinge pattern are obtained.

(a) Roof displacement history



(b) *Plastic hinge pattern*



It is evident that the plastic hinge pattern obtained from nonlinear response history analysis and pushover analysis are quite similar, despite the difference in maximum roof displacements. This is a natural consequence of capacity design.

References

- Acun B, Sucuoğlu H (2010) Performance of reinforced concrete columns designed for flexure under severe displacement cycles. *ACI Struct J* 107(3):364–371
- Akkar S, Bommer JJ (2010) Empirical equations for the prediction of PGA, PGV and spectral accelerations in Europe, the mediterranean region and the middle east. *Seismol Res Lett* 81:195–206
- ACI Committee 318 (2008) Building code requirements for structural concrete (ACI 318-08) and commentary. American Concrete Institute, Farmington Hills
- American Society of Civil Engineers (1998) Minimum design loads for buildings and other structures. ASCE 7-98, Reston
- American Society of Civil Engineer (2002) Minimum design loads for buildings and other structures. ASCE 7-02, Reston
- American Society of Civil Engineers (2005) Minimum design loads for buildings and other structures. ASCE 7-05, Reston
- American Society of Civil Engineers (2010) Minimum design loads for buildings and other structures. ASCE 7-10, Reston
- Building Seismic Safety Council (1997) NEHRP recommended provisions for seismic regulations for new buildings and other structures. FEMA 303, FEMA, Washington
- Building Seismic Safety Council (2000) NEHRP recommended provisions for seismic regulations for new buildings and other structures. FEMA 368, FEMA, Washington
- Building Seismic Safety Council (2003) NEHRP recommended provisions for seismic regulations for new buildings and other structures. FEMA 450, FEMA, Washington
- Building Seismic Safety Council (2009) NEHRP recommended provisions for seismic regulations for new buildings and other structures. FEMA P-750, FEMA, Washington
- Cornell A (1968) Engineering seismic risk analysis. *Bull Seismol Soc Am* 58:1583–1606
- Cornell CA, Banon H, Shakal AF (1979) Seismic motion and response prediction alternatives. *Earthq Eng Struct Dynam* 7:295–315
- Engdahl ER, Villaseñor A (2002) Global seismicity: 1900–1999. In: Lee WHK, Kanamori H, Jennings JC, Kisslinger C (eds) *International handbook of earthquake and engineering seismology*. Academy Press, San Diego, pp 665–690
- Eurocode 2: Design of Concrete Structures (2004) EN-1992. European Committee for Standardization, Brussels
- Eurocode 8: Design of Structures for Earthquake Resistance- Part 1: General Rules, Seismic Actions and Rules for Buildings (2004) EN-1998-1. European Committee for Standardization, Brussels
- Ersoy U, Özcebe G, Tankut T (2003) Reinforced concrete. METU, Ankara
- Fardis MN (2009) Seismic design, assessment and retrofitting of concrete buildings, based on Eurocode 8. Springer, Dordrecht
- Grunthal G (ed) (1998) European macroseismic scale 1998. *Cahiers de Centre Européen de Géodynamique et de Séismologie* 15, Luxembourg

- Gutenberg B, Richter CF (1944) Frequency of earthquakes in California. *Bull Seismol Soc Am* 34:1985–1988
- Hanks TC, Kanamori H (1979) A moment magnitude scale. *J Geophys Res* 77:4393–4405
- International Code Council ICC (2012) International building code. Washington
- Isacks B, Oliver J, Sykes LR (1968) Seismology and the new global tectonics. *J Geophys Res* 73:5855–5899
- Joyner WB, Boore DM (1981) Peak horizontal acceleration and velocity from strong-motion records including records from the 1979 imperial valley, California, earthquake. *Bull Seismol Soc Am* 71:2011–2038
- Kárník V, Procházková D, Schenková Z, Drimmel J, Mayer-Rosa D, Cvijanovic D, Kuk V, Milošević A, Giorgetti F, Janský J (1978) Ioseismals of the strongest Friuli aftershocks of September 1976. *Stud Geophys Geod* 22:411–414
- Lawson AC (1908) The California earthquake of April 18, 1906. Report of the state earthquake investigation commission. The Carnegie Institution of Washington, Washington (reprinted in 1965)
- Leonard M (2010) Earthquake fault scaling: self-consistent relating of rupture length, width, average displacement, and moment release. *Bull Seismol Soc Am* 100:1971–1988
- McGuire RK (2004) Seismic hazard and risk analysis. Earthquake Engineering Research Institute Monograph. MNO-10, Oakland
- McGuire RK, Arabasz WJ (1990) An introduction to probabilistic seismic hazard analysis, in geotechnical and environmental geophysics (ed Ward SH). *Soc Explor Geophys* 1:333–353
- McKenzie DP (1968) Speculations on the consequences and causes of plate motions. *Geophys J Roy Astron Soc* 18:1–32
- Moehle JP, Ghannoum W, Bozorgnia Y (2004) Collapse of lightly reinforced concrete frames during earthquakes. In: Proceedings of the international conference in commemoration of the 5th anniversary of the 1999 Chi-Chi earthquake. Taipei, Taiwan, 8–9 Sep
- Mueller CS (2010) The influence of maximum magnitude on seismic-hazard estimates in the central and eastern United States. *Bull Seismol Soc Am* 100:699–711
- Press F, Siever R (1986) *Earth*, 4th edn. Freeman, New York
- Reid HF (1910) The California earthquake of April 18, 1906: report of the state earthquake investigation commission, Volume II: the mechanics of the earthquake. The Carnegie Institution of Washington, Washington (reprinted in 1965)
- Reiter L (1990) *Earthquake hazard analysis: issues and insights*. Columbia University Press, New York
- Richter CF (1935) An instrumental earthquake magnitude scale. *Bull Seismol Soc Am* 25:1–32
- Shearer PM (1999) *Introduction to seismology*, Cambridge University Press, New York
- Sucuoğlu H (2013) Implications of masonry infill and partition damage on the performance perception in residential buildings after a moderate earthquake. *Earthquake Spectra* 29(2):661–668
- Turkish Ministry of Construction and Settlement (2007) *Design Code for Buildings in Seismic Regions*, Ankara
- Youngs RR, Coppersmith J (1985) Implications of fault slip rates and earthquake recurrence models to probabilistic seismic hazard assessments. *Bull Seismol Soc Am* 75:939–964
- Wells DL, Coppersmith J (1994) New empirical relationships among magnitude, rupture length, rupture width, rupture area, and surface displacement. *Bull Seismol Soc Am* 84:974–1002

Index

A

Accelerogram, 1, 24–26, 51
Accelerograph, 24, 25, 87
ACI 318, 242, 246, 247, 263
ASCE 7, 118, 124, 125, 128, 136, 141, 226, 231, 234, 242

B

Base isolated buildings
 critical issues, 197
 design displacement, 195
 effective period, 195
 effective stiffness, 195
 equivalent linear analysis, 195
 seismic isolation devices, 190
Base shear force
 base shear coefficient, 97
 minimum base shear force, 141, 172, 215
Behavior factor, 140
Building separations, 237

C

Capacity design, 141, 179, 241–243, 256, 270, 272
Confinement reinforcement, 244, 248, 266
Convection currents, 4, 6
Corner period(s), 109, 120–122, 134
Cramer's Rule, 153

D

Damage grades, 31, 32
Damping force, 146
Damping matrix
 Rayleigh damping, 149
Damping ratio, 80, 81, 86, 93, 135, 190, 192, 195
Damping scaling factor, 120, 123, 136

Degree(s) of freedom

 dynamic degrees of freedom, 145, 149, 150, 203, 204, 206
 static degrees of freedom, 149, 151, 205, 206

Demand

 displacement, 34, 100, 188, 281
 ductility, 108
 elastic force, 101, 108, 140
 strength, 98, 234

Design earthquake

 design spectrum, 141, 172, 215
 elastic design spectrum, 117–120, 124, 128, 135
 inelastic design spectrum, 117, 118, 137, 242
 type 1 spectrum, 119, 121, 122
 type 2 spectrum, 119, 121
 vertical design spectrum, 121, 132, 135, 142

Drift sensitivity coefficient, 236

Ductility

 ductility class, 141
 ductility in reinforced concrete, 241, 243, 246
 ductility ratio, 101, 106
 ordinary ductility, 141, 242
 special ductility, 242

Dynamic stiffness, 91

E

Earth Structure

 asthenosphere, 3, 4
 crust, 1, 3
 inner core, 1
 lithosphere, 3
 moho discontinuity, 2
 outer core, 1, 4

Earthquake induced landslide, 34, 38

- Earthquake recurrence models
 - a and b parameters, 72
 - characteristic recurrence model, 45
 - earthquake catalog, 42
 - Gutenberg-Richter recurrence model, 70
 - maximum magnitude, 44
 - mean annual rate of exceedance, 42, 44
 - minimum magnitude, 42
 - seismic activity, 42
 - truncated Gutenberg-Richter recurrence model, 45
 - Earthquakes
 - in slab, 10
 - interface, 10
 - interplate, 8, 10
 - intraplate, 8, 10
 - Eccentricity
 - accidental, 218, 233
 - amplification, 233
 - Effective force, 79, 98, 184
 - Effective modal mass, 165, 180
 - Effective stiffness, 84, 98
 - Eigenvalue analysis
 - buildings, 190, 203, 210
 - characteristic equation, 154, 211
 - eigenvalue, 153, 154
 - eigenvector, 153, 155
 - frames, 203, 210
 - trivial solution, 153
 - Elastic rebound theory, 14
 - Equal displacement rule, 110
 - Equation of motion
 - MDOF systems under earthquake base excitation, 148
 - MDOF systems under external force, 147
 - SDOF systems- direct equilibrium, 77
 - SDOF systems under earthquake base excitation, 147
 - SDOF systems under external force, 146
 - Equivalent static lateral load procedure, 215, 227, 232, 233
 - Eurocode 2, 242
 - Eurocode 8, 242, 246, 252, 263, 266
- F**
- Faults
 - dip angle, 16
 - footwall, 16
 - hanging wall, 16
 - normal fault, 16
 - oblique fault, 17
 - rake angle, 16
 - reverse fault, 16
 - strike, 16
 - strike-slip fault, 16, 17, 52, 57
 - thrust fault, 16
 - Forced vibration response
 - SDOF response to earthquake excitation, 87, 100, 160, 203, 250
 - SDOF response to harmonic base excitation, 85
 - Free vibration response
 - damped free vibration of SDOF systems, 75, 81, 85, 93, 96
 - undamped free vibration of SDOF systems, 75, 80, 81, 96, 112, 151
 - Frequency response function, 86
- G**
- Gondwanaland, 4
 - Ground motion attenuation, 26
 - Ground motion prediction equations, 50, 52, 57, 62
 - Ground motions
 - deterministic and probabilistic ground motions, 41, 124
 - maximum direction of ground motions, 128
- H**
- Hysteresis, 75, 98
 - Hysteresis model
 - elasto-plastic, 99, 100, 102, 110, 138
 - stiffness degrading, 99–102
- I**
- Importance factor, 119, 120, 122, 136, 137, 235
 - Inertial force, 34, 78, 149, 150, 204, 205, 229
 - Influence vector, 148, 205, 218
 - Intensity of earthquakes
 - European macroseismic scale (EMS), 30–32
 - macroseismic intensity, 1, 24, 28
 - modified mercalli (MM) scale, 30
 - MSK scale, 30
 - Intensity of ground motions
 - peak ground acceleration, 25, 41, 51, 119, 123
 - peak ground velocity, 41
 - spectral ordinates, 25, 50, 63, 64, 70, 118, 120, 121, 124, 125, 128, 130, 134, 136, 281
 - Interstory drift, 203, 230, 231, 233, 234, 241, 242

Interstory drift limitation, 233

Irregularities

in elevation, 231

in plan, 230, 232

Isoseismal map, 33

L

Lateral spreading, 37, 38

Laurasia, 4

Liquefaction, 34, 36, 37

M

Magnitude of earthquakes

body-wave magnitude, 21, 23

local magnitude, 21, 22

magnitude saturation, 22, 23

moment magnitude, 22, 24, 46

seismic moment, 22

surface-wave magnitude, 21, 23, 119, 121

Mass

distributed, 76, 204

lumped, 75, 147, 197

mass moment of inertia, 205

Mass matrix

diagonal mass matrix, building systems, 183

diagonal mass matrix, plane frames, 183

Material nonlinearity, 98

Maximum considered earthquake (MCE)

risk targeted maximum considered earthquake, 128

Mid-oceanic ridge, 4–6

Modal base shear force, 165, 180, 183, 192, 218

Modal combination rules

complete quadratic combination (CQC), 163

square root of the sum of squares (SRSS), 163

Modal displacement vector, 153, 174, 181

Modal expansion of displacements, 159

Modal superposition procedure

minimum number of modes, 218

modal damping, 160, 161, 163

modal damping ratio, 86

modal excitation factor, 160, 171

modal mass, 160

modal stiffness, 160

modal vibration frequency, 153, 161

Modal vector

modal force vectors, 170, 174, 180, 227

normalization of modal vectors, 157

orthogonality of modal vectors, 158, 160

Mode shapes, 215

coupled mode shapes, 213, 215

effect of building symmetry, 212

uncoupled mode shapes, 212

Multi degree of freedom (MDOF) systems, 145

N

Natural frequency of vibration, 80, 83, 86

Natural mode shapes, 152

NEHRP provisions, 117, 118, 124, 128–134, 136

Newmark's method, 87

Newton's law, 34, 77, 78, 84, 97, 147

Newton-Raphson iteration, 103

Nonlinear static (pushover) analysis, 138

capacity curve, 139, 186

plastic hinge, 139, 184, 247, 253, 265

roof displacement, 138, 189, 281

target displacement, 187, 189

Nonlinear systems, 100, 102, 108, 186

Numerical evaluation of dynamic response

constant average acceleration, 88

step-by-step direct integration, 87, 102

Numerical evaluation of nonlinear dynamic response

direction reversal, 103

slope change, 104

P

Pangaea, 4

performance requirements

life safety, 124, 229

limited damage, 137

no collapse, 137

Plane frame idealization, 183

Plate boundary

convergent, 6, 9

divergent, 6

transform, 7, 9, 17, 161

Plate tectonics, 5, 6

Poisson process, 46–48, 70

Pounding, 203, 237, 238

Probability

axioms of probability, 64

collectively exhaustive, 64, 65

conditional probability, 64, 67

cumulative distribution function, 69, 70

mutually exclusive, 64, 65

null event, 64

probability density function, 50, 53, 66

- probability mass function, 67
 - random variable, 63, 66
 - total probability theorem, 65, 66
- Probability distributions
 - log-normal distribution, 50, 124
 - normal distribution, 50, 124
 - uniform distribution, 229
- R**
- Reduction factor
 - ductility, 75, 108
 - overstrength, 140
- Resonance, 86, 87
- Response spectra
 - pseudo velocity, 95
 - acceleration, 93, 95, 99, 109
 - design, 95, 97, 109
 - displacement, 93, 94, 113
 - ductility, 75
 - inelastic, 109, 117
 - pseudo acceleration, 95, 113
 - strength, 75
- Response spectrum analysis, 145, 162, 203, 215, 217, 274–277
- Restoring force, 98, 102, 103
- Return period, 46, 49, 56, 57, 59, 72, 119, 124, 137, 228, 233
- Rigid floor diaphragm, 203, 205, 229
- Risk coefficients, 130, 133
- S**
- Sea-floor spreading, 4, 7
- Second order (P delta) effects, 203, 235, 237
- Seismic design
 - beam-column joints, 241, 260
 - beams, 241, 245, 246, 260
 - columns, 241, 245
 - shear walls, 241, 245
- Seismic Hazard Assessment
 - controlling earthquake scenario, 61
 - deterministic, 61, 124
 - hazard curve, 56
 - probabilistic, 41, 46, 53, 128
- Seismic regulations, 118
- Seismic sources
 - area sources, 42
 - faults, 42
- Seismic waves
 - love wave, 20
 - P-wave, 17, 19
 - Rayleigh wave, 20
 - S-wave, 17, 19
- Seismic weight, 225
- Shear design
 - beams, 248, 254
 - columns, 254, 278
- Shear frame, 145–148, 152, 166, 192, 195
- Shear stiffness, 146, 149
- Short column, 259, 260
- Simple harmonic motion, 75, 80, 154
- Single degree of freedom (SDOF) systems
 - ideal, 75–77
 - idealized, 76, 77
- Site amplification, 26, 125
- Site factors, 120, 125, 130
- Solution of second order ordinary differential equations (ODE)
 - homogeneous solution, 79
 - method of undetermined coefficients, 85
 - particular solution, 79, 85
 - general solution, 85
- Static condensation, 145, 149, 151, 167, 205
- Stiffness matrix
 - condensed stiffness matrix, 150, 168, 173, 207
 - direct stiffness method, 206, 209
 - stiffness coefficients, 207
 - stiffness coupling, 208, 214
 - tri-diagonal stiffness matrix, 147
- Strong column-weak beam, 241, 253, 269, 272
- Subduction, 4, 6, 8, 34
- T**
- Tectonic plates, 4, 8, 9, 16
- Tension shift, 268, 272
- Torsional coupling, 203, 211, 216
- U**
- Uniform hazard spectrum, 41, 63, 64, 121, 128
- United States Geological Survey, 12
- V**
- Volcanic activity, 5, 10, 12
- Vulnerability classes, 31, 32
- Y**
- Yield pseudo acceleration, 188